CENTRO DE INVESTIGACIÓN Y DE ESTUDIOS AVANZADOS DEL INSTITUTO POLITÉCNICO NACIONAL

UNIDAD ZACATENCO

PROGRAMA DE DOCTORADO EN
NANOCIENCIAS Y NANOTECNOLOGÍA

“Céldas solares de perovskita híbridas basadas en formamidinio-cesio (FA-Cs): una simulación completa y un análisis experimental.”

TESIS

Que presenta

Karthick SEKAR

Para obtener el grado de

DOCTOR EN CIENCIAS

EN

NANOCIENCIAS Y NANOTECNOLOGÍA

Directores de la Tesis

Dr. Velumani Subramaniam (CINVESTAV-IPN, México)

Dr. Johann Bouclé (Xlim, Limoges University, Francia)

Ciudad de México, México Marzo 2021

CENTER FOR RESEARCH AND ADVANCED STUDIES OF THE NATIONAL POLYTECHNIC INSTITUTE

ZACATENCO UNIT

DOCTORATE PROGRAM IN
NANOSCIENCES AND NANOTECHNOLOGY

"Formamidinium- Cesium (FA-Cs) based hybrid perovskite solar cells: A comprehensive simulation and experimental analysis."

THESIS

Presented by

Karthick SEKAR

To obtain the degree of
DOCTORATE IN SCIENCE

IN
NANOSCIENCE AND NANOTECHNOLOGY

Thesis Directors
Dr. Velumani Subramaniam (CINVESTAV-IPN, Mexico)
Dr. Johann Bouclé (Xlim, Limoges University, France)

Mexico City, Mexico March 2021

ABSTRACT

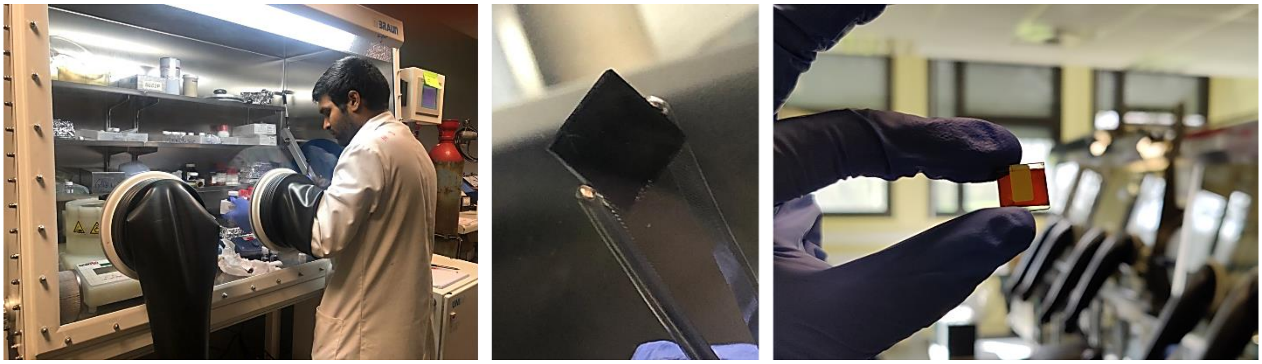

In a short period, the hybrid organic-inorganic perovskite solar cells demonstrated a higher power conversion efficiency (PCE) than other solar cells. However, the stability and toxicity issues restrict from entering into commercialization. Therefore, this thesis aims to tackle both mentioned issues to enhance the solar cell photovoltaic (PV) performance from a laboratory perspective. Especially, doping with cesium and bromide into formamidinium lead iodide ($FAPbI_3$) perovskite to improve the phase stability. Also, using Copper and Bismuth is particularly relevant to diminish the lead content in the active layer while reducing the intrinsic limitations of $FAPbI_3$ devices in terms of stability and defect states. Additionally, the $FAPbI_3$ perovskite structure was modeled using Materials Studio *software*, and the numerical simulation of various solar cell models developed using SCAPS-1D *software*, which provides a physics insight into its operation. Both experimental and theoretical analyses allow us to understand the charge generation mechanism and the limitations of device current-voltage characteristics based on different doping/interlayer strategies over the perovskite composition to improve the device performance.

The structural and mechanical stability behavior of the α-phase $FAPbI_3$ unit cell was systematically investigated based on all the twelve possible orientations of organic FA cation inside the inorganic cubic cage. The lattice parameters, iodine shift, elastic-constant values, electron density difference (EDD), and Mulliken charge analysis provide factual justifications to understand the mechanism. From the computational perspective, the stable structure was found while applying an initial amplitude limit (0.02), which is attributed to the balanced charge distribution in between the hydrogens (H_4, H_5, and H_2, H_3) to the specific iodine (I_2) atom. Surprisingly, with increasing

amplitude (0.04), the structure was unstable due to their disturbed charge distribution and FA cation tilting as found from the EDD spectrum.

Experimental PV performance and their numerical SCAPS-1D simulations are compared for methylammonium-free perovskite solar devices based on the FA organic cation absorbers (i.e., Pristine $FAPbI_3$, $FA_{0.85}Cs_{0.15}PbI_3$, and $FA_{0.85}Cs_{0.15}Pb(I_{0.85}Br_{0.15})_3$). Experimentally, it is established that the incorporation of small amounts of cesium and bromide into $FAPbI_3$ stabilizes the optically active $\alpha - FAPbI_3$ black phase and boosts the PCE of associated devices from 4 to 15% under standard illumination. The effect of series and shunt resistances was theoretically evaluated and discussed by modeling the cell's electrical characteristics as a function of active layer composition using the SCAPS-1D *software*. Ideal devices built without these parasitic resistances do not match the experimental trends, although they reflect the influence of bandgap edge on the photocurrent generation. Feeding the experimental R_{series} and R_{shunt} values to SCAPS allows us to interpret the main limitations to the device current-voltage characteristics. The pure $FAPbI_3$ phase's instability is responsible for the drastic deterioration in R_{series} and R_{shunt}, ultimately influencing the fill factor. These results clearly confirm the beneficial effect of mixed cation and mixed halides on device operation.

The effect of copper iodide (CuI) and Bismuth iodide (BiI_3) partial incorporation into the $FA_{0.85}Cs_{0.15}Pb(I_{0.85}Br_{0.15})_3$ perovskite structure was systematically investigated as a function of the atomic fraction (x) of CuI or BiI_3 instead of PbI_2, using structural, morphological, and optical characterization techniques. CuI or BiI_3 doped solar cells exhibit reduced performance than the undoped device due to the evolution of active layer morphology and structure, along with faster recombination kinetics probed by transient photovoltage measurements. The doping by the trivalent metallic cation (Bi) largely perturbs the perovskite structure compared to the substitution of monovalent metal (Cu). Furthermore, the effect of BiI_3 interfacial layer (IL) with different hole transport layers (HTL) and various electrodes in $FA_{0.85}Cs_{0.15}Pb(I_{0.85}Br_{0.15})_3$ device models were numerically investigated using SCAPS-1D. The addition of a thin BiI_3 layer at the interface between the Perovskite active layer and the HTL efficiently improves hole extraction by defect passivation, enhancing the device PV performance. The energy band misalignment between the HTL and the metallic top electrode restricts charge collection, directly associated with low work

functions. As a result, high work function electrodes such as Au, Ni, and Pt have to be preferred in the presence or absence of the interlayer.

Keywords: formamidinium-lead-iodide-perovskite, density-functional-theory, van der Waals, elastic constant, stability, perovskite solar cells, SCAPS-1D simulation, series and shunt resistances, Copper iodide, Bismuth iodide, interfacial layer, HTL.

RESUMEN

En un corto período las céldas solares híbridas, orgánica-inorgánica, con estructura tipo perovskita demostraron tener una mayor eficiencia de conversión de energía (PCE) que otras céldas solares. Sin embargo, los problemas de estabilidad y toxicidad restringen su comercialización. Por lo tanto, esta tesis tiene como objetivo abordar ambos problemas para mejorar el rendimiento de la célda solar fotovoltaica (PV) desde una perspectiva de laboratorio. Especialmente, al dopar con cesio y bromo la perovskita de yoduro de plomo formamidinio ($FAPbI_3$) para mejorar la estabilidad de la fase. Además, el uso de cobre y bismuto es particularmente relevante para disminuir el contenido de plomo en la capa activa al tiempo que reduce las limitaciones intrínsecas de los dispositivos $FAPbI_3$ en términos de estabilidad y estados de defectos. Además, la estructura perovskita de $FAPbI_3$ modelada con el *software* Materials Studio y la simulación numérica de varios modelos de céldas solares desarrollados con el *software* SCAPS-1D, proporciona una visión física de su funcionamiento. Tanto el análisis experimental como el teórico nos permite comprender el mecanismo de generación de carga y las limitaciones de las características de corriente-voltaje del dispositivo en función de diferentes estrategias de dopaje / capa intermedia sobre la composición de la perovskita para mejorar el rendimiento del dispositivo.

El comportamiento de la estabilidad estructural y mecánica de la célda unitaria de $FAPbI_3$ de fase t α se investigó sistemáticamente basándose en las doce posibles orientaciones del catión orgánico FA dentro de la sub-red cúbica inorgánica. Los parámetros de red, el desplazamiento de los átomos de yodo, los valores de la constante elástica, la diferencia de la densidad de electrones (EDD) y el análisis de carga de Mulliken proporcionan justificaciones fácticas para comprender el mecanismo. Desde la perspectiva computacional, la estructura estable se encontró aplicando como límite la amplitud inicial (0.02), el cual se atribuye a la distribución de carga equilibrada entre los hidrógenos (H_4, H_5 y H_2, H_3) y el átomo de yodo específico (I_2). Sorprendentemente, al aumentar la amplitud a (0,04), la estructura era inestable debido a su distribución de carga alterada y a la inclinación de los cationes FA como se encuentra en el espectro de EDD.

El rendimiento fotovoltaico experimental y sus simulaciones numéricas de SCAPS-1D se compararon para dispositivos solares de tipo perovskita sin metilamonio basados en los absorbentes de cationes orgánicos FA (es decir, Pristine $FAPbI_3$, $FA_{0.85}Cs_{0.15}PbI_3$ y $FA_{0.85}Cs_{0.15}Pb(I_{0.85}Br_{0.15})_3$).

Experimentalmente, se establece que la incorporación de pequeñas cantidades de cesio y bromo en $FAPbI_3$ estabiliza la fase α-$FAPbI_3$ ópticamente activa y aumenta la PCE de los dispositivos asociados del 4 al 15% bajo iluminación estándar. El efecto de las resistencias en serie y de fuga se evaluó y discutió teóricamente modelando las características eléctricas de la célda en función de la composición de la capa activa, utilizando el *software* SCAPS-1D. Los dispositivos ideales construidos sin estas resistencias espurias no coinciden con las tendencias experimentales, aunque reflejan la influencia del margen de la banda prohibida en la generación de fotocorriente. La alimentación de los valores experimentales de R_{series} y R_{shunt} en SCAPS permite interpretar las principales limitaciones de las características de corriente-voltaje del dispositivo. La inestabilidad de la fase $FAPbI_3$ pura es responsable del drástico deterioro en R_{series} y R_{shunt}, lo que en última instancia influye en el factor de llenado. Estos resultados confirman claramente el efecto benéfico de la mezcla del catión y haluros en el funcionamiento del dispositivo.

El efecto de la incorporación parcial de yoduro de cobre (CuI) y yoduro de bismuto (BiI_3) en la perovskita $FA_{0.85}Cs_{0.15}Pb(I_{0.85}Br_{0.15})_3$ se investigó sistemáticamente en función de la fracción atómica (x) de CuI o BiI_3 que sustituye a PbI_2, utilizando técnicas de caracterización estructural, morfológica y óptica. Las células solares dopadas con CuI o BiI_3 exhiben un rendimiento reducido respecto al dispositivo no dopado debido a la evolución de la estructura y morfología de la capa activa, junto con una cinética de recombinación más rápida probada por mediciones de fotovoltaje transitorio. El dopaje por el catión metálico trivalente (Bi) perturba en gran medida la estructura de la perovskita en comparación con la sustitución del metal monovalente (Cu). Además, el efecto de la capa interfacial BiI_3 (IL) con diferentes capas de transporte de huecos (HTL) y varios electrodos en modelos de dispositivo $FA_{0.85}Cs_{0.15}Pb(I_{0.85}Br_{0.15})_3$ se investigaron numéricamente utilizando SCAPS-1D. La adición de una capa delgada de BiI_3 en la interfaz entre la capa activa de Perovskita y el HTL mejora de manera eficiente la extracción de huecos por pasivación de defectos, mejorando el rendimiento PV del dispositivo. La desalineación de las bandas de energía entre del HTL y del electrodo superior metálico restringe la recolección de carga, directamente asociada con las funciones de trabajo bajas. Como resultado, los electrodos de alta función de trabajo alta tales como Au, Ni y Pt se deben de preferir ya sea en presencia o ausencia de la capa intercapa.

Palabras clave: formamidinio-yoduro-plomo-perovskita, teoría funcional de la densidad, van der Waals, constante elástica, estabilidad, céldas solares con estructura perovskita, simulación SCAPS-1D, resistencias en serie y de fuga, yoduro de cobre, yoduro de bismuto, capa interfacial, HTL.

Title (in French): “Cellules solaires pérovskite hybrides à base de formamidinium-césium (FA-Cs) : simulation et analyse expérimentale."

En peu de temps, les cellules solaires hybrides pérovskites organique-inorganiques ont démontré une efficacité de conversion d'énergie (PCE) très impressionante. Cependant, la stabilité réduite et la toxicité intrinsèque liée au Plomb sont un frein à leur future commercialisation. Cette thèse propose ainsi plusieurs stratégies pour adresser ces limitations, aussi bien d’un point de vue des simulation numériques que par une approche expérimentale. Dans un premier temps, l’utilisation d’un cation (Cs) et d’un halogène (Br) additionels permettent d’envisager une meilleure stabilité de la phase référence $FAPbI_3$ (*formamidinium lead iodide*). Ainsi, nous avons comparé les performances photovoltaïques expérimentales et simulées (à l’aide du logiciel SCAPS-1D) en fonction de la composition de la pérovskite. Il est ainsi établi que l'incorporation de petites quantités de Cs et de Br permet de stabiliser la phase pérovskite optiquement active, conduisant à une augmentation significative du rendement de conversion de puissance de 4 à 15% sous illumination standard. L'effet des résistances parasites a de plus été théoriquement évalué et discuté.

Dans un second temps, nous avons cherché à réduire la teneur en plomb par un dopage avec du Cuivre ou du Bismuth par un ajout de d'iodure de cuivre (CuI) ou d'iodure de bismuth (BiI_3) dans la solution précurseur permettant le dépôt de la couche active, en observant l’influence de ces éléments sur les performances et la stabilité des dispositifs fabriqués à l’échelle du laboratoire. Les cellules solaires dopées Cu ou Bi présentent des performances réduites par rapport au dispositif non dopé en raison de l'évolution de la morphologie et de la structure de la couche active, ainsi que d'une cinétique de recombinaison plus rapide sondée par des mesures de photo-tensions résolus en temps. Des simulations numériques utilisant SCPAS-1D ont en parallèle permis de préciser l’influence d’une couche interfaciale de BiI_3 associée à différentes couches de transport de trous (HTL) et diverses électrodes. Cette dernière améliore efficacement l'extraction des trous par passivation des défauts, améliorant les performances PV du dispositif.

En parallèle, la structure de la pérovskite $FAPbI_3$ a été modélisée à l'aide du logiciel Materials Studio afin d’identifier les processus fondamentaux en lien avec la présence du cation organique. Le comportement de stabilité structurelle et mécanique de la cellule unitaire $FAPbI_3$ en phase α a été systématiquement étudié sur la base des douze orientations possibles du cation organique formamidinium (FA) à l'intérieur de la cage cubique inorganique. Les paramètres de réseau, le déplacement de l'iode, les valeurs de constante élastique, la différence de densité électronique (EDD) et l'analyse de charge Mulliken fournissent des justifications factuelles pour préciser les phénomènes mis en jeu.

Mots clés: pérovskites halogénées, FAPI, théorie de la fonctionnelle de la densité, van der Waals, constante élastique, stabilité, cellules solaires pérovskite, simulation SCAPS-1D, résistances série et shunt, iodure de cuivre, iodure de bismuth, couche interfaciale, HTL.

ACKNOWLEDGEMENT

First, I would like to thank my thesis supervisors Prof. Velumani Subramaniam, CINVESTAV-IPN, Mexico, and Prof. Johann Bouclé, XLIM, University of Limoges, France, for their guidance throughout my thesis's contract. Their knowledge about semiconductor device physics and their invaluable suggestions helped me a lot to complete the task. I also express my gratitude to my committee members Prof. Arturo Maldonado Alvarez, Prof. Yasuhiro Matsumoto Kuwahara, Prof. Mauricio Ortega Lopez, Prof. José Á. Chávez-Carvayar, Prof. Miguel Garcia Rocha, Prof. Jacky Even, Prof. Dmitry Aldakov for their valuable supports and suggestions. This thesis work would not have been possible without the institutions, Centro de Investigación y de Estudios Avanzados del Instituto Politécnico Nacional (CINVESTAV-IPN) and the Université de Limoges (XLIM), France. Mainly, I would like to thank the Consejo Nacional de Ciencia y Tecnología (the National Council of Science and Technology – simply CONACYT) scholarship program of Mexico for providing invaluable support throughout my doctorate (CONACYT-SENER 263043 project SEP-CINVESTAV-200, and CeMIE Sol P-55). Also, I am grateful to the ELITE groups - Printed Electronics for Telecoms and Energy, Institut de recherche (XLIM), France, for hosting my research visits and guaranteeing that my stay was enjoyable throughout.

Prof. Bernard Ratier, Prof. Rémi Antony, Prof. Sylvain Vedraine, Dr. Eman A. Gaml (Damietta University, Egypt), Dr. Talaat Abdel Hamid (National Research Centre, Egypt), and Hesham Hawashin all are must be acknowledged for sharing their knowledge with me regarding the fabrication and characterization of perovskite solar cells (in France). I also express my gratitude to Nicolas Parou (Technician) for helping me through my lab work in XLIM, France.

In addition, I would like to thank several of my colleagues in CINVESTA-IPN, Mexico, and XLIM, France, who have become good friends throughout my thesis. Special thanks to Dr. José Jorge Ríos Ramírez for introducing me to the simulation world in my first year. His valuable supports and guidance always boost my self-confidence level to move forward. I am grateful to Srikanth Chakaravarthy, Dr. Vinoth Kumar Jayaraman, and Dr. Ravichandran Manisekaran for their research and outfield guidelines. And, I would like to acknowledge Dr. Jaime Vega Pérez, Dra. Myriam Solís Lopez, Dra. Araceli Romero Nuñez, and my other CINVESTAV-IPN group members Mercyrani Babudurai, Nwakanma Onyekachi Michael, Drisya Karathuparathottathil

Damodharan, Christeena Theresa Thomas, Ganesh Regmi, Ashok Adhikari, Ing. Francisco Álvarado César, Josué Raúl Ramírez Paulino, and Ayde Fernanda Rivera Lima. I would like to thank Goban and Sandeep for their lovable support always. I also express my gratitude to Prof. José Gerardo Cabañas Moreno (coordinator) and all other faculty and employees in the Nanoscience and Nanotechnology program, CINVESTAV, and Xlim faculty members for their complete support throughout my Ph.D. program.

Besides, I would like to be grateful to Prof. Rajni Swamy, Dr. Vivekanandha, and their family from the bottom of my heart for helping me through a tough time and who taught me to improve myself in every situation. I'm also thankful to Dr. R. Srinivasan for his invaluable supports.

Finally, I would like to thank all my family members, especially my parents (Mr. Sekar and Mrs. Meena) and my brothers (Mr. Muthukumaran and Mr. Bala Murugan) and my friends, who believed, supported, and loved me unconditionally. My special thanks to my lovable family kids, Shanmugavel, Raja Lakshmi, Sabari, Raja Ruban, and Karthick, for their innocent love to make me happy in all the situations.

"*Difficulties in your life do not come to destroy you but to help you realize your hidden potential and power. Let difficulties know that you are too difficult*."

- Dr. A. P. J. Abdul Kalam.

தெய்வத்தான் ஆகா தெனினும் முயற்சிதன்

மெய்வருத்தக் கூலி தரும்.

- திருவள்ளுவர்.

Thank you all.

With regards,

Karthick SEKAR.

Table of Contents

1. CHAPTER – I. INTRODUCTION TO PEROVSKITE MATERIALS AND SOLAR CELLS 1

1.1. LITERATURE REVIEW 1

1.1.1. Solar cell technology 2

1.1.2. Perovskite structure 4

1.1.3. Perovskite solar cells 5

1.1.4. $FAPbI3$ Crystal structure and its phase transition 11

1.1.5. Mixed cation $FAPbI3$ Perovskites 15

1.1.6. Low Pb content Perovskites 17

1.1.7. Conclusion 18

1.2. OBJECTIVE AND BRIEF OUTLINE OF THE THESIS 19

REFERENCES 20

2. CHAPTER II. THEORY AND SIMULATIONS 30

2.1. MATERIALS STUDIO (MS) SIMULATION *SOFTWARE* 30

2.2. CASTEP 30

2.2.1. Pseudopotential description 31

2.2.2. Geometry optimization 32

2.2.3. Dialogs in MS-CASTEP 32

2.3. CONSTRUCTION OF FORMAMIDINIUM (FA) LEAD IODIDE ($FAPbI3$) PEROVSKITE UNIT CELL 33

2.3.1. Construction of $FAPbI3$ perovskite Supercells 35

2.3.2. Computational details of $FAPbI3$ perovskite Structure 36

2.3.3. Elastic constant calculations 36

2.3.4. Electron density difference (EDD) analysis 41

2.3.5. Mulliken charge (MC) population analysis 42

REFERENCES 43

3. CHAPTER III. EXPERIMENTAL DETAILS 46

3.1. MATERIALS 46

3.2. FTO SUBSTRATE ETCHING AND CLEANING 46

3.3. PRECURSOR'S PREPARATION - SOLUTION PROCESS METHOD 47

3.3.1. Preparation of Tin oxide (SnO_2) solution 47

3.3.2. Preparation of Formamidinium lead iodide ($FAPbI_3$) perovskite solution 48

3.3.3. Preparation of Cesium and Bromide doped perovskite ($FACsPbI_3$ and ($FACsPb(IBr)_3$) solutions 48

3.3.4. Preparation of Copper iodide (CuI) and Bismuth iodide (BiI_3) incorporated perovskite ($FACsPb(IBr)_3)Mx$) (where M=CuI or BiI) solution 49

3.3.5. Preparation of Spiro-OMeTAD solution 49

3.4. THIN-FILM CHARACTERIZATIONS 50

REFERENCES 51

4. CHAPTER IV. SOLAR CELL FABRICATION 52

4.1. FRONT CONTACT FTO 52

4.2. DEPOSITION OF THE ELECTRON TRANSPORT LAYER (ETL – SnO_2) 52

4.3. DEPOSITION OF DIFFERENT PEROVSKITE ABSORBER LAYERS BY ONE-STEP SOLUTION PROCESS WITH ANTISOLVENT TREATMENT 53

4.4. Deposition of the hole transport layer (HTL – Spiro-OMeTAD) 53
4.5. Deposition of gold (Au) electrode 54
4.6. Solar cell Characterizations 55
  4.6.1. Current density- Voltage (I-V) measurement 55
  4.6.2. External quantum efficiency (EQE) measurement 58
  4.6.3. Initial device stability (or aging) measurement 59
References 60

5. CHAPTER V. NUMERICAL SIMULATION – SCAPS – 1D 61

5.1. SCAPS-1D 61
5.2. Advantages and limitations in SCAPS-1D 65
5.3. Numerical simulation of ideal perovskite devices using SCAPS-1D 66
5.4. Numerical simulation of ideal perovskite devices with BiI$_3$ – interlayer 68
References 71

6. CHAPTER VI. STRUCTURAL AND MECHANICAL STABILITY BEHAVIOR OF FAPBX$_3$ PEROVSKITES. 74

6.1. Introduction 74
6.2. Result and discussion 76
  6.2.1. 12 Possible Orientations of organic Formamidinium cation and its structural analysis using vdW+DFT 76
  6.2.2. Stability threshold of FAPbI$_3$ determined by strain amplitudes 82
  6.2.3. Mechanical stability study of bulk FABX$_3$ perovskites 96
6.3. Conclusion 101
References 102

7. CHAPTER VII. EXPERIMENTAL AND SCAPS SIMULATED FORMAMIDINIUM PEROVSKITE SOLAR CELLS: A COMPARISON OF DEVICE PERFORMANCE. 104

7.1. Introduction 104
7.2. Results and Discussion 105
  7.2.1. Determination of the absorber layer bandgaps 105
  7.2.2. Simulation of ideal devices 106
  7.2.3. Experimental devices 109
  7.2.4. Effect of $Rseries$ *and* $Rshunt$ *..... 115*
7.3. Conclusion 118
References 118

8. CHAPTER VIII. EFFECT OF COPPER IODIDE AND BISMUTH IODIDE INCORPORATION INTO THE FA-CS PEROVSKITE SOLAR CELLS. 121

8.1. Introduction 121
8.2. Results and Discussion 122
  8.2.1. CuI and BiI$_3$ incorporated mixed cation perovskite solar cells 122
  8.2.2. BiI$_3$ interfacial layer with different HTL's in FA-Cs perovskite solar cell – SCAPS - 1D study . 146
8.3. Conclusion 167
References 168
General conclusion 176
Future directions 178

LIST OF PUBLICATIONS 179

ANNEX I 180

LIST OF FIGURES

Fig. 1.1. *Electricity generation from listed fuels [1].* *1*
Fig. 1.2. *Solar cell structure [4].* *2*
Fig. 1.3. *PV technology classifications and the perovskite solar cell efficiency chart [5]–[7].* *3*
Fig. 1.4. *General perovskite cubic structure.* *4*
Fig. 1.5. *The ideal cubic perovskite unit cell. (A) A-cations (blue) occupy the lattice corners, B cations (green) occupy the interstitial site, and X anions (red) occupy lattice faces. (B) An alternative view depicting B cations assembled around X anions to form* $BX6$ *octahedra, as* $B - X$ *bonds are responsible for determining electrical properties. (C) Tilting of* $BX6$ *octahedra occurring from nonideal size effects and other factors, inducing strain on the B-X bonds. Reprinted from ref [12], Nano Today. 10 (2015) 355-396, DOI: https://doi.org/10.1016/j.nantod.2015.04.009.* *5*
Fig. 1.6. *The tolerance and octahedral factors for different perovskite compounds. Reprinted from ref [23], Rev. Adv. Mater. Sci. 2020; 59:264–305, DOI: https://doi.org/10.1515/rams-2020-0015.* *7*
Fig. 1.7. *Schematics of frequently used device configurations in perovskite solar cells.* *9*
Fig. 1.8. *Schematic of thermal decomposition reaction of formamidine [114], [117].* *13*
Fig. 2.1. *Representation of conventional* $FAPbI3$ *Perovskite unit cell, and each carbon atom positions.* *34*
Fig. 2.2. *Representation of the twelve different orientations of the FA cation in XY, YZ, and XZ planes (top left to right 12'o clock, 3'o clock, 6'o clock, and 9'o clock).* *34*
Fig. 2.3. *Representation of 211, 311, and 411 supercell models of* $FAPbI3$ *Perovskite structure.* *35*
Fig. 2.4. *EDD graph of* $FAPbI3$ *Perovskite structure.* *42*
Fig. 3.1. *Represents the FTO substrate dimension and covering procedures.* *47*
Fig. 3.2. *Schematic of ETL solution preparation procedures.* *48*
Fig. 3.3. *Schematic of absorber layer solution making procedures.* *49*
Fig. 3.4. *Schematic of HTL solution preparation procedures.* *50*
Fig. 4.1. *Schematic of ETL deposition procedures.* *52*
Fig. 4.2. *Schematic of perovskite absorber layer deposition.* *53*
Fig. 4.3. *Schematic of HTL layer deposition.* *54*
Fig. 4.4. *Schematic of Au contact deposition.* *54*
Fig. 4.5. *Schematic of the complete perovskite device.* *55*
Fig. 4.6. *Schematic representation of a solar cell equivalent circuit under illumination.* *55*
Fig. 4.7. *Schematic of the solar simulator and the representation of typical I-V curve of an illuminated solar cell.* ... *57*
Fig. 4.8. *Effect of parasitic resistances* $(Rseries\ and\ Rshunt)$ *on the J-V characteristics of a solar cell.* *58*
Fig. 4.9. *A typical EQE curve (https://www.pveducation.org), and with EQE equipment.* *59*
Fig. 5.1. *SCAPS-1D software startup panel setup.* *63*
Fig. 5.2. *SCAPS-1D solar cell definition panel (a) with Perovskite structure (b).* *64*
Fig. 5.3. *Material and defect definition panel in SCAPS-1D for the Perovskite layer.* *65*
Fig. 5.4. *Simplified flat band energy diagram of ETL, HTL and pristine* $FAPbI3$ *(D-A),* $FA0.85Cs0.15PbI3$ *(D-B) and* $FA0.85Cs0.15Pb(I0.85Br0.15)3$ *(D-C) perovskite active layers.* *67*
Fig. 5.5. *The n-i-p typical perovskite solar cell structure (left) and with* $BiI3$ *IL (right).* *69*
Fig. 5.6. *Band alignments between ETL, different HTL's with perovskite absorber, including* $BiI3$ *IL.* *70*
Fig. 6.1. *Results of energy, volume, lattice parameters, b/a, and c/a ratios for all 12 orientations of* $FAPbI_3$*. In this graph, x-axis indicate each orientation like (1, 2, 3, 4 = 12, 03,06, 09'o clock in XY plane) (5, 6, 7, 8=12, 03,06, 09'o clock in YZ plane) (9, 10, 11, 12=12, 03, 06, 09'o clock in XZ plane). For all the orientations, we get the energy range of ~-3380 eV, and we subtract that value for all the 12 orientations in order to compute the values in the same graph. The same procedure followed in the unit cell volume also (~261 - 262 Å*^{3}*), and finally, the lattice parameters are in the range of Å.* *77*
Fig. 6.2. *Calculated delta difference of iodine movement for all the 12 orientations of FA cation. This graph follows the same notation in the x-axis as in* ***Fig. 6.1*** *and the y-axis in the range of Å.* *79*
Fig. 6.3. *The calculated electron density difference for XY plane 12'o clock FA cation orientation.* *80*
Fig. 6.4. *General representation of the orthorhombic strain tensors. The top three show the uniaxial (from left to right:* D_1*,* D_2*,* D_3*) and planar (middle from left to right:* D_4*,* D_5*,* D_6*) bottom from left to right:* D_7*,* D_8*,* D_9*). The top three*

figures indicate uniaxial-$\delta_{\parallel}$, uniaxial-$\delta_{\perp}$, uniaxial-$\delta_{regular}$, from left to right, respectively. Both the middle and bottom rows of the Figure are referred to as planar-$\delta_{\parallel}$, planar-$\delta_{\perp}$, planar-$\delta_{regular}$ deformations, respectively. 84
Fig. 6.5. Electron Density Difference (EDD) of a strained lattice generated at the boundary of a uniaxial deformation (uniaxial-δregular, uniaxial-δ∥, and uniaxial-δ⊥, from left to right). Blue-White-Red spectrum displays the electron lack to enrichment, showing a marked diminish of the charge distribution among H_3-I_2 & H_2-I_2, for both uniaxial-δ∥ and uniaxial-δ⊥, with respect to the uniaxial-δregular. 86
Fig. 6.6. The figures displayed from (a) to (c) show the ΔEi vs. δi plots along with their respective EC values, from (d) to (f), determined within the strain amplitude δmax<0.02. The associated c_{11}, c_{22}, and c_{33} values show a fluctuating behavior, among three possible elastic responses, as a result of a combination of the FA orientation and the uniaxial deformation case (uniaxial-δregular, uniaxial-δ∥, and uniaxial-δ⊥). The first four points of the orientation-axis displayed from (d) to (f)) correspond to the [XY] FA plane alignment, meanwhile, the remaining two sets of four points hold for both [YZ] and [XZ] FA planes, respectively, all of them following the order: 12:00 to 9:00, in clockwise FA alignments. The calculated uncertainty from every c_{ii} value is depicted by error bars centered at each point, and the shape symbol of the possible results correspond to the respective ΔEi vs. δi plots from which it's determined. 87
Fig. 6.7. (a) to (c) show the ΔEi vs. δi plots along with their respective EC values, from (d) to (f), determined within the strain amplitude δmax<0.02. The associated c_{44}, c_{55}, and c_{66} values show a fluctuating behavior, among three possible elastic responses, as a result of a combination of the FA orientation and the planar deformation case (planar-δregular, planar-δ∥, planar-δ⊥). The first four points of the orientation-axis (displayed from (d) to (f)) correspond to the [XY] FA plane alignment, meanwhile, the remaining two sets of four points hold for both [YZ] and [XZ] FA planes, respectively, all of them following the order: 12:00 to 9:00, in clockwise FA alignments. The calculated uncertainty from every cii value is depicted by error bars centered at each point, and the shape symbol of the possible results correspond to the respective ΔEi vs. δi plots from which it's determined. 88
Fig. 6.8. The figures displayed from (a) to (c) show the ΔEi vs. δi plots along with their respective EC values, from (d) to (f), determined within the strain amplitude δmax<0.02. The associated c_{12}, c_{13}, and c_{23} values show a fluctuating behavior, among three possible elastic responses, as a result of a combination of the FA orientation and the planar deformation case (planar-δregular, planar-δ∥, planar-δ⊥). The first four points of the orientation-axis displayed from (d) to (f)) correspond to the [XY] FA plane alignment, meanwhile, the remaining two sets of four points hold for both [YZ] and [XZ] FA planes, respectively, all of them following the order: 12:00 to 9:00, in clockwise FA alignments. The calculated uncertainty from every c_ii value is depicted by error bars centered at each point, and the shape symbol of the possible results correspond to the respective ΔEi vs. δi plots from which it's determined................................ 89
Fig. 6.9. Deformation energies obtained for the strain tensors: D_4, D_5, and D_6 (from left to right) applied to the ground state of the [XY] FA 12 o'clock, under the strain amplitude δmax=0.04. The planar-δ∥ strain shows only energy points below the ground state maximum, generating a negative c_{55} value at the strain amplitudes...................................... 93
Fig. 6.10. The EDD plots at the strain boundaries for the elastic components: c_{44}, c_{55}, and c_{66} of the [XY] FA 12 o'clock configurations, the results are shown for both δmax<0.02 and δmax>0.02 strain amplitudes. Blue-White-Red spectrum displays the electron lack to enrichment, showing a marked charge transfer that describes the FA cation tilting, around the C-H_1 axis for the exchange of the iodine position and around the plane axis while transferring the charge among hydrogen terminations, for c_{66}, at the structure instability state, respectively. 95
Fig. 6.11. $FABX_3$ cubic representation. Where B is lead (Pb) or tin (Sn); X_1 is I_1, Cl_1, Br_1; X_2 is I_2, Cl_2, Br_2, and X_3 is I_3, Cl_3, Br_3.. 97
Fig. 6.12. Results of lattice parameters (a, b, c), volume, and ground-state energy for optimized $FAMX_3$ structures. In X-axis 1, 2, 3, 4, 5 and 6 belongs to $FAPbI_3$, $FAPbBr_3$, $FAPbCl_3$, $FASnI_3$, $FASnBr_3$, $FASnCl_3$, respectively. 98
Fig. 7.1. UV-visible absorbance spectra of pristine $FAPbI3$, $FA0.85Cs0.15PbI3$, and $FA0.85Cs0.15Pb(I0.85Br0.15)3$ perovskite films. The inset shows the corresponding Tauc's plot used for bandgap calculations. 106
Fig. 7.2. Simulated J-V characteristics of ideal D-A, D-B, and D-C perovskite devices, respectively. 108
Fig. 7.3. Cross-sectional SEM image of FTO/ $SnO2$/ $FA0.85Cs0.15Pb(I0.85Br0.15)3$/Spiro/Au device. 109
Fig. 7.4. Experimental J-V characteristics of D-A, D-B, and D-C perovskite devices, respectively. 110
Fig. 7.5. Photographs of fresh (top) and exposed to air for 10 min (bottom) D-A, D-B, and D-C devices. 111
Fig. 7.6. External quantum efficiency spectra of experimental and simulated (D-A, D-B, and D-C) perovskite solar cells. 113

Fig. 7.7. Effect of $Rseries$ in the performance of simulated D-A, D-B, and D-C devices. $Rshunt$ is assumed as infinite in this case 116

Fig. 7.8. Simulated J-V characteristic results of D-A, D-B, and D-C 117

Fig. 8.1. SEM photographs of undoped $FA0.85Cs0.15Pb(I0.85Br0.15)3$ as well as both Cu and Bi - doped perovskite films. Scale bar: 500 nano-meter 124

Fig. 8.2. AFM topographical images of undoped $FA0.85Cs0.15Pb(I0.85Br0.15)3$, as well as both Cu- and Bi-doped perovskite films. Horizontal scale bar: 2 µm. 125

Fig. 8.3. SEM and AFM images corresponding to fully doped $Cu100\%$ and $Bi100\%$ layers. Scale bar: 500 nm for SEM and Horizontal scale bar: 2 µm for AFM images. 126

Fig. 8.4. XRD diffractogram of Cu-doped (a) and Bi-doped (b) perovskite films, including the undoped reference. In the XRD patterns, □ symbols represent the reference $FACsPbIBr$ crystalline α - phase and * represent the presence of $PbI2$ phase. 128

Fig. 8.5. Magnified XRD diffractogram of 100 planes for Cu (a) and Bi (b) doped perovskite films. Evolution of the FWHM (c) of the perovskite (100) plane around $2\theta = 14.2°$ as a function of doping ratio x in both cases. 129

Fig. 8.6. Recorded XRD diffractogram of both $Cu100\%$ and $Bi100\%$ doped perovskite films. 130

Fig. 8.7. Uv-vis absorbance spectra of Cu- (a) and Bi-doped (b) perovskite films. Optical bandgap Eg values (c) estimated from Tauc's law of both Cu- and Bi-doped perovskite films. 131

Fig. 8.8. Recorded Uv-spectrophotometer photographs of both $Cu100\%$ and $Bi100\%$ doped perovskite films. 132

Fig. 8.9. (a) Photographs of reference as well as both Cu and Bi-doped perovskite solar cells as a function of dopant content ($x = 0.01$). The substrates are $1{,}2 \times 1{,}2\ mm$. (b) Cross-sectional SEM image of reference device based on the planar FTO/ $SnO2/perovskites/Sprio/Au$ device configuration. 132

Fig. 8.10. Cross-sectional SEM images of $Cu\ x = 0.15$ (a) and Bi $(x = 0.15)$ (b) doped devices based on the planar FTO/ $SnO2/perovskites/Sprio/Au$ device configuration. 133

Fig. 8.11. Backward scanned J-V characteristics under standard illumination of undoped, as well as Cu- (a) and Bi-doped (b) perovskite solar devices, as a function of doping ratio x. 134

Fig. 8.12. Recorded J-V characteristics of both $Cu\ a\ and\ b$ & Bi $(c\ and\ d)$ incorporated perovskite devices. Both FW and BW corresponding to the forward and backward scans, respectively. 135

Fig. 8.13. EQE spectra of undoped, and Cu- (a) and Bi-doped perovskite devices as a function of dopant fraction x. 137

Fig. 8.14. Decay time extracted from transient photovoltage decay curves under open-circuit conditions as a function of bias-light induced VOC for perovskite devices based on the undoped and doped active layer for $x = 0{,}15$. The recombination regime under high light intensity (hence at high bias-induced VOC) are emphasized by dotted lines in each case. 138

Fig. 8.15. Evolution of normalized PV parameters under ISOS-D-1 aging conditions (no encapsulation, ambient atmosphere, one sun continuous illumination). The doping level is $x = 0{,}01$ for both Cu- and Bi-doped devices. . 141

Fig. 8.16. Evolution of normalized PV parameters under ISOS-D-1 aging tests for Cu-doped devices. 142

Fig. 8.17. Evolution of normalized PV parameters under ISOS-D-1 aging tests for Bi-doped devices. 143

Fig. 8.18. I-V characteristic curves of both ideal device structures (with and without $BiI3$ IL). The inset represents the energy band diagram. 147

Fig. 8.19. QE graph of both ideal device structures (with and without $BiI3$ IL). 147

Fig. 8.20. Energy band diagram for the reference device (a), including $BiI3$ IL (b) with different HTL candidates. 150

Fig. 8.21. shows the I-V characteristic curves of both ideal device structures (with and without $BiI3$ IL) with $Cu2O$-HTL. The insets represent the energy band diagram. 153

Fig. 8.22. shows the I-V characteristic curves of both ideal device structures (with and without $BiI3$ IL) with $SrCu2O2$ – HTL. The insets represent the energy band diagram. 153

Fig. 8.23. shows the I-V characteristic curves of both ideal device structures (with and without $BiI3$ IL) with $PTAA$-HTL. The insets represent the energy band diagram. 154

Fig. 8.24. shows the I-V characteristic curves of both ideal device structures (with and without $BiI3$ IL) with $CuAlO2$-HTL. The insets represent the energy band diagram. 154

Fig. 8.25. *shows the I-V characteristic curves of both ideal device structures (with and without* $BiI3$ *IL) with* $CuSbS2$*-HTL. The insets represent the energy band diagram.* 155
Fig. 8.26. *shows the I-V characteristic curves of both ideal device structures (with and without* $BiI3$ *IL) with* $CuSCN$*-HTL. The insets represent the energy band diagram.* 155
Fig. 8.27. *shows the I-V characteristic curves of both ideal device structures (with and without* $BiI3$ *IL) with* CuI*-HTL. The insets represent the energy band diagram.* 156
Fig. 8.28. *shows the I-V characteristic curves of both ideal device structures (with and without* $BiI3$ *IL) with* $P3HT$*-HTL. The insets represent the energy band diagram.* 156
Fig. 8.29. *Energy band diagram for the reference device, including* $BiI3$ *IL with different electrodes.* 158
Fig. 8.30. *The photovoltaic parameters for the reference device with different HTL's and electrodes.* 159
Fig. 8.31. *The photovoltaic parameters for the* BiI_3 *IL contained devices with different HTL and electrodes.* 160
Fig. 8.32. *Quantum efficiency graph for the reference device (a) and* $BiI3$ *IL contained device (b) with different electrodes.* 161
Fig. 8.33. *The variation of PCE (a) with different perovskite layer (500 nm to 1000 nm) and* $BiI3$ *IL (10 nm to 100 nm) thickness.* 165
Fig. 8.34. *QE and J-V characteristics (inset) of a different perovskite absorber layer thickness (500 nm to 1000 nm), including 70 nm of* $BiI3$ *IL.* 165
Fig. 8.35. *Effect of* $Rseries$ *(a) and* $Rshunt$ *(b) in the performance of simulated* $Cu2O$*-HTL device with* $BiI3$ *IL.* 166

LIST OF TABLES

***Table 1.1**. The effective ionic radii of various cations and anions applicable for perovskite structure [14], [15], [17]–[19].* 6

***Table 2.1**. Atomic positions of all atoms.* 33

***Table 5.1**. Details of input parameters used for the simulation of FA-based perovskite solar cells. When data are extracted from the literature, the corresponding reference is indicated.* 67

***Table 5.2.** Details of primary input parameters used for the simulation of FAPI based perovskite solar cells.* 70

***Table 5.3**. Input parameters for proposed different HTL materials.* 71

***Table 6.1**. The tendency of lattice parameters.* 78

***Table 6.2**. Atomic populations (Mullikens)* 80

***Table 6.3**. Bond populations (Mullikens).* 81

***Table 6.4.** Orthorhombic EC values calculated for the clockwise configurations of the [XY] FA cation structure, including the propagated uncertainty. The present δmax<0.02 results are in good agreement with pseudo-cubic EC values determined by first-principles calculations, based on DFT+vdW-DF2 [15], and two sets of cubic EC values experimentally measured by INS [4] and a theoretically determined by a DFT+vdW-TS scheme [9].* 89

***Table 6.5.** Calculated Bulk (B) and Shear (G) moduli determined by the Hill-Reuss-Voigt equations, including the propagated uncertainty from the set of c_ij values. For all clockwise orientations of [XY] FA configurations with δmax<0.02. The provided comparison is against experimental [4] and ab initio DFT+vdW-TS [9] as well as DFT-vdW-DF2 [15] results.* 91

***Table 6.6.** Elastic components values of c_{44}, c_{55}, and c_{66} for all clockwise rotations of the [XY] FA configuration, the values are calculated with six deformations steps under the two tested strain amplitudes: δmax=0.02 and δmax=0.04, with its corresponding standard error.* 92

***Table 6.7** The MC analysis at the strained boundaries of the elastic components c_{44}, c_{55}, and c_{66} of the structure [XY] 12'o clock. Both bond population and bond length values at the unstrained are: -0.12 e, 2.82312 Å; -0.12 e, 2.82313 Å;-0.03 e, 2.90293 Å, and -0.03 e, 2.90294 Å, for H_4-I_2, H_5-I_2, H_2-I_2, and H_3-I_2, respectively.* 93

***Table 6.8**. The Mulliken-charge analysis of $FABX_3$ conventional models.* 98

***Table 6.9**. Calculated EC values of six different FA-based perovskite models.* 100

***Table 7.1.** Summarized photovoltaic parameters of ideal devices D-A, D-B, and D-C using different HTL thickness values, respectively.* 107

***Table 7.2.** Summarized photovoltaic parameters of ideal devices D-A, D-B, and D-C, respectively.* 108

***Table 7.3.** Summarized photovoltaic parameters (such as short-circuit density (Jsc), fill factor (FF), open-circuit voltage (Voc), power conversion efficiency (PCE), series and shunt resistance ($Rshunt$ and $Rseries$) values) of experimental D-A, D-B, and D-C devices, respectively. The following table demonstrates three (3) solar cell performances for each case (in similar conditions). The calculated average mean values presented with standard errors.* 110

***Table 7.4.** Comparison of experimental FW scan device performances of D-A, D-B, and D-C with the simulated devices (after feeding $Rseries$ and $Rshunt$).* 117

***Table 8.1.** Estimated grain size and RMS roughness values for the different layers.* 126

***Table 8.2.** Estimated RMS value for both $Cu100\%$ and $Bi100\%$ doped perovskite films.* 126

***Table 8.3**. Summarized photovoltaic performance of undoped as well as Cu (a) & Bi (b) doped perovskite devices, respectively. Average values are given in the Table, except for the reference FACs device for which the champion cell is also detailed.* 135

***Table 8.4.** Recorded $\boldsymbol{JSC}$ values from EQE measurement for reference, Cu – and Bi-doped devices compared with measured $\boldsymbol{JSC}$ values.* 137

***Table 8.5**. Simulated photovoltaic parameters for $FTO/SnO2/perovskite/Spiro - OMeTAD/Au$ device.* 149

***Table 8.6** Recorded photovoltaic parameters for proposed different HTL materials.* 157

***Table 8.7.** Recorded photovoltaic parameters for $FTO/SnO2/perovskite/HTL/Au$ devices. Where HTL = $Spiro - OMeTAD, Cu2O, CuI, CuAlO2, CuSbS2, SrCu2O2, CuSCN, PTAA, P3HT$.* 162

LIST OF ABBREVIATIONS

AFM	Atomic force microscopy
Ag	Silver
a-Si	Amorphous silicon
Au	Gold
BFGS	Broyden-Fletcher-Goldfarb-Shanno method
bFPI	Bis-fulleropyrrolidiumiodide
BiI_3	Bismuth iodide
BO	Born-Oppenheimer approximation
Br	Bromide
CASTEP	Cambridge Serial Total Energy Package
$CaTiO_3$	Calcium titanate oxide
CB	Chlorobenzene
CdI_2	Cadmium iodide
CdTe	Cadmium telluride
CIGS	Copper indium gallium selenide
CIS	Copper indium selenide
Cl	Chloride
Cr	Chromium
Cs	Cesium
$CsPbI_3$	Cesium lead iodide
Cu	Copper
Cu_2O	Cuprous oxide
$CuAlO_2$	Cuprous Aluminate
CuI	Copper iodide or Cuprous iodide
$CuSbS_2$	Copper antimony sulfide
CuSCN	Cupric thiocyanate
DE	Diethyl ether

DFT	Density functional theory
DM	N2,N2′,N7,N7′-tetrakis(9,9-dimethyl-9H-fluoren-2-yl)-N2,N2′,N7,N7′-tetrakis(4 methoxyphenyl)-9,9′ -spirobi[fluorene]-2,2′ ,7,7′ -tetraamine
DMD	Damped molecular dynamics
DMF	N-N dimethylformamide
DMSO	Dimethyl sulfoxide
DOS	Density of states
DSSC	Dye-sensitized solar cells
EB	Energy band
EC	Elastic constant
EDD	Electron density difference
ELF	Electron localization function
EQE	External quantum efficiency
ETL	Electron transport layer
FA	Formamidinium
FACl	Formamidinium chloride
$FAPbI_3$	Formamidinium lead iodide
FF	Fill factor
FTO	Fluorine-doped tin oxide
GGA	Generalized gradient approximations
GTF	Goldschmidt tolerance factor
HOMO	Highest Occupied Molecular Orbital
HTL	Hole transport layer
I	Iodide
IL	Interfacial layer or interlayer
IPCE	Incident photon to charge-carrier efficiency
ISOS	International Summit on Organic PV Stability
ITC	Temperature crystallization method
ITO	Indium tin oxide

I-V	Current density- Voltage
J_{sc}	Short-circuit current density
LUMO	Lowest unoccupied molecular orbital
MA	Methylammonium
MACl	Methylammonium chloride
$MAPbI_3$	Methylammonium lead iodide
$MDACl_2$	Methylenediamine dihydrochloride
MS	Materials Studio simulation *software*
NCP	Norm-conserving pseudopotentials
NH_3	Ammonia
Ni	Nickel
OF	Octahedral factor
OPV	Organic PV
P3HT	Poly(3-hexylthiophene-2,5-diyl)
Pb	Lead
PBE	Perdew-Burke-Enzerhof
PCE	Power conversion efficiency
PEAI	Phenethylammonium iodide
Pt	Platinum
PTAA	Poly(triarylamine)
PTFE	Polytetrafluoroethylene
PV	Photovoltaic
QD	Quantum dots
Rb	Rubidium
RMS	Root mean square roughness
Rseries	Series resistance
Rshunt	Shunt resistance
SCAPS	Solar Cell Capacitance Simulator
SCF	Self-consistent field method

SE	Standard error
SEM	Scanning electron microscopy
Sn	Tin
SnO_2	Tin oxide
Spiro-OmeTAD	2,2',7,7'-Tetrakis[N, N-di(4-methoxyphenyl)amino]-9,9'-spirobifluorene
SQ	Shockley-Queisser limit
$SrCu_2O_2$	Strontium Cuprate
TCO	Transparent conducting oxide
TPSD	Two-Point Steepest Descent algorithm
TPV	Transient photovoltage
TS	Tkatchenko-Scheffler dispersion
USP	Ultrasoft pseudopotentials
Uv-Vis	Uv-visible spectroscopy
V_{bi}	Build-in potential
V_{oc}	Open-circuit voltage
WF	Work function
XRD	X-ray diffraction

1. CHAPTER – I. Introduction to Perovskite materials and solar cells

1.1. Literature Review

Energy is one of the unavoidable sources in human life. Today, most things require electricity, and it is essential in the human race. To date, the world depends on fossil fuels such as coal, crude oil or petroleum, and natural gases, which are the primary energy resources. Due to the sizeable population and industrialization evolution, the energy demand is increasing upward day by day. Fossil fuels produce environmental risks by releasing poisonous gases while burning, which led to global warming. So, energy demands, the reduction of fossil fuels, and ecological pollution give the alarm to find an alternative eco-friendly energy source.

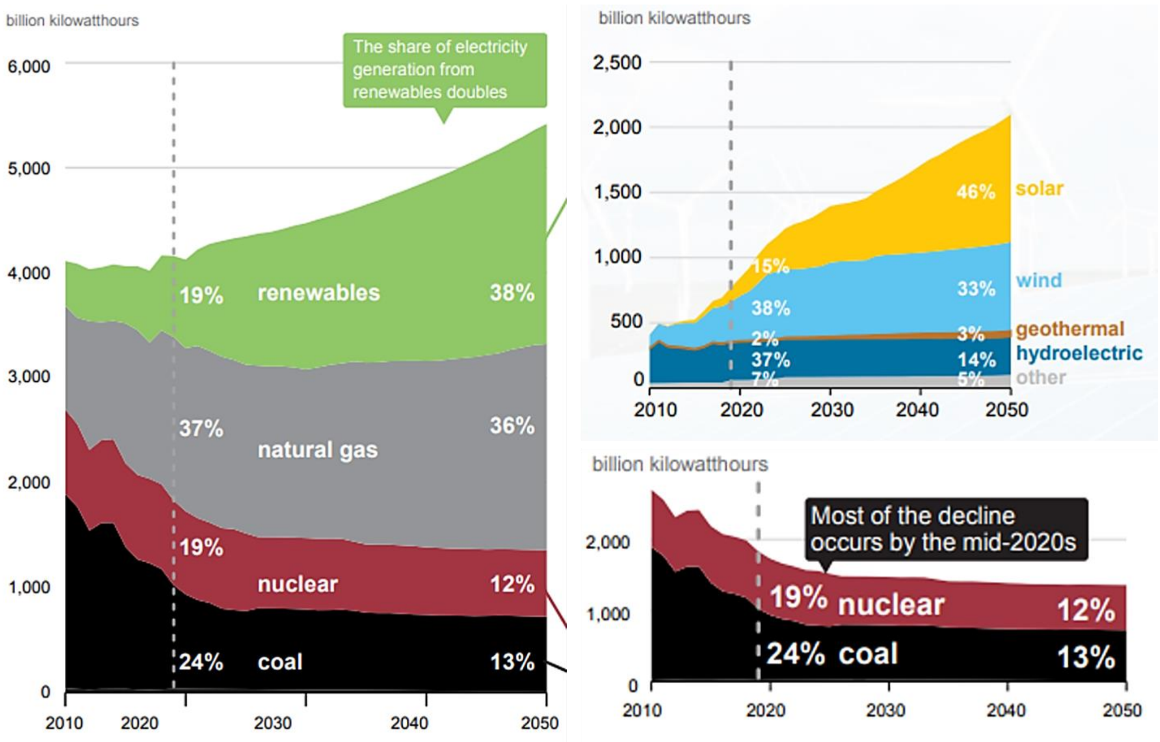

Fig. 1.1. Electricity generation from listed fuels [1].

In this context, renewable energy sources (solar, wind, geothermal, biomass, and hydroelectricity) are considered as potential candidates instead of fossil fuels (see **Fig. 1.1**). Because it is an unlimited source, and mainly, it is less hazardous to the environment. Among them, Solar energy is considered the most significant alternative source due to its advantages. Solar energy is an unlimited, free, and hugely available source in this world. It is also easy to install everywhere, such as small and large areas, such as building windows, streetlights, tiny house roofs, etc. Solar cell technology, especially on the fourth-generation perovskite material and its solar cell applications, is briefly discussed below.

1.1.1. Solar cell technology

A solar cell, generally called photovoltaics (PV), is an electrical device that generates electrical energy from the sunlight using semiconducting absorber materials followed by the photovoltaic or the Becquerel effect, and it was discovered in 1839 by Alexandre-Edmond Becquerel [2]. In 1884, Charles Fritts experimented with the first solar device, giving poor efficiency [3]. The cross-sectional solar cell image is illustrated in **Fig. 1.2**. Principally, a solar cell is a p-n junction diode, and it is different from the conventional diode. The device contains the p-type and n-type semiconducting materials (acted as p-n junction) with electrodes. After exposure to sunlight, photons strike on the absorbing materials, and it generates charge carriers (i.e., several electron-hole pairs). So, the free electrons and holes in the depletion region rapidly move towards the junction's p-type and n-type sides. As a consequence, electron flow through the circuit generates electricity.

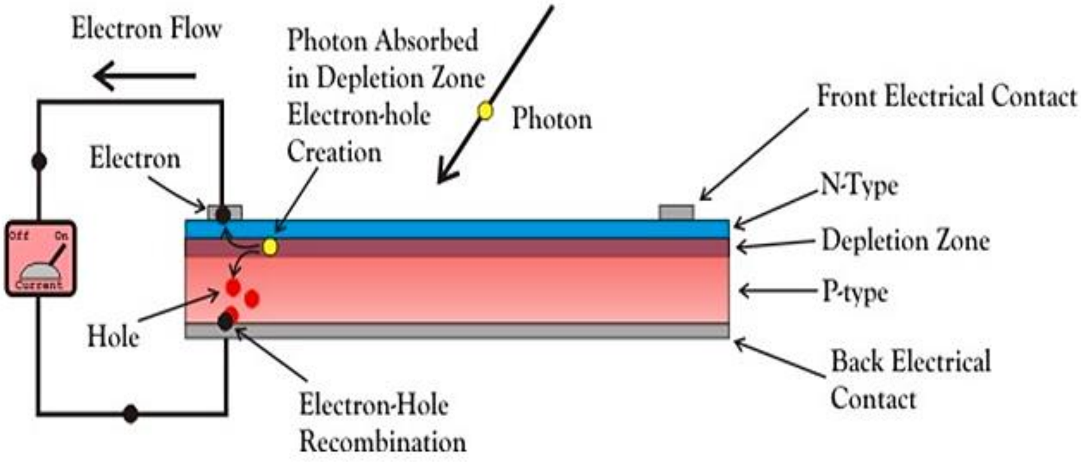

Fig. 1.2. *Solar cell structure [4].*

Solar cell technology is generally categorized into four different generations: first, second, third, and fourth. The traditional wafer-based both poly and monocrystalline silicon solar cells are called first generations, and it's occupied around 85 % of the PV market. Moreover, the efficiency reaches about 27 %.

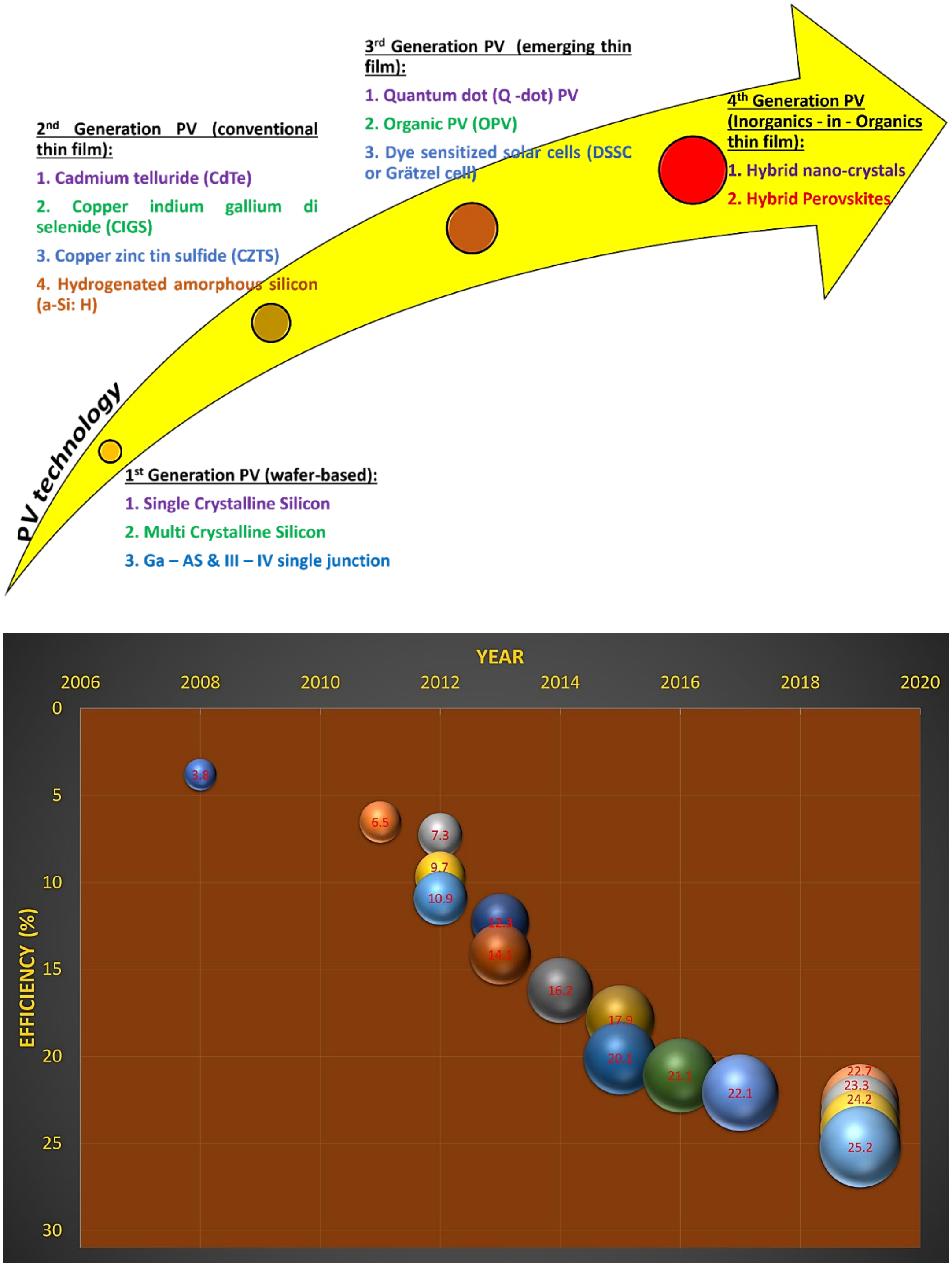

***Fig. 1.3**. PV technology classifications and the perovskite solar cell efficiency chart [5]–[7].*

Thin film technology, so-called the second generation, such as amorphous silicon (a-Si), cadmium telluride (CdTe), copper indium selenide (CIS), and copper indium gallium selenide (CIGS) employed as an absorber. It is cheap, and it provides lower efficiency than first-generation cells.

Third and fourth-generation cells, also known as emerging photovoltaics, include nanocrystals (quantum dots - QD) and polymer-based solar cells, dye-sensitized solar cells (DSSC), organic PV (OPV), and perovskite solar cells, which has many advantages over than other two generations. For example, it contains lighter-weight materials, low manufacturing costs, and it could allow large-scale productions. Compared to all other cells, the fourth generation perovskite solar cells gain more attention due to their sky-rocketed efficiency from 3.8 % to 25.2 % (see **Fig. 1.3**) [5]. Therefore, the following section covers a detailed explanation regarding the perovskite solar cells.

1.1.2. Perovskite structure

Calcium titanate oxide ($CaTiO_3$) crystal structure is the basic structure of any perovskite material [8]. In 1839 it was first discovered by German mineralogist Gustav Rose in the Ural Mountains, Russia. Later, it is named after Russian mineralist Lev Alekseyevich von Perovski (L. A. Perovski (1792–1856)) [9].

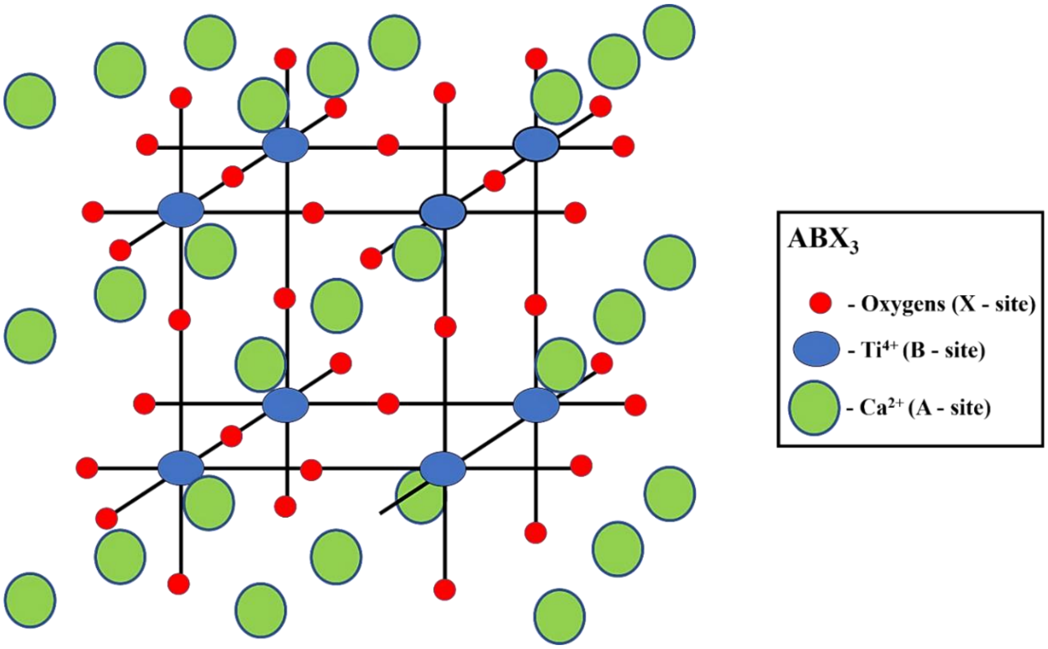

Fig. 1.4. *General perovskite cubic structure.*

ABX_3 is the general perovskite chemical formula for any perovskite compounds, where A is the bigger cation compared to B cation, and X is an anion. In the ideal cubic structure contains the B cation in 6-fold coordination, which is surrounded by an octahedron of anions, as well as the A cation in 12-fold cuboctahedral coordination demonstrated in **Fig. 1.4**. The perovskite compounds have many symmetries, such as cubic, orthorhombic, tetragonal, or trigonal, for examples, $SrTiO_3, CaRbF_3, FeTiO_3, BaTiO_3, BiFeO_3, PbTiO_3$, etc [10], [11].

1.1.3. Perovskite solar cells

The general formula ABX_3 is used for the 3D organic-inorganic halide perovskites, and the structure is shown in **Fig. 1.5**. Where A is the organic or inorganic cation such as methylammonium (MA^+), formamidinium (FA^+), or cesium (Cs^+), rubidium (Rb^+), B is a metal anion like lead (Pb^+) or tin (Sn^+), and X is halogens such as chloride (Cl^-), bromide (Br^-), or iodide (I^-). The various suitable cations and anions are distinguished with their ionic radii value in **Table 1.1**.

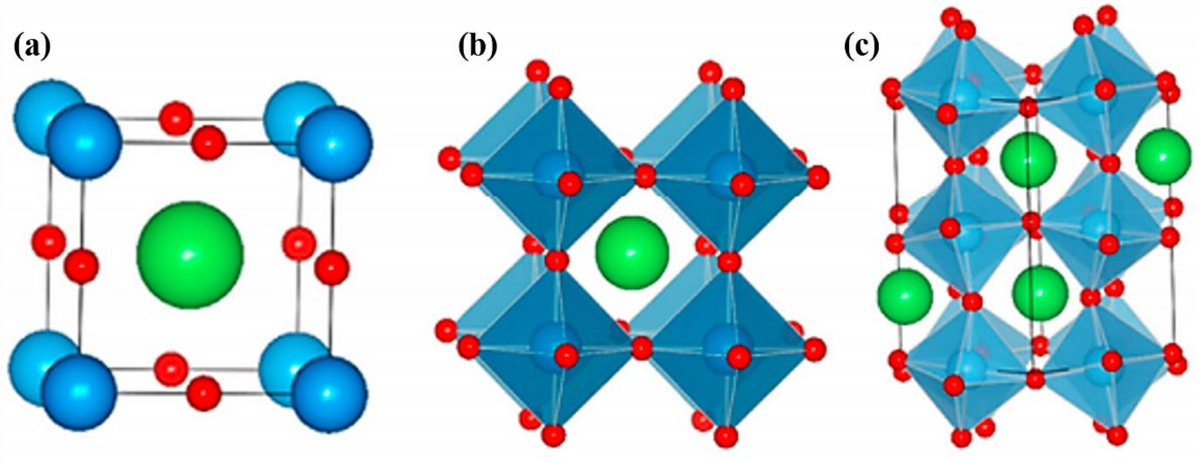

Fig. 1.5. *The ideal cubic perovskite unit cell. (A) A-cations (blue) occupy the lattice corners, B cations (green) occupy the interstitial site, and X anions (red) occupy lattice faces. (B) An alternative view depicting B cations assembled around X anions to form BX_6 octahedra, as $B-X$ bonds are responsible for determining electrical properties. (C) Tilting of BX_6 octahedra occurring from nonideal size effects and other factors, inducing strain on the B-X bonds. Reprinted from ref [12], Nano Today. 10 (2015) 355-396, DOI: https://doi.org/10.1016/j.nantod.2015.04.009.*

The suitable formation of A, B, and X site components must fulfill the Goldschmidt tolerance factor (GTF or simply t) [13]–[16] to define the structural stability of these hybrid organic-inorganic perovskite material using the following formula,

$$t = \frac{r_A + r_X}{\sqrt{2}\,(r_B + r_X)} \qquad (1.1)$$

Where, r_A, r_B and r_X are the effective ionic radii of A, B, and X-sites, respectively.

Table 1.1. *The effective ionic radii of various cations and anions applicable for perovskite structure* [14], [15], [17]–[19].

	ABX_3			
A – site (Å)	B – site (Å)			X – site (Å)
${NH_4}^+$ - 1.46	Be^{2+} - 0.45	Ti^{2+} - 0.86	Eu^{3+} - 0.95	F - 1.29
NH_3OH^+ - 2.16	Pd^{2+} - 0.86	Cd^{2+} - 0.95	Co^{2+} - 0.75	I - 2.20
$CH_3{NH_3}^+$ - 2.17	Dy^{2+} - 1.07	Cu^+ - 0.77	Sm^{2+} - 1.22	Cl - 1.80
$NH_3{NH_2}^+$ - 2.17	Ce^{2+} - 1.01	Gd^{3+} - 0.94	Ni^{2+} - 0.69	$HCOO$ - 1.36
$(CH_2)_3{NH_2}^+$ - 2.50	Mg^{2+} - 0.72	V^{2+} - 0.79	Eu^{2+} - 1.17	Br - 1.96
$CH{(NH_2)_2}^+$ - 2.53	Pt^{2+} - 0.80	Hg^{2+} - 1.02	Lu^{3+} - 0.86	SCN - 2.17
$C_3N_2{H_5}^+$ - 2.58	Tm^{2+} - 1.03	Ag^+ - 1.15	Bi^{3+} - 1.03	
$NC_4{H_8}^+$ - 2.72	Pr^{3+} - 0.99	Dy^{3+} - 0.91	Pu^{3+} - 1.00	
$(CH_3)_2{NH_2}^+$ - 2.72	Ca^{2+} - 1.00	Cr^{2+} - 0.80	La^{3+} - 1.03	
$CH_3CH_2{NH_3}^+$ - 2.74	Cu^{2+} - 0.73	Ge^{2+} - 0.73		
$(NH_2)_3C^+$ - 2.78	Yb^{2+} - 1.02	Au^+ - 1.37		
$(CH_3)_4N^+$ - 2.92	Nd^{3+} - 0.98	Er^{3+} - 0.89		
$C_3H_4NS^+$ - 3.20	Sr^{2+} - 1.18	Mn^{2+} - 0.83		
$C_7{H_7}^+$ - 3.33	Ag^{2+} - 0.94	Sn^{2+} - 1.15		
$C_4H_{12}{N_2}^{2+}$ - 3.22	Np^{2+} - 1.10	Au^{3+} - 0.85		
$C_6H_{14}{N_2}^{2+}$ - 3.39	Sm^{3+} - 0.96	Tm^{3+} - 0.88		
K^+ - 1.64	Ba^{2+} - 1.35	Fe^{2+} - 0.78		
Rb^+ - 1.72	Zn^{2+} - 0.74	Pb^{2+} - 1.19		
Cs^+ - 1.88	Tl^+ - 1.50	Sb^{3+} - 0.76		

Generally, the t value should lies between 0.8 to 1.1 to form the stable perovskite crystal structure, such as cubic [17]. If the t value is low (around 0.8), the lower crystal symmetries are formed due to an increased BX_6 octahedra tilting, and if the t value is too low ($t < 0.8$) it does not forming the perovskite crystals. If the t value is high ($t > 1$), the complex crystal structure is formed with intermolecular distortion [20]. Another estimation method is called an octahedral factor (OF or simply μ) [21], [22], which is specifically used to determine the tilting between B and X sites because GTF is not a direct option to describe the stability of the crystal structure [14]. The μ is expressed by,

$$\mu = \frac{r_B}{r_X} \qquad (1.2)$$

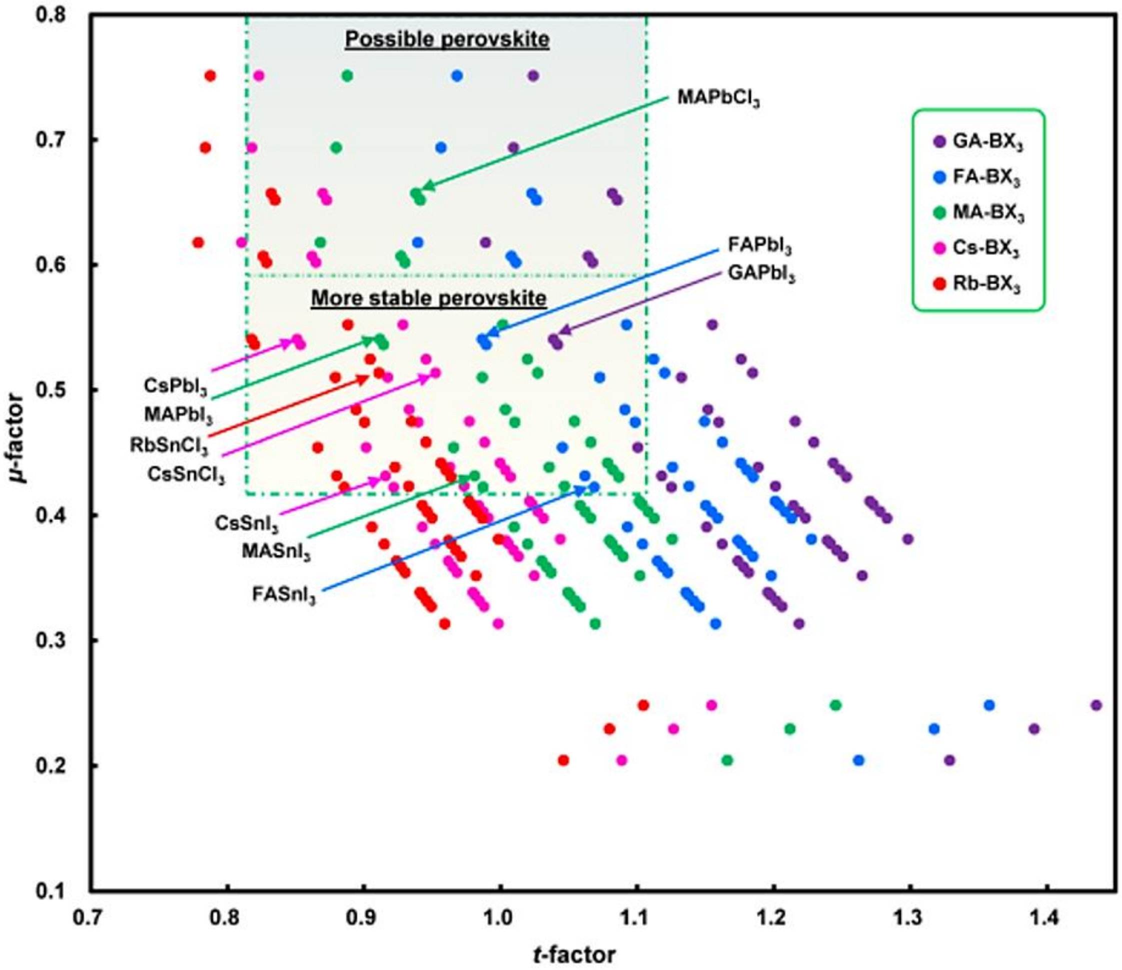

Fig. 1.6. *The tolerance and octahedral factors for different perovskite compounds. Reprinted from ref* [23], *Rev. Adv. Mater. Sci. 2020; 59:264–305, DOI: https://doi.org/10.1515/rams-2020-0015.*

Therefore, both t and μ values are essential to define the organic-inorganic perovskite crystal structure stability. According to the previous reports, the perovskite structures are formed in the range of $0.813 \leq t \leq 1.107$ and $0.442 \leq \mu \leq 0.895$ [24]–[26]. Hence, the chosen cation and anions' effective ionic size modifies the perovskite crystal symmetry [27]. The t and μ values of different perovskite compounds are demonstrated in **Fig. 1.6** [23].

1.1.3.1. A, B, and X - site substitutions

A-site cation substitution, especially the chosen cation's size, alters the distortion degree and affects the electronic properties [28]–[31]. Organic MA^+, FA^+, or inorganic Cs^+, Rb^+ cations are frequently used A – site cations in the perovskite composition [32]–[36]. Pb^+ or Sn^+ are mostly used B – site divalent metal cations [37]–[40]. And, Cl^-, Br^-, or I^- are repeatedly used X – site halogens [41], [42]. Mixed A - site cation/B – site cation/X-site halogens perovskite compositions permits the strong characteristics of the individual components, and it efficiently influencing the structural, morphological, optical and electrical properties as well as the solar cell performance [43]–[52].

1.1.3.2. Why FA cation-based perovskites

In the initial stage, Methylammonium lead iodide ($MAPbI_3$) perovskite (i.e., state of the art) is a widely used absorber layer compound in solar cells. Many researchers have studied $MAPbI_3$ crystal structure, and they found that the phase transition occurs from cubic to tetragonal to orthorhombic (~330 K to ~160 K) based on the temperature range [53]–[56]. At room temperature, the $MAPbI_3$ perovskite adopting the bandgap value of 1.51 eV which is larger than the optimized bandgap value (i.e., 1.34 eV) according to the Shockley-Queisser limit (SQ) curve (for single bandgap solar cells) [57]. Also, substituting different halogens such as Cl^-, Br^- with $MAPbI_3$, it increasing the bandgap value from 1.5 eV to 3.6 eV [58]–[61]. Inorganic Cs^+ cation based Cesium lead iodide ($CsPbI_3$) perovskites also have higher bandgap value of 1.71 eV, and several phase transition happens this material as well [62], [63]. In this context, the organic larger FA^+ cation based lead iodide perovskites (simply - $FAPbI_3$) provides significant bandgap value (1.48 eV) as well as the higher symmetry perovskite structure than other two cation based perovskites [64]. According to the t and μ values, $MAPbI_3$ (t = 0.912 and μ = 0.541) and $CsPbI_3$ (t = 0.851 and μ = 0.541) perovskite are somewhat unstable than $FAPbI_3$ (t = 0.987 and μ = 0.541) perovskites [23]. Moreover, previous reports show that the $MAPbI_3$ or $CsPbI_3$ are thermally less stable compared to $FAPbI_3$ perovskites [65]–[68]. The following sections covers the fabrication methods, as well as the structural, morphological, optical and electrical properties of FA cation-based perovskites.

1.1.3.3. Structure of perovskite devices

In general, Perovskite solar cells consist of Perovskite active or absorber layer that is fit in between the electron transport layer (ETL) and the hole transport layer (HTL). Both ETL and HTL play a crucial role in determining the Perovskite device performance. The function of ETL (HTL) is to collect the electrons (holes) from the absorber layer and transport it towards the cathode (anode) as well as blocking the holes (electrons). The normally used HTL materials must have the highest occupied molecular orbital (HOMO) value, which is slightly higher than the absorber layer. For example, organic Spiro-OMeTAD, PTAA, P3HT, PEDOT: PSS, Poly-TPD, EH44, and inorganic CuSCN, NiO, CuO, CuCrO, CuI, CrO [69]. The ETL materials must have a higher transmittance in the UV region to allow more photons to the absorber layer, its HOMO, and the lowest unoccupied molecular orbital (LUMO) values higher than the active layer [33]. For example, TiO_2, SnO_2, ZnO, PCBM, C60, Al_2O_3 [69]. Frequently used TCO materials are ITO, FTO, IZO, AZO, and the anodes: Au, Ag, Cu, Cr, MoO, or ZnO/Al [69]. If the incident light penetrates through the TCO/ETL side, it is described as an n-i-p or regular structure, and if it goes through the HTL side, it is named as p-i-n or inverted structure [70].

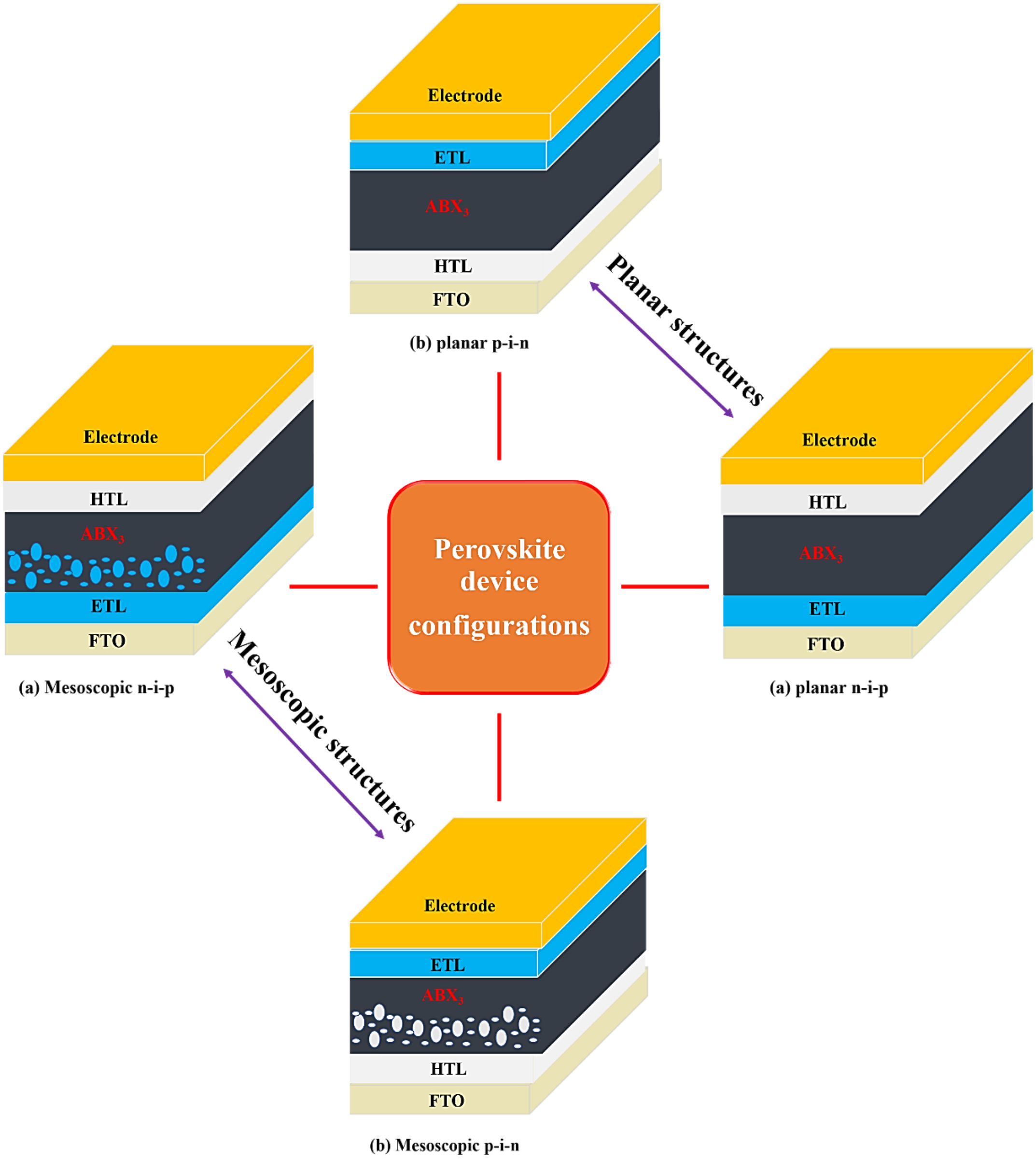

Fig. 1.7. *Schematics of frequently used device configurations in perovskite solar cells.*

The device configuration is divided into two, such as Mesocscopic and Planar structures. Therefore, there are four main possible option available for the device configurations shown in **Fig. 1.7** [71]–[73], such as

- TCO/ETL/Mesoporous ETL/Perovskite/HTL/Electrode (n-i-p)
- TCO/HTL/Mesoporous HTL/Perovskite/ETL/Electrode (p-i-n)
- TCO/ETL/Perovskite/HTL/Electrode (n-i-p)
- TCO/HTL/Perovskite/ETL/Electrode (p-i-n).

Due to the ambipolar behavior of the perovskite layer, it can separate and transport the electrons and holes itself [74], and the mentioned above configurations are further reduced in the following format,

- TCO/Perovskite/HTL/Electrode (ETL-free device)
- TCO/ETL/Perovskite/Electrode (HTL-free device)

1.1.3.4. Fabrication techniques

The film crystallinity, surface morphology, film thickness, and film quality are generally influencing the device performance. Hence, the proper understanding of the fabrication techniques is necessary to make efficient perovskite solar cells. The categorized techniques are, such as single or one-step spin-coating method [75], two-step spin-coating method [76], sequential deposition method [77], vapor assisted solution process technique [78], physical and chemical vapor deposition method [79]–[81], blade coating [82], slot die coating [83], [84], spray coating [85], inkjet printing [86], screen printing [87], pulsed laser deposition [88], drop-casting method [89], and hydrothermal method [90]. The structural and optoelectronic properties depend on the chosen perovskite composition. It is also influenced by the film fabrication method, annealing temperature, added solvent, and environmental conditions such as oxygen, moisture, and temperature [33]. The perovskite solar cells achieved almost equal efficiency compared to Silicon solar cells. However still, Si-based models dominate the PV market due to the more extensive lifetime (25 years) than perovskites (~ 1 year) [91], [92]. Usually, the perovskites solar cell stability is affected by moisture, oxygen, temperature, light (UV), biasing, ion migration, interfacial degradation, and more [93]. Many published reports [94]–[96] show that using encapsulation in perovskite devices helps to avoid contact between moisture and oxygen to enhance the device stability. Even though the encapsulation does not protect the device entirely due to other factors such as thermal issues (i.e., heat, and illumination) [70], [97]. Many approaches possibly enhance device stability, such as composition engineering, additive, precursor and solvent engineering, interface engineering, surface passivation engineering, mixed dimension 2D-3D perovskite engineering, and more [98]–[101].

Jialiu Ma and Da Guo reported a comprehensive data review on 69 certified Pb-based perovskite solar cell devices from 2013 to 2020 [102]. The results demonstrate that the device fabrication methods and device configurations mainly influence the device PV performance. Based on the device aperture size, they divided the certified devices into three classes, such as sub-cell device (close to 0.1 cm^2), cell device (1 cm^2), and sub-module device (over 10 cm^2). Large solar cell modules deliver lower efficiencies than smaller size devices [104] due to scaling up issues. According to published results, spin-coating is a widely used technique to fabricate the perovskite absorber layer, especially in the lab-scale format. However, fabricating the large volume spin-coating film is not an easy task. Non-spin-coating methods (around 13%) demonstrate lower device performance for certified Pb-based solar cells than spin-coating techniques (around 20%) [102]. Notably, thirty-five certified Pb-based device modules out of 69 devices are based on the n-i-p planar configurations. Twenty-six devices are adopting the n-i-p mesoscopic structures; only eight devices were adopting the inverted p-i-n architecture [102]. Generally, two types of TCO materials are used in Pb-based certified devices, such as FTO (42 devices) and ITO (27 devices), as well as mostly used perovskite absorber materials are briefly discussed in the previous report [102]. The upcoming sections cover the organic FA cation-based perovskite absorber layer properties and its device performance.

1.1.4. $\boldsymbol{FAPbI_3}$ Crystal structure and its phase transition

$FAPbI_3$ perovskites exhibit multiple optically active polymers, such as black-colored cubic (α-phase), tetragonal (β-phase), orthorhombic (γ-phase) phases, and the non-photoactive yellow-colored hexagonal δ-phase [103]–[105]. The optically active α-phase is attained at 150° C to 185° C [106], while β and γ-phases are formed at -122° C and -182° C [104]. The δ-phase is a well-known stable phase than other phases at room temperature. X-ray diffraction (XRD), neutron powder diffraction, and synchrotron powder diffraction measurements are crucial techniques to verify the crystal structures of $FAPbI_3$ perovskites. The early reports show that the black phase adopts the trigonal symmetry with the space group of *P3m1* (a = b = 8.982 Å and c = 11.006 Å), and the yellow phase has hexagonal symmetry with *P63mc* space group (a = b = 8.660 Å and c = 7.902 Å) [32], [65], [107]. Later, Weller *et al.* found that α-phase adopts cubic symmetry with a *Pm3m* space group (a = 6.632 Å) instead of trigonal symmetry using high-resolution neutron powder diffraction [105]. Fabini *et al.* discussed that the β and γ-phases are adopting the tetragonal and orthorhombic symmetries with *P4/mbm* space group (a = b = 8.9 Å and c = 6.3 Å for β-phase, a = b = 8.8 Å and c = 6.2 Å for γ-phase) using high-resolution synchrotron powder diffraction [104]. Chen *et al.* studied the structural transition of $FAPbI_3$ perovskites and they found three phases, first one is cubic at 390 K (*Pm3m*, a = 6.385 Å), and two hexagonal phases, such as Hex-1T at 220 K ($P6_3/mmc$, a = b = 8.62 Å and c = 7.94 Å), and Hex-LT at 15 K ($P6_3/m$, a = b = 8.50 Å and c = 7.95 Å), respectively [108].

The annealing temperature modifies not only the phase but also the film morphologies. The grain size (139 nm to 261 nm) values and the root mean square roughness (5.7 nm to 10.7 nm) values are significantly enhanced from δ - α phase conversion while increasing the annealing temperature from 70° C to above 140° C [75], [109]–[111]. $FAPbI_3$ film showing better thermal stability than $MAPbI_3$, even though if it is annealed at/over 170° C for a longer time, it decomposed to PbI_2 [112], [113]. E. J. Juarez-Perez *et al.* studied the thermal stability and decomposition products of FA based perovskites (i.e., $FAPbI_3$ and $FAPbBr_3$) using quadrupole mass spectroscopy technique with thermal gravimetric differential thermal analysis (TG - DTA) [114]. Explains that, while heating $FAPbX_3$, it decomposes into *sym*-triazine, hydrogen cyanide (HCN), formamidine, and also it relasing the by products of ammonia (NH_3). Three thermal decomposition reaction of formamidine is demonstrated in **Fig. 1.8** [114], [115].

A. Baltakesmez *et al.* studied the effect of annealing temperature over the $FAPbI_3$ perovskite films and found that 170° C annealing film exhibits enhanced surface coverage with reduced voids. Also, the peak shoulder in absorbance spectrum (around 550 nm) is attributed to the presence of PbI_2 residual, it is noticed in the 130° C film [76]. G. Murugadass *et al.* investigates the solvent effect (chlorobenzene, diethyl ether, and toluene) on the structure and morphology of $FAPbI_3$ perovskite using hydrothermal method, and their FTIR analyses shows that the strong peak appeared between 3500 cm^{-1} and 3200 cm^{-1} range is corresponding to N-H stretching from FA^+ cation, and 1526

cm^{-1} range associated with $C = O$ bond. Also, the strong stretching vibration noticed at 1706 cm^{-1} and 3156 cm^{-1} which are related with FA^+ and $NH_4{}^+$ [116].

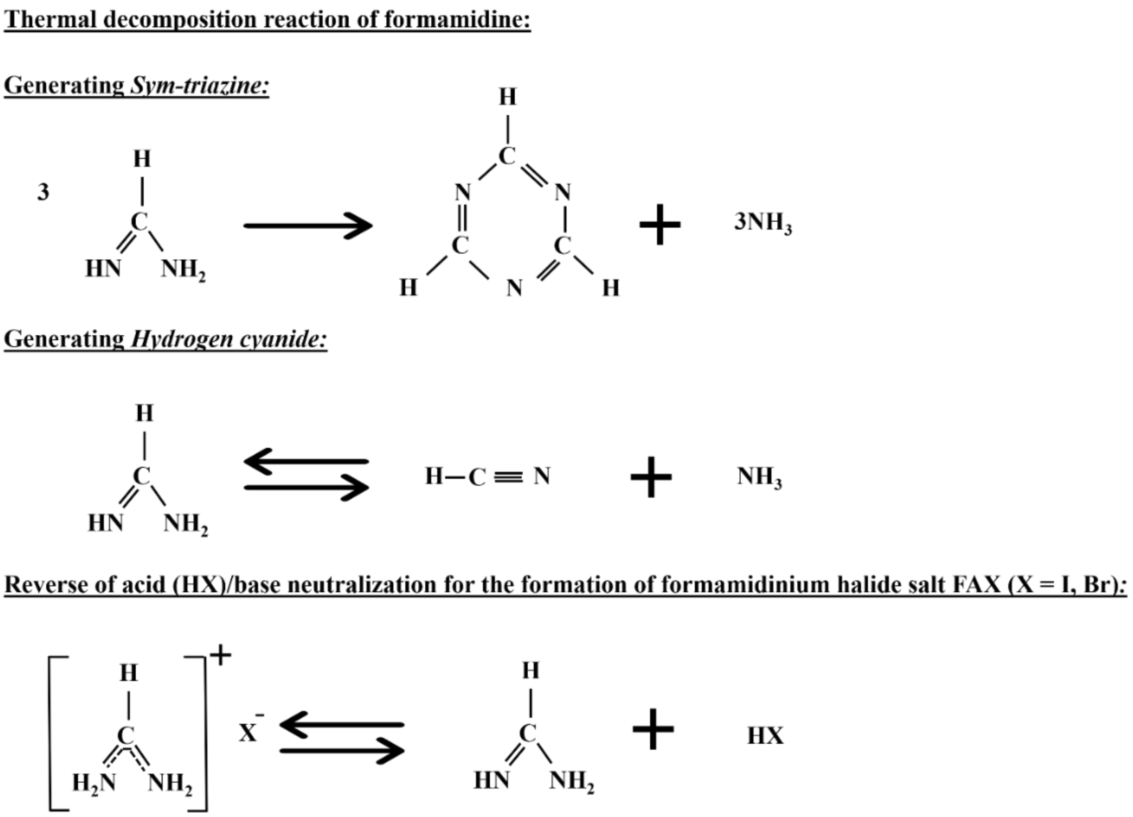

Fig. 1.8. *Schematic of thermal decomposition reaction of formamidine* [114], [117].

The pristine $FAPbI_3$ perovskite devices are examined in detail in the following discussions. In the initial stage, the pristine $FAPbI_3$ perovskite devices were showing poor stability due to their unavoidable phase change in ambient conditions. Therefore, several strategies were used by researchers to overcome this issue to enhance device stability as well as efficiency. Both one-step and two-step solution processing methods are commonly used techniques to fabricate the absorber layer [99], [118]. The mixture of organic and lead halide precursors dissolved in common solvent or solvent mixture spin-coated, with or without antisolvent, is known as a one-step process. In a two-steps process, first the PbI_2 mixed solvent spin-coated, then the organic precursor solution dropped, or the prepared film dipped to form the perovskites.

Recently, it was reported that the addition of $MACl$ into $FAPbI_3$ perovskite solution efficiently enhances the layer morphology and the crystallinity because of the additive, it effectively suppressing the unwanted $FAPbI_3$ phase change. Moreover, the device with n-Octylammonium iodide ($NOAI$) interlayer and the fluorinated isomeric HTMs offers a highly efficient charge transfer and fast charge extraction result, the device showing a higher PCE of around 24.8 % [119]. Methylenediamine dihydrochloride ($MDACl_2$) was also used as an additive that does not affect the morphological features (i.e., grain size and surface roughness) of the $FAPbI_3$ absorber. The inclusion significantly lowered lattice strain, it increases charge carrier lifetime and it reduced defect concentration and Urbach energy. Besides, the Phenethylammonium iodide (PEAI) interlayer efficiently passivate the surface of perovskite films, and the controlled device demonstrates around 23 % [120] and 24 % efficiency [121]. M. Kim *et al.* investigates $FAPbI_3$ perovskite device performance with several chloride additives such as formamidnium chloride ($FACl$), guanidium chloride ($GuCl$), cesium chloride ($CsCl$), rubidium chloride ($RbCl$), and potassium chloride (KCl). They obtained a higher efficiency (23.3 %) while using $CsCl$ due to their appropriate cation size, which influence the grain size and the crystallinity [122]. H. Lu *et al.* carefully introduce the FA or MA thiocyanate ($FASCN\ and\ MASCN$) vapor treatment to convert the $\delta - FAPbI_3$ to $\alpha - FAPbI_3$ phase. After the vapor treatment, the films showed a stronger absorbption over all wavelengths, the grain size significantly increased upto 1 μm, and the lifetime is 3.7 times higher than untreated film, which are efficiently promotes the formation and stabilization of $\alpha - FAPbI_3$. As a consequence, using vapor treatment with choline chloride interlayer device offers an improved efficiency of 23.1 % [78]. Addition of methylammonium chloride ($MACl$) into the pure $FAPbI_3$ solution, efficiently stabilize the black phase and it reduces the surface roughness of the film which provide the smooth charge transfer. Also, introducing the iso-butylammonium iodide ($IBAI$) interlayer helps to passivate the surface defects, and the device achieved an efficiency over 22.7% [123]. Noticeably, the perovskite powder approach offers a highly homogeneous surface photocurrent compared to precursor mixed film, which is associated with phase stability and low FA defect. This powder-based device with $MACl$ additive demonstrates PCE around 21.9 %, due to the high quality film which assigned with better junction, and interfaces that effectively reduce the trap-assited non-radiative recombination [124]. Sulfonyl fluoride-functionalized phenethylammonium salt ($SE - PEA$) used as an additive to stabilize the $\alpha - FAPbI_3$, while annealing, the crystallization velocity decreases due to the interaction between sulfonyl group with PbI_2 precursor, it enhance the crystalline quality and diminish the structural defects, as a consequence, it restricts the phase change leading to higher efficiecncy 21.2 % [125]. 1,8-octanediammonium iodide ($ODAI$) interlayer with $MACl$ additive based $FAPbI_3$ device displays PCE 21.1 %, due to improved interface energy band alignment between Perovskite/HTL interface, which enhance the device V_{oc} [126]. The improvement in the charge carrier lifetime and the diminishment in the trap density both are responsible for the PCE enhancement up to 21.1 %, while using alkaline earth metal $MgCl_2$ halide additive with $FAPbI_3$ precursor solution. Moreover, $CaCl_2, SrCl_2$ and $BaCl_2$ additives are not completely suppress the PbI_2 presence compared to $MgCl_2$ [127]. 1-hexyl-3-methylimidazolium iodide ($HMII$) ionic liquid additive effectively reducing the activation energy of the grain boundary migration and also creates a moisture barrier to restrict the $FAPbI_3$ phase transition, which is beneficial to the PCE (20.6 %) improvement [128]. Using BA_2PbX_4 (where $X = I, Br, Cl$) additive with (3,9-bis(2-methylene-(3-(1,1-dicyanomethylene)-indanone))-5,5,11,11-tetrakis(4-hexylphenyl)-dithieno[2,3-d:20,30-d0]-s-indaceno[1,2-b:5,6-b0]dithiophene) (simply - $ITIC$) or rhodanine-benzothiadiazole-coupled indacenodithiophene (simply - $IDTBR$) anti-solvent dripping, which is efficiently separate the charges at molecule – perovskite heterojunction, and acts as a highly active bridge for integrain charge transfer, as a result, it boosts up the PCE to 20.6 % [129]. X. Shi *et al.* team studied the effect of CaI_2 incorporation into PbI_2 precursor solution using a two-step process to form the stable $FAPbI_3$ perovskite. The results explain that it reduces the local nucleation sites, which is beneficial for perovskite conversion with higher crystallinity and larger grains. Also, the presence of CaI_2 at the surface and grain boundaries help to passivate the crystal defects to get an enhanced efficiency of 20.3 % [130]. Similarly to $FACl$, $MACl$, $CsCl$ and $MABr$ additives, HI [131], SCN [132], CN [133], and $thiouriea$ [134] additives also influences the $FAPbI_3$ film, resulting in films with enhanced film quality and morphology, favor the phase restriction and smooth charge transfer between the layers.

1.1.5. Mixed cation $\mathbf{FAPbI_3}$ Perovskites

Inorganic Cs^+ cation has been a well-known effective dopant for stabilizing $FAPbI_3$ perovskites compared to other cations such as MA^+ and Rb^+ due to its ionic radii and its external long-term thermal stability. Also, Cs^+ doping into $FAPbI_3$ efficiently altered the tolerance factor value between 0.9 to 1.0, which is beneficial for the stable perovskite structure [135]. The phase and photo stabilities are highly enhanced while doping Cs^+ due to the enhancement in the interaction between the FA^+ and I^- [136]. Moreover, the incorporation efficiently reduces the non-radiative or trap-assisted recombination, and it improves the build-in potential (V_{bi}), as a result, the device provides a higher V_{oc} with the improved photovoltaic performance. Also, the addition effectively suppresses the δ phase formation, or in other words, it promotes the α phase stabilization. The FA-species enrichment at the perovskite surface and the enhanced film homogeneity occur in Cs-doped films rather than pristine films, which helps to achieve the high crystallinity film with low trap density [137]–[139]. An appropriate amount of Br incorporation into the $FA_{0.95}Cs_{0.05}PbI_3$ solution highly beneficial to improve the device stability by minimizing initial trap density in the perovskite absorber. Also, it promotes the 001 preferential orientation lattice plane in $\alpha - FAPbI_3$ [139].

Also, the black colored $FAPbI_3$ perovskite phase stabilized with the incorporation of organic MA cation due to the TF alteration and the hydrogen bonds enhancement because of the higher dipole moment magnitude of MA [140]. The more stable material structure is basically having a stronger dipole moment. In perovskite, the Coulomb interactions between organic cation and the inorganic cage are proportional to the dipole moment's strength [141]. Therefore, the stable structure is formed while doping with MA cation. Several published results demonstrate that the $FA - MA$ composition based device with different additives and interlayer inclusion significantly enhance the device performance and stability than the pristine device [142]–[147]. While incorporating multiple cations (i.e., $FAMACs, FAMARb, FACsRb,$ and $FAMACsRb$) into the perovskite composition, it suppresses non-radiative charge carrier recombination, and it enhances the film quality by promoting favorable grain orientation and improved diffusion lengths and carrier mobilities. Besides, the additives significantly interact with the halogens in the perovskite solution, which improves the film morphology, and the charge carrier dynamics affected due to the isotope exchange in nitrogen to hydrogen site. Overall, the mixed cation incorporation helps to passivate the defects at the absorber surface and grain boundaries (i.e., prevents the ion migration in the surface nor interface) due to the strong electrostatic interaction between hydrogen and iodine bonds, which helps stabilize the lattice structure. Using triple-cation perovskite, the researchers were employed several strategies to improve the phase, film quality, device stability, and efficiency [142]–[160]. Also, the quadrupole organic-inorganic cation mixed perovskite solar cells show reduced charge carrier recombination and impedance of charge carriers, which is favorable for device enhancement due to the diminishment in the absorber surface iodide deficiency and restricting the surface iodide vacancy formation [161]–[163]. Both phase segregation and the vacancy defect generation are entirely suppressed, which prevents the degradation/decomposition [96].

1.1.6. Low Pb content Perovskites

Apart from the stability problem of Pb-contained PSCs, the toxicity behavior of Pb (i.e., harmful to the environment and it creates several health issues to humans) is considered as another major challenge that needs to be addressed [164], [165]. To get the environmental lead-free or low Pb contained PSCs, numerous research community peoples have been focussing on suitable element substitution or partial doping (instead of/with Pb) technique. Precisely partial substitution of the following elements such as group 14 elements, transition and alkaline earth metals, lanthanides substitution (i.e., Sn (tin), Ge (germanium), Sr (strontium), Cd (cadmium), Ca (calcium), Hg (mercury), In (indium), Al (aluminum), Ag (silver), Sb (antimony), Na (sodium), Fe (iron), Ni (nickel), Co (cobalt), Mg (magnesium), Mn (manganese), Ba (Barium), Bi (bismuth), Cu (cupper)) with Pb gain more attention, which significantly alters the active layer properties, to fabricate the appropriate unharmful device [37]. For example, the most commonly used alternative element Sn has a similar electronic configuration with Pb; additionally, $Pb - Sn$ based single cation perovskite material (i.e., $MASn_xPb_{1-x}I_3$) showed optimum bandgap value from 1.10 to 1.51 eV, which is suitable for solar cells; meanwhile, the oxidation of Sn^{2+} to Sn^{4+} led to poor air stability [41]. Moreover, the appropriate amount of $Pb - Sn$ based mixed cation PSCs ($ASn_xPb_{1-x}I_3, where\ A = MA - Cs\ (or)\ FA - Cs$) provides decent PCE [166]. Likewise, Ge also have the same oxidation state as Pb, and it delivers a similar properties like lead [37], in general, pure Ge based perovskites provide higher E_g value. Due to their low binding energy of its $4s^2$ electron, the stability of Ge^{2+} is reduced, which means Ge contained devices directed towards the instability region; besides, Ge included materials led to lower dimensional structures with poor conductive properties [37]. Incorporation of $Sr, Cd, Ca, Sn,$ into $MAX_xPb_{1-x}I_3$ perovskites study revealed that the addition of Sr^{2+} significantly reducing the crystallinity of the active layer compared to $Sn^{2+},$ meanwhile the residuals of PbI_2 and CdI_2 occurred in Cd^{2+} doped samples, surprisingly Ca^{2+} contained samples showing the cubic phase instead of the tetragonal phase [167], [168]. Also, the results explain that $Cd - I$ interaction is more vital than other elements to iodine interactions such as $Ca - I$ and $Sr - I$ due to more ionic behavior in nature; as a result, it provides lower E_g value, i.e., $Pb^{2+} \geq Sn^{2+} > Cd^{2+} > Ca^{2+} > Ba^{2+} > Sr^{2+}$. Pure

Mg^{2+} substitution into $AMgX_x$ (where $A = MA^+,\ FA^+,\ Cs^+$) perovskites, significantly reduce the E_g value, which is more suitable for solar cells; however, it is not considerable than other elements due to its higher sensitivity behavior [168]. Partial substitution of $Co, Cu, Fe, Mg, Ni, Sn, Sr, Zn = B$ into $MA(Pb{:}B)I_x$ perovskite composition reveals that the appropriate amount of $Co - Pb$ included PSCs provides the highest efficiency, and there might be the possibility to obtain similar results for Mg, Ni, Zn element substitution [169]. The higher amount of Hg^{2+} (< 30%) incorporation into the perovskite composition influence the original material properties and also distorted the structure; meanwhile, an appropriate amount of dopant (i.e., Hg^{2+} - 10%) based PSCs provides respectable PCE [170]. While substituting the Sb^{3+} into MAPI perovskites (i.e., $MASb_xPb_{1-x}I_3$), the increment was observed in the E_g value (i.e., $MAPbI_3 = 1.55\, eV$, $MASb_xPb_{1-x}I_3 = 1.6\ to\ 1.9\ eV$) [171]. The main drawback of Ag^+ incorporation into perovskite material, which does not attach with I^- halogen due to its less ionic valency compared to Pb^+ [172]. Based on these observations, less toxicity and suitable element substitution into the perovskite composition is essential to get an environmental-lead free or low lead contained PSCs.

1.1.7. Conclusion

Due to the excellent and sky-rocketed efficiency within a short period, perovskite solar cells hold an unavoidable spot in the PV field. Nowadays, many researchers aim to resolve device stability issues to fulfill the commercialization requirement, such as reproducible and scalable fabrication techniques. Therefore, it is crucial to understanding the correlation between film fabrication/deposition conditions, film properties, and device performance. In this context, plenty of reports showing that the double ($FAMA, FACs, FARb$), triple ($FAMACs, FAMARb, FACsRb$) and quadrupole ($FAMACsRb$) cation composition strategy with surface or interface passivation treatment and/or with additives helps to achieve a high-quality film with improved crystallinity and with film morphology. As a result, double, triple, and quadrupole cation mixing with or without halide incorporation is an effective way to enhance the film properties by restricting the phase, and halide segregation, lead to higher efficiency.

To summarize, mixed organic FA cation-based perovskites are a promising material that shows excellent efficiency and device stability than mono-cation devices. However, they also suffer from several issues; for example, fabricating a highly reproducible device with long-term stability is not easy. Therefore, there is still an insightful investigation to be needed to understand the device mechanism clearly. Besides the absorber, chosen ETL and HTL layers and their fabrication conditions also play a vital role in deciding the device performance. Hence, the selected materials (perovskite, ETL, HTL), fabrication methods with surface passivation/additives (using spin-coating, spray coating, dip coating, etc.), and environments (room temperature or in an inert atmosphere) together decide the device performance. Once the issues are sorted out, the perovskites are going to rule the commercialization area compared to any other device in the near future.

1.2. Objective and Brief outline of the thesis

According to the published reports and the above discussions inform us that there is a significant need for innovative PV technologies, especially highly efficient, stable, and Pb-free or low Pb involved devices. Therefore, this study has been dedicated to studying formamidinium-cesium based devices; specifically, Copper and Bismuth iodide incorporated solar cells correlated to the simulation/theoretical study to reach more efficient PV performance devices with reduced Pb content. Therefore, based on the ideas, this thesis is composed of eight chapters, and the chapter-wise brief description is provided in the following table.

CHAPTER	CONTENT
CHAPTER I	a literature review based on recent reports regarding perovskite solar cells will be advantageous for the readers. Also, it covers different fabrication techniques and different possible perovskite compositions.
CHAPTER II	focused on the detailed information about the basic simulation theory used to build the perovskite unit cell using the Materials Studio *software*.
CHAPTER III	covers a brief explanation of materials and experimental methods, especially preparation of ETL, perovskite, and HTL solution, including substrate cleaning, etc.
CHAPTER IV	carries out detailed information about the techniques used for each layer deposition and the fabrication of a complete perovskite device with characterization procedures.
CHAPTER V	explains the comprehensive knowledge about the numerical simulations used to construct a perovskite device using the SCAPS-1D *software*.

CHAPTER VI	Structural and mechanical stability behavior of $FAPbX_3$ perovskites (Based on the published research paper and conference proceedings).
CHAPTER VII	Experimental and SCAPS simulated Formamidinium perovskite solar cells: A comparison of device performance. (Based on the published research paper).
CHAPTER VIII	Effect of Copper iodide and Bismuth iodide incorporation into the FA-Cs perovskite solar cells. (Based on the published papers).
General conclusion and Future prospects	

References

[1] "U.S. Energy Information Administration, Annual Energy Outlook 2020 (AEO2020).".

[2] A. E. Becquerel, “Memoire sur les Effects d’Electriques Produits Sous l’Influence des Rayons Solaires,” *Comptes Rendus l’Academie des Sci.*, vol. 9, pp. 561–567, 1839.

[3] C. E. Fritts, "On a new form of selenium cell, and some electrical discoveries made by its use," *Am. J. Sci.*, 1883, doi: 10.2475/ajs.s3-26.156.465.

[4] "Solar Cell: Working Principle & Construction," 2020. https://www.electrical4u.com/solar-cell/.

[5] NREL, "Best Research-Cell Efficiency Chart | Photovoltaic Research | NREL 2020." 2020, [Online]. Available: https://www.nrel.gov/pv/cell-efficiency.html.

[6] S. A. Olaleru, J. K. Kirui, D. Wamwangi, K. T. Roro, and B. Mwakikunga, "Perovskite solar cells: The new epoch in photovoltaics," *Solar Energy*. 2020, doi: 10.1016/j.solener.2019.12.025.

[7] M. I. H. Ansari, A. Qurashi, and M. K. Nazeeruddin, "Frontiers, opportunities, and challenges in perovskite solar cells: A critical review," *Journal of Photochemistry and Photobiology C: Photochemistry Reviews*. 2018, doi: 10.1016/j.jphotochemrev.2017.11.002.

[8] Hans-Rudolf Wenk and Andrei Bulakh, *Minerals: Their Constitution and Origin*. Cambridge University Press, 2004.

[9] M. M. E. M. De Graef, *Structure of Materials An Introduction to Crystallography, Diffraction and Symmetry 2nd Edition*. Cambridge University Press, 2012.

[10] A. Navrotsky, "Energetics and Crystal Chemical Systematic among Ilmenite, Lithium Niobate, and Perovskite Structures," *Chemistry of Materials*. 1998, doi: 10.1021/cm9801901.

[11] M. Johnsson and P. Lemmens, "Crystallography and Chemistry of Perovskites," in *Handbook of Magnetism and Advanced Magnetic Materials*, 2007.

[12] Q. Chen *et al.*, "Under the spotlight: The organic-inorganic hybrid halide perovskite for optoelectronic applications," *Nano Today*. 2015, doi: 10.1016/j.nantod.2015.04.009.

[13] V. M. Goldschmidt, “Die Gesetze der Krystallochemie,” *Naturwissenschaften*, 1926, doi: 10.1007/BF01507527.

[14] W. Travis, E. N. K. Glover, H. Bronstein, D. O. Scanlon, and R. G. Palgrave, "On the application of the tolerance factor to inorganic and hybrid halide perovskites: A revised system," *Chem. Sci.*, 2016, doi: 10.1039/c5sc04845a.

[15] S. F. Hoefler, G. Trimmel, and T. Rath, “Progress on lead-free metal halide perovskites for photovoltaic applications: a review,” *Monatshefte fur Chemie*. 2017, doi: 10.1007/s00706-017-1933-9.

[16] C. J. Bartel *et al.*, "New tolerance factor to predict the stability of perovskite oxides and halides," *Sci. Adv.*, 2019, doi: 10.1126/sciadv.aav0693.

[17] G. Kieslich, S. Sun, and A. K. Cheetham, "An extended Tolerance Factor approach for organic-inorganic perovskites," *Chem. Sci.*, 2015, doi: 10.1039/c5sc00961h.

[18] F. Sani, S. Shafie, H. N. Lim, and A. O. Musa, "Advancement on lead-free organic-inorganic halide perovskite solar cells: A review," *Materials*. 2018, doi: 10.3390/ma11061008.

[19] Y. Lou *et al.*, "Rod-shaped thiocyanate-induced abnormal band gap broadening in SCN− doped CsPbBr3 perovskite nanocrystals," *Nano Res.*, 2018, doi: 10.1007/s12274-017-1901-z.

[20] D. S. Narges Yaghoobi Ni and A. D. C. Alessandro Lorenzo Palma, "CHAPTER FIVE Perovskite solar cells," in *Solar Cells and Light Management*, Elsevier, 2020.

[21] M. Becker, T. Klüner, and M. Wark, "Formation of hybrid ABX3 perovskite compounds for solar cell application: first-principles calculations of effective ionic radii and determination of tolerance factors," *Dalt. Trans.*, 2017, doi: 10.1039/c6dt04796c.

[22] M. D. Sampson, J. S. Park, R. D. Schaller, M. K. Y. Chan, and A. B. F. Martinson, "Transition metal-substituted lead halide perovskite absorbers," *J. Mater. Chem. A*, 2017, doi: 10.1039/C6TA09745F.

[23] T. Oku, "Crystal structures of perovskite halide compounds used for solar cells," *Reviews on Advanced Materials Science*. 2020, doi: 10.1515/rams-2020-0015.

[24] C. Li, X. Lu, W. Ding, L. Feng, Y. Gao, and Z. Guo, "Formability of ABX 3 (X = F, Cl, Br, I) halide perovskites," *Acta Crystallogr. Sect. B Struct. Sci.*, 2008, doi: 10.1107/S0108768108032734.

[25] Z. Xiao and Y. Yan, "Progress in Theoretical Study of Metal Halide Perovskite Solar Cell Materials," *Advanced Energy Materials*. 2017, doi: 10.1002/aenm.201701136.

[26] Y. Fu *et al.*, "Incorporating Large A Cations into Lead Iodide Perovskite Cages: Relaxed Goldschmidt Tolerance Factor and Impact on Exciton-Phonon Interaction," *ACS Cent. Sci.*, 2019, doi: 10.1021/acscentsci.9b00367.

[27] W. Li, Z. Wang, F. Deschler, S. Gao, R. H. Friend, and A. K. Cheetham, "Chemically diverse and multifunctional hybrid organic-inorganic perovskites," *Nature Reviews Materials*. 2017, doi: 10.1038/natrevmats.2016.99.

[28] Y. H. Chang, C. H. Park, and K. Matsuishi, "First-principles study of the structural and the electronic properties of the lead-halide-based inorganic-organic perovskites (CH 3NH 3)PbX 3 and CsPbX 3 (X = Cl, Br, I)," *J. Korean Phys. Soc.*, 2004.

[29] S. Pang *et al.*, "NH2CH=NH2PbI3: An alternative organolead iodide perovskite sensitizer for mesoscopic solar cells," *Chem. Mater.*, 2014, doi: 10.1021/cm404006p.

[30] J. H. Im, J. Chung, S. J. Kim, and N. G. Park, "Synthesis, structure, and photovoltaic property of a nanocrystalline 2H perovskite-type novel sensitizer (CH3CH2NH3)PbI3," *Nanoscale Res. Lett.*, 2012, doi: 10.1186/1556-276X-7-353.

[31] S. Aharon, A. Dymshits, A. Rotem, and L. Etgar, "Temperature dependence of hole conductor free formamidinium lead iodide perovskite based solar cells," *J. Mater. Chem. A*, 2015, doi: 10.1039/c4ta05149a.

[32] C. C. Stoumpos, C. D. Malliakas, and M. G. Kanatzidis, "Semiconducting tin and lead iodide perovskites with organic cations: Phase transitions, high mobilities, and near-infrared photoluminescent properties," *Inorg.*

Chem., 2013, doi: 10.1021/ic401215x.

[33] P. Roy, N. Kumar Sinha, S. Tiwari, and A. Khare, "A review on perovskite solar cells: Evolution of architecture, fabrication techniques, commercialization issues and status," *Solar Energy*. 2020, doi: 10.1016/j.solener.2020.01.080.

[34] "Factors affecting the stability of perovskite solar cells: a comprehensive review," *J. Photonics Energy*, 2019, doi: 10.1117/1.jpe.9.021001.

[35] J. Burschka *et al.*, "Sequential deposition as a route to high-performance perovskite-sensitized solar cells," *Nature*, 2013, doi: 10.1038/nature12340.

[36] Z. Zhu *et al.*, "Metal halide perovskites: stability and sensing-ability," *Journal of Materials Chemistry C*. 2018, doi: 10.1039/C8TC03164A.

[37] S. Chatterjee and A. J. Pal, "Influence of metal substitution on hybrid halide perovskites: Towards lead-free perovskite solar cells," *J. Mater. Chem. A*, 2018, doi: 10.1039/c7ta09943f.

[38] P. Umari, E. Mosconi, and F. De Angelis, "Relativistic GW calculations on CH3 NH3 PbI 3 and CH3 NH3 SnI3 Perovskites for Solar Cell Applications," *Sci. Rep.*, 2014, doi: 10.1038/srep04467.

[39] F. Hao, C. C. Stoumpos, D. H. Cao, R. P. H. Chang, and M. G. Kanatzidis, "Lead-free solid-state organic-inorganic halide perovskite solar cells," *Nat. Photonics*, 2014, doi: 10.1038/nphoton.2014.82.

[40] C. Liu, W. Li, J. Fan, and Y. Mai, "A brief review on the lead element substitution in perovskite solar cells," *Journal of Energy Chemistry*. 2018, doi: 10.1016/j.jechem.2017.10.028.

[41] Y. Ogomi *et al.*, "CH3NH3SnxPb(1-x)I3 perovskite solar cells covering up to 1060 nm," *J. Phys. Chem. Lett.*, 2014, doi: 10.1021/jz5002117.

[42] Z. Wang, Z. Shi, T. Li, Y. Chen, and W. Huang, "Stability of Perovskite Solar Cells: A Prospective on the Substitution of the A Cation and X Anion," *Angewandte Chemie - International Edition*. 2017, doi: 10.1002/anie.201603694.

[43] N. Pellet *et al.*, "Mixed-Organic-Cation Perovskite Photovoltaics for Enhanced Solar-Light Harvesting," *Angew. Chemie*, 2014, doi: 10.1002/ange.201309361.

[44] A. D. Jodlowski *et al.*, "Large guanidinium cation mixed with methylammonium in lead iodide perovskites for 19% efficient solar cells," *Nat. Energy*, 2017, doi: 10.1038/s41560-017-0054-3.

[45] H. F. Zarick, N. Soetan, W. R. Erwin, and R. Bardhan, "Mixed halide hybrid perovskites: A paradigm shift in photovoltaics," *Journal of Materials Chemistry A*. 2018, doi: 10.1039/c7ta09122b.

[46] C. H. Lu, G. V. Biesold-McGee, Y. Liu, Z. Kang, and Z. Lin, "Doping and ion substitution in colloidal metal halide perovskite nanocrystals," *Chemical Society reviews*. 2020, doi: 10.1039/c9cs00790c.

[47] A. Urbina, "The balance between efficiency, stability and environmental impacts in perovskite solar cells: a review," *J. Phys. Energy*, 2020, doi: 10.1088/2515-7655/ab5eee.

[48] A. Toshniwal and V. Kheraj, "Development of organic-inorganic tin halide perovskites: A review," *Solar Energy*. 2017, doi: 10.1016/j.solener.2017.03.077.

[49] H. Tsai *et al.*, "Light-induced lattice expansion CsFAMAIBr Solar Cell," *Science (80-.).*, 2018, doi: 10.1126/science.aap8671.

[50] D. Ghosh, A. R. Smith, A. B. Walker, and M. S. Islam, "Mixed A-Cation Perovskites for Solar Cells: Atomic-Scale Insights into Structural Distortion, Hydrogen Bonding, and Electronic Properties," *Chem. Mater.*, 2018, doi: 10.1021/acs.chemmater.8b01851.

[51] U. B. Cappel *et al.*, "Partially Reversible Photoinduced Chemical Changes in a Mixed-Ion Perovskite Material for Solar Cells," *ACS Appl. Mater. Interfaces*, 2017, doi: 10.1021/acsami.7b10643.

[52] L. K. Ono, E. J. Juarez-Perez, and Y. Qi, "Progress on Perovskite Materials and Solar Cells with Mixed Cations and Halide Anions," *ACS Applied Materials and Interfaces*. 2017, doi: 10.1021/acsami.7b06001.

[53] T. Chen *et al.*, "Rotational dynamics of organic cations in the CH3NH3PbI3 perovskite," *Phys. Chem. Chem. Phys.*, 2015, doi: 10.1039/c5cp05348j.

[54] P. S. Whitfield *et al.*, "Structures, Phase Transitions and Tricritical Behavior of the Hybrid Perovskite Methyl Ammonium Lead Iodide," *Sci. Rep.*, 2016, doi: 10.1038/srep35685.

[55] A. Halder, Y. Rakita, D. Cahen, and S. K. Sarkar, "Effect of Low Pressure on Tetragonal to Cubic Phase Transition of Methylammonium Lead Iodide Perovskite," *J. Phys. Chem. Lett.*, 2020, doi: 10.1021/acs.jpclett.9b03895.

[56] G. Sombrio *et al.*, "Charge Transport in MAPbI3Pellets across the Tetragonal-to-Cubic Phase Transition: The Role of Grain Boundaries from Structural, Electrical, and Optical Characterizations," *J. Phys. Chem. C*, 2020, doi: 10.1021/acs.jpcc.0c00887.

[57] S. Rühle, "Tabulated values of the Shockley-Queisser limit for single junction solar cells," *Sol. Energy*, 2016, doi: 10.1016/j.solener.2016.02.015.

[58] J. H. Noh, S. H. Im, J. H. Heo, T. N. Mandal, and S. Il Seok, "Chemical management for colorful, efficient, and stable inorganic-organic hybrid nanostructured solar cells," *Nano Lett.*, 2013, doi: 10.1021/nl400349b.

[59] C. Lin, S. Li, W. Zhang, C. Shao, and Z. Yang, "Effect of Bromine Substitution on the Ion Migration and Optical Absorption in MAPbI3 Perovskite Solar Cells: The First-Principles Study," *ACS Appl. Energy Mater.*, 2018, doi: 10.1021/acsaem.8b00026.

[60] H. Zhang, Q. Liao, X. Wang, K. Hu, J. Yao, and H. Fu, "Controlled Substitution of Chlorine for Iodine in Single-Crystal Nanofibers of Mixed Perovskite MAPbI3–xClx," *Small*, 2016, doi: 10.1002/smll.201601201.

[61] M. Li, T. Liu, Y. Wang, W. Yang, and X. Lü, "Pressure responses of halide perovskites with various compositions, dimensionalities, and morphologies," *Matter and Radiation at Extremes*. 2020, doi: 10.1063/1.5133653.

[62] B. Wang, N. Novendra, and A. Navrotsky, "Energetics, Structures, and Phase Transitions of Cubic and Orthorhombic Cesium Lead Iodide (CsPbI3) Polymorphs," *J. Am. Chem. Soc.*, 2019, doi: 10.1021/jacs.9b05924.

[63] J. A. Steele *et al.*, "Thermal unequilibrium of strained black CsPbI3 thin films," *Science (80-.).*, 2019, doi: 10.1126/science.aax3878.

[64] G. E. Eperon, S. D. Stranks, C. Menelaou, M. B. Johnston, L. M. Herz, and H. J. Snaith, "Formamidinium lead trihalide: A broadly tunable perovskite for efficient planar heterojunction solar cells," *Energy Environ. Sci.*, 2014, doi: 10.1039/c3ee43822h.

[65] Q. Han *et al.*, "Single Crystal Formamidinium Lead Iodide (FAPbI3): Insight into the Structural, Optical, and Electrical Properties," *Adv. Mater.*, 2016, doi: 10.1002/adma.201505002.

[66] F. Cordero *et al.*, "Stability of Cubic FAPbI3 from X-ray Diffraction, Anelastic, and Dielectric Measurements," *J. Phys. Chem. Lett.*, 2019, doi: 10.1021/acs.jpclett.9b00896.

[67] G. Liu *et al.*, "Pressure-Induced Bandgap Optimization in Lead-Based Perovskites with Prolonged Carrier Lifetime and Ambient Retainability," *Adv. Funct. Mater.*, 2017, doi: 10.1002/adfm.201604208.

[68] A. Francisco-López *et al.*, "Phase Diagram of Methylammonium/Formamidinium Lead Iodide Perovskite Solid Solutions from Temperature-Dependent Photoluminescence and Raman Spectroscopies," *J. Phys. Chem. C*, 2020, doi: 10.1021/acs.jpcc.9b10185.

[69] E. Leccisi and V. Fthenakis, "Life-cycle environmental impacts of single-junction and tandem perovskite PVs: a critical review and future perspectives," *Prog. Energy*, 2020, doi: 10.1088/2516-1083/ab7e84.

[70] R. Wang, M. Mujahid, Y. Duan, Z. K. Wang, J. Xue, and Y. Yang, "A Review of Perovskites Solar Cell

Stability," *Advanced Functional Materials*. 2019, doi: 10.1002/adfm.201808843.

[71] Z. Song, S. C. Watthage, A. B. Phillips, and M. J. Heben, "Pathways toward high-performance perovskite solar cells: review of recent advances in organo-metal halide perovskites for photovoltaic applications," *J. Photonics Energy*, 2016, doi: 10.1117/1.jpe.6.022001.

[72] N. Torabi *et al.*, "Progress and challenges in perovskite photovoltaics from single- to multi-junction cells," *Materials Today Energy*. 2019, doi: 10.1016/j.mtener.2018.12.009.

[73] Z. Li *et al.*, "Scalable fabrication of perovskite solar cells," *Nature Reviews Materials*. 2018, doi: 10.1038/natrevmats.2018.17.

[74] J. M. Ball, M. M. Lee, A. Hey, and H. J. Snaith, "Low-temperature processed meso-superstructured to thin-film perovskite solar cells," *Energy Environ. Sci.*, 2013, doi: 10.1039/c3ee40810h.

[75] M. Zhang *et al.*, "High-Performance Photodiode-Type Photodetectors Based on Polycrystalline Formamidinium Lead Iodide Perovskite Thin Films," *Sci. Rep.*, 2018, doi: 10.1038/s41598-018-29147-6.

[76] A. Baltakesmez, "FAPbI3 perovskite thin film having α/δ phase junction and its light harvesting performance in solar cell," *J. Mater. Sci. Mater. Electron.*, 2020, doi: 10.1007/s10854-020-04331-5.

[77] M. Mozaffari, A. Behjat, and B. B. F. Mirjalili, "The effect of solution process control on the formation of the A-FAPbI3 perovskite: FAPbI3 versus MAPbI3 solar cells," *Sol. Energy*, 2018, doi: 10.1016/j.solener.2018.09.067.

[78] H. Lu *et al.*, "Vapor-assisted deposition of highly efficient, stable black-phase FAPbI3 perovskite solar cells," *Science (80-.).*, vol. 370, no. 6512, Oct. 2020, doi: 10.1126/SCIENCE.ABB8985.

[79] M. R. Leyden, Y. Jiang, and Y. Qi, "Chemical vapor deposition grown formamidinium perovskite solar modules with high steady state power and thermal stability," *J. Mater. Chem. A*, 2016, doi: 10.1039/c6ta04267h.

[80] J. Ávila, C. Momblona, P. P. Boix, M. Sessolo, and H. J. Bolink, “Vapor-Deposited Perovskites: The Route to High-Performance Solar Cell Production?,” *Joule*. 2017, doi: 10.1016/j.joule.2017.07.014.

[81] J. C. S. Costa, J. Azevedo, L. M. N. B. F. Santos, and A. Mendes, "On the Deposition of Lead Halide Perovskite Precursors by Physical Vapor Method," *J. Phys. Chem. C*, 2017, doi: 10.1021/acs.jpcc.6b11625.

[82] W. Q. Wu, P. N. Rudd, Q. Wang, Z. Yang, and J. Huang, "Blading Phase-Pure Formamidinium-Alloyed Perovskites for High-Efficiency Solar Cells with Low Photovoltage Deficit and Improved Stability," *Adv. Mater.*, 2020, doi: 10.1002/adma.202000995.

[83] A. Vijayan, M. B. Johansson, S. Svanström, U. B. Cappel, H. Rensmo, and G. Boschloo, "Simple Method for Efficient Slot-Die Coating of MAPbI3Perovskite Thin Films in Ambient Air Conditions," *ACS Appl. Energy Mater.*, 2020, doi: 10.1021/acsaem.0c00039.

[84] L. Gao, K. Huang, C. Long, F. Zeng, B. Liu, and J. Yang, "Fully slot-die-coated perovskite solar cells in ambient condition," *Appl. Phys. A Mater. Sci. Process.*, 2020, doi: 10.1007/s00339-020-03628-w.

[85] H. Cai *et al.*, "High Efficiency Over 20% of Perovskite Solar Cells by Spray-Coating via a Simple Process," *ACS Appl. Energy Mater.*, p. acsaem.0c01129, Sep. 2020, doi: 10.1021/acsaem.0c01129.

[86] F. Mathies, H. Eggers, B. S. Richards, G. Hernandez-Sosa, U. Lemmer, and U. W. Paetzold, "Inkjet-Printed Triple Cation Perovskite Solar Cells," *ACS Appl. Energy Mater.*, 2018, doi: 10.1021/acsaem.8b00222.

[87] I. A. Howard *et al.*, "Coated and Printed Perovskites for Photovoltaic Applications," *Adv. Mater.*, 2019, doi: 10.1002/adma.201806702.

[88] S. Hoffmann-Urlaub, Y. Zhang, Z. Wang, B. Kressdorf, and T. Meyer, “Fabrication of tin-based halide perovskites by pulsed laser deposition,” *Appl. Phys. A Mater. Sci. Process.*, 2020, doi: 10.1007/s00339-020-03699-9.

[89] A. F. Xu, R. T. Wang, L. W. Yang, E. E. Liu, and G. Xu, "An environmentally stable organic–inorganic hybrid perovskite containing py cation with low trap-state density," *Crystals*, 2020, doi: 10.3390/cryst10040272.

[90] G. Murugadoss, R. Thangamuthu, and M. Rajesh Kumar, "Formamidinium lead iodide perovskite: Structure, shape and optical tuning via hydrothermal method," *Mater. Lett.*, 2018, doi: 10.1016/j.matlet.2018.08.003.

[91] Q. Wang, N. Phung, D. Di Girolamo, P. Vivo, and A. Abate, "Enhancement in lifespan of halide perovskite solar cells," *Energy and Environmental Science*. 2019, doi: 10.1039/c8ee02852d.

[92] L. Meng, J. You, and Y. Yang, "Addressing the stability issue of perovskite solar cells for commercial applications," *Nature Communications*. 2018, doi: 10.1038/s41467-018-07255-1.

[93] Q. Wali, F. J. Iftikhar, M. E. Khan, A. Ullah, Y. Iqbal, and R. Jose, "Advances in stability of perovskite solar cells," *Organic Electronics*. 2020, doi: 10.1016/j.orgel.2019.105590.

[94] F. U. Kosasih and C. Ducati, "Characterising degradation of perovskite solar cells through in-situ and operando electron microscopy," *Nano Energy*. 2018, doi: 10.1016/j.nanoen.2018.02.055.

[95] F. Corsini and G. Griffini, "Recent progress in encapsulation strategies to enhance the stability of organometal halide perovskite solar cells," *J. Phys. Energy*, 2020, doi: 10.1088/2515-7655/ab8774.

[96] S. Ma *et al.*, "1000 h Operational Lifetime Perovskite Solar Cells by Ambient Melting Encapsulation," *Adv. Energy Mater.*, 2020, doi: 10.1002/aenm.201902472.

[97] M. I. Asghar, J. Zhang, H. Wang, and P. D. Lund, "Device stability of perovskite solar cells – A review," *Renewable and Sustainable Energy Reviews*. 2017, doi: 10.1016/j.rser.2017.04.003.

[98] Y. Li *et al.*, "A review on morphology engineering for highly efficient and stable hybrid perovskite solar cells," *Journal of Materials Chemistry A*. 2018, doi: 10.1039/c8ta04120b.

[99] Y. Li *et al.*, "Formamidinium-Based Lead Halide Perovskites: Structure, Properties, and Fabrication Methodologies," *Small Methods*, 2018, doi: 10.1002/smtd.201700387.

[100] Y. Fan, H. Meng, L. Wang, and S. Pang, "Review of Stability Enhancement for Formamidinium-Based Perovskites," *Solar RRL*. 2019, doi: 10.1002/solr.201900215.

[101] S. Liu *et al.*, "A Review on Additives for Halide Perovskite Solar Cells," *Advanced Energy Materials*. 2020, doi: 10.1002/aenm.201902492.

[102] J. Ma and D. Guo, "A data review on certified perovskite solar cells efficiency and I-V metrics: Insights into materials selection and process scaling up," *Solar Energy*. 2020, doi: 10.1016/j.solener.2020.08.090.

[103] S. Masi, A. F. Gualdrón-Reyes, and I. Mora-Seró, "Stabilization of Black Perovskite Phase in FAPbI3and CsPbI3," *ACS Energy Letters*. 2020, doi: 10.1021/acsenergylett.0c00801.

[104] D. H. Fabini *et al.*, "Reentrant Structural and Optical Properties and Large Positive Thermal Expansion in Perovskite Formamidinium Lead Iodide," *Angew. Chemie - Int. Ed.*, 2016, doi: 10.1002/anie.201609538.

[105] M. T. Weller, O. J. Weber, J. M. Frost, and A. Walsh, "Cubic Perovskite Structure of Black Formamidinium Lead Iodide, α-[HC(NH2)2]PbI3, at 298 K," *J. Phys. Chem. Lett.*, 2015, doi: 10.1021/acs.jpclett.5b01432.

[106] Y. Zhang, S. G. Kim, D. K. Lee, and N. G. Park, "CH3NH3PbI3 and HC(NH2)2PbI3 Powders Synthesized from Low-Grade PbI2: Single Precursor for High-Efficiency Perovskite Solar Cells," *ChemSusChem*, 2018, doi: 10.1002/cssc.201800610.

[107] T. M. Koh *et al.*, "Formamidinium-containing metal-halide: An alternative material for near-IR absorption perovskite solar cells," *J. Phys. Chem. C*, 2014, doi: 10.1021/jp411112k.

[108] T. Chen *et al.*, "Entropy-driven structural transition and kinetic trapping in formamidinium lead iodide perovskite," *Sci. Adv.*, 2016, doi: 10.1126/sciadv.1601650.

[109] F. Ma, J. Li, W. Li, N. Lin, L. Wang, and J. Qiao, "Stable α/δ phase junction of formamidinium lead iodide

perovskites for enhanced near-infrared emission," *Chem. Sci.*, 2016, doi: 10.1039/c6sc03542f.

[110] Y. Zhang *et al.*, "Efficient inverted planar formamidinium lead iodide perovskite solar cells via a post improved perovskite layer," *RSC Adv.*, 2016, doi: 10.1039/c6ra15210d.

[111] M. Kato *et al.*, "Universal rules for visible-light absorption in hybrid perovskite materials," *J. Appl. Phys.*, 2017, doi: 10.1063/1.4978071.

[112] V. L. Pool *et al.*, "Thermal engineering of FAPbI3 perovskite material via radiative thermal annealing and in situ XRD," *Nat. Commun.*, 2017, doi: 10.1038/ncomms14075.

[113] J. A. Aguiar *et al.*, "In situ investigation of the formation and metastability of formamidinium lead tri-iodide perovskite solar cells," *Energy Environ. Sci.*, 2016, doi: 10.1039/c6ee01079b.

[114] E. J. Juarez-Perez, L. K. Ono, and Y. Qi, "Thermal degradation of formamidinium based lead halide perovskites into: Sym -triazine and hydrogen cyanide observed by coupled thermogravimetry-mass spectrometry analysis," *J. Mater. Chem. A*, 2019, doi: 10.1039/c9ta06058h.

[115] A. F. Akbulatov *et al.*, "Intrinsic thermal decomposition pathways of lead halide perovskites APbX3," *Sol. Energy Mater. Sol. Cells*, 2020, doi: 10.1016/j.solmat.2020.110559.

[116] G. Murugadoss, P. Kuppusami, and M. Rajesh Kumar, "Solvent effect on structure and morphology of formamidinium lead tri-iodide perovskite via hydrothermal method," *Inorg. Chem. Commun.*, 2020, doi: 10.1016/j.inoche.2020.108059.

[117] L. Ma *et al.*, "Temperature-dependent thermal decomposition pathway of organic-inorganic halide perovskite materials," *Chem. Mater.*, 2019, doi: 10.1021/acs.chemmater.9b03190.

[118] R. Szostak *et al.*, "Exploring the formation of formamidinium-based hybrid perovskites by antisolvent methods: In situ GIWAXS measurements during spin coating," *Sustain. Energy Fuels*, 2019, doi: 10.1039/c9se00306a.

[119] M. Jeong *et al.*, "Stable perovskite solar cells with efficiency exceeding 24.8% and 0.3-V voltage loss," *Science*, 2020, doi: 10.1126/science.abb7167.

[120] H. Min *et al.*, "Efficient, stable solar cells by using inherent bandgap of a-phase formamidinium lead iodide," *Science (80-.).*, 2019, doi: 10.1126/science.aay7044.

[121] G. Kim, H. Min, K. S. Lee, D. Y. Lee, S. M. Yoon, and S. Il Seok, "Impact of strain relaxation on performance of α-formamidinium lead iodide perovskite solar cells," *Science*, 2020, doi: 10.1126/science.abc4417.

[122] M. Kim *et al.*, "Effects of cation size and concentration of cationic chlorides on the properties of formamidinium lead iodide based perovskite solar cells," *Sustain. Energy Fuels*, 2020, doi: 10.1039/d0se00382d.

[123] Y. Liu *et al.*, "Stabilization of Highly Efficient and Stable Phase-Pure FAPbI3 Perovskite Solar Cells by Molecularly Tailored 2D-Overlayers," *Angew. Chemie - Int. Ed.*, 2020, doi: 10.1002/anie.202005211.

[124] Y. Zhang *et al.*, "Achieving Reproducible and High-Efficiency (>21%) Perovskite Solar Cells with a Presynthesized FAPbI3 Powder," *ACS Energy Lett.*, pp. 360–366, 2020, doi: 10.1021/acsenergylett.9b02348.

[125] C. Shen *et al.*, "Stabilizing Formamidinium Lead Iodide Perovskite by Sulfonyl-Functionalized Phenethylammonium Salt via Crystallization Control and Surface Passivation," *Sol. RRL*, 2020, doi: 10.1002/solr.202000069.

[126] W. Luo *et al.*, "Efficient and Stable Perovskite Solar Cell with High Open-Circuit Voltage by Dimensional Interface Modification," *ACS Appl. Mater. Interfaces*, 2019, doi: 10.1021/acsami.8b22040.

[127] M. Lyu, D. K. Lee, and N. G. Park, "Effect of alkaline earth metal chloride additives BCl2 (B = Mg, Ca, Sr and Ba) on the photovoltaic performance of FAPbI3 based perovskite solar cells," *Nanoscale horizons*, 2020, doi: 10.1039/d0nh00263a.

[128] S. Akin, E. Akman, and S. Sonmezoglu, "FAPbI3-Based Perovskite Solar Cells Employing Hexyl-Based Ionic Liquid with an Efficiency Over 20% and Excellent Long-Term Stability," *Adv. Funct. Mater.*, 2020, doi: 10.1002/adfm.202002964.

[129] T. Niu *et al.*, "High performance ambient-air-stable FAPbI 3 perovskite solar cells with molecule-passivated Ruddlesden-Popper/3D heterostructured film," *Energy Environ. Sci.*, 2018, doi: 10.1039/c8ee02542h.

[130] X. Shi *et al.*, "Efficient Formamidinium-Based Planar Perovskite Solar Cells Fabricated through a CaI2-PbI2 Precursor," *ACS Sustain. Chem. Eng.*, 2020, doi: 10.1021/acssuschemeng.9b07738.

[131] J. Kim *et al.*, "Nucleation and Growth Control of HC(NH2)2PbI3 for Planar Perovskite Solar Cell," *J. Phys. Chem. C*, 2016, doi: 10.1021/acs.jpcc.6b02443.

[132] X. Xu *et al.*, "Elimination of Yellow Phase: An Effective Method to Achieve High Quality HC(NH2)2PbI3-based Perovskite Films," *ChemSusChem*, 2020, doi: 10.1002/cssc.201903216.

[133] Q. Wei *et al.*, "Effective solvent-additive enhanced crystallization and coverage of absorber layers for high efficiency formamidinium perovskite solar cells," *RSC Adv.*, 2016, doi: 10.1039/c6ra10007d.

[134] J. W. Lee, H. S. Kim, and N. G. Park, "Lewis Acid-Base Adduct Approach for High Efficiency Perovskite Solar Cells," *Acc. Chem. Res.*, 2016, doi: 10.1021/acs.accounts.5b00440.

[135] Z. Li, M. Yang, J. S. Park, S. H. Wei, J. J. Berry, and K. Zhu, "Stabilizing Perovskite Structures by Tuning Tolerance Factor: Formation of Formamidinium and Cesium Lead Iodide Solid-State Alloys," *Chem. Mater.*, 2016, doi: 10.1021/acs.chemmater.5b04107.

[136] J. W. Lee, D. H. Kim, H. S. Kim, S. W. Seo, S. M. Cho, and N. G. Park, "Formamidinium and cesium hybridization for photo- and moisture-stable perovskite solar cell," *Adv. Energy Mater.*, 2015, doi: 10.1002/aenm.201501310.

[137] Y. Liu *et al.*, "Formamidinium-Based Perovskite Solar Cells with Enhanced Moisture Stability and Performance via Confined Pressure Annealing," *J. Phys. Chem. C*, 2020, doi: 10.1021/acs.jpcc.0c02289.

[138] J. Yang *et al.*, "Crystallization tailoring of cesium/formamidinium double-cation perovskite for efficient and highly stable solar cells," *J. Energy Chem.*, 2020, doi: 10.1016/j.jechem.2020.01.012.

[139] L. Xie *et al.*, "Revealing the compositional effect on the intrinsic long-term stability of perovskite solar cells," *J. Mater. Chem. A*, 2020, doi: 10.1039/d0ta01668c.

[140] A. Binek, F. C. Hanusch, P. Docampo, and T. Bein, "Stabilization of the trigonal high-temperature phase of formamidinium lead iodide," *J. Phys. Chem. Lett.*, 2015, doi: 10.1021/acs.jpclett.5b00380.

[141] J. M. Frost, K. T. Butler, F. Brivio, C. H. Hendon, M. Van Schilfgaarde, and A. Walsh, "Atomistic origins of high-performance in hybrid halide perovskite solar cells," *Nano Lett.*, 2014, doi: 10.1021/nl500390f.

[142] N. Yaghoobi Nia *et al.*, "Solution-based heteroepitaxial growth of stable mixed cation/anion hybrid perovskite thin film under ambient condition via a scalable crystal engineering approach," *Nano Energy*, 2020, doi: 10.1016/j.nanoen.2019.104441.

[143] Z. Li *et al.*, "Minimized surface deficiency on wide-bandgap perovskite for efficient indoor photovoltaics," *Nano Energy*, 2020, doi: 10.1016/j.nanoen.2020.105377.

[144] T. Bu *et al.*, "Surface modification via self-assembling large cations for improved performance and modulated hysteresis of perovskite solar cells," *J. Mater. Chem. A*, 2019, doi: 10.1039/c8ta12284a.

[145] F. Penã-Camargo *et al.*, "Halide Segregation versus Interfacial Recombination in Bromide-Rich Wide-Gap Perovskite Solar Cells," *ACS Energy Lett.*, 2020, doi: 10.1021/acsenergylett.0c01104.

[146] A. Kogo and M. Chikamatsu, "Electron band tuning of organolead halide perovskite materials by methylammonium and formamidinium halide post-treatment for high-efficiency solar cells," *Chem. Commun.*, 2020, doi: 10.1039/c9cc09002a.

[147] I. M. Pavlovetc *et al.*, "Suppressing Cation Migration in Triple-Cation Lead Halide Perovskites," *ACS Energy Lett.*, 2020, doi: 10.1021/acsenergylett.0c01207.

[148] N. Arora *et al.*, "Perovskite solar cells with CuSCN hole extraction layers yield stabilized efficiencies greater than 20%," *Science (80-.).*, 2017, doi: 10.1126/science.aam5655.

[149] H. Wei, S. Chen, J. Zhao, Z. Yu, and J. Huang, "Is Formamidinium Always More Stable than Methylammonium?," *Chem. Mater.*, 2020, doi: 10.1021/acs.chemmater.9b05101.

[150] S. Shi *et al.*, "Room-temperature synthesized SnO2 electron transport layers for efficient perovskite solar cells," *RSC Adv.*, vol. 9, no. 18, pp. 9946–9950, Mar. 2019, doi: 10.1039/C8RA10603G.

[151] Z. Xing *et al.*, "Mixed Fullerene Electron Transport Layers with Fluorocarbon Chains Assembling on the Surface: A Moisture-Resistant Coverage for Perovskite Solar Cells," *ACS Appl. Mater. Interfaces*, 2020, doi: 10.1021/acsami.0c10074.

[152] J. Ye *et al.*, "Enhanced Moisture Stability of Perovskite Solar Cells With Mixed-Dimensional and Mixed-Compositional Light-Absorbing Materials," *Sol. RRL*, 2017, doi: 10.1002/solr.201700125.

[153] D. Magaldi, M. Ulfa, S. Péralta, F. Goubard, T. Pauporté, and T. T. Bui, "Carbazole-based material: synthesis, characterization, and application as hole transporting material in perovskite solar cells," *J. Mater. Sci. Mater. Electron.*, 2020, doi: 10.1007/s10854-020-04021-2.

[154] M. Salado *et al.*, "Towards Extending Solar Cell Lifetimes: Addition of a Fluorous Cation to Triple Cation-Based Perovskite Films," *ChemSusChem*, 2017, doi: 10.1002/cssc.201700797.

[155] Y. Sun, J. Peng, Y. Chen, Y. Yao, and Z. Liang, "Triple-cation mixed-halide perovskites: Towards efficient, annealing-free and air-stable solar cells enabled by Pb(SCN) 2 additive," *Sci. Rep.*, 2017, doi: 10.1038/srep46193.

[156] S. Sánchez, J. Jerónimo-Rendon, M. Saliba, and A. Hagfeldt, "Highly efficient and rapid manufactured perovskite solar cells via Flash InfraRed Annealing," *Mater. Today*, 2020, doi: 10.1016/j.mattod.2019.11.003.

[157] S. H. Turren-Cruz *et al.*, "Enhanced charge carrier mobility and lifetime suppress hysteresis and improve efficiency in planar perovskite solar cells," *Energy Environ. Sci.*, 2018, doi: 10.1039/c7ee02901b.

[158] H. Tan *et al.*, "Efficient and stable solution-processed planar perovskite solar cells via contact passivation," *Science (80-.).*, 2017, doi: 10.1126/science.aai9081.

[159] H.-S. Kim *et al.*, "Reduced Graphene Oxide Improves Moisture and Thermal Stability of Perovskite Solar Cells," *Cell Reports Phys. Sci.*, 2020, doi: 10.1016/j.xcrp.2020.100053.

[160] C. Ge, Z. Yang, X. Liu, Y. Song, A. Wang, and Q. Dong, "Stable and Highly Flexible Perovskite Solar Cells with PCE Approaching 20% by Elastic Grain-Boundary Encapsulation," *CCS Chem.*, 2020, doi: 10.31635/ccschem.020.202000335.

[161] C. Dong *et al.*, "Lead Oxalate-Induced Nucleation Retardation for High-Performance Indoor and Outdoor Perovskite Photovoltaics," *ACS Appl. Mater. Interfaces*, 2020, doi: 10.1021/acsami.9b18230.

[162] S. Yu, H. Liu, S. Wang, H. Zhu, X. Dong, and X. Li, "Hydrazinium cation mixed FAPbI3-based perovskite with 1D/3D hybrid dimension structure for efficient and stable solar cells," *Chem. Eng. J.*, 2021, doi: 10.1016/j.cej.2020.125724.

[163] S. Wu, Z. Li, J. Zhang, T. Liu, Z. Zhu, and A. K. Y. Jen, "Efficient large guanidinium mixed perovskite solar cells with enhanced photovoltage and low energy losses," *Chem. Commun.*, 2019, doi: 10.1039/c9cc00016j.

[164] H. Fu, "Review of lead-free halide perovskites as light-absorbers for photovoltaic applications: From materials to solar cells," *Sol. Energy Mater. Sol. Cells*, 2019, doi: 10.1016/j.solmat.2018.12.038.

[165] J. Li, J. Duan, X. Yang, Y. Duan, P. Yang, and Q. Tang, "Review on recent progress of lead-free halide perovskites in optoelectronic applications," *Nano Energy*. 2021, doi: 10.1016/j.nanoen.2020.105526.

[166] X. Liu *et al.*, "Improved efficiency and stability of Pb-Sn binary perovskite solar cells by Cs substitution," *J. Mater. Chem. A*, 2016, doi: 10.1039/c6ta07712a.

[167] J. Navas *et al.*, "New insights into organic-inorganic hybrid perovskite CH3NH3PbI3 nanoparticles. An experimental and theoretical study of doping in Pb2+ sites with Sn2+, Sr2+, Cd2+ and Ca2+," *Nanoscale*, 2015, doi: 10.1039/c5nr00041f.

[168] M. R. Filip and F. Giustino, "Computational Screening of Homovalent Lead Substitution in Organic-Inorganic Halide Perovskites," *J. Phys. Chem. C*, 2016, doi: 10.1021/acs.jpcc.5b11845.

[169] M. T. Klug *et al.*, "Tailoring metal halide perovskites through metal substitution: Influence on photovoltaic and material properties," *Energy Environ. Sci.*, 2017, doi: 10.1039/c6ee03201j.

[170] L. A. Frolova, D. V. Anokhin, K. L. Gerasimov, N. N. Dremova, and P. A. Troshin, "Exploring the Effects of the Pb2+ Substitution in MAPbI3 on the Photovoltaic Performance of the Hybrid Perovskite Solar Cells," *J. Phys. Chem. Lett.*, 2016, doi: 10.1021/acs.jpclett.6b02122.

[171] J. Zhang *et al.*, "N-Type Doping and Energy States Tuning in CH3NH3Pb1-xSb2x/3I3 Perovskite Solar Cells," *ACS Energy Lett.*, 2016, doi: 10.1021/acsenergylett.6b00241.

[172] S. Shahbazi *et al.*, "Ag Doping of Organometal Lead Halide Perovskites: Morphology Modification and p-Type Character," *J. Phys. Chem. C*, 2017, doi: 10.1021/acs.jpcc.6b09722.

2. CHAPTER II. Theory and simulations

2.1. Materials Studio (MS) simulation *software*

In recent days, simulation and modeling play an essential role in the research field. BIOVIA MS simulation software is a versatile modeling and simulation platform [1], which provides plenty of options to researchers to develop new materials and analyze the behavior and properties with atomic and molecular structure levels. MS environment can perform the calculations for all types of materials such as nanomaterials, catalysts, batteries and fuel, pharmaceuticals, polymers and composites, metals and alloys, and more. It provides a complete graphical visualization environment for researchers. It will help construct, manipulate, and view the molecule models, crystalline materials, polymers, surfaces, and mesoscale structures through animation images, graphs, tables, and textual data. Notably, MS affords a comprehensive and complete range of simulation and modeling capabilities from quantum, atomistic, mesoscale, statistical, analytical, and crystallization tools [1]. Especially, the Cambridge Serial Total Energy Package (CASTEP) tool helps us simulate the fundamental properties of solids, surfaces, and interfaces for different materials, including semiconductors, metals, and ceramics, using a plane-wave density functional method. In this thesis, the CASTEP program is utilized to construct and analyze the perovskite structure's fundamental properties. Therefore, the following section explains the detailed information about CASTEP quantum simulation tools to investigate the perovskite structure and its properties.

2.2. CASTEP

The CASTEP is a quantum mechanics based versatile program created for solid-state material science, which employs the DFT with plane-wave pseudopotential set, which permits to perform the first-principles calculations in order to explore the fundamental properties (i.e., surface and structural properties, band structure, the density of states (DOS), optical properties, elastic constants, and other mechanical properties, etc.) of crystals and surfaces in materials like semiconductors, metals, liquids, amorphous materials, ceramics and zeolites, and more. In Cambridge, the Cavendish laboratory (TCM group) was design the CASTEP in the early 1990s [2], and it was initially a Fortran 77 code-based program. CASTEP license was extended to academic and commercial use world-wide in 2019, and the users can purchase the program as part of Biovia's MS package [3]. In MS - CASTEP program, the following concepts are crucial to understanding the calculation and the results.

2.2.1. Pseudopotential description

In general, electrons are categorized into two parts, such as valence electrons and inner core or ion core electrons (i.e., tightly bound with nuclei) based on many-electron Schrödinger equation. The valence electrons only contribute to finding the atoms' chemical binding properties, and the inner core electrons are not involved and considered frozen; it is called a pseudopotential approach. This pseudopotential approximation generated the weaker pseudopotential employing a set of pseudo wave functions instead of inner core electrons and the Coulomb potential, and it contains a small number of Fourier coefficients. The mixture of pseudopotential concept and the plane wave mechanism helps explain atoms' chemical bonding [4]. The general form of pseudopotential expressed by,

$$NL = \sum |lm\rangle\, V_l \langle lm| \qquad (2.1),$$

Where V_l is the pseudopotential and $|lm\rangle$'s are the spherical harmonics.

The commonly used pseudopotentials are Norm-conserving pseudopotentials (NCP) and Ultrasoft pseudopotentials (USP). Usually, the pseudopotentials are differentiated as soft and hard based on the presence of no. of Fourier components (i.e., a small no. of Fourier components for soft, and several for hard) to get an accurate representation. Hamann, Schluter, and Chiang generated the NCP in 1979 [5], and it's a nonlocal pseudopotential. In contrast, local pseudopotential means using the same potential in each particle wave function in the same way, and it is more efficient than the other one. The convergence properties are significantly low in NCP (i.e., hard) [6], [7], and several schemes have been tried to enhance the convergence properties of NCP [8], [9]. NCP's are mainly designed to carry out two conditions to reproduce correctly; the first one is, all electron and pseudo wave functions to be equal outside the core radius (r_c), and the second one is, inside the core radius, each pseudo wave function to be identical to its corresponding all-electron wave function [6]. It is necessary to generate the softer pseudopotential to relax the NCP's, in 1990, Vanderbilt proposed the USP method to reduce the basis set size with the lowest possible cutoff energy by introducing generalized eigenvalue formalism [10]. The USP's scheme is much softer than the NCP's, and it provides highly accurate results.

2.2.2. Geometry optimization

In MS, the CASTEP program adopts two geometry optimization methods, such as the Broyden-Fletcher-Goldfarb-Shanno method (BFGS) [11] and the damped molecular dynamics (DMD) [12] method. The BFGS method is capable of performing cell optimization, even at fixed external stress, and it mainly optimizes the lattice parameters and atomic coordinates of the system. For an extensive system, the LBFGS (low memory BFGS) algorithm is used for geometry optimization [13], [14], and a finite basis set correction term is suggested to run the cell optimization. CASTEP allows us to perform the constrained geometry optimization to fix the atom positions (i.e., fixing the atoms' fractional position) and lattice parameters. Especially, fixing the lattice parameters is helpful in phase stability studies [15]. In 1988, Barzilai – Borwein discovered the Two-Point Steepest Descent (TPSD) algorithm [16], and it effectively permits solving the larger range problem with constraints. Another available geometry optimization method in CASTEP is DMD (solves the first-order equations) that involves only internal coordinates by means the cell parameters are fixed, and it is less efficient. Two different kinds of modes are considered in the DMD, such as coupled modes and independent modes; both modes take more time steps than undamped molecular dynamics simulations.

2.2.3. Dialogs in MS-CASTEP

The MS-CASTEP permits first-principles quantum mechanical calculations to study crystals and surfaces' desired properties in solid-state. In MS-CASTEP, there are two different types of dialog options available. The first one is the calculation dialog option (to set up and run a CASTEP calculation). This option contains four following categorized taps to set up the CASTEP calculation: the setup tab, electronic tab, properties tab, and the job control tab. Each tab contains several parameters to define the type of calculation we want. The second one is the analysis dialog option (to analyze the results of a CASTEP calculation). This option permits an analysis of the results of a CASTEP calculation. The following properties are available to analyze in MS-CASTEP. Such as Band structure selection, Core level spectroscopy selection, the density of states selection (DOS), Elastic constants selection, Electron density selection, and Electron density difference (EDD) selection, Electron localization function (ELF) selection, Energy evolution selection, and Fermi surface selection, IR spectrum selection and NMR selection, Optical properties selection and Orbitals selection, Phonon dispersion selection and Phonon density of states selection, Population analysis selection, Potentials selection and Reaction kinetics selection, Raman spectrum selection, STM profile selection, and Structure selection, Thermodynamic properties selection. Therefore, MS-CASTEP allows you to perform different types of calculations based on the user requirement. The following section will provide detailed information regarding the formamidinium lead iodide ($FAPbI_3$) perovskite unit cell construction and optimization methods.

2.3. Construction of formamidinium (FA) lead iodide ($FAPbI_3$) perovskite unit cell

Generally, MS needs a specific atomic position to construct any structure. In the case of $FAPbI_3$ perovskites (i.e., chemical formula - $CH_5I_3N_2Pb$) structure contains one carbon, five hydrogens, three iodides, two nitrogens, and one lead atom. Therefore, at first, to build the $FAPbI_3$ unit cell, the initial lattice parameter (a = 6.36 Å), and the reduced coordinates for every atom, as well as the space group (Pm3m), were taken from a previously published result [17], shown in **Table 2.1**. The cubic $FAPbI_3$ with lead iodide framework, organic FA cation placed inside the inorganic cage, demonstrated in **Fig. 2.1**.

***Table 2.1**. Atomic positions of all atoms.*

Atom	x	y	z
C	0.5	0.5726	0.5
H_1	0.5	0.7447	0.5
H_2	0.8142	0.568	0.5
H_3	0.1858	0.568	0.5
H_4	0.7025	0.318	0.5
H_5	0.2975	0.318	0.5
I_1	0	0.5	0
I_2	0	0	0.5
I_3	0.5	0	0
N_1	0.682	0.4781	0.5
N_2	0.318	0.4781	0.5
Pb	0	0	0

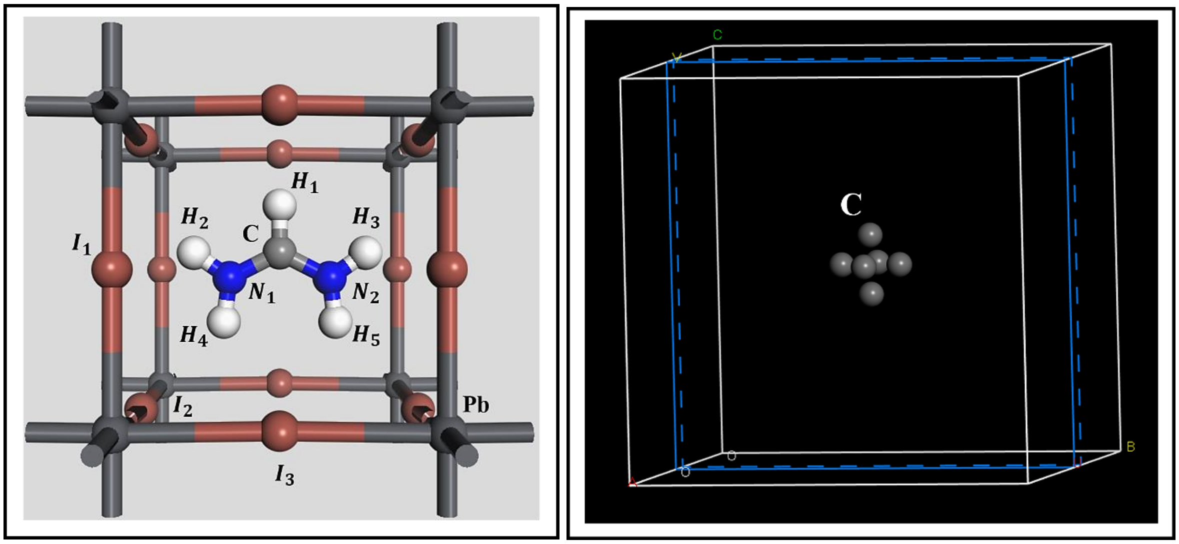

Fig. 2.1. *Representation of conventional $FAPbI_3$ Perovskite unit cell, and each carbon atom positions.*

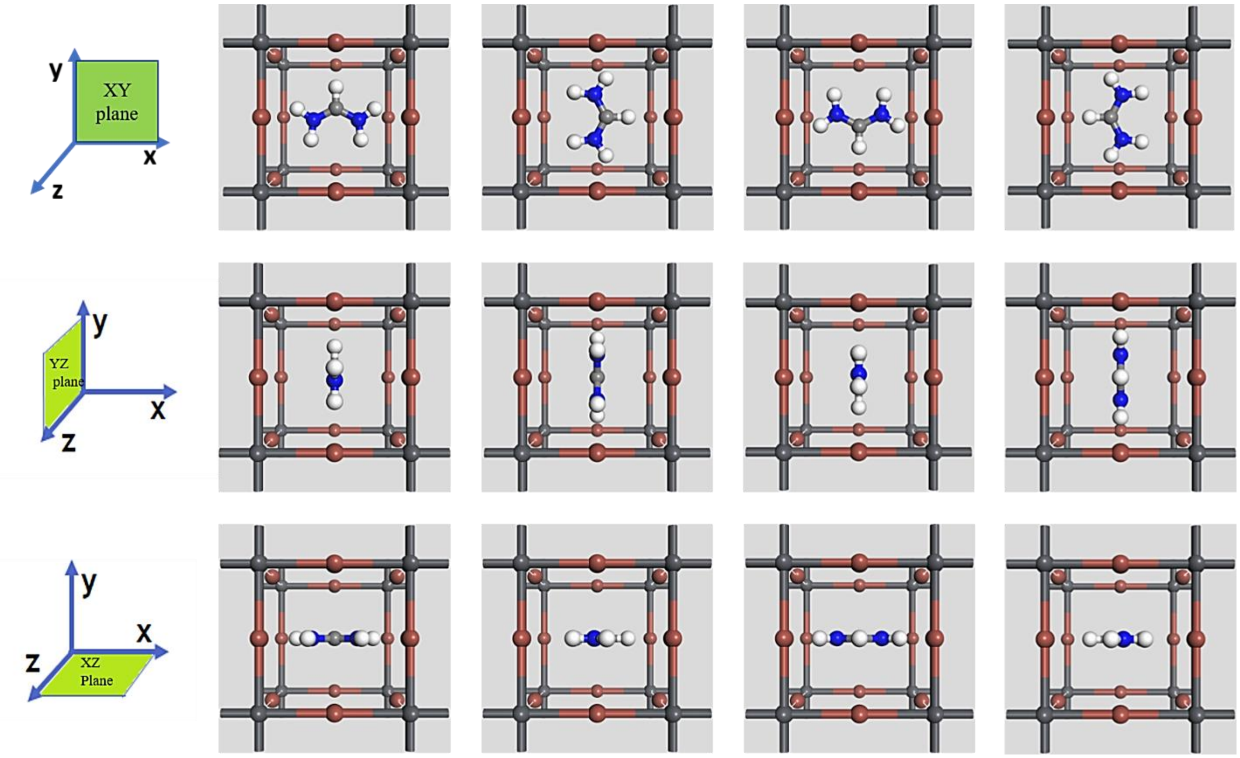

Fig. 2.2*. Representation of the twelve different orientations of the FA cation in XY, YZ, and XZ planes (top left to right 12'o clock, 3'o clock, 6'o clock, and 9'o clock).*

The twelve possible orientations of FA cation were generated for each main plane of the cube, locating the carbon atom is in the following positions generated from the space group: (u, ½, ½), (½, u, ½), (½, ½, u), (-u, ½, ½), (½, -u, ½), (½, ½, -u), where u=0.5726, demonstrated in **Fig. 2.1**. Each carbon position defines two FA molecules parallel to the remaining reference planes, which are perpendicular to the normal plane vector of the carbon atom, inside the cubic cage. Therefore, the twelve structures were generated by the rotation of the organic FA cation inside the inorganic cage, orienting the FA molecule in a clockwise direction using the $C - H_1$ bond as the hour hand of a clock, namely 12:00, 03:00, 06:00, and 09:00 hrs. Positions, with the carbon atom pointing outwards at each angular position. The twelve possibilities are generated for the three crystalline planes [(100) 12:00 to 09:00, (010) 12:00 to 09:00, and (001) 12:00 to 09:00], as it is represented by the space group Pm-3m, shown in **Fig. 2.2.**

2.3.1. Construction of $FAPbI_3$ perovskite Supercells

Fundamentally, a crystal structure is described by a unit cell. It is also possible to describe the same crystal with a large number of unit cells with different shapes and sizes; it's called supercells. Supercells allow determining some properties which cannot be determined by the unit cell. Therefore, in this thesis, we modeled different types of supercells such as 211, 311, and 411 in a particular direction (i.e., x). In general, the supercells contained different atoms than unit cells; for example, 24 atoms for the 211-supercell model, 36 atoms for the 311-supercell model, and 48 atoms for the 411-supercell model demonstrated in **Fig. 2.3**.

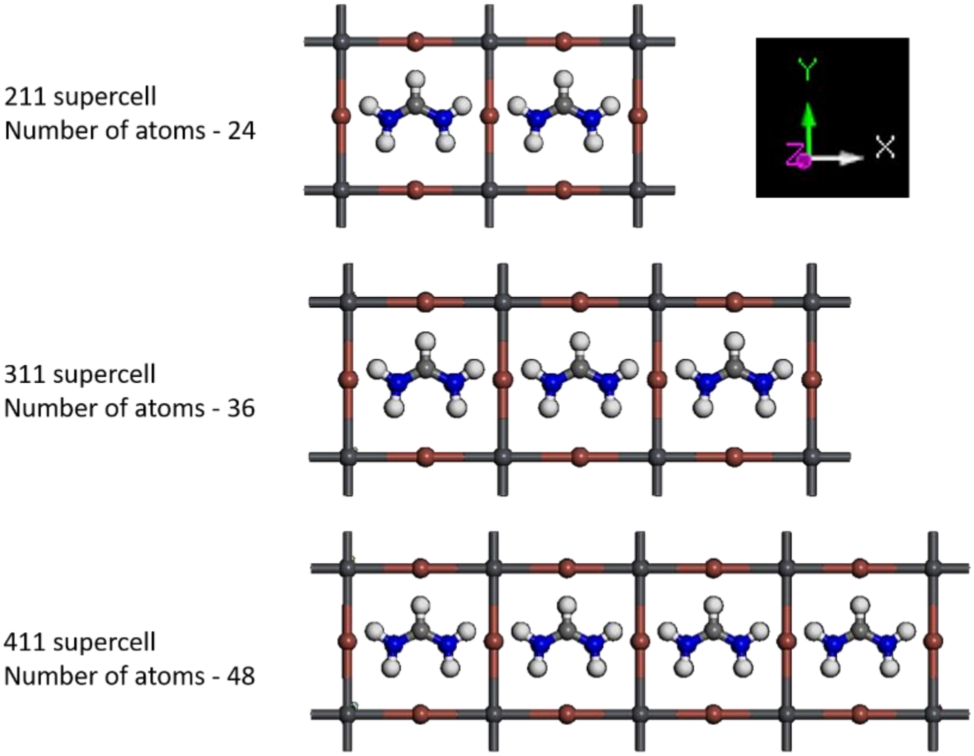

Fig. 2.3. *Representation of 211, 311, and 411 supercell models of* $FAPbI_3$ *Perovskite structure.*

2.3.2. Computational details of $FAPbI_3$ perovskite Structure

All the calculations were performed using the DFT - vdW scheme (i.e., vdW interactions), by the Tkatchenko-Scheffler dispersion model [18], through the CASTEP [19] module available in the MS software [1]. For all calculations, the $GGA - PBE$ exchange-correlation function [20] was considered, with ultrasoft pseudopotentials [10]. In the initial stage, several calculations were performed to find the ground state energy, such as in the plane wave cut off energy range (300 eV, 350 eV, 380 eV, 400 eV, 450 eV, and 500 eV), k-point mesh (3 ×3 ×3, 4 × 4 × 4, 5 × 5 × 5, 6 × 6 × 6, 7 × 7 × 7, and 8 × 8 × 8), etc. Based on calculations as mentioned above, a k-point mesh of 4 × 4 × 4 for all the conventional unit cell models (32 points and a 0.035 grid separation) along with a plane wave cutoff energy of 400 eV were chosen by carefully testing the convergence on the unit cell volume, lattice parameters, b/a and c/a ratio’s, displacement of the iodide atoms and the ground state energy of the fully optimized unit cell under the BFGS algorithm [11]. After the unit cell optimization, the MS provides the output file at the end of the calculation, containing several details such as the ground state energy, lattice parameters, the cell volume, etc. It will allow us to explore and investigate the structural behavior of $FAPbI_3$ Perovskite structure. The same computational parameters were used for other eleven FA cation orientations-based structures to study and compare their structural properties.

2.3.3. Elastic constant calculations

The elastic constants of a material describe its response to applied stress or, equally, the stress required to maintain a given deformation. According to Hooke’s law, especially in the elastic region, the relation between the stress (σ_{ij}) and strain (ε_{kl}) can be expressed by,

$$\sigma_{ij} = -\sum_{k=1}^{3}\sum_{l=1}^{3} c_{ijkl}\varepsilon_{kl} \qquad (2.2)$$

Where c_{ijkl} are elastic constants, and i, j = 1, 2, 3.

3 × 3 matrices generally represent the stress and strain tensors for a cartesian coordinate system, therefore six components in total, and it is expressed by,

$$\sigma = \begin{bmatrix} \sigma_{11} & \sigma_{12} & \sigma_{13} \\ \sigma_{21} & \sigma_{22} & \sigma_{23} \\ \sigma_{31} & \sigma_{32} & \sigma_{33} \end{bmatrix} \text{ and } \varepsilon = \begin{bmatrix} \varepsilon_{11} & \varepsilon_{12} & \varepsilon_{13} \\ \varepsilon_{21} & \varepsilon_{22} & \varepsilon_{23} \\ \varepsilon_{31} & \varepsilon_{32} & \varepsilon_{33} \end{bmatrix} \qquad (2.3)$$

Nye and Lindsay discussed the complete details of the symmetry of stress, strain, and elastic constants [21]. Due to different symmetries, the independent elastic constants are reduced to 21

[22], [23], and it is further reduced like 3 for cubic symmetry, 9 for an orthorhombic crystal, and 5 for the hexagonal structure [24]. Elastic constant values (c_{ij}) are helping to get the properties like bulk modulus, shear modulus, Poisson coefficient, Lame constant, elastic Debye temperature, etc. In MS, determining the elastic constants from first principles usually involves setting either the stress or the strain to a finite value, re-optimizing any free parameters. The important parameter is applied deformation, which decides the elastic constant calculation. The finite strain technique has been effectively used to study the elastic properties of a range of materials, including metallic systems: Al [25], TiN [26], TiB_2, and MgB_2 [27], for minerals: $MgSiO_3$ [28], Li_2O [29], MgO [30], silica polymorphs [31], aluminum hydroxide polymorphs [32], and compound semiconductors: $AgGaSe_2$ [33]. Based on previous reports, the accuracy of DFT-based elastic constant calculated values is equivalent to experimental results (within 10% or even less). These observations permit to do the calculation of the elastic constants for new materials [27], and for the materials that do not have the available experimental data [34], also to calculate elastic properties under pressure [31], and to resolve discrepancies between contradictory experimental results [35].

In MS, CASTEP elastic constant task contains two tabs, such as the elastic constants tab and options tab. The elastic constants tab permits to define the parameters to calculate the elastic constants, for example, the number of steps for each strain, maximum strain amplitude range, strain pattern, etc. The options tab allows us to specify the convergence level of the elastic constant calculation. It is possible to set the convergence thresholds for energy change, maximum force, and maximum displacement between each cycle to define the calculation quality. It will help perform geometry optimization, which is necessary for the calculation of the elastic constants. Once the above-mentioned criteria are satisfied, the calculation will be stoped automatically. There are four sets of convergence thresholds available; Coarse, Medium, Fine, and Ultra-fine, and it is shown in the following table. Also, the maximum iterations option, which is useful to specify the maximum number of elastic constants cycles. If this number of cycles is reached, the calculation will stop even if the convergence criteria are not satisfied.

Table 2.2. The values of each convergence threshold.

Quality	Energy ($^{eV}/_{atom}$)	Force ($^{eV}/_{Å}$)	Displacement (Å)
Coarse	1×10^{-5}	0.02	0.001

Medium	4×10^{-6}	0.01	4×10^{-4}
Fine	2×10^{-6}	0.006	2×10^{-4}
Ultrafine	1×10^{-6}	0.002	1×10^{-4}

2.3.3.1. c_{ij} Calculation method

In this work, the finite deformation method is defined by two strain amplitudes ($\delta_{max} = 0.02\ and\ \delta_{max} = 0.04$) that establish different deformation boundaries within six strain steps $\{\delta_i = \pm 0.004, \pm 0.012\ and\ \pm 0.020\}\ and\ \{\delta_i = \pm 0.008, \pm 0.024\ and\ \pm 0.040\}$, for each deformation boundaries respectively, in agreement with recommended deformation boundaries [36], with both parameters carefully tested against the point dispersion of the strain energy difference ($\Delta \boldsymbol{E_i}$).

The strained structures are generated by means of a transformation of the optimized set of lattice parameters [36] given as:

$$\left\{\begin{matrix} x' \\ y' \\ z' \end{matrix}\right\} = (D(e) + I) \left\{\begin{matrix} x \\ y \\ z \end{matrix}\right\} \qquad (2.4)$$

Where, $\left\{\begin{matrix} x' \\ y' \\ z' \end{matrix}\right\}$ is the new set of strained vectors and $\left\{\begin{matrix} x \\ y \\ z \end{matrix}\right\}$ corresponds to any ground state lattice vector to be modified by the strained tensor $(D(e) + I)$. For an orthorhombic structure, nine independent strain patterns are needed to determine the adiabatic EC values. The first three of them act along a single direction ($D_1,\ D_2,\ D_3$), meanwhile, the remaining six modify an entire crystalline plane, i.e., the deformation acts along with two directions ($D_4,\ D_5,\ D_6, D_7,\ D_8, D_9$), both sets of strain patterns are written as [37], [38]:

$$D_1 = \left\{\begin{matrix} (1+\delta) & 0 & 0 \\ 0 & 1 & 0 \\ 0 & 0 & 1 \end{matrix}\right\}, \qquad (2.5)$$

$$D_2 = \left\{\begin{matrix} 1 & 0 & 0 \\ 0 & (1+\delta) & 0 \\ 0 & 0 & 1 \end{matrix}\right\}, \qquad (2.6)$$

$$D_3 = \begin{Bmatrix} 1 & 0 & 0 \\ 0 & 1 & 0 \\ 0 & 0 & (1+\delta) \end{Bmatrix}, \qquad (2.7)$$

$$D_4 = \begin{Bmatrix} u & 0 & 0 \\ 0 & u & \delta u \\ 0 & \delta u & u \end{Bmatrix}, \qquad (2.8)$$

$$D_5 = \begin{Bmatrix} u & 0 & \delta u \\ 0 & u & 0 \\ \delta u & 0 & u \end{Bmatrix}, \qquad (2.9)$$

$$D_6 = \begin{Bmatrix} u & \delta u & 0 \\ \delta u & u & 0 \\ 0 & 0 & u \end{Bmatrix}, \qquad (2.10)$$

$$D_7 = \begin{Bmatrix} (1+\delta)u & 0 & 0 \\ 0 & (1-\delta)u & 0 \\ 0 & 0 & u \end{Bmatrix}, \qquad (2.11)$$

$$D_8 = \begin{Bmatrix} (1+\delta)u & 0 & 0 \\ 0 & u & 0 \\ 0 & 0 & (1-\delta)u \end{Bmatrix}, \qquad (2.12)$$

$$D_9 = \begin{Bmatrix} u & 0 & 0 \\ 0 & (1+\delta)u & 0 \\ 0 & 0 & (1-\delta)u \end{Bmatrix}, \qquad (2.13)$$

Where the $\boldsymbol{u}$ is a parameter defined as:

$$\boldsymbol{u} = \frac{\mathbf{1}}{(\mathbf{1}-\boldsymbol{\delta}^{\mathbf{2}})^{\frac{\mathbf{1}}{\mathbf{2}}}} \qquad (2.14)$$

The strained structures were generated by either just the positive δ_i steps for the symmetric deformations (D_4, D_5, D_6) or both positive and negative for asymmetric ones (D_1, D_2, D_3, D_7, D_8, D_9) within the strain amplitudes. Each of the energy difference values represents the total energy subtraction of one strained state, defined by δ_i, from the optimized ground state at $\delta_i = 0(\Delta E_i = E_i(V,\delta) - E(V_0, 0))$. The calculations of such strained states were performed initially from the converged ground state, modifying the real lattice matrix to the nearest strain step, following the latter procedure to the immediate subsequent deformation, until the strain amplitude is reached (δ_{max}). With each δ_i step representing a geometrical relaxation, in which the base vectors are optimized under the BFGS algorithm; meanwhile, the strained lattice parameters are kept fixed.

The total energy difference of the nine strain paths ($E_1, E_2, E_3, E_4, E_5, E_6, E_7, E_8, E_9$), are written in terms of a Taylor expansion [37], [38] as:

$$\Delta E_1 = \upsilon_0 \left(\tau_1 \delta + \frac{C_{11}}{2} \delta^2 \right), \tag{2.15}$$

$$\Delta E_2 = \upsilon_0 \left(\tau_2 \delta + \frac{C_{22}}{2} \delta^2 \right), \tag{2.16}$$

$$\Delta E_3 = \upsilon_0 \left(\tau_3 \delta + \frac{C_{33}}{2} \delta^2 \right), \tag{2.17}$$

$$\Delta E_4 = \upsilon_0 (2\tau_4 \delta + 2C_{44} \delta^2), \tag{2.18}$$

$$\Delta E_5 = \upsilon_0 (2\tau_5 \delta + 2C_{55} \delta^2), \tag{2.19}$$

$$\Delta E_6 = \upsilon_0 (2\tau_6 \delta + 2C_{66} \delta^2), \tag{2.20}$$

$$\Delta E_7 = \upsilon_0 \left((\tau_1 - \tau_2) \delta + \frac{C_{11} + C_{22} - 2C_{12}}{2} \delta^2 \right), \tag{2.21}$$

$$\Delta E_8 = \upsilon_0 \left((\tau_1 - \tau_3) \delta + \frac{C_{11} + C_{33} - 2C_{13}}{2} \delta^2 \right), \tag{2.22}$$

$$\Delta E_9 = \upsilon_0 \left((\tau_2 - \tau_3) \delta + \frac{C_{22} + C_{33} - 2C_{23}}{2} \delta^2 \right). \tag{2.23}$$

Where the second-order coefficient represents the EC values for each strain tensor. The dispersed points from $\boldsymbol{\Delta E_i}$ were fitted by a third-order polynomial to finally obtain such elastic moduli.

The structural stability from all twelve models is determined by the set of the adiabatic EC values as [24]:

$$\begin{gathered} C_{11} > 0, \\ C_{11} C_{22} > {C_{12}}^2, \\ C_{44} > 0, \\ C_{55} > 0, \\ C_{66} > 0, \\ C_{11} C_{22} C_{33} + 2C_{12} C_{13} C_{23} - C_{11} {C_{23}}^2 - C_{22} {C_{13}}^2 - C_{33} {C_{12}}^2 > 0. \end{gathered} \tag{2.24}$$

At last, the standard error (SE) was determined by the calculation of the statistical deviation from the number of considered deformation steps as:

$$\sigma_x = \frac{\sigma}{\sqrt{n}}. \qquad (2.25)$$

where $\boldsymbol{\sigma_x}$ is the standard error, $\boldsymbol{\sigma}$ is the standard population deviation and $\sqrt{\boldsymbol{n}}$ is the square root from the number of deformation steps. Here, the standard deviation is equivalent to the square root of the variance.

2.3.4. Electron density difference (EDD) analysis

In general, EDD maps are used to investigates the changes that occur when an atom or a molecule changes its state or their relative positions are generally helpful and depend on one molecular density distribution subtracted from the other [39], [40].

CASTEP – MS offers to generate the EDD in two possible ways,

- EDD with respect to a linear combination of the atomic densities indicates the changes in the electron distribution due to the formation of all the bonds in the system.
- EDD with respect to a linear combination of the densities of sets of atoms in the model helps show the formation of bonds between atoms in different sets and charge redistribution within the sets.

In MS, the EDD is generated based on the second option and is calculated with the following equation,

$$\Delta\rho_{(EDD)} = \rho_{(FAPbI_3)} - \left(\rho_{(FA)} + \rho_{(Inorg)}\right) \qquad (2.26)$$

Where $\rho_{(FAPbI_3)}$ is the electron density of the total system ($FAPbI_3$), and both $\rho_{(FA)}$ and $\rho_{(Inorg)}$ represent the separated electron densities of the organic cation and the inorganic cage, respectively.

Before running the EDD calculation, it is necessary to define the fragments, and also, it must contain the desired name with Density Difference in order for CASTEP-MS to recognize the set as a fragment. The single-point energy calculation is sufficient to get the EDD results for an already optimized system. The isosurface tab provides the option to define the values in order to differentiate the electron enrichment (color in red) and the electron diminishment (color in blue) with respect to the fragments. The create slices tool is efficiently useful to create a 2D slice from the data, and it offers the axis view such as A & B, B & C, and C & A. Then, the color maps option permits to change the color of electron enrichment and diminishment based on the Blue-White-Red spectrum value. The final image should resemble the one shown in **Fig. 2.4**.

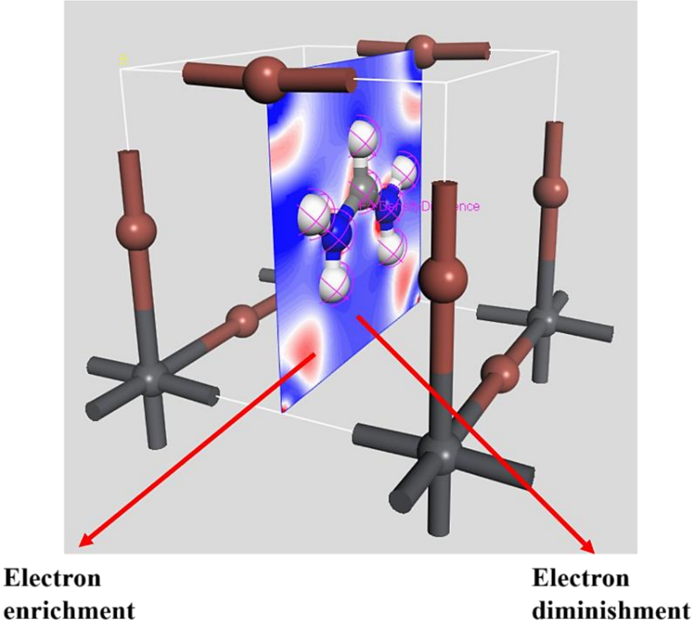

Fig. 2.4. *EDD graph of* $FAPbI_3$ *Perovskite structure.*

2.3.5. Mulliken charge (MC) population analysis

The basis states' delocalized nature using a plane-wave basis set does not provide any details about the localization of the electron in the considered system. Using the Linear combination of atomic orbitals (LCAO) basis set offers to study the bond population, charge transfer, an atomic charge, etc. Sanchez-Portal et al. suggested the technique to perform the population analysis in CASTEP using a projection of plane-wave states onto a localized basis [41]. Mulliken's formalism was proposed Mulliken in 1955 to investigate population analysis, which is a commonly used technique for electronic structure calculations with LCAO basis sets [42]. The spin density matrix and atomic overlap matrix are used to partition charges among the atoms, and it is called Mulliken charge analysis, which is one of the familiar methods to investigate charge analysis. In Mulliken analysis, the charge associated with a given atom A is expressed by,

$$Q\ (A) = \sum_k \omega_k \sum_{\mu}^{on\ A} \sum_{v} P_{\mu v}(k)\, S_{v\mu}(k) \qquad (2.27)$$

Where, $S_{v\mu}(k)$ is the overlap matrix, $P_{\mu v}(k)$ is the density matrix with wave vector k, and ω_k are the weights associated with the calculated k-points in the Brillouin-zone. The overlap population between two atoms (A & B) is described as,

$$n\,(AB) = \sum_k \omega_k \sum_{\mu}^{on\ A} \sum_{v}^{on\ B} 2.P_{\mu v}(k) S_{v\mu}(k) \qquad (2.28)$$

In CASTEP-MS, Segall et al. formalism is used to calculate the Mulliken charges and bond populations [43], [44]. After completing the calculation, the system provides the Mulliken and Hirshfeld charge population analysis information to study their population properties. The difference between the molecular and unrelaxed atomic charge densities are defined as Hirshfeld charge deformation density [45].

References

[1] “BIOVIA Materials Studio, Discovery Studio Modeling Environment.” San Diego: Dassault systems, r2 (17.2.0.1626) ed. (2017), Accelrys Software Inc., 2017.

[2] “TCM’s web site, history section.” http://www.tcm.phy.cam.ac.uk/about/history/.

[3] “Getting CASTEP.” http://www.castep.org/CASTEP/GettingCASTEP.

[4] G. P. Srivastava and D. Weaire, “The theory of the cohesive energies of solids,” *Adv. Phys.*, 1987, doi: 10.1080/00018738700101042.

[5] D. R. Hamann, M. Schlüter, and C. Chiang, “Norm-Conserving Pseudopotentials,” *Phys. Rev. Lett.*, 1979, doi: 10.1103/PhysRevLett.43.1494.

[6] G. B. Bachelet, D. R. Hamann, and M. SchÏter, “Pseudopotentials that work: From H to Pu,” *Phys. Rev. B*, 1982, doi: 10.1103/PhysRevB.26.4199.

[7] G. P. Kerker, “Non-singular atomic pseudopotentials for solid state applications,” *J. Phys. C Solid State Phys.*, 1980, doi: 10.1088/0022-3719/13/9/004.

[8] N. Troullier and J. L. Martins, “Efficient pseudopotentials for plane-wave calculations,” *Phys. Rev. B*, 1991, doi: 10.1103/PhysRevB.43.1993.

[9] J. S. Lin, A. Qteish, M. C. Payne, and V. Heine, “Optimized and transferable nonlocal separable ab initio pseudopotentials,” *Phys. Rev. B*, 1993, doi: 10.1103/PhysRevB.47.4174.

[10] D. Vanderbilt, “Soft self-consistent pseudopotentials in a generalized eigenvalue formalism,” *Phys. Rev. B*, 1990, doi: 10.1103/PhysRevB.41.7892.

[11] B. G. Pfrommer, M. Côté, S. G. Louie, and M. L. Cohen, “Relaxation of Crystals with the Quasi-Newton Method,” *J. Comput. Phys.*, 1997, doi: 10.1006/jcph.1996.5612.

[12] M. I. J. Probert, “Improved algorithm for geometry optimisation using damped molecular dynamics,” *J. Comput. Phys.*, 2003, doi: 10.1016/S0021-9991(03)00308-5.

[13] J. Aarons, “A New CASTEP and ONETEP Geometry Optimiser.” A New CASTEP and ONETEP Geometry Optimiser.

[14] D. Packwood *et al.*, “A universal preconditioner for simulating condensed phase materials,” *J. Chem. Phys.*, 2016, doi: 10.1063/1.4947024.

[15] B. Winkler and V. Milman, “Polymorphism of CsI,” *J. Phys. Condens. Matter*, 1997.

[16] J. Barzilai and J. M. Borwein, “Two-point step size gradient methods,” *IMA J. Numer. Anal.*, 1988, doi: 10.1093/imanum/8.1.141.

[17] M. T. Weller, O. J. Weber, J. M. Frost, and A. Walsh, “Cubic Perovskite Structure of Black Formamidinium

Lead Iodide, α-[HC(NH2)2]PbI3, at 298 K," *J. Phys. Chem. Lett.*, 2015, doi: 10.1021/acs.jpclett.5b01432.

[18] A. Tkatchenko and M. Scheffler, "Accurate molecular van der Waals interactions from ground-state electron density and free-atom reference data," *Phys. Rev. Lett.*, 2009, doi: 10.1103/PhysRevLett.102.073005.

[19] M. D. Segall *et al.*, "First-principles simulation: Ideas, illustrations and the CASTEP code," *J. Phys. Condens. Matter*, 2002, doi: 10.1088/0953-8984/14/11/301.

[20] J. P. Perdew, K. Burke, and M. Ernzerhof, "Generalized gradient approximation made simple," *Phys. Rev. Lett.*, 1996, doi: 10.1103/PhysRevLett.77.3865.

[21] J. F. Nye and R. B. Lindsay, " Physical Properties of Crystals: Their Representation by Tensors and Matrices ," *Phys. Today*, 1957, doi: 10.1063/1.3060200.

[22] G. L. Belen'kí, Y. Salaev, and R. A. Suïeimanov, "Deformation effects in layer crystals," *Sov. Phys. - Uspekhi*, 1988, doi: 10.1070/PU1988v031n05ABEH003546.

[23] Von N. W. Ashcroft; N. D. Mermin, *Solid State Physics. , New York 1976, XXII, 826 Seiten*. 1976.

[24] F. Mouhat and F. X. Coudert, "Necessary and sufficient elastic stability conditions in various crystal systems," *Phys. Rev. B - Condens. Matter Mater. Phys.*, 2014, doi: 10.1103/PhysRevB.90.224104.

[25] V. B. Deyirmenjian, V. Heine, M. C. Payne, V. Milman, R. M. Lynden-Bell, and M. W. Finnis, "Ab initio atomistic simulation of the strength of defective aluminum and tests of empirical force models," *Phys. Rev. B*, 1995, doi: 10.1103/PhysRevB.52.15191.

[26] M. Marlo and V. Milman, "Density-functional study of bulk and surface properties of titanium nitride using different exchange-correlation functionals," *Phys. Rev. B - Condens. Matter Mater. Phys.*, 2000, doi: 10.1103/PhysRevB.62.2899.

[27] V. Milman and M. C. Warren, "Elastic properties of TiB2 and MgB2," *J. Phys. Condens. Matter*, 2001, doi: 10.1088/0953-8984/13/24/304.

[28] B. B. Karki, L. Stixrude, S. J. Clark, M. C. Warren, G. J. Ackland, and J. Crain, "Elastic properties of orthorhombic MgSiO3 perovskite at lower mantle pressures," *Am. Mineral.*, 1997, doi: 10.2138/am-1997-5-623.

[29] A. De Vita, M. J. Gillan, J. S. Lin, M. C. Payne, I. St, and L. J. Clarke, "Defect energetics in oxide materials from first principles," *Phys. Rev. Lett.*, 1992, doi: 10.1103/PhysRevLett.68.3319.

[30] B. B. Karki, L. Stixrude, S. J. Clark, M. C. Warren, G. J. Ackland, and J. Crain, "Structure and elasticity of MgO at high pressure," *Am. Mineral.*, 1997, doi: 10.2138/am-1997-1-207.

[31] B. B. Karki, L. Stixrude, and J. Crain, "Ab initio elasticity of three high-pressure polymorphs of silica," *Geophys. Res. Lett.*, 1997, doi: 10.1029/97GL53196.

[32] J. D. Gale, A. L. Rohl, V. Milman, and M. C. Warren, "An ab initio study of the structure and properties of aluminum hydroxide: Gibbsite and bayerite," *J. Phys. Chem. B*, 2001, doi: 10.1021/jp011795e.

[33] B. B. Karki, S. J. Clark, M. C. Warren, H. C. Hsueh, G. J. Ackland, and J. Crain, "Ab initio elasticity and lattice dynamics of AgGaSe2," *J. Phys. Condens. Matter*, 1997, doi: 10.1088/0953-8984/9/2/005.

[34] B. Winkler, M. Hytha, M. C. Warren, V. Milman, J. D. Gale, and J. Schreuer, "Calculation of the elastic constants of the Al2SiO5 polymorphs andalusite, sillimanite and kyanite," *Zeitschrift fur Krist.*, 2001, doi: 10.1524/zkri.216.2.67.20336.

[35] B. Winkler, C. J. Pickard, M. D. Segall, and V. Milman, "Density-functional study of charge disordering in Cs2Au(I)Au(III)Cl6 under pressure," *Phys. Rev. B - Condens. Matter Mater. Phys.*, 2001, doi: 10.1103/PhysRevB.63.214103.

[36] L. Vitos, *Computational Quantum Mechanics for Materials Engineers: The EMTO Method and Applications*. 2007.

[37] A. H. Reshak and M. Jamal, “DFT calculation for elastic constants of orthorhombic structure within WIEN2K code: A new package (ortho-elastic),” *J. Alloys Compd.*, 2012, doi: 10.1016/j.jallcom.2012.07.107.

[38] P. Ravindran, L. Fast, P. A. Korzhavyi, B. Johansson, J. Wills, and O. Eriksson, “Density functional theory for calculation of elastic properties of orthorhombic crystals: Application to TiSi2,” *J. Appl. Phys.*, 1998, doi: 10.1063/1.368733.

[39] E. Steiner, “Density-difference maps in quantum chemistry,” *Theor. Chim. Acta*, 1982, doi: 10.1007/BF00549611.

[40] J. F. Harrison, “On the role of the electron density difference in the interpretation of molecular properties,” *Journal of Chemical Physics*. 2003, doi: 10.1063/1.1610432.

[41] D. Sanchez-Portal, E. Artacho, and J. M. Soler, “Projection of plane-wave calculations into atomic orbitals,” *Solid State Commun.*, 1995, doi: 10.1016/0038-1098(95)00341-X.

[42] R. S. Mulliken, “Electronic population analysis on LCAO-MO molecular wave functions. I,” *J. Chem. Phys.*, 1955, doi: 10.1063/1.1740588.

[43] M. D. Segall, C. J. Pickard, R. Shah, and M. C. Payne, “Population analysis in plane wave electronic structure calculations,” *Mol. Phys.*, 1996, doi: 10.1080/002689796173912.

[44] M. Segall, R. Shah, C. Pickard, and M. Payne, “Population analysis of plane-wave electronic structure calculations of bulk materials,” *Phys. Rev. B - Condens. Matter Mater. Phys.*, 1996, doi: 10.1103/PhysRevB.54.16317.

[45] F. L. Hirshfeld, “Bonded-atom fragments for describing molecular charge densities,” *Theor. Chim. Acta*, 1977, doi: 10.1007/BF00549096.

3. CHAPTER III. Experimental details

3.1. Materials

Formamidinium iodide (FAI) (≥ 90%, Great cell Solar (Dyesol)), Cesium iodide (CsI) (99.9%, trace metals basis, Sigma Aldrich), lead iodide (PbI_2) (99%, Sigma Aldrich), lead bromide ($PbBr_2$) (≥ 98%, Sigma Aldrich), Bismuth (III) iodide (BiI_3) (≥ 99.9%, trace metals basis, Sigma Aldrich), copper iodide (CuI) (99%, Sigma Aldrich), tin oxide nanoparticle colloidal solution (SnO_2) (15% in H_2O colloidal dispersion, Alfa Aesar), Spiro-OMeTAD (99% HPLC, Sigma Aldrich), 4-tert-butylpyridine (96%, Sigma Aldrich), Bis (trifluoromethane) sulfonimide lithium salt (99.95%, Li-TFSI, trace metals basis, Sigma Aldrich), chlorobenzene (CB, anhydrous, 99.8%, Sigma Aldrich), N-N dimethylformamide (DMF, anhydrous, 99.8%, Sigma Aldrich), dimethyl sulfoxide (DMSO, anhydrous, ≥ 99.9%, Sigma Aldrich), Acetonitrile (anhydrous, 99.8%, Sigma Aldrich) Zinc purum powder (Sigma Aldrich), diethyl ether (DE, ≥ 99.5%, GC, Sigma Aldrich), isopropanol (IPA, anhydrous, 99.5%, Sigma Aldrich), hydrochloric acid (HCl, ACS reagent, 37%, Sigma Aldrich), acetone and ethanol (99%, denature, Lamberty - sarp industries, France) were used as received without any further purification.

3.2. FTO Substrate etching and cleaning

The FTO substrate cleaning procedure presented in the following details:

- 2 mm thick 12 mm * 12 mm FTO substrates are used.
- Write the number or identity on the right corner of the glass side using a diamond tip to differentiate the substrate and glass sides (see **Fig. 3.1a**).
- Cover the desired area with two different scotch/adhesive tape types demonstrated in **Fig. 3.1 (b-d).**
- Place a little zinc powder on the selected area, dip a cotton swab in HCl solution, and then rub over that area (approximately 1 to 2 mins).
- Take the cotton cloth to clean/rub the reacted area first, then clean with distilled water to stop the chemical reaction.
- Remove the scotch tapes and check the cleaned area with the multimeter to confirm the etching, which means there is no FTO.

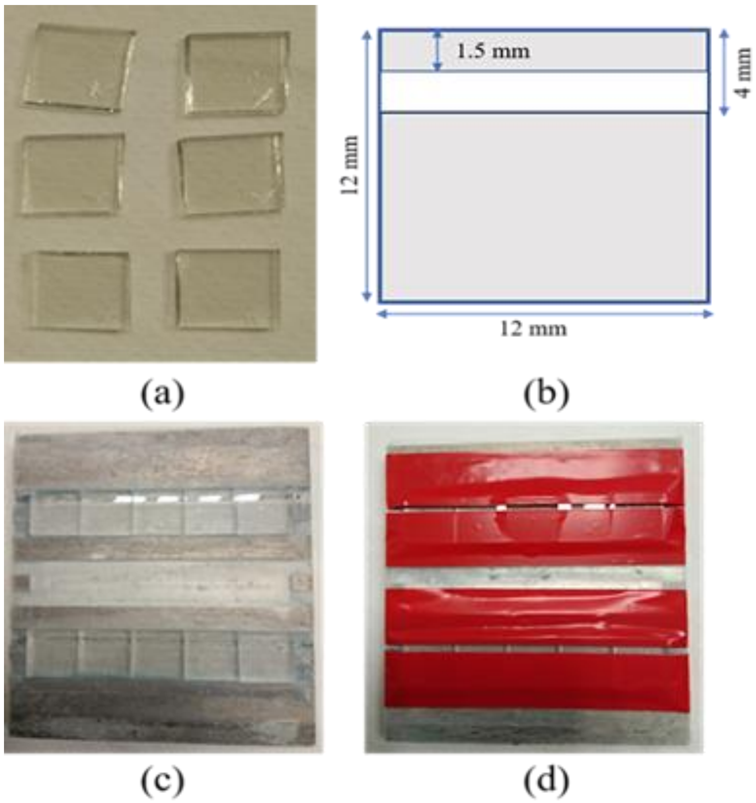

Fig. 3.1. *Represents the FTO substrate dimension and covering procedures.*

- Put the etched substrates in the beaker within deionized water, and acetone then placed in an ultrasonic bath (10 mins). Later, take the cotton cloth, and cotton swab sticks to rubbing over the FTO side.
- Then, ultrasonic bath for the following order:
    - 15 mins in acetone, 15 mins in isopropanol, and 15 mins in ethanol.
- Finally, use the Nitrogen gas flow to dry the cleaned FTO substrates.

3.3. Precursor's preparation - solution process method

3.3.1. Preparation of Tin oxide (SnO_2) solution

The tin oxide ETL solution is prepared from a mother colloidal solution (1 ml) containing 10 μl of isopropanol, which was stirred for more than one hour at room temperature in a closed vial (5 ml) using the stirring hotplate machine, shown in **Fig.3.2**. Before using, the prepared solution was filtered with a PTFE 0.45 µm filter.

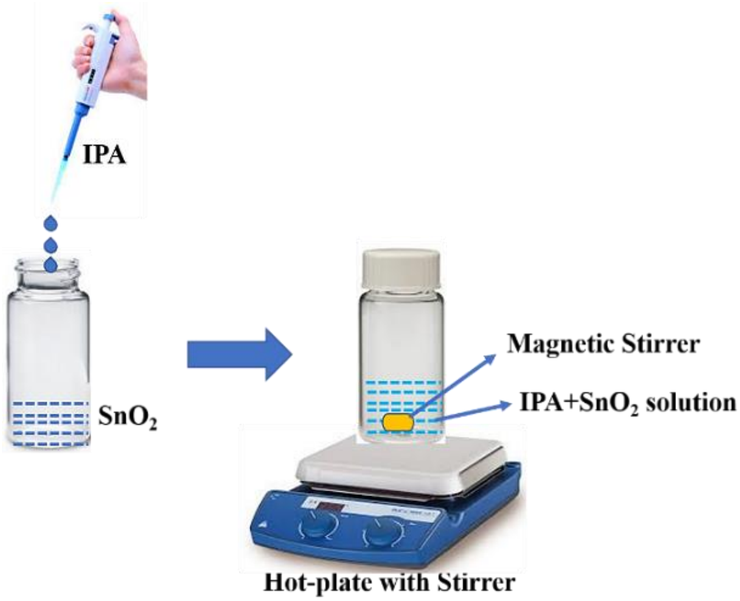

Fig. 3.2. *Schematic of ETL solution preparation procedures.*

3.3.2. Preparation of Formamidinium lead iodide ($FAPbI_3$) perovskite solution

The $FAPbI_3$ perovskite precursor solutions were initially prepared in the glovebox following the recipe described below. The suitable amounts of precursors were dissolved in a mixture of DMF (600 ml) and DMSO (78 μl): in the case of pure $FAPbI_3$ perovskite, the precursors correspond to 172 mg of FAI and 461 mg of PbI_2 taken, and the prepared precursor solutions (**see Fig. 3.3a**) were stirred at 65 °C for about three hours. Before using, the prepared solution was filtered with a PTFE 0.45 μm filter.

3.3.3. Preparation of Cesium and Bromide doped perovskite ($FACsPbI_3$ and ($FACsPb(IBr)_3$) solutions

As mentioned before, all the preparation processes carried out inside the glovebox. For $FA_{0.85}Cs_{0.15}PbI_3$, we used 146.3 mg of FAI, 39 mg of CsI, and 461 mg of PbI_2; and for $FA_{0.85}Cs_{0.15}Pb(I_{0.85}Br_{0.15})_3$, we used 146.3 mg of FAI, 39 mg of CsI, 392 mg of PbI_2, and 55.4 mg of $PbBr_2$. In both cases, the precursors were dissolved in a mixture of DMF (600 ml) and DMSO (78 μl) to get the desired perovskite solution. All precursor solutions were stirred at 65 °C for about three hours (**see Fig. 3.3b**). Before using, the prepared solution was filtered with a PTFE 0.45 μm filter.

3.3.4. Preparation of Copper iodide (CuI) and Bismuth iodide (BiI_3) incorporated perovskite ($FACsPb(IBr)_3)Mx$) (where M=CuI or BiI) solution

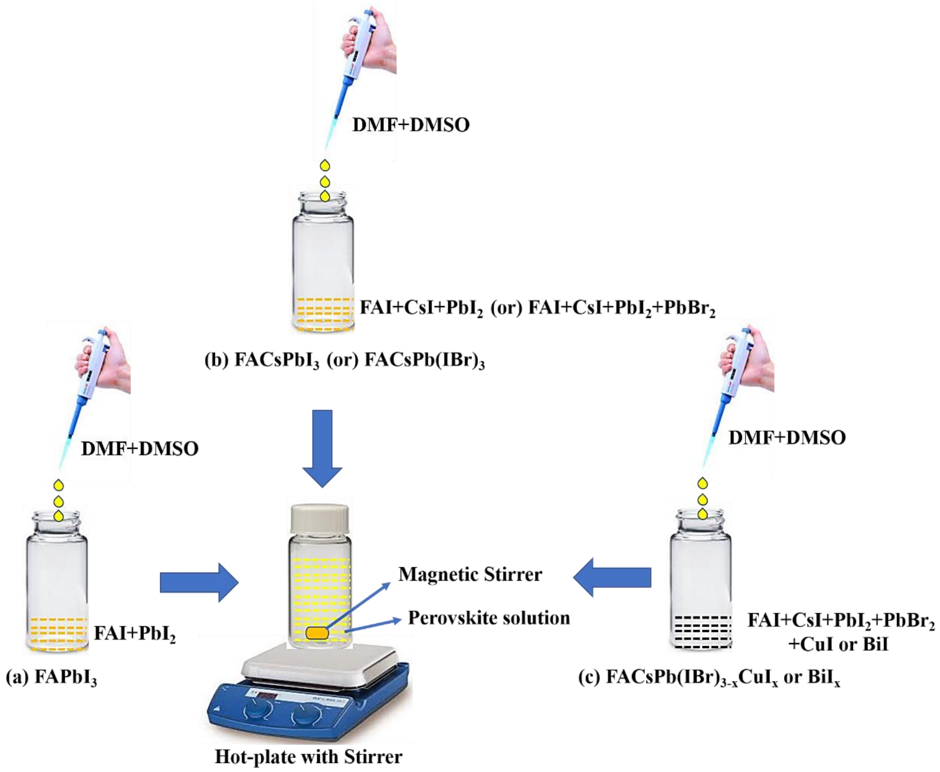

Fig. 3.3. *Schematic of absorber layer solution making procedures.*

The following amount of CuI_x and $BiI_x \ where, x = 0.01, 0.05, 0.10, 0.15$ doping concentrations were substitutes instead of PbI_2 content in the undoped solution (i.e., $FA_{0.85}Cs_{0.15}Pb(I_{1-x}Br_{0.15})_3CuI_x \ or \ FA_{0.85}Cs_{0.15}Pb(I_{1-x}Br_{0.15})_3BiI_x$). For CuI_x doping 2 mg, 9.53 mg, 19.2 mg, and 28.6 mg, respectively, and for BiI_x doping 5.9 mg, 29.5 mg, 59 mg, and 88.5 mg, respectively, incorporated into the perovskite solution. All the mentioned precursor solutions stirred at 65° C (3 hours) using a hotplate (**see Fig. 3.3c**). Before using, the prepared solution was filtered with a PTFE 0.45 µm filter.

3.3.5. Preparation of Spiro-OMeTAD solution

The following steps were carried out to prepare the Spiro-OMeTAD HTL solution (**see Fig. 3.4**).

Step-1: (Inside the Glovebox)

- 106 mg Li-TFSI -Salt dissolved in 200 µl of acetonitrile. (Solution A)

Step-2: (in ambient condition)

- 73.2 mg of Spiro-OMeTAD powder mixed with 1 ml of chlorobenzene, 17.5 µl of Solution A, and 28.8 µl of tBP (4-tert-Butylpyridine). Before using, the prepared solution was filtered with a PTFE 0.45 µm (PTFE) filter. This HTL solution was prepared almost 2 to 3 days before making the device.

Fig. 3.4. *Schematic of HTL solution preparation procedures.*

3.4. Thin-film Characterizations

All the following measurements were made in ambient conditions a few hours after thin film deposition. X-ray diffraction (XRD) is a widely used non-destructive technique to investigate the desired materials' structural properties, especially to identify the crystalline material phase. It also helps to extract the preferred crystal orientation, average crystallite size, strain, crystallinity, miller indices, and lattice mismatch. In this work, the XRD patterns were recorded using the D-8 Advance Bruker diffractometer (Karlsruhe, Germany) to investigate the structural quality of the layers. Ultraviolet spectroscopy is also known as absorbance or reflectance spectroscopy, is a technique commonly used in analytical chemistry, and it is carried out using an ultraviolet spectrophotometer (simply Uv-Vis) [1]–[4]. All the absorbance spectra of undoped and doped perovskite thin films were measured using an Agilent Cary 300 UV–visible spectrometer, allowing us to calculate the absorption coefficient and an optical bandgap value from the basic absorption edge estimation. Scanning electron microscopy (SEM) is a powerful technique to get higher resolution surface images using an electron beam. Morphological and device cross-sectional electron microscope images were gathered using Zeiss Leo high resolution scanning electron microscope. The atomic force microscopy (AFM) is a frequently used technique to measure the samples' surface topography

[5]. The Nano-Observer atomic force microscope from CSI instruments was used to obtain the topographical images of deposited perovskite films. It allows us to evaluate the root mean square roughness (RMS), skewness, kurtosis, etc.

References

[1] D. A. Skoog, F. J. Holler, and S. R. Crouch, *principles of instrumental analysis sixth edition*. 2007.

[2] G. F. Burkhard, E. T. Hoke, and M. D. McGehee, "Accounting for interference, scattering, and electrode absorption to make accurate internal quantum efficiency measurements in organic and other thin solar cells," *Adv. Mater.*, 2010, doi: 10.1002/adma.201000883.

[3] H. J. Snaith and C. Ducati, "SnO2-Based dye-sensitized hybrid solar cells exhibiting near unity absorbed photon-to-electron conversion efficiency," *Nano Lett.*, 2010, doi: 10.1021/nl903809r.

[4] A. Braeuer, "Absorption Spectroscopy," in *Supercritical Fluid Science and Technology*, 2015.

[5] B. Cappella and G. Dietler, "Force-distance curves by atomic force microscopy," *Surf. Sci. Rep.*, vol. 34, no. 1–3, pp. 1–3, Jan. 1999, doi: 10.1016/S0167-5729(99)00003-5.

4. CHAPTER IV. Solar cell fabrication

4.1. Front contact FTO

The FTO is known as a transparent conducting oxide (TCO), and it is an n-type semiconducting material, which is an alternative for indium tin oxide (ITO) [1]. It possesses a direct electronic bandgap of $E_g = 3.6\ eV$ [2], and an optical bandgap can exceed upto 4 eV based on the fluorine substitution [3]. Also, it demonstrates an outstanding optical transmission behavior (around 80%) in the visible region [4], and it has a lower resistivity than ITO ($2 \sim 4 \times 10^{-4}\ \Omega.cm$) [5], [6]. Moreover, it is highly thermally stable compared to the ITO substrate [7]; due to this reason, FTO is widely used as a front contact in perovskite solar cells. In this work, we used a 2 mm thick (12 * 12 mm) FTO substrate for all the perovskite device fabrication, the cleaning and etching procedure mentioned in the previous chapter. The cleaned substrates were consequently exposed to UV-ozone treatment (20 mins) to clean the FTO substrate's surface before depositing the ETL.

4.2. Deposition of the electron transport layer (ETL – SnO_2)

A simple solution process method is used to deposit the ETL layer [8], and the filtered SnO_2 solutions (see previous chapter) were spin-coated (4000 rpm with 30s) on UV-ozone treated FTO/glass substrate in the ambient condition. Later, the ETL deposited substrates were etched using deionized water and the cotton swab sticks. Then, the etched films were immediately transferred onto the hotplate and dried at 150 °C for 30 mins. The schematic representation of SnO_2 – ETL deposition demonstrated in **Fig. 4.1**. After that the SnO_2 deposited FTO/glass films directly moved into the glovebox.

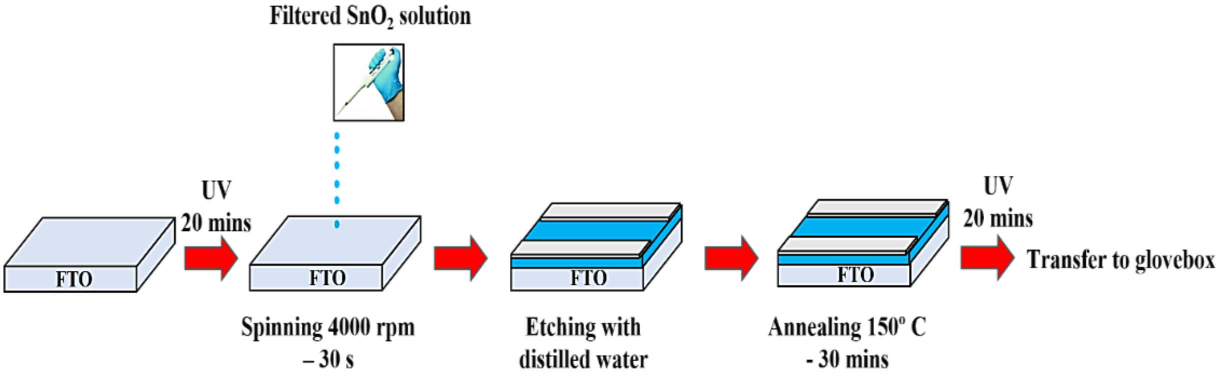

Fig. 4.1. *Schematic of ETL deposition procedures.*

4.3. Deposition of different perovskite absorber layers by one-step solution process with antisolvent treatment

The prepared perovskite precursor solutions (such as pure $FAPbI_3$, $FA_{0.85}Cs_{0.15}PbI_3$, $FA_{0.85}Cs_{0.15}Pb(I_{0.85}Br_{0.15})_3$ and Bi, as well as Cu incorporated $FA_{0.85}Cs_{0.15}Pb(I_{0.85}Br_{0.15})_3$), were deposited under the ambient condition or inside the nitrogen-filled glovebox (H_2O < 0.1 ppm, O_2<~45 ppm).

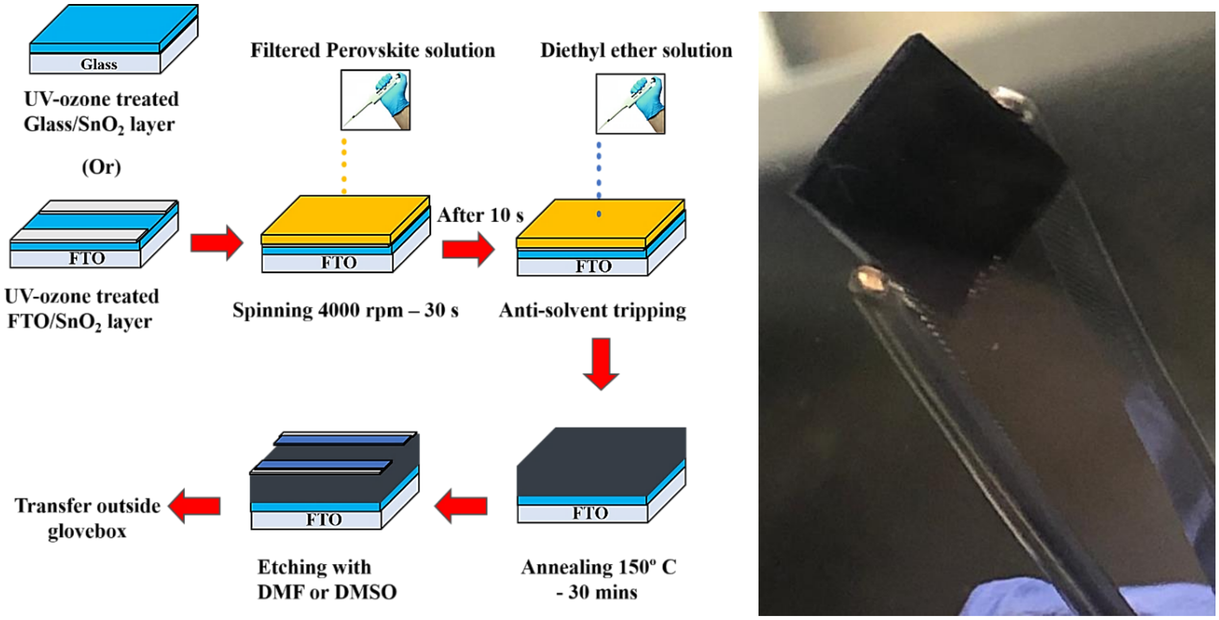

Fig. 4.2. Schematic of perovskite absorber layer deposition.

The prepared perovskite solutions were spin-coated (4000 rpm with 30s) on UV-ozone treated SnO_2 – ETL, after 10s, the anti-solvent treatment was applied by dropping 500 µl of diethyl ether (DE) onto the spinning substrate. The prepared perovskite films were immediately transferred onto the hotplate and preheated at 100 °C for 5 mins and at 150 °C for 15 mins. Then, the perovskite films were etched using DMF or DMSO solution and the cotton swab sticks (see **Fig. 4.2**). Finally, the etched perovskite films were carefully shifted to room atmosphere to deposit the HTL.

4.4. Deposition of the hole transport layer (HTL – Spiro-OMeTAD)

After moving the perovskite films, the prepared Li-TFSI and 4-tertbutylpyridine doped Spiro-OMeTAD – HTL solution (see the previous chapter) were deposited by spin-coating method (3000 rpm with 30s) according to the previous report [9], shown in Fig. 3. Later, the HTL deposited films were etched using CB solution and the cotton swab sticks (see **Fig. 4.3**). Finally, the etched HTL films were immediately transferred onto a high vacuum thermal evaporator to deposit the gold (Au) contact.

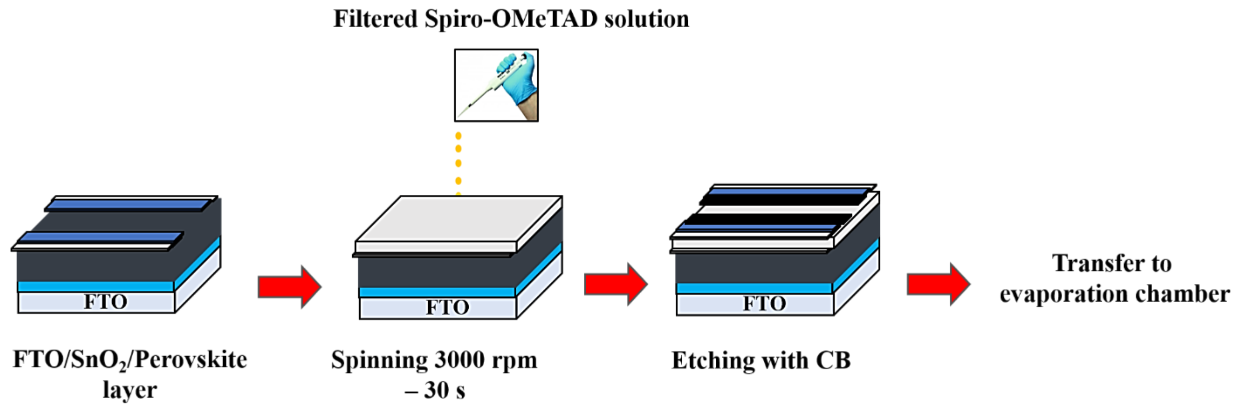

Fig. 4.3. *Schematic of HTL layer deposition.*

4.5. Deposition of gold (Au) electrode

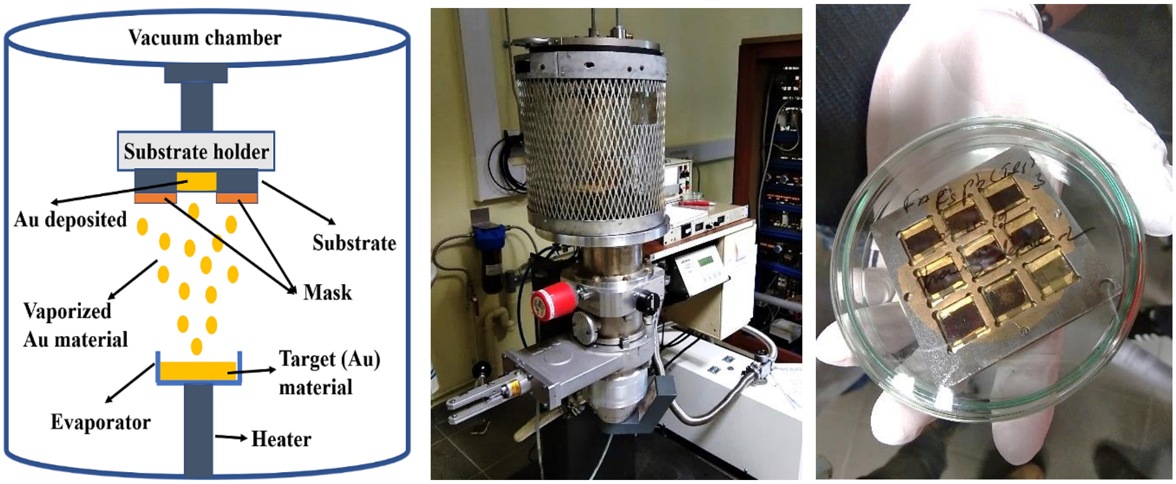

Fig. 4.4. *Schematic of Au contact deposition.*

Finally, 100 nm of gold contact electrode was deposited on the HTL using a mechanical shadow mask at a pressure of 10^{-6} mbar, demonstrated in **Fig. 4.4**. The active area of the device is larger than 0.2 cm^2. The complete device configuration is demonstrated in **Fig. 4.5.**

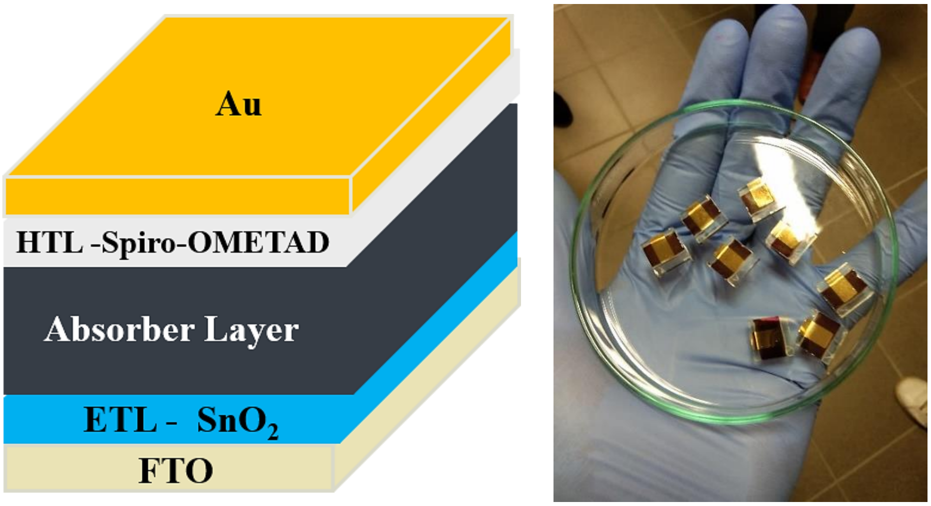

Fig. 4.5. Schematic of the complete perovskite device.

4.6. Solar cell Characterizations

In this section, some essential device characterization techniques and the measurement setup are presented, and all the following measurements were carried out in ambient air without encapsulation (i.e., the relative moisture level of 50–60%).

4.6.1. Current density- Voltage (I-V) measurement

In semiconductor devices, one of the essential and basic measurements is called current vs. voltage measurement.

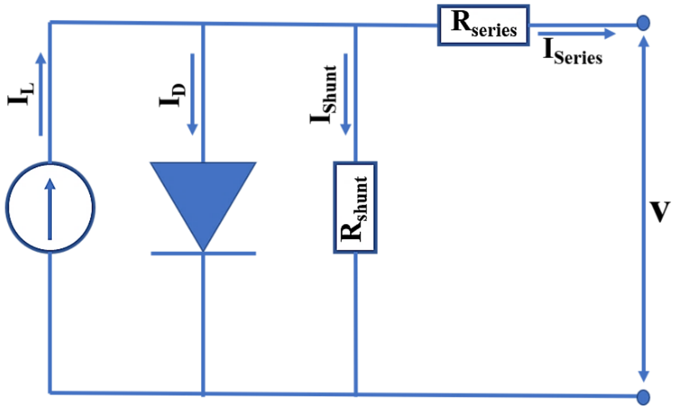

Fig. 4.6. Schematic representation of a solar cell equivalent circuit under illumination.

It is determined by the current flowing through the device while varying the voltage within it. Before going to the current vs. voltage measurement in the solar cell, it is better to understand how the solar cell equivalent circuit model works because it will help realize its working mechanism. **Fig. 4.6** demonstrates the solar cell equivalent circuit under illumination.

$$I = I_L - I_0\, e^{\frac{q(V+IR_{series})}{kT}} - \frac{V+IR_{series}}{R_{shunt}} \qquad (4.1)$$

Where I_L is the light generated current, I_D is the diode current, V is the voltage across the terminals, and R_{series}, as well as R_{shunt}, are the series and shunt resistances, respectively. Equation 4.1 governs the current response of a solar device in both dark and light conditions.

Here, a computer-controlled Keithley 2405 source-measure unit was used to probe the current density–voltage characteristics of the device under simulated solar emission using a 1600 W NEWPORT solar simulator equipped with an AM1.5G filter (see **Fig. 4.7**). The irradiance was calibrated using a certified silicon detector and after spectral mismatch correction to ensure a 100mWcm^{-2} light power density on the tested sample. The active area of all perovskite devices was 0.2cm^2 as defined by an aperture.

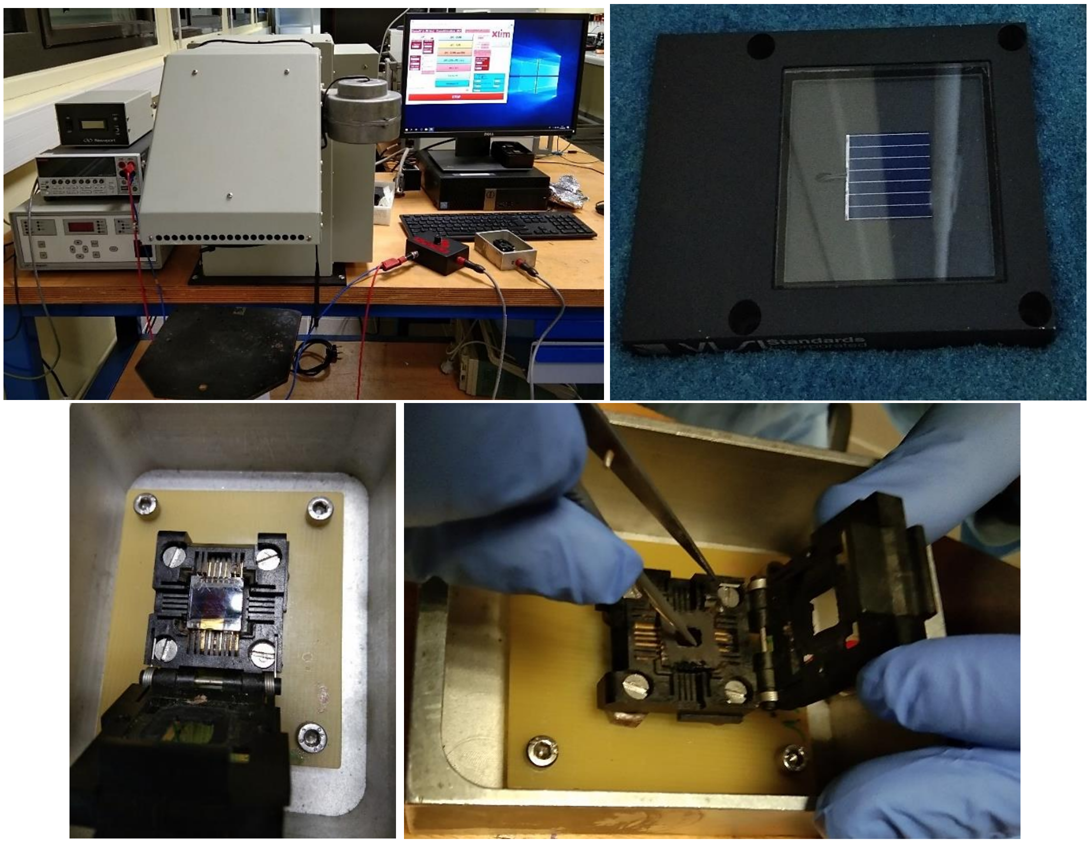

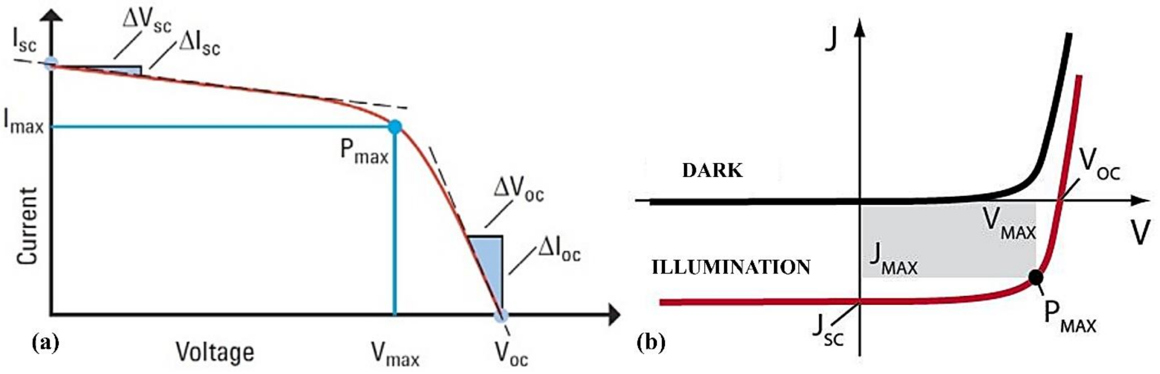

Fig. 4.7. *Schematic of the solar simulator and the representation of typical I-V curve of an illuminated solar cell.*

Determining the solar cell power conversion efficiency (PCE) is the most crucial characterization in the photovoltaic field, schematic demonstrated in **Fig. 4.7**. It is usually determined by doing a current density – voltage (J-V) measurement. During this measurement, the solar device electrodes are connected and exposed to the simulated solar light. After illumination, it is possible to extract a few important parameters, such as short-circuit current density (J_{sc}), open-circuit voltage (V_{oc}), fill factor (FF), and the device PCE. J_{sc} being the current-density when the bias voltage across the device is zero, and V_{oc} is the voltage when the net current is zero. The total power output of the solar device is the product of voltage and current, i.e., $P = I * V$, and the Maximum power (P_{Max}) indicates the combination of I and V.

$$P_{Max} = J_{Max} * V_{Max} \quad (4.2),$$

The FF of the solar cell described as,

$$FF = \frac{P_{Max}}{J_{sc} * V_{oc}} = \frac{J_{Max} * V_{Max}}{J_{sc} * V_{oc}} \quad (4.3),$$

And the PCE of the device determined by the following equation,

$$P_{Max} = FF * J_{sc} * V_{oc} \quad (4.4),$$

$$Efficiency\ (\eta) = \frac{P_{Max}}{P_{incident}} = \frac{FF * J_{sc} * V_{oc}}{area * 100\, {}^{mW}\!/_{cm^2}} \quad (4.5),$$

In general, the I-V measurement is the simplest way to find out the resistance problem in a solar cell, and the known parasitic resistances are series and shunt resistance ($R_{series}\ and\ R_{shunt}$). The effect of parasitic resistances on the I-V characteristics of a solar cell is demonstrated in **Fig. 4.8**.

The R_{series} mainly affect the device FF value (see **Fig. 4.7**) and higher R_{series} significantly reduce the J_{sc} values. Low R_{shunt} leading an alternative current path, triggering the power losses in solar devices and influencing photovoltage loss. The following equation is used to understand the consequences of R_{series} and R_{shunt} on the single-diode device performance,

$$I = I_L - I_O \left[e^{\frac{q(V+I*R_{series})}{Ak_BT}} - 1 \right] - \frac{V+I*R_{series}}{R_{shunt}} \quad (4.6)$$

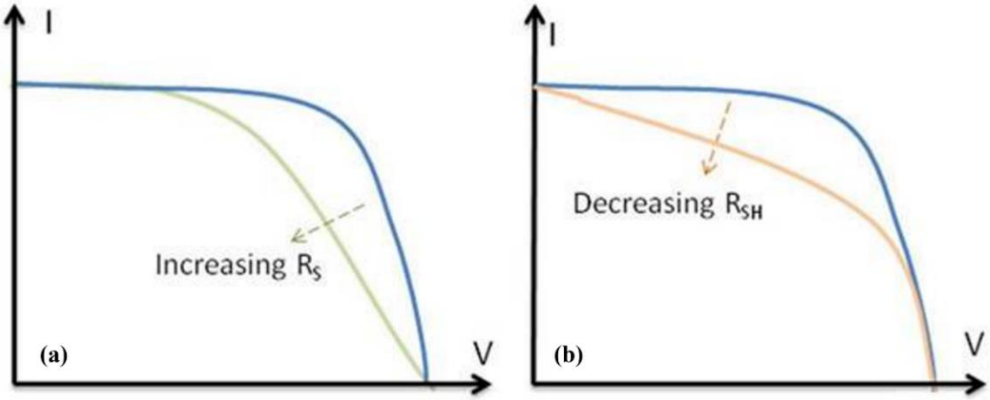

Fig. 4.8. Effect of parasitic resistances (R_{series} and R_{shunt}) on the J-V characteristics of a solar cell.

4.6.2. External quantum efficiency (EQE) measurement

EQE or IPCE (Incident Photon to Charge-carrier Efficiency) is a method to identify the photon absorption and charge-carrier collection issues in a complete solar device. It is generally defined as the ratio of the number of an incident photon on a solar cell to the number of a generated electron, and the following equation describes it,

$$EQE = \frac{1240}{\lambda\,(nm)} * \frac{J_{sc}\,(A.cm^{-2})}{P_{incident\,photon}\,(W.cm^{-2})} \quad (4.7)$$

The ideal EQE should be 100%, but in reality, the solar devices are hurt from several kinds of losses, such as recombination and optical losses (transmission and reflection). All the EQE spectra were recorded using the QER apparatus, Enli Co., Ltd (DC mode without any bias light). Also, similar EQE results were obtained in AC mode using a white LED bias light during the measurement. **Fig. 4.9.** demonstrates the typical EQE curve and EQE measurement machine. There is a considerable signal reduction that occurred in the short and long-wavelength regions due to the front and back surface recombination issues. The overall significant diminishment in the EQE curve is related to the transmission losses (or low diffusion length) in the main absorber layer. There is no EQE signal acquired after a certain wavelength due to nill absorption.

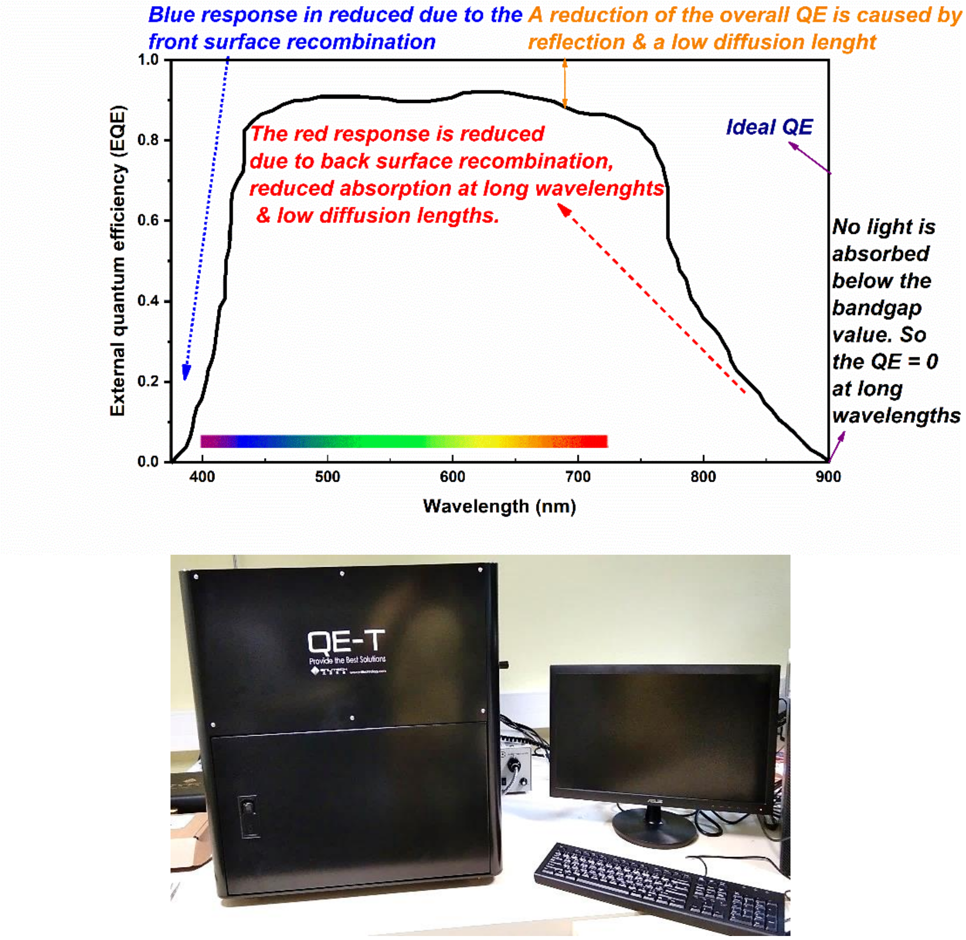

Fig. 4.9. *A typical EQE curve (https://www.pveducation.org), and with EQE equipment.*

The relation between the EQE spectra to the measured J_{sc} from the solar simulator, as described by the following equation,

$$J_{sc} = q \int F(\lambda).\, EQE(\lambda)\, d(\lambda) \quad (4.8)$$

Where, $F(\lambda)$ is the photon flux, and q is the elementary charge.

4.6.3. Initial device stability (or aging) measurement

The device stability measurement is a crucial parameter to determine any PV device's real life-time, especially in PSC. However, the aging test completely varies depending on the lab condition and the measurement parameters, which means there is still a lack of uniformity and repeatability in the measurement process to compare the stability data results with other reported data [10]. The exiting International Summit on Organic PV Stability (ISOS) protocols distinguish the testing methods based on the applied stresses such as dark storage testing, outdoor testing, thermal cycling testing, light-soaking testing, and the combination of light-humidity-thermal cycling testing [11].

Recently recommended three types of stability testing regimes for PSC, such as basic or level 1 (ISOS-D-1, intermediate or level 2 (ISOS-D-2), and advanced or level 3 (ISOS-D-3) [12]. The basic (ISOS-D-1) testing method should need the least inexpensive instrumentation setup and the protocol requirements, which means the testing environment is not finally controlled. The intermediate (ISOS-D-2) testing procedures should require the appropriate tools (such as solar simulators and oven) to get the J-V curve, and many research laboratories adopted this method. The last and final advanced (ISOS-D-3) procedures require more dedicated instruments (such as the controlled environmental chamber and maximum power point tracker, etc.), and this method provides a higher level of precision results than the other two.

References

[1] J. E. N. Swallow *et al.*, "Self-Compensation in Transparent Conducting F-Doped SnO2," *Adv. Funct. Mater.*, 2018, doi: 10.1002/adfm.201701900.

[2] X. H. Shi and K. J. Xu, "Properties of fluorine-doped tin oxide films prepared by an improved sol-gel process," *Mater. Sci. Semicond. Process.*, 2017, doi: 10.1016/j.mssp.2016.09.038.

[3] H. Kim, R. C. Y. Auyeung, and A. Piqué, "Transparent conducting F-doped SnO2 thin films grown by pulsed laser deposition," *Thin Solid Films*, 2008, doi: 10.1016/j.tsf.2007.11.079.

[4] N. Noor, C. K. T. Chew, D. S. Bhachu, M. R. Waugh, C. J. Carmalt, and I. P. Parkin, "Influencing FTO thin film growth with thin seeding layers: a route to microstructural modification," *J. Mater. Chem. C*, 2015, doi: 10.1039/c5tc02144h.

[5] N. Noor and I. P. Parkin, "Enhanced transparent-conducting fluorine-doped tin oxide films formed by Aerosol-Assisted Chemical Vapour Deposition," *J. Mater. Chem. C*, 2013, doi: 10.1039/c2tc00400c.

[6] L. T. C. Tuyen, S. R. Jian, N. T. Tien, and P. H. Le, "Nanomechanical and material properties of fluorine-doped tin oxide thin films prepared by ultrasonic spray pyrolysis: Effects of F-doping," *Materials (Basel).*, 2019, doi: 10.3390/ma12101665.

[7] C. Sima, C. Grigoriu, and S. Antohe, "Comparison of the dye-sensitized solar cells performances based on transparent conductive ITO and FTO," *Thin Solid Films*, 2010, doi: 10.1016/j.tsf.2010.07.002.

[8] Q. Jiang, X. Zhang, and J. You, "SnO2: A Wonderful Electron Transport Layer for Perovskite Solar Cells," *Small*. 2018, doi: 10.1002/smll.201801154.

[9] M. Saliba *et al.*, "Cesium-containing triple cation perovskite solar cells: Improved stability, reproducibility and high efficiency," *Energy Environ. Sci.*, 2016, doi: 10.1039/c5ee03874j.

[10] A. Tiihonen, K. Miettunen, J. Halme, S. Lepikko, A. Poskela, and P. D. Lund, "Critical analysis on the quality of stability studies of perovskite and dye solar cells," *Energy Environ. Sci.*, 2018, doi: 10.1039/c7ee02670f.

[11] M. O. Reese *et al.*, "Consensus stability testing protocols for organic photovoltaic materials and devices," *Sol. Energy Mater. Sol. Cells*, 2011, doi: 10.1016/j.solmat.2011.01.036.

[12] M. V. Khenkin *et al.*, "Consensus statement for stability assessment and reporting for perovskite photovoltaics based on ISOS procedures," *Nat. Energy*, 2020, doi: 10.1038/s41560-019-0529-5.

5. CHAPTER V. Numerical simulation – SCAPS – 1D

5.1. SCAPS-1D

Nowadays, numerical simulation is a crucial and cost-effective technique to study the physical mechanism behind solar devices' fundamental properties, especially without making any real devices. It can save time and money in device development. There are several simulation *software* available such as Quokka2, PC1D, ADEPT, OPV LAB, WXAMPS-1D, GPVDM-1D, AFORS-HET, and SCAPS-1D in order to construct the solar device structures and also explore the fundamental properties like current density – voltage characteristics, including device power conversion efficiency, fill factor, open-circuit voltage, and short circuit current. SCAPS-1D (Solar Cell Capacitance Simulator) is a one-dimensional simulation program freely available to the solar cell research groups, developed at the Electronics and Information Systems (ELIS) department, University of Gent, Belgium [1]. SCAPS-1D is initially created for $CuInSe_2$ and $CdTe$ solar cell family, and now its capablilities extended for many devices such as crystalline as well as amorphous cells be means Si, $GaAs$, $CIGS, CZTS, Perovskite$, and so on [2]–[8]. The main aspects of the most recent version of SCAPS-1D are given below:

- ❖ It is possible to create up to seven semiconductor layers.
- ❖ All the parameters can be graded: the optical band gap (E_g), electron affinity (χ), dielectric constant (ε), conduction and valence band density of states ($N_C\ and\ N_V$), electron and hole mobility ($\mu_n\ and\ \mu_p$), acceptor and donor dopant concentration (NA and ND), thermal velocity of charge carriers (Vthn and Vthp), working temperature (T), absorption model, and all traps (defects) Nt are defined.
- ❖ Recombination mechanisms: band-to-band (direction), Auger, and SRH-type.
- ❖ Defect levels:
  - in bulk or at the interface; their charge state and recombination is accounted for
  - charge type: no charge (idealization), monovalent (single donor and acceptor), divalent (double donor and acceptor, amphoteric), multivalent (user-defined)
  - energetic distributions: single level, uniform, Gauss, tail, or combinations.
  - optical property: direct excitation with light possible (impurity photovoltaic effect-IPV)

  - metastable transitions between defects
- Contact: work function or flat-band; optical property filter (Reflection of transmission filter)
- Tunneling: intra-band tunneling (within a conduction or valence band); tunneling to and from interface states.
- Generation: either from internal calculation or from user-supplied $G(x)$ file.
- Illumination: standard and other spectra included (AM0, AM1.5D, AM1.5G, AM1.5G-edition2, monochromatic, White, etc.)
- Illumination: from either P-side or the N-side; spectrum cut-off and attenuation
- Working point for calculations: Voltage, frequency, and temperature (user-defined).
- The SCAPS-1D package determines;
  - Energy bands,
  - Concentrations and currents at a given working point.
  - Current density – voltage characteristics
  - AC characteristics (C and G as a function of V and/or f)
  - Spectral response with/without bias light or voltage)
- Batch calculation possible; presentation of results and settings as a function of batch parameters.
- Loading and saving of all settings;
  - Startup of SCAPS-1D in a personalized configuration
  - Script language, with a free user function.
- Very intuitive user interface
- A script language facility to run SCAPS from a "script file"; all internal variables can be accessed and plotted using the script.
- A built-in curve fitting facility
- A separate panel to interpret the admittance measurements.

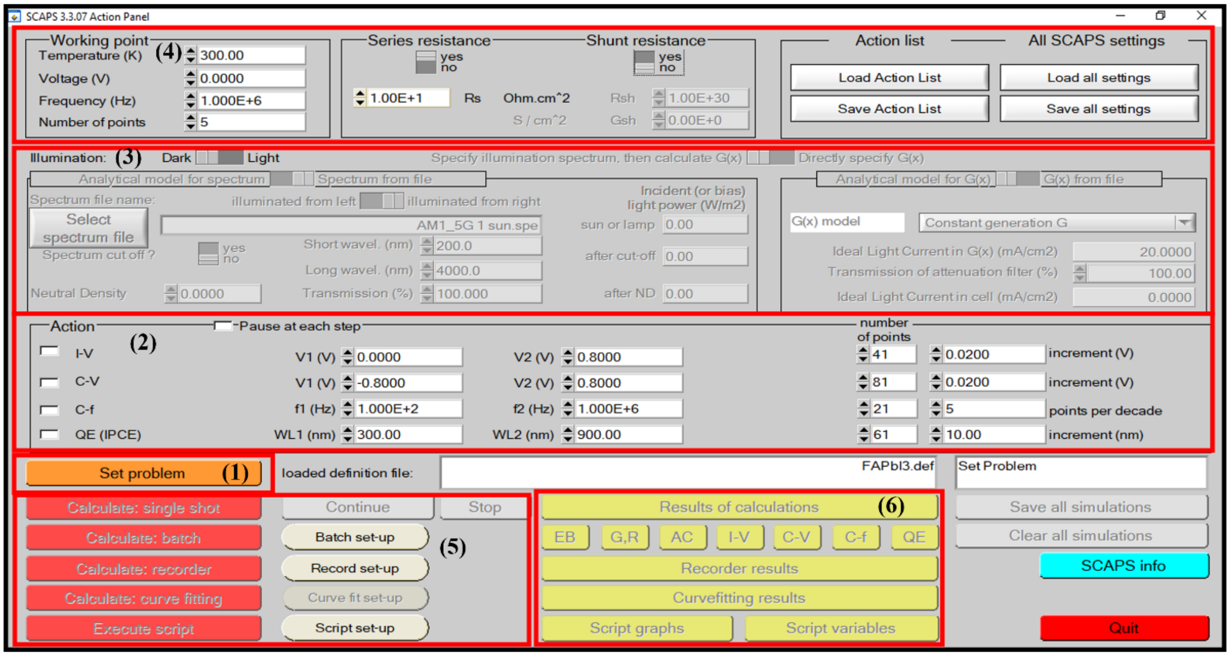

Working point
Temperature (K) 300.00
Voltage (V) 0.0000
Frequency (Hz) 1.000E+6
Number of points 5

Series resistance: yes / no; 1.00E+1 Rs Ohm.cm^2 S / cm^2
Shunt resistance: yes / no; Rsh 1.00E+30; Gsh 0.00E+0

Illumination: Dark / Light
Specify illumination spectrum, then calculate G(x) / Directly specify G(x)
Analytical model for spectrum / Spectrum from file
Spectrum file name: illuminated from left / illuminated from right
AM1_5G 1 sun.spe
Spectrum cut off ? yes / no
Short wavel. (nm) 200.0
Long wavel. (nm) 4000.0
Neutral Density 0.0000
Transmission (%) 100.000
Incident (or bias) light power (W/m2)
sun or lamp 0.00
after cut-off 0.00
after ND 0.00
Analytical model for G(x) / G(x) from file
G(x) model: Constant generation G
Ideal Light Current in G(x) (mA/cm2) 20.0000
Transmission of attenuation filter (%) 100.00
Ideal Light Current in cell (mA/cm2) 0.0000

Action ☐ Pause at each step

Action					number of points		
☐ I-V	V1 (V)	0.0000	V2 (V)	0.8000	41	0.0200	increment (V)
☐ C-V	V1 (V)	-0.8000	V2 (V)	0.8000	81	0.0200	increment (V)
☐ C-f	f1 (Hz)	1.000E+2	f2 (Hz)	1.000E+6	21	5	points per decade
☐ QE (IPCE)	WL1 (nm)	300.00	WL2 (nm)	900.00	61	10.00	increment (nm)

loaded definition file: FAPbI3.def
Set Problem

Fig. 5.1. SCAPS-1D software startup panel setup.

Several sections are available in the SCAPS-1D startup panel (see **Fig. 5.1**) that are numbered from 1 to 6. Section 1 shows that the set problem box is allowed to define a complete solar cell structure containing several layers and physical properties. In section 2, the action box permits to define the I-V characteristics scale settings, Quantum efficiency (QE or IPCE) measurement scale settings, capacitance-voltage (C - V) as well as capacitance – frequency (C – f) measurements scale settings. In section 3, the illumination box provides the option to select the light and dark conditions for the simulation and the required spectrum file. In section 4, the working point box allows us to define the working temperature as well as permits us to describe the parasitic resistances, such as series and shunt resistance. In section 5 is for single shot calculations, batch calculations, curve fitting calculations. Also, the recording setup and script setup options are available. Finally, in section 6, the "results of calculations" box gives the options to check the simulated device results, such as energy band (EB), I-V, QE characteristics, etc.

In **Fig. 5.2**, there are three different sections available, and it will offer the options to construct the desired solar cell structure with/without the interface layer. Section 1 helps us to define the different layers to complete the device structure, including front and back contact. Section 3 displays the constructed device, and there are some other options to select the light illumination and applied voltage sides using either from the front contact side or back contact side. Section 3 is useful for creating the new structure file or loading the available file and saving the required device structure file.

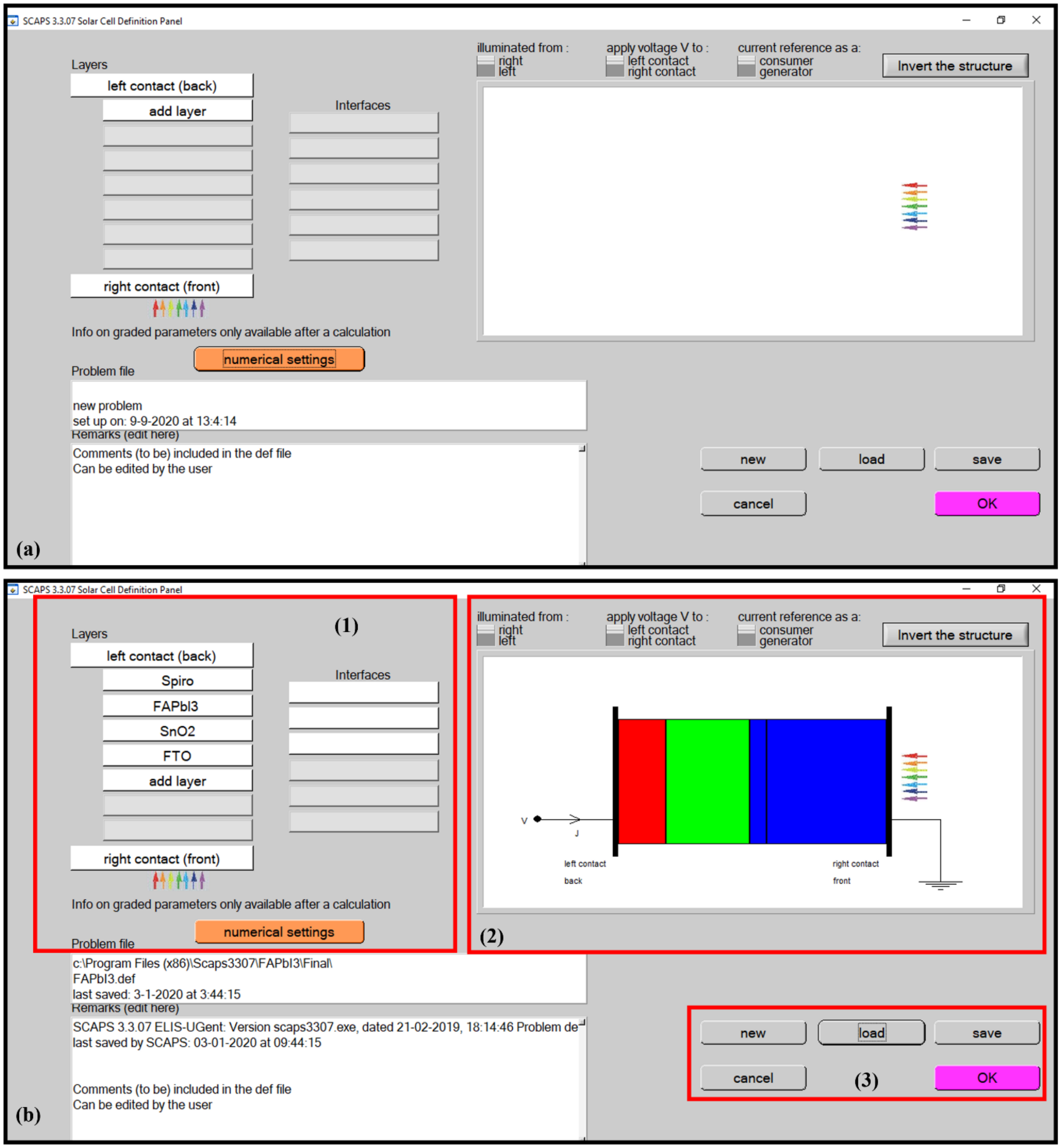

(a)

Info on graded parameters only available after a calculation

new problem
set up on: 9-9-2020 at 13:4:14

Comments (to be) included in the def file
Can be edited by the user

(b)

Info on graded parameters only available after a calculation

c:\Program Files (x86)\Scaps3307\FAPbI3\Final\
FAPbI3.def
last saved: 3-1-2020 at 3:44:15

SCAPS 3.3.07 ELIS-UGent: Version scaps3307.exe, dated 21-02-2019, 18:14:46 Problem de
last saved by SCAPS: 03-01-2020 at 09:44:15

Comments (to be) included in the def file
Can be edited by the user

***Fig. 5.2**. SCAPS-1D solar cell definition panel (a) with Perovskite structure (b).*

Fig. 5.3 demonstrated the material and defect definition panel, which provides the option to define the physical parameters of each layer, such as E_g, χ, ε, N_C, N_V, μ_n, μ_p, NA, ND, Vthn, Vthp, T, absorption model, and Nt, etc.

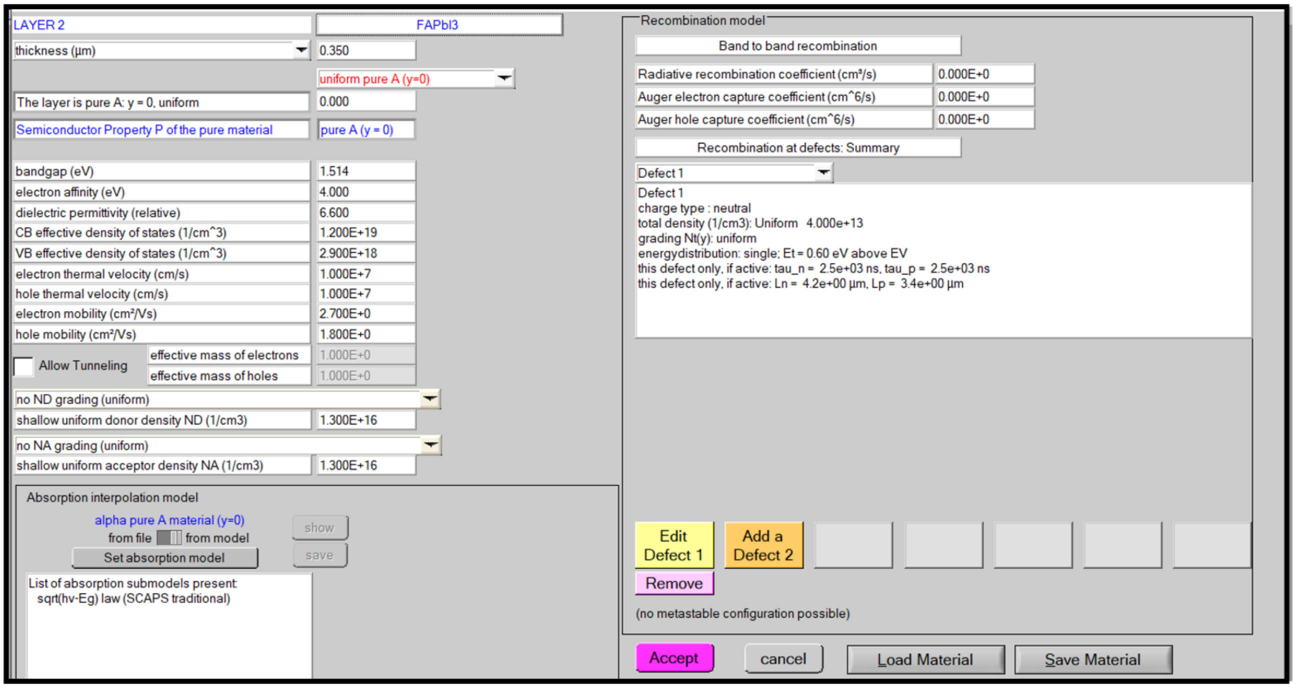

LAYER 2	FAPbI3
thickness (μm)	0.350
The layer is pure A: y = 0, uniform	0.000
Semiconductor Property P of the pure material	pure A (y = 0)
bandgap (eV)	1.514
electron affinity (eV)	4.000
dielectric permittivity (relative)	6.600
CB effective density of states (1/cm^3)	1.200E+19
VB effective density of states (1/cm^3)	2.900E+18
electron thermal velocity (cm/s)	1.000E+7
hole thermal velocity (cm/s)	1.000E+7
electron mobility (cm^2/Vs)	2.700E+0
hole mobility (cm^2/Vs)	1.800E+0
☐ Allow Tunneling — effective mass of electrons	1.000E+0
effective mass of holes	1.000E+0
shallow uniform donor density ND (1/cm3)	1.300E+16
shallow uniform acceptor density NA (1/cm3)	1.300E+16

alpha pure A material (y=0)

List of absorption submodels present:
sqrt(hv-Eg) law (SCAPS traditional)

Band to band recombination

Radiative recombination coefficient (cm^3/s)	0.000E+0
Auger electron capture coefficient (cm^6/s)	0.000E+0
Auger hole capture coefficient (cm^6/s)	0.000E+0

Recombination at defects: Summary

Defect 1

Defect 1
charge type : neutral
total density (1/cm3): Uniform 4.000e+13
grading Nt(y): uniform
energydistribution: single; Et = 0.60 eV above EV
this defect only, if active: tau_n = 2.5e+03 ns, tau_p = 2.5e+03 ns
this defect only, if active: Ln = 4.2e+00 µm, Lp = 3.4e+00 µm

***Fig. 5.3**. Material and defect definition panel in SCAPS-1D for the Perovskite layer.*

5.2. Advantages and limitations in SCAPS-1D

The SCAPS-1D system has several advantages [9], [10],

- The parameter setting is graded for each layer, which is useful for studying the composite layer through interdiffusion between different layers. To introduce the defects in bulk and interfaces, including defect charge and the energy distribution induced by defects.
- It is easy to define the layer parameters, even in the interfaces. It allows us to save the files to ASCII code format, and it will be beneficial to read from outside. It provides scriptwriting language options for the users to run the simulation.
- Each and every layer parameter detail are displayed in a separate window to define easily. It offers several numbers of electrical measurement simulations, such as J (V), C (V), C (f), and spectral response. Once the simulation is completed, the system displays the characteristics, and also it provides a comparison with the other previous simulation results.

Limitations

- ❖ Generally, ID software like SCAPS-1D considers only the thickness variation but not the complete device's width and length.

- SCAPS-1D permits the addition of only seven semiconducting layers. It is mainly designed for thin-film solar cells.
- The calculation accuracy is insufficient for semiconducting material-based simulations due to the small resolution number ($< 10^{-15}$).

5.3. Numerical simulation of ideal perovskite devices using SCAPS-1D

In general, Solar cell modeling/simulation is an effective medium to gain more insight into device physics, and it provides a reliable way to enhance device PCE after the optimization of various physical parameters. Notably, a complete set of device characteristics, especially I-V and EQE, can easily be generated with less time and effort. In SCAPS-1D, different input or physical parameters (such as layer thickness, bandgap, electron affinity, permittivity, the effective density of states, charge mobility, thermal velocities, doping densities, and defect densities, etc.) are crucial to solve the basic semiconductors equations in order to simulate the required device model. The reported experimental data (for example, thickness) is generally employed as the physical or input parameters in SCAPS to design the solar cell model. In the early stage of this thesis simulation work, the one-dimensional planar n-i-p ideal perovskite devices (FTO/SnO_2/FA perovskites/Spiro/Au) were carefully optimized without considering R_{series} and R_{shunt} resistances by using the SCAPS-1D *software*. This process, although nonrealistic, but an excellent tool to evaluate the higher limit of device performance considering an optimal operation. Three different types of FA cation-based perovskite absorber layers were used, namely pristine $FAPbI_3$, $FA_{0.85}Cs_{0.15}PbI_3$, and $FA_{0.85}Cs_{0.15}Pb(I_{0.85}Br_{0.15})_3$. The three devices are referred to as D-A, D-B, and D-C, respectively, for the rest of this study. The optical bandgap of the active layers and their thickness (around 350 nm in all cases) are obtained from experimental absorption spectra, and mechanical profilometry measurements are used in order to compare the practical device PV performance with the simulated results, especially based on the doping behavior. Weakly-bounded excitons are generated in the perovskite layer when the device is exposed under a light. Rapid exciton dissociation then occurs before electrons and holes are rapidly collected by their respective selective contacts, as depicted in **Fig 5.4**. The simulation, which is based on a classical drift-diffusion model, is carried out at 300-K under one sun (AM1.5G, $100mW\ cm^{-2}$) irradiation. The experimental thickness of the SnO_2 ETL (70 nm) was also used for the simulation. Other parameters, such as electron affinity, permittivity, the effective density of states, charge mobility, thermal velocities, doping densities, and defect densities) were extracted from the literature, based on the different perovskite compositions [11]–[16] as detailed in **Table 5.1**.

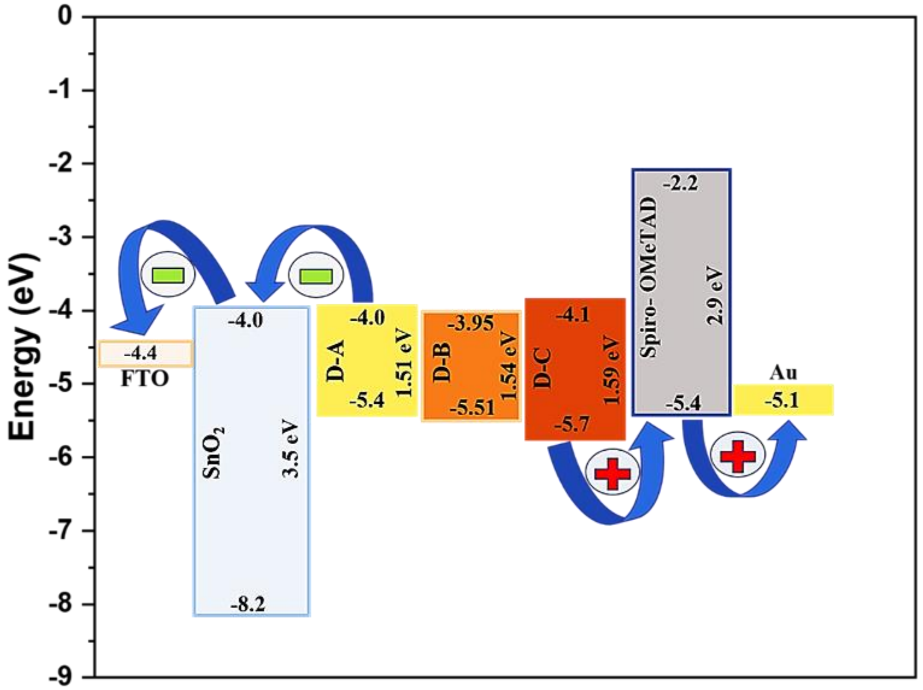

Fig. 5.4. *Simplified flat band energy diagram of ETL, HTL and pristine* $FAPbI_3$ *(D-A),* $FA_{0.85}Cs_{0.15}PbI_3$ *(D-B) and* $FA_{0.85}Cs_{0.15}Pb(I_{0.85}Br_{0.15})_3$ *(D-C) perovskite active layers.*

Table 5.1. *Details of input parameters used for the simulation of FA-based perovskite solar cells. When data are extracted from the literature, the corresponding reference is indicated.*

Parameters	**FTO**	**ETL-($\mathbf{SnO_2}$)**	**D-A**	**D-B**	**D-C**	**HTL (Spiro-OMeTAD)**
Thickness (nm)	500*	70*	350*	350*	350*	200*
Band gap (eV)	3.5	3.5	1.51*	1.55*	1.59*	2.9
e^- affinity (eV)	4.0	4.0	4.0 [17], [18]	3.95 [19]	4.09 [19]	2.2
Permittivity	9.0	9.0	6.6 [20]	6.6	6.6	3.0
Effective density of states at CB ($\mathbf{cm^{-3}}$)	2.2×10^{18}	2.2×10^{17}	1.2×10^{19} [21]	2×10^{19}	2×10^{19}	2.2×10^{18}
Effective density of states at VB ($\mathbf{cm^{-3}}$)	2.2×10^{18}	2.2×10^{17}	2.9×10^{18} [22]	2×10^{18}	2×10^{18}	2.2×10^{18}
e^- thermal velocity ($\mathbf{cm.s^{-1}}$)	1×10^7	1×10^7	1×10^7	1×10^7	1×10^7	1×10^7

h^+ thermal velocity ($\mathbf{cm.s^{-1}}$)	1×10^7	1×10^7	1×10^7	1×10^7	1×10^7	1×10^7
Mobility of e^- ($\mathbf{cm^2.V^{-1}s^{-1}}$)	20	20	2.7 [22]	0.28 [19]	8.16 [19]	1×10^{-4}
Mobility of h^+ ($\mathbf{cm^2.V^{-1}s^{-1}}$)	10	10	1.8 [22]	2	2	1×10^{-4}
Density of n-type doping ($\mathbf{cm^{-3}}$)	1×10^{15}	1×10^{15}	1.3×10^{16}	1.3×10^{16}	1.3×10^{16}	0
Density of p-type doping ($\mathbf{cm^{-3}}$)	0	0	1.3×10^{16}	1.3×10^{16}	1.3×10^{16}	1.3×10^{18}
Density of defects ($\mathbf{cm^{-3}}$)	10^{18}	10^{18}	4×10^{13}	4×10^{13}	4×10^{13}	10^{15}

* indicates this current work.

5.4. Numerical simulation of ideal perovskite devices with BiI_3 – interlayer

Designing and simulating the solar cell structure using SCAPS helps the researchers to evaluate their solar cell model before experimentally fabricating the same device structure. From our experimental observation, it was found that the optical bandgap value does not modify that much while partially incorporating Bismuth iodide (BiI_3) into the $FA_{0.85}Cs_{0.15}Pb(I_{0.85}Br_{0.15})_3$ perovskite composition. Also, we don't have physical parameter values for the doped layer, such as electron affinity, permittivity, the effective density of states, charge mobility, doping densities, defect densities, etc. Therefore, it is not easy to simulate the BiI_3 – doped perovskite device without having proper input parameters. But, there is a possibility to use a separate thin BiI_3 – interlayer in between the perovskite/HTL interface to understand the impact. As from our experimental analysis and previous reports, the device performance is highly affected by interface recombination. Therefore, in this work, the effect of different HTL (also electrodes) with and without BiI_3 – interlayer was systematically analyzed. It was found that the valence band offset (simply VBO) can play a prominent role in the device results by creating an electron barrier at the interface and reducing the interface recombination. The chosen n-i-p device composed of FTO/SnO_2 (ETL)$/FA_{0.85}Cs_{0.15}Pb(I_{0.85}Br_{0.15})_3/BiI_3$ (with and without - IL)$/Spiro-OMeTAD$ (HTL)$/$ Au, shown in **Fig. 5.5**. In this study, all the simulations were carried out using SCAPS-1D to solve the Poisson and continuity equations [1]**.** The simulated device was illuminated under one sun AM 1.5 G (100 mW cm^{-2}) solar spectrum with 300 k temperature, and the parasitic resistances (R_{Series} and R_{Shunt}) are not taken into these initial simulations. After illumination (photons strike) from

ETL to HTL side (see **Fig. 5.5**), the perovskite layer creates charge carriers, and diffuse into the electron (e^-) and hole (h^+) transport layers. Finally, $e^-{}'s$ and $h^+{}'s$ were collected by desired electrodes. The optimized absorber layer (500 nm), ETL (70 nm), all the HTL (150 nm), and IL (30 nm) thicknesses, as well as all other parameters such as e^- and h^+ mobility, e^- affinity, permittivity, the effective density of states, doping densities, and defect densities, are taken from previously published experimental and theoretical results, listed in **Table 5.2**. [11], [19], [23]–[30] The employed e^- and h^+ velocity values are considered as $1 \times 10^7\ cm/s$. The work function of TCO (front contact - FTO) and electrode (back contact – Au) are set to 4.4 eV and 5.1 eV, respectively. All the simulation was done, without considering the optical reflectance of each layers at the interface nor surface. Simulating ideal devices is a first step to emphasize the influence of the IL on device operation, independently of the main electrical losses that are found in realistic devices. It is designed to help the experimentalist to tailor their experiments [8]. The energy band alignment between the absorber layer, ETL, IL, and all HTL illustrated in **Fig. 5.6**.

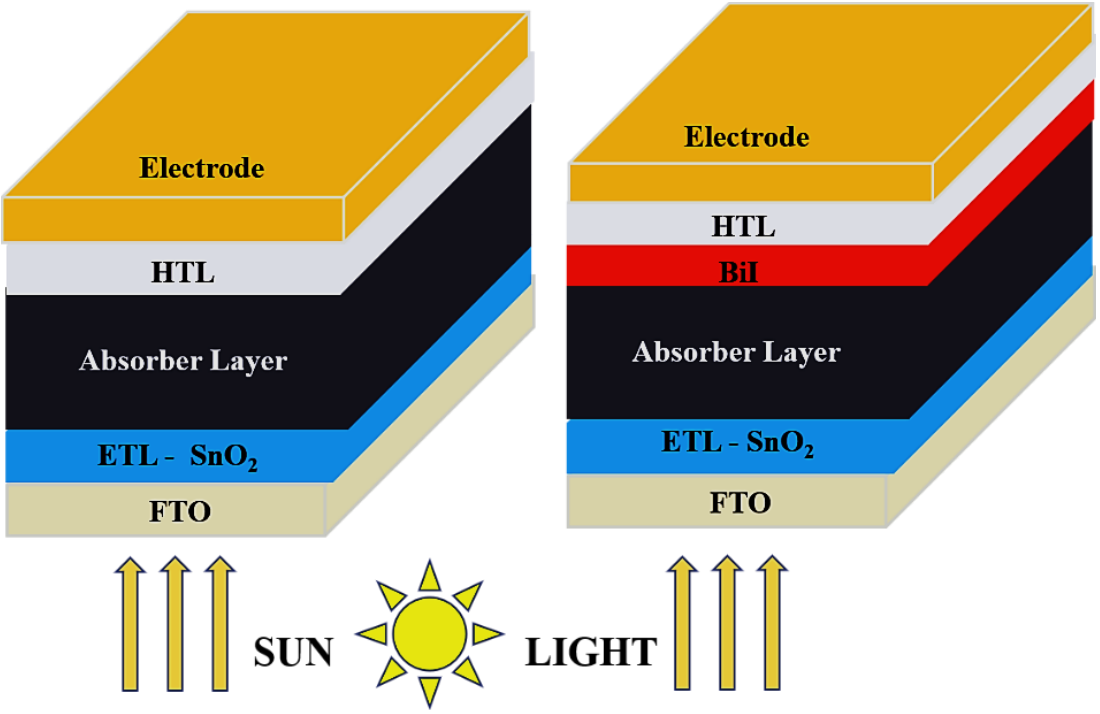

Fig. 5.5. *The n-i-p typical perovskite solar cell structure (left) and with BiI_3 IL (right).*

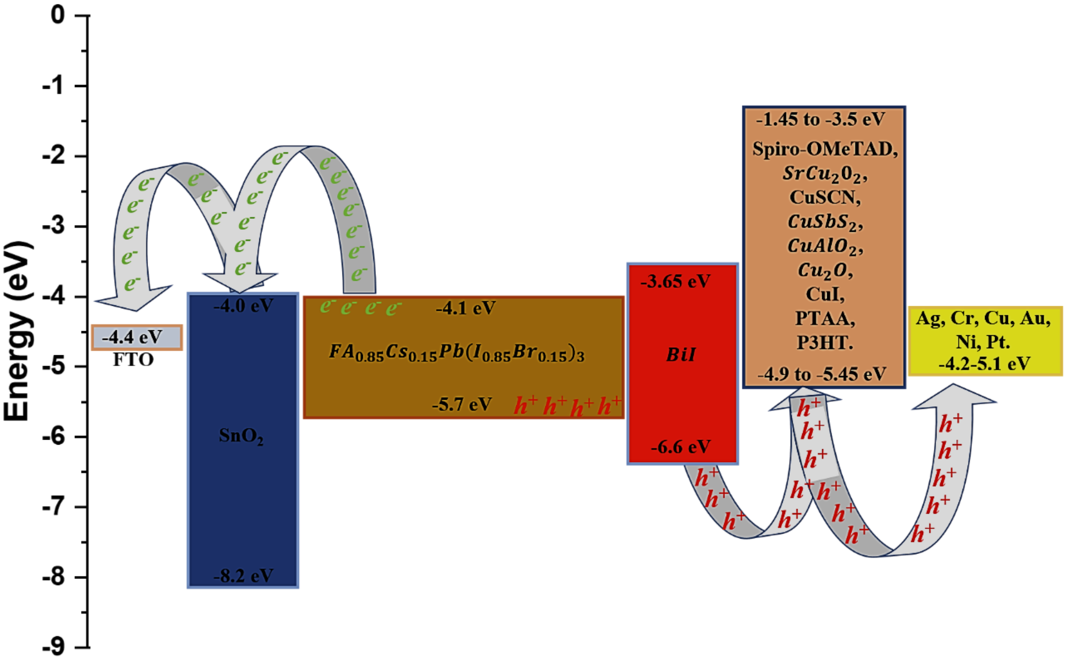

Fig. 5.6. *Band alignments between ETL, different HTL's with perovskite absorber, including* BiI_3 *IL.*

Table 5.2. *Details of primary input parameters used for the simulation of FAPI based perovskite solar cells.*

Parameters	**FTO**	**ETL (SnO_2)**	**$FA_{0.85}Cs_{0.15}Pb(I_{0.85}Br_{0.15})_3$**	**BiI_3 (IL)**	**HTL (Spiro-OMETAD)**
Thickness(nm)	500	70 [8]	500	30	150
Band gap (eV)	3.50	3.50	1.59	1.72 [23]	2.9
E Affinity	4.00	4.00	4.09 [19]	4.10 [24]	2.2
Permittivity	9.00	9.00	6.600	5.78 [25]	3.00
Effective density of states at CB	2.2×10^{18}	2.2×10^{17}	2.0×10^{19}	2.5×10^{19}	2.2×10^{19}
Effective density of states at VB	2.2×10^{18}	2.2×10^{17}	2.0×10^{18}	2.5×10^{19}	2.2×10^{19}
Mobility of e^-	20	20	8.16 [19]	600 [26]	1.0×10^{-4}
Mobility of h^+	10	10	2	200 [31]	1.0×10^{-4}
Density of n-type doping	1.0×10^{15}	1.0×10^{17}	1.3×10^{16}	1.0×10^{16}	0
Density of p-type doping	0	0	1.3×10^{16}	1.0×10^{16}	1.0×10^{18}
Density of defects	Donor- 1.0×10^{18}	Donor – 1.0×10^{15}	Neutral- 4×10^{13}	Neutral- 1×10^{15}	Acceptor- 1.0×10^{15}

After testing the Spiro-HTL based device with BiI_3 – interlayer, we carefully investigated the same device performance using different HTL candidates, such as a cuprous oxide (Cu_2O), Strontium Cuprate ($SrCu_2O_2$), Cuprous Aluminate ($CuAlO_2$), copper antimony sulfide ($CuSbS_2$), cupric thiocyanate ($CuSCN$), Cuprous iodide (CuI), Poly(triarylamine) ($PTAA$), poly(3-hexylthiophene-2,5-diyl) ($P3HT$) with and without BiI_3 IL. Also, we evaluated the effect of several electrodes (Ag,Cr,Cu,Au,Ni,Pt) based on their work function (WF) value with the above-mentioned HTL's. Finally, the effect of parasitic resistances (R_{Series} & R_{Shunt}) are also carried out. All the physical parameter values for the different HTL's are taken from previously published experimental and theoretical reports, listed in **Table 5.3**.

Table 5.3*. Input parameters for proposed different HTL materials.*

Parameters	**$SrCu_2O_2$**	**Cu_2O**	**$CuAlO_2$**	**CuSCN**	**$CuSbS_2$**	**CuI**	**PTAA**	**P3HT**
Thickness (nm)	150	150	150	150	150	150	150	150
Bandgap (eV)	3.3	2.17	3.46	3.2	1.58	2.98	2.96	1.8
E Affinity	2.2	3.2	2.5	1.9	4.2	2.1	2.3	3.9
Permittivity	9.77	7.1	60	10	14.6	6.5	9	3
Effective density of states at CB	2.0×10^{20}	2.1×10^{17}	2.0×10^{20}	2.2×10^{19}	2.2×10^{18}	2.8×10^{19}	2.0×10^{21}	2.0×10^{20}
Effective density of states at VB	2.0×10^{21}	1.0×10^{19}	1.0×10^{22}	1.8×10^{19}	2.2×10^{19}	2.0×10^{19}	2.0×10^{21}	2.0×10^{20}
Mobility of e^-	0.1	200	2	1.0×10^{-4}	49	100	1	1.0×10^{-4}
Mobility of h^+	0.46	80	8.6	1.0×10^{-1}	49	43.9	40	1.0×10^{-3}
Density of n type doping	0	0	0	0	0	0	0	0
Density of p-type doping	1.0×10^{17}	1.0×10^{18}	1.0×10^{20}	1.0×10^{18}	1.0×10^{18}	1.0×10^{18}	1.0×10^{18}	1.0×10^{18}
Density of defects	Acceptor-1.0×10^{15}	Acceptor-1.0×10^{15}	Acceptor-1.0×10^{15}	Acceptor-1.0×10^{15}	Acceptor-1.0×10^{15}	Acceptor-1.0×10^{15}	Acceptor-1.0×10^{15}	Acceptor-1.0×10^{15}
References	[27]	[27] [29]	[27]	[11] [32]	[33]	[30] [11]	[30]	[30] [11]

References

[1] M. Burgelman, P. Nollet, and S. Degrave, "Modelling polycrystalline semiconductor solar cells," *Thin Solid Films*, 2000, doi: 10.1016/S0040-6090(99)00825-1.

[2] K. Decock, P. Zabierowski, and M. Burgelman, "Modeling metastabilities in chalcopyrite-based thin film solar cells," *J. Appl. Phys.*, 2012, doi: 10.1063/1.3686651.

[3] J. Verschraegen and M. Burgelman, "Numerical modeling of intra-band tunneling for heterojunction solar cells

in scaps,” *Thin Solid Films*, 2007, doi: 10.1016/j.tsf.2006.12.049.

[4] A. Niemegeers and M. Burgelman, "Numerical modelling of ac-characteristics of CdTe and CIS solar cells," in *Conference Record of the IEEE Photovoltaic Specialists Conference*, 1996, doi: 10.1109/pvsc.1996.564274.

[5] F. Belarbi, W. Rahal, D. Rached, S. benghabrit, and M. Adnane, "A comparative study of different buffer layers for CZTS solar cell using Scaps-1D simulation program," *Optik (Stuttg).*, 2020, doi: 10.1016/j.ijleo.2020.164743.

[6] F. Merad, A. Guen-Bouazza, A.-A. Kanoun, and A. E. Merad, "Optimization of Ultra-Thin CIGS Based Solar Cells by Adding New Absorber Layers: InGaAs and AlGaAs," 2020.

[7] S. T. Hwang *et al.*, "Bandgap grading and Al0.3Ga0.7As heterojunction emitter for highly efficient GaAs-based solar cells," *Sol. Energy Mater. Sol. Cells*, 2016, doi: 10.1016/j.solmat.2016.06.009.

[8] S. Karthick, S. Velumani, and J. Bouclé, "Experimental and SCAPS simulated formamidinium perovskite solar cells: A comparison of device performance," *Sol. Energy*, 2020, doi: 10.1016/j.solener.2020.05.041.

[9] M. Burgelman, J. Verschraegen, S. Degrave, and P. Nollet, “Modeling thin-film PV devices,” *Prog. Photovoltaics Res. Appl.*, 2004, doi: 10.1002/pip.524.

[10] M. Burgelman and S. D. Koen Decock, Alex Niemegeers, Johan Verschraegen, “SCAPS manual.” 2019.

[11] F. Azri, A. Meftah, N. Sengouga, and A. Meftah, "Electron and hole transport layers optimization by numerical simulation of a perovskite solar cell," *Sol. Energy*, 2019, doi: 10.1016/j.solener.2019.02.017.

[12] G. Haidari, "Comparative 1D optoelectrical simulation of the perovskite solar cell," *AIP Adv.*, 2019, doi: 10.1063/1.5110495.

[13] Y. Kuang *et al.*, "Low-Temperature Plasma-Assisted Atomic-Layer-Deposited SnO2 as an Electron Transport Layer in Planar Perovskite Solar Cells," *ACS Appl. Mater. Interfaces*, 2018, doi: 10.1021/acsami.8b09515.

[14] L. Lin, L. Jiang, Y. Qiu, and Y. Yu, "Modeling and analysis of HTM-free perovskite solar cells based on ZnO electron transport layer," *Superlattices Microstruct.*, 2017, doi: 10.1016/j.spmi.2017.02.028.

[15] K. Tan, P. Lin, G. Wang, Y. Liu, Z. Xu, and Y. Lin, "Controllable design of solid-state perovskite solar cells by SCAPS device simulation," *Solid. State. Electron.*, 2016, doi: 10.1016/j.sse.2016.09.012.

[16] Y. Chen, Y. Hu, Q. Meng, H. Yan, W. Shuai, and Z. Zhang, "Natively textured surface of Ga-doped ZnO films electron transporting layer for perovskite solar cells: further performance analysis from device simulation," *J. Mater. Sci. Mater. Electron.*, 2019, doi: 10.1007/s10854-019-00766-7.

[17] S. Tao *et al.*, "Absolute energy level positions in tin- and lead-based halide perovskites," *Nat. Commun.*, 2019, doi: 10.1038/s41467-019-10468-7.

[18] L. C. Chen, Z. L. Tseng, and J. K. Huang, "A study of inverted-type perovskite solar cells with various composition ratios of (FAPBI3)1−x(MAPbBr3)x," *Nanomaterials*, 2016, doi: 10.3390/nano6100183.

[19] S. Prathapani, P. Bhargava, and S. Mallick, "Electronic band structure and carrier concentration of formamidinium-cesium mixed cation lead mixed halide hybrid perovskites," *Appl. Phys. Lett.*, 2018, doi: 10.1063/1.5016829.

[20] F. Ma, J. Li, W. Li, N. Lin, L. Wang, and J. Qiao, "Stable α/δ phase junction of formamidinium lead iodide perovskites for enhanced near-infrared emission," *Chem. Sci.*, 2016, doi: 10.1039/c6sc03542f.

[21] Y. Zhou and G. Long, "Low density of conduction and valence band states contribute to the high open-circuit voltage in perovskite solar cells," *J. Phys. Chem. C*, 2017, doi: 10.1021/acs.jpcc.6b10914.

[22] M. C. Gélvez-Rueda, N. Renaud, and F. C. Grozema, "Temperature Dependent Charge Carrier Dynamics in Formamidinium Lead Iodide Perovskite," *J. Phys. Chem. C*, 2017, doi: 10.1021/acs.jpcc.7b09303.

[23] N. F. Coutinho *et al.*, "The Thermomechanical Properties of Thermally Evaporated Bismuth Triiodide Thin

Films," *Sci. Rep.*, 2019, doi: 10.1038/s41598-019-48194-1.

[24] L. C. Lee, T. N. Huq, J. L. Macmanus-Driscoll, and R. L. Z. Hoye, "Research Update: Bismuth-based perovskite-inspired photovoltaic materials," *APL Materials*. 2018, doi: 10.1063/1.5029484.

[25] R. E. Brandt, V. Stevanović, D. S. Ginley, and T. Buonassisi, "Identifying defect-tolerant semiconductors with high minority-carrier lifetimes: Beyond hybrid lead halide perovskites," *MRS Commun.*, 2015, doi: 10.1557/mrc.2015.26.

[26] H. Han *et al.*, "Defect engineering of BiI3 single crystals: Enhanced electrical and radiation performance for room temperature gamma-ray detection," *J. Phys. Chem. C*, 2014, doi: 10.1021/jp411201k.

[27] M. Shasti and A. Mortezaali, "Numerical Study of Cu2O, SrCu2O2, and CuAlO2 as Hole-Transport Materials for Application in Perovskite Solar Cells," *Phys. Status Solidi Appl. Mater. Sci.*, 2019, doi: 10.1002/pssa.201900337.

[28] S. Abdelaziz, A. Zekry, A. Shaker, and M. Abouelatta, "Investigating the performance of formamidinium tin-based perovskite solar cell by SCAPS device simulation," *Opt. Mater. (Amst).*, 2020, doi: 10.1016/j.optmat.2020.109738.

[29] L. Lin *et al.*, "Simulated development and optimized performance of CsPbI3 based all-inorganic perovskite solar cells," *Sol. Energy*, 2020, doi: 10.1016/j.solener.2020.01.081.

[30] A. B. Coulibaly, S. O. Oyedele, N. R. Kre, and B. Aka, "Comparative Study of Lead-Free Perovskite Solar Cells Using Different Hole Transporter Materials," *Model. Numer. Simul. Mater. Sci.*, 2019, doi: 10.4236/mnsms.2019.94006.

[31] A. Callahan, D. Cote, G. Capobianco, and M. Balicki, "Experimental and Theoretical Optimization of BiI3 Selective-Contact Solar Cell Materials," *Major Qualif. Proj. (All Years)*, Apr. 2018, Accessed: May 11, 2020. [Online]. Available: https://digitalcommons.wpi.edu/mqp-all/324.

[32] K. Chakraborty, M. G. Choudhury, and S. Paul, "Numerical study of Cs2TiX6 (X = Br−, I−, F− and Cl−) based perovskite solar cell using SCAPS-1D device simulation," *Sol. Energy*, 2019, doi: 10.1016/j.solener.2019.11.005.

[33] C. Devi and R. Mehra, "Device simulation of lead-free MASnI3 solar cell with CuSbS2 (copper antimony sulfide)," *J. Mater. Sci.*, 2019, doi: 10.1007/s10853-018-03265-y.

6. CHAPTER VI. Structural and mechanical stability behavior of $FAPbX_3$ perovskites.

6.1. Introduction

Due to the unique properties of $FAPbI_3$ perovskites, it's gained great attention among the researchers compared to all other perovskites (see chapter 1), considering it a favorable candidate for its application as an absorber layer in solar cells. According to the reports, at room temperature, the α- phase (black phase) and β-phase of $FAPbI_3$ adopt the space group P3m1 and P3. On the other hand, the non-perovskite δ-phase shows a hexagonal $P6_3mc$ phase, which is not suitable for photovoltaic applications [1]. Therefore, the structural stability from the α-phase of the $FAPbI_3$ perovskite has turned into an active research topic.

A. A. Zhumekenov et al. [2] synthesized both $FAPbI_3$ & $FAPbBr_3$ single crystals by the inverse temperature crystallization method (ITC). The authors obtained cubic structures for both cases with a space group Pm-3m and lattice parameters equal to a=5.940 Å for $FAPbBr_3$ & a=6.357 Å for $FAPbI_3$. The degradation was tested both at room temperature and at 185^o C for one hour, and the annealed samples had long-term stability (~ 7 days) compared to the former case (~ 7 hours). The authors also showed that lower carrier mobility might be related to the instability of the $FAPbI_3$ perovskites. A recent investigation demonstrated that the materials, architecture, and structure of the perovskite interface might play a crucial role in both degradation rates and durability of the photovoltaic device [3]. A. C. Ferreira et al. [4] investigated the cubic α-$FAPbI_3$ single-crystal by coherent inelastic neutron scattering spectroscopy (INS), Brillouin light scattering (BLS), and low-frequency acoustic phonon measurements, the authors provide the complete set of elastic constant values (EC) at room temperature, mentioning that both the structural stability and the ultra-low thermal conductivity are related to the softness of the FA and MA cations. A negative value in c_{12} is obtained, explaining that in its uniaxial compression along [100], compared to [010] and [001], the structure tries to maintain an anisotropic behavior. Such a value generates a low bulk modulus with the fulfillment of the stability criteria. The authors mainly noticed that the structural instability occurred when the lattice parameters exceed 6.4 Å, decreasing both c_{11} and the bulk modulus magnitudes. Their results concluded that iodide-based materials have the lowest elastic stiffness compared to bromide-based materials.

E. D. Indari et al. computationally studied the electronic structure of $FAPbI_3$ (Pseudo-cubic) and $MAPbI_3$ (tetragonal, Pseudo-cubic) structures without VdW interaction. The results explain that $FAPbI_3$ has a lower DOS than $MAPbI_3$ [5]. S. X. Tao et al. calculated the electronic structure of nine different AMX_3 perovskites structure (Pseudo-cubic, tetragonal, orthorhombic) at room temperature using DFT-1/2 method with and without spin-orbital coupling, and they predict this method provides the accurate bandgap values [6]. D. Li et al. investigated the electronic structures of nine Pseudo-cubic halide perovskites using the first-principles method in order to understand the low loss mechanism of organic-inorganic perovskites. They found the overlap integral charge density of $FAPbI_3$ is less than to the $MAPbI_3$ [7]. First principle calculations by J. F. Wang et al. studied the electrical and optical properties of the $FAPbI_3$ perovskite structure by means of a DFT+vdW [8] scheme. The authors found a lattice parameter equal to a=6.353 Å, with hydrogen bonds in between the NH_2 group and the I atom, as well as the hybridization among Pb(s)-I(p) in the Valence Band Maximum (VBM) as a prominent feature for the stability of the $FAPbI_3$ structure. On the other hand, the three EC of the cubic $FAPbI_3$ (c_{11},c_{12},c_{44}) fulfills the stability conditions [9]. With respect to the organic cation rotation, M.A. Carignano et al. investigated $FAPbI_3$ by means of first-principles molecular dynamics along with group theory, finding that the rotation along the N-N axis of the FA cation is anisotropic at room temperature, and a ΔT activates the C-N bond axis mode, concluding that the instability of the $FAPbI_3$ structure is related with the three M^{+3} modes in collaboration with a rotation of the PbI_6 octahedra and with the effect of the reorientation of the organic FA cation [10]. Meanwhile, S. Kanno et al. theoretically analyzed the energy barriers as well as the potential energy surfaces obtained by the rotation of the organic FA cation inside the cubic cage, finding that the FA cation freely rotates around the N-N bond axis (φ) as compared to the least favorable one defined by the sum of the two vectors of the C-N bond axis (θ). Based on a vdW-DF2 [11] method, the authors calculated a compressed set of $FAPbI_3$ lattice parameters (a=6.50 Å, b=6.48 Å, and c=6.53 Å) compared to the one determined by a plane DFT method (a=6.58 Å, b=6.59 Å, and c=6.60 Å), obtaining a pseudo-cubic structure for both cases. The author reported that the rotational barrier heights (RBH) for both angles (φ & θ) follows the halogen-based order as: I<Br<Cl, concluding that the halogen substitution significantly influences the θ RBH alone, consolidating a way to control the rotation of the FA cation [12].

The following section covers the systematic investigation of the structural and mechanical stability behavior of the $FAPbI_3$ pseudo-cubic unit cell.

6.2. Result and discussion

6.2.1. 12 Possible Orientations of organic Formamidinium cation and its structural analysis using vdW+DFT

In this sub-section, we have performed first-principles calculations based on DFT considering vdW interaction (TS scheme) [8] for pseudocubic $FAPbI_3$ perovskite crystal structures. Specifically, to analyze 12 different possible orientations of the organic FA cation along three different planes: XY, YZ, XZ, and four different cation orientations for each plane (see section 2.3). We systematically investigate the total energy, unit cell volume, lattice parameters, b/a, c/a ratios, and EDD distribution for all the 12 different orientations of the FA cation inside the pseudocubic cage.

Our obtained results show that the organic FA cation and its 12 possible orientations along the XY, YZ, and XZ planes play a crucial role in getting the observed lattice parameters, unit cell volume, and the bandgap at the minimum energy of the system [5]–[7], [12]. Here, we rotate the FA molecule in the clockwise direction inside the cubic cage, such as 12, 03, 06, 09'o clock based on C-H_1 bonding (see section 2.3). The results merely explicit the vdW interactions between the Organic cation placed in the middle of the cubic unit cell in the inorganic framework. The calculated lattice parameters, b/a, and c/a ratios, the displacement of the iodide atoms, EDD, volume, and the energy of the 12 possible orientations are used to characterize the optimized frameworks of the $FAPbI_3$ structure.

Our obtained result shows (shown in **Fig. 6.1**) a negligible level of variations in the energy and in the unit cell volume for all 12 orientations. The equilibrium lattice parameters follow two types of tendencies for all three planes (XY, YZ, XZ). For the XY plane, the FA molecule rotates from 12 to 9'o clock, and we observed the "zig-zag" behavior of "a" and "b" lattice parameters while "c" is uniform. The lattice parameter behavior changes from "c" to "a" and "b" depending on the orientation and the plane of the cation, shown in **Fig. 6.1** and **table 6.1**.

In **Fig. 6.1,** due to the lattice parameters' variation, the b/a, and c/a ratios exhibit, different ratio values for each orientation (based on the plane). Few of the acquired values are nearly close to the perfect-cubic range (b/a=c/a=1), especially in the YZ plane orientation. For the XY and XZ planes seem like the ratios are interchanged. We calculate the iodine atoms' displacement for all the cation orientations from the conventional structure to the optimized pseudocubic position for every direction (**Fig. 6.2**). There is a different shift of the iodine atom for each plane, and the highest one is found in the "z" direction (XY plane). For the XY plane (12'o clock), the bond population of both H$_4$-I$_2$ and H$_5$-I$_2$ has the highest occupancies, an effect that could be associated with the highest iodine movement (shown in **Table. 6.3**).

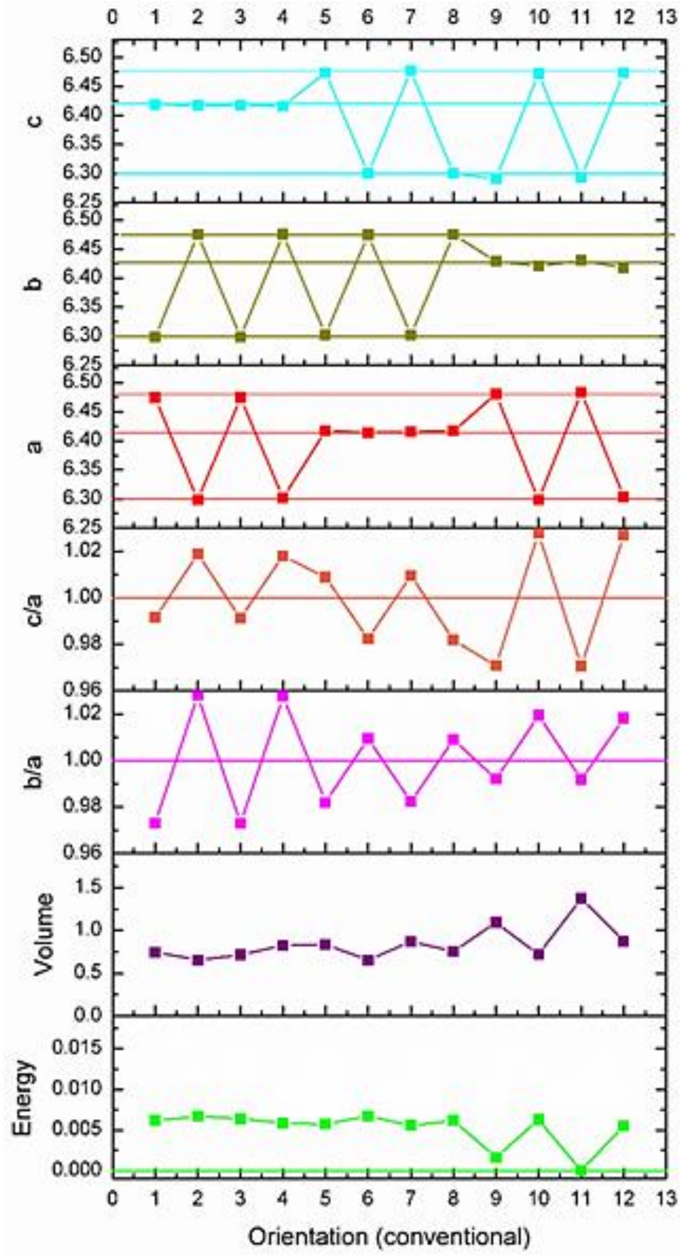

Fig. 6.1. *Results of energy, volume, lattice parameters, b/a, and c/a ratios for all 12 orientations of FAPbI*$_3$*. In this graph, x-axis indicate each orientation like (1, 2, 3, 4 = 12, 03,06, 09'o clock in XY plane) (5, 6, 7, 8=12, 03,06, 09'o clock in YZ plane) (9, 10, 11, 12=12, 03, 06, 09'o clock in XZ plane). For all the orientations, we get the energy range of ~-3380 eV, and we subtract that value for all the 12 orientations in order to compute the values in the same graph. The same procedure followed in the unit cell volume also (~261 - 262 Å*^{3}*), and finally, the lattice parameters are in the range of Å.*

***Table 6.1**. The tendency of lattice parameters.*

Plane	**12 possible Orientations**	**Lattice parameters (Å)**		
		a	***b***	***c***
XY	1 (12’o clock)	6.474018	6.298995	6.418537
	2 (3’o clock)	6.297951	6.474562	6.416806
	3 (6’o clock)	6.474372	6.298912	6.417500
	4 (9'o clock)	6.302035	6.475739	6.415712
YZ	1 (12’o clock)	6.417515	6.302336	6.473847
	2 (3’o clock)	6.414375	6.474191	6.300726
	3 (6’o clock)	6.415587	6.301889	6.477063
	4 (9’o clock)	6.416828	6.474940	6.299993
XZ	1 (12’o clock)	6.480471	6.429008	6.290808
	2 (3’o clock)	6.298303	6.420395	6.472220
	3 (6’o clock)	6.483331	6.430551	6.293202
	4 (9’o clock)	6.303073	6.417920	6.473625

We explored the EDD for all the 12 possible orientations of FA cation. The electron charge density difference is evaluated with respect to the definition of a fragment; in such a set of atoms, the whole cation is contained, as described in Equation 2.48. This equation is useful to define the contribution of charge in between the molecule and the bonding. The iso-surfaces range was determined from the obtained result of Mulliken charge and bond population analysis. The calculated values are -0.0060746 to 0.0230376, and we used the Blue -white- Red color spectrum in-order to differentiate the electron enrichment (red) and the electron diminution (blue) (shown in **Fig. 6.3**).

The EDD results show that compared to the other atoms in the FA molecule, the hydrogen atoms (particularly H_4 and H_5) contribute more electron charge distributions to the iodine atoms and fewer electron distribution to the lead atoms (shown in **Fig. 6.3**). Those observations are complemented by the obtained results of mullikens bond population analysis, especially in H_4-I_2 and H_5-I_2 bonding (shown in **Table 6.3**).

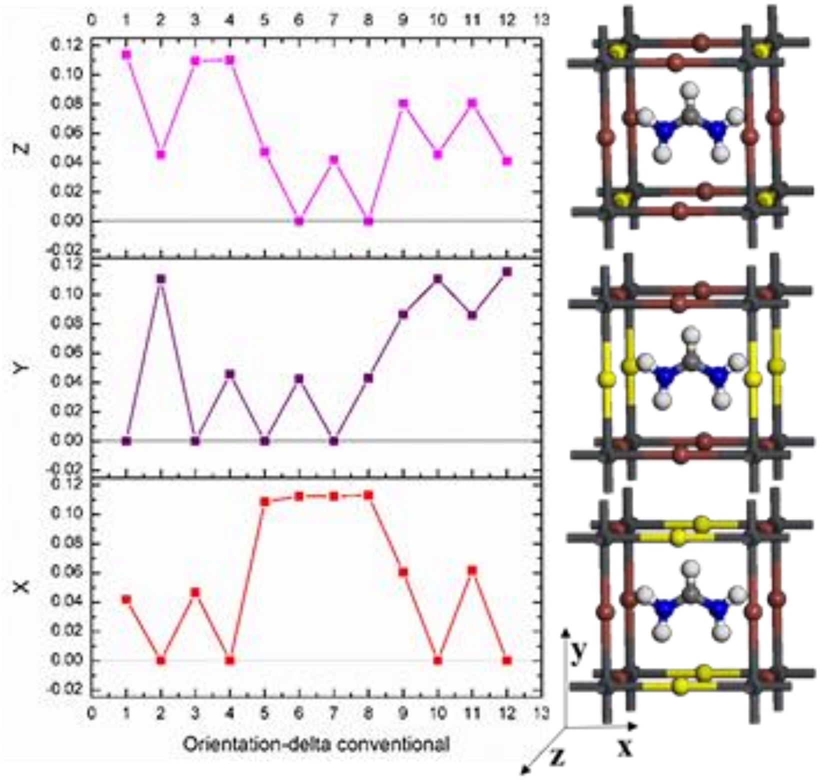

Fig. 6.2. *Calculated delta difference of iodine movement for all the 12 orientations of FA cation. This graph follows the same notation in the x-axis as in* ***Fig. 6.1*** *and the y-axis in the range of Å.*

The EDD results show that the iodide movement (shown in **Fig. 6.3**) and the bending acquired in the Pb-I-Pb bonding angle totally depend on the H_4 and H_5 atoms. For instance, in the XY plane, the conventional structure has Pb-I- Pb=180◦ degree and the optimized pseudocubic structure has 178.519 Å in the "x" direction, 179.999 Å in the "y" direction, and 175.934 Å in the "z" direction due to the considerable electron charge distribution of H_4 and H_5 atoms to the iodine. It is prominent to mention here that the above reason varies the lattice parameters, b/a, and c/a values and iodine displacements. The 12 possible FA cation orientations directly influence the inorganic cubic cage, and it represents the main reason for the stability of the whole perovskite structure [12].

The EDD for the XY plane for FA cation orientation (12'o clock) is shown in **Fig. 6.3**. Here, we slice the FA cation in a different direction, and it shows the electron density distribution for the total system. The other atoms contribute less to the EDD compared to the Hydrogen atoms (especially H_4 and H_5) due to the stronger charge population of both H_4-I_2 and H_5-I_2. The shorter distance between those bonding compared to H_2-I_2 and H_3-I_2 bonding is influenced by the charge distribution between hydrogen and iodine, the iodine movement, and the reducing Pb-I-Pb angle, which affect the regularity.

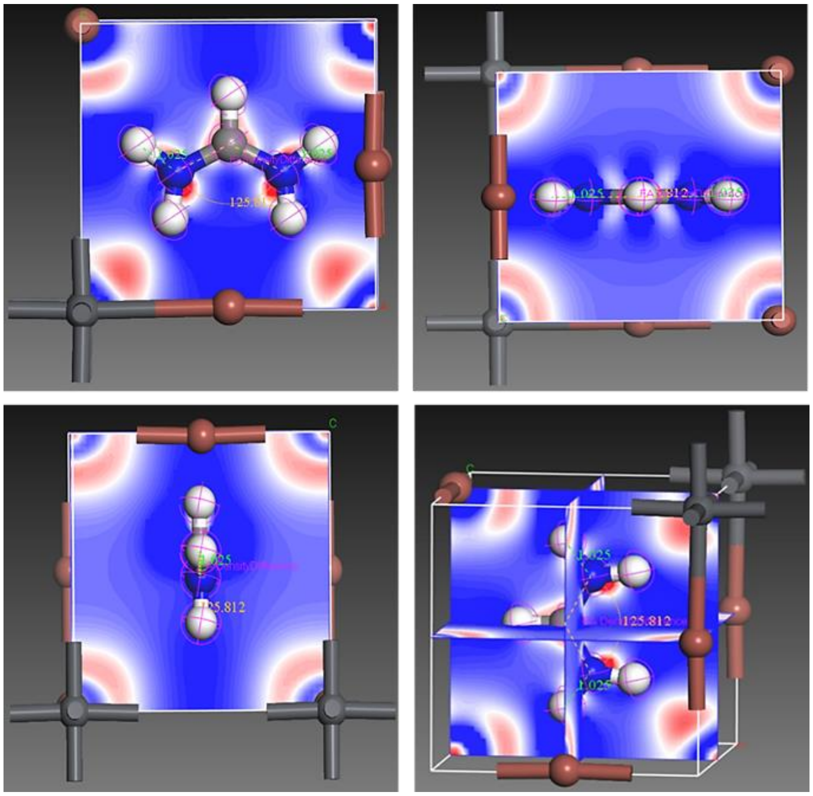

Fig. 6.3. *The calculated electron density difference for XY plane 12'o clock FA cation orientation.*

Table 6.2. *Atomic populations (Mullikens)*

species	**Ions**	**s**	**p**	**d**	**f**	**total**	**Charge (e)**
H	1	0.74	0.00	0.00	0.00	0.740	0.26
H	2	0.63	0.00	0.00	0.00	0.630	0.37
H	3	0.63	0.00	0.00	0.00	0.630	0.37
H	4	0.64	0.00	0.00	0.00	0.640	0.36
H	5	0.64	0.00	0.00	0.00	0.640	0.36
C	1	1.07	2.78	0.00	0.00	3.850	0.15
N	1	1.49	4.20	0.00	0.00	5.690	-0.69
N	2	1.49	4.20	0.00	0.00	5.690	-0.69
I	1	2.04	5.45	0.00	0.00	7.490	-0.49
I	2	1.90	5.47	0.00	0.00	7.380	-0.38

I	3	2.03	5.47	0.00	0.00	7.500	-0.50
Pb	1	1.54	1.58	10.0	0.00	13.12	0.88

***Table 6.3**. Bond populations (Mullikens).*

Bond	**Population (e)**	**Length (Å)**
H_2-N_1	0.77	1.02475
H_3-N_2	0.77	1.02478
H_4-N_1	0.76	1.02894
H_5-N_2	0.76	1.02895
H_1-C_1	0.94	1.09107
C_1-N_2	1.01	1.31466
C_1-N_1	1.01	1.31471
H_2-H_4	-0.08	1.75561
H_3-H_5	-0.08	1.75563
H_3-C_1	-0.15	2.00851
H_2-C_1	-0.15	2.00853
H_1-N_2	-0.12	2.05593
H_1-N_1	-0.12	2.05596
H_5-C_1	-0.13	2.08056
H_4-C_1	-0.13	2.08058
H_1-H_3	-0.04	2.29062
H_1-H_2	-0.04	2.29063
N_1-N_2	-0.20	2.34012
H_2-H_3	-0.01	2.45702
H_4-H_5	0.01	2.61267
H_4-N_2	-0.02	2.67818
H_5-N_1	-0.02	2.67820
H_4-I_2	-0.12	2.82312
H_5-I_2	-0.12	2.82313

H_2-I_2	-0.03	2.90293
H_3-I_2	-0.03	2.90294

6.2.2. Stability threshold of $FAPbI_3$ determined by strain amplitudes

In this sub-section, the mechanical stability study from the pseudo-cubic unit cell of the pristine formamidinium lead iodide perovskite was systematically investigated and presented by means of a finite deformation method solved by density functional theory calculations. It is shown for the first time that the stability conditions from this orthorhombic model were fulfilled uniquely whether the boundary of deformation, known as strain amplitude, was kept below 0.02 for the nine strain tensors. Furthermore, it is evidently identified a direct correlation in the material's elastic response with respect to the main charge distribution, found in between the cation terminations and the halogens lattice, a fact that is thoroughly validated in a set of twelve FA cation orientations provided by its space group. The mechanical instability is finally found for a strain amplitude equal to 0.04. Specifically for two-dimensional deformations that alter the interactions among the hydrogen-nitrogen terminations and the iodine positions. In addition to this prominent result, it was seen that the atomic relaxation, at this level of strain, collectively drives the whole organic cation outside its initial position into a tilted orientation that follows a charge rearrangement. The present contribution provides novel descriptions aiming to tackle the instability related to the degradation process from the alpha perovskite phase. This report evidently explains pristine $FAPbI_3$ perovskites' instability issue based on their elastic-constant results correlated with their electron density difference and Mulliken charge values (both bond population and bond length).

The previous section explains the structural analysis of $FAPbI_3$ perovskite showed the equilibrium lattice parameters follow two tendencies as a function of the FA cation's clockwise rotation. For the first case, the length of the lattice parameter that is parallel to the N-N axis is larger, and the one perpendicular diminishes its length, becoming the most compact. This geometrical relaxation occurred only to the lattice parameters extended along the FA cation plane. For the second case, the direction that is perpendicular to the planar cation does not show any variations during the cell optimization, consolidating a uniform behavior. Despite these results, both b/a and c/a ratios acquire close values with respect to the cubic symmetry (b/a=0.973,c/a=0.991), in agreement with early cited pseudo-cubic results [12]. The strongest modification in the inorganic sub-cell was observed in the iodine positions, measured with the aid of the Pb-I-Pb angle, in which the iodine tends to reduce the distance to the N-H terminations at the ground state. Finally, the EDD exhibits a stronger electronic density distribution among the H_4 and H_5 hydrogen and the I_2 atoms (see **Fig. 6.4**), meanwhile, a weaker distribution of charge is found in between the lead atoms and the FA cation. Hence in the present work, we report the evaluation of the structural stability from the pseudo-cubic $FAPbI_3$ perovskites, as generated by the Pm-3m space group, by means of the EC $\{c_{ij}\}$ set calculation. The results show that a specific strain above a critical deformation could turn the structure unstable, followed by a FA cation tilting along with disproportionation of bonds, hence, defining a possible structural indicator to track the stability of pure $FAPbI_3$.

As shown in **Fig. 6.4**, it is possible to separate the strain tensors for an orthorhombic structure into two categories. The first three applied strains (D_1, D_2, D_3) are called uniaxial since the deformations act along any of the coordinate axis D_1 for the x-axis [100], D_2 for the y-axis [010], and D_3 for the z-axis [001]. Meanwhile, the remaining set of strains (D_4, D_5, D_6, D_7, D_8, D_9) are referred to as planar since two different lattice deformations consolidate a modified crystalline plane in the following manner: D_4 and D_9 for YZ plane (100), D_5 and D_8 for XZ plane (010) and finally D_6 and D_7 for XY planes (001).

For the set of uniaxial deformations, whether the normal vector of the cation plane appears to be parallel to the applied strain, it will be defined as regular behavior ($\delta_{regular}$). Meanwhile, when the deformation is applied in a perpendicular direction with respect to the organic cation plane, two different tendencies are seen. In one of them, the strain will be parallel to the N-N axis of the FA cation ($\delta_{\parallel}$), and for the second one, the strain tensor modifies the lattice parameters perpendicular to the former axis ($\delta_{\perp}$). For the set of planar deformations, if the applied strain acts on the same plane of the FA cation, it is called regular ($\delta_{regular}$), meanwhile, if any of the applied deformation components are parallel to the N-N axis, they are denoted as $\delta_{\parallel}$, for the immediate next case, if one of the strain components appears to be perpendicular to N-N it will be designated as $\delta_{\perp}$.

The uniaxial-$\delta_{regular}$ behavior is obtained for the following combinations of strain paths and FA planes: D_1 [YZ], D_2 [XZ], and D_3 [XY]. On the other hand, the planar-$\delta_{regular}$ behavior is shown for: D_4 [YZ], D_5 in [XZ], D_6 [XY], and D_7 [XY], D_8 [XZ] and D_9 [YZ]. For all the cases, both ΔEi vs. δi plots and their corresponding EC values are independent with respect to the FA clockwise orientation.

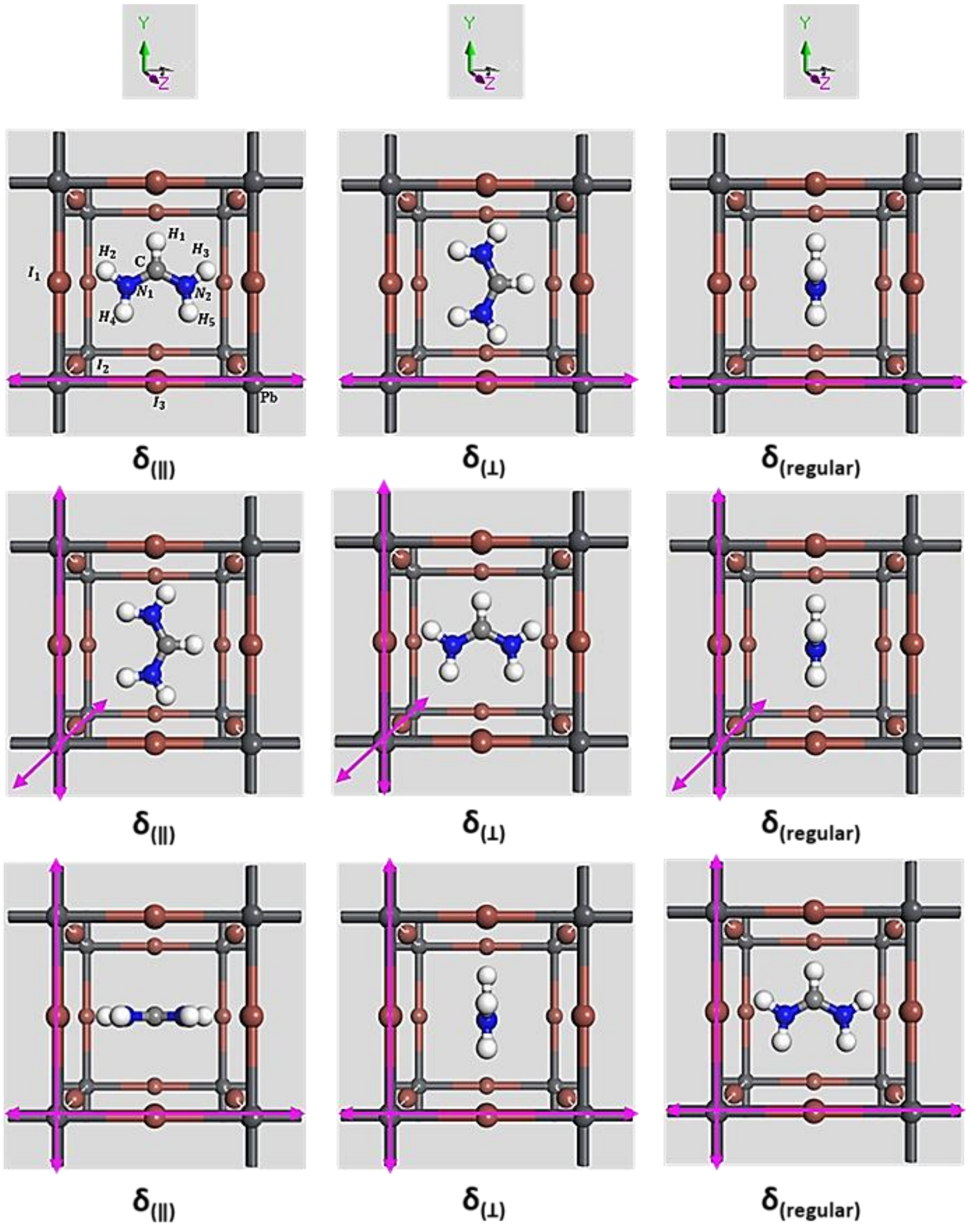

Fig. 6.4. *General representation of the orthorhombic strain tensors. The top three show the uniaxial (from left to right: D_1, D_2, D_3) and planar (middle from left to right: D_4, D_5, D_6) bottom from left to right: D_7, D_8, D_9). The top three figures indicate uniaxial-$\delta_{\|}$, uniaxial-$\delta_{\perp}$, uniaxial-$\delta_{regular}$, from left to right, respectively. Both the middle and bottom rows of the Figure are referred to as planar-$\delta_{\|}$, planar-$\delta_{\perp}$, planar-$\delta_{regular}$ deformations, respectively.*

The respective planes and orientations of the FA cation within the inorganic cage for the uniaxial-$\delta_{\parallel}$ cases were obtained for: D_1 [XY 12:00], D_2 [YZ 03:00], and D_3 [XZ 03:00]. Meanwhile, the planar-$\delta_{\parallel}$ elastic responses were seen for: D_4 [XY 03:00], D_5 [XY 12:00], D_6 [YZ 03:00], D_7 [XZ 12:00], D_8 [YZ 12:00] and D_9 [XZ 03:00]. Finally, the uniaxial-$\delta_{\perp}$ mode occurred for: D_1 in [XY 03:00], D_2 in [YZ 12:00] and D_3 in [XZ 12:00]. With planar-$\delta_{\perp}$ obtained for: D_4 [XY 12:00], D_5 [XY 03:00], D_6 [YZ 12:00], D_7 [XZ 03:00], D_8 [YZ 03:00] and D_9 [XZ 12:00], following the notation [plane, orientation].

6.2.2.1. Strain amplitude equal to 0.02

The Mulliken charge population analysis for the uniaxial-$\delta_{regular}$ at $\delta i=-\delta_{max}$ shows a high bond population in the order of -0.11 e, with a bond length around 2.83 Å, both values found among H_5-I_2 & H_4-I_2 bonds. Meanwhile, a much smaller population is obtained in between H_3-I_2 & H_2-I_2 bonds (-0.04 e & 2.90 Å), which is similar to the charge distribution found at the $FAPbI_3$ ground state [14]. At the opposite strain boundary $\delta i=\delta_{max}$, the MC bond population shows similar results as the former case (-0.11 e for both H_5-I_2 & H_4-I_2 and -0.02 e for both H_3-I_2 & H_2-I_2), however, a slight exchange in the bond length is observed, since the values are now distributed as: 2.87 Å and 2.84 Å, for both H_5-I_2 & H_4-I_2 and H_3-I_2 & H_2-I_2, respectively. Considering the MC of the rest of the deformation steps from all the uniaxial-$\delta_{regular}$ results, it is possible to generalize that the H_4, H_5 atoms share a stronger charge distribution in between those halogens situated along a lattice axis perpendicular to the plane of the cation, in comparison with the remaining N-H terminations, i.e., the H_2, H_3 atoms. Even more, for all these three cases, the applied strain tensors (D_1, D_2, D_3) act along a crystalline direction that does not affect the cation plane, consolidating a uniform elastic behavior, as in the following discussion. At the strain state boundary ($\delta i=\pm\delta max$) from both $\delta\parallel$ and $\delta\perp$ uniaxial cases, the MC analysis shows a different scenario, since the only significant charge distribution occurs just in between H_4-I_2 & H_5-I_2. For all FA planes, the uniaxial-$\delta\parallel$ case shows that the bond population is around -0.10 e with an increased bond length of 2.95 Å. Compared to a slightly lower set of results for the uniaxial-$\delta\perp$ case (-0.09 e and 2.94 Å), however, both H_2 and H_3 atoms do not have any bond charge contribution in between either of the iodine atoms, which may be explained due to the presence of a modified distance, as complemented by the EDD analysis (see **Fig. 6.5**).

Regarding the ΔEi vs. δi plots, it is clear that there is a strong difference between each strain schemes, the set of uniaxial strains (see **Fig. 6.6** (a) to (c)) show that it is actually possible to achieve lower energy states as δ_i tends to the positive strain boundary (δmax), i.e., a possible minimum energy without the geometry from the unstrained state. For each uniaxial-δregular, uniaxial-δ‖ and uniaxial-δ⊥ plots, the minimum energy occurs approximately at: $\delta regular^{min}=0.015$, $\delta\|^{min}=0.019$ and $\delta\perp^{min}=0.009$, respectively, generating the following b/a and c/a lattice ratios: 0.967 & 0.993, 1.028 & 0.982 and 1.078 & 1.008, respectively, which may stay within the agreement of a pseudo-cubic structure (ground state ratios b/a=0.982, c/a=1.008). The uniaxial EC values (c_{11}, c_{22}, c_{33}) exhibit in general three different tendencies as a function of the FA orientation (see **Fig. 6.6 (d)** to (f)). The higher uniaxial c_{ii} value (approximately 48 GPa) is always generated when a perpendicular strain with respect to the FA N-N axis is applied, i.e., a uniaxial-δ⊥, since for all the latter cases, the strain path tends to alter the main electronic distribution among the FA cation and the inorganic sub-lattice (H_4-I_2 & H_5-I_2). The second case appears around 8 GPa below, and such intermediate EC values are likewise a result of a certain combination of both strains and FA orientations that modify the structure in a parallel direction to the N-N axis (uniaxial-δ‖), which is related to the spatial deformation of the charge distribution among the N-H termination from the FA cation and the halogens. On the other hand, it is found that the lowest elastic stiffness response from the three uniaxial deformations is generated by the δregular case, with a value around 32 GPa, consistently with a deformation that yields the material with relative ease, since the FA cation plane is not modified.

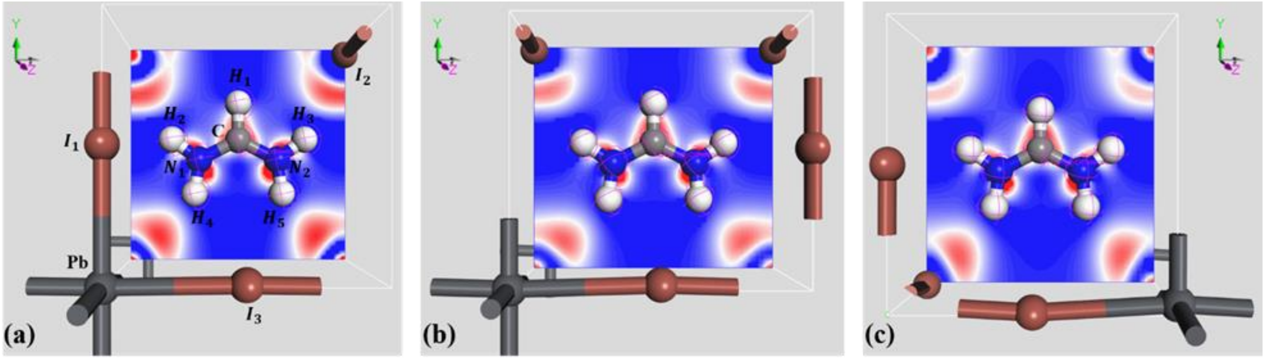

Fig. 6.5. *Electron Density Difference (EDD) of a strained lattice generated at the boundary of a uniaxial deformation (uniaxial-δregular, uniaxial-δ‖, and uniaxial-δ⊥, from left to right). Blue-White-Red spectrum displays the electron lack to enrichment, showing a marked diminish of the charge distribution among* H_3-I_2 *&* H_2-I_2*, for both uniaxial-δ‖ and uniaxial-δ⊥, with respect to the uniaxial-δregular.*

The EC values determined from the set of planar deformations: D_4 to D_6, are generated out of symmetrical ΔEi vs. δi plots around the unstrained state (see **Fig. 6.7** (a) to (c)), i.e., with no energy value exceeding the ground state. In the current description, it is possible to separate them into three different elastic stiffness responses. The EC values that appear to have an independent behavior as a function of the cation orientation (planar-δregular) possess now the highest magnitude, with a value approximately equal to 1.7 GPa, this upper limit is a result of both strain tensors components applied over the FA plane, i.e., the structure is modified with a fraction of planar-δ‖ and planar-δ⊥ simultaneously. As for the case of the uniaxial elastic response, this higher value is related to a direct modification of the charge distribution among all hydrogen terminations and perpendicular halogens to the FA cation plane. Estimated unbalance population and bond length values were -0.11 e, 2.91139 Å; -0.12 e, 2.73227 Å; -0.03 e, 2.83458 Å, and -0.03 e, 2.97583 Å, for H_4-I_2, H_5-I_2, H_2-I_2, and H_3-I_2, respectively (also further discussed in **Table 6.7**). Approximately 0.4 GPa and 0.7 GPa below, appear both planar-δ‖ and planar-δ⊥, for the intermediate and lowest limit, respectively (**Fig. 6.7** (d) to (f)).

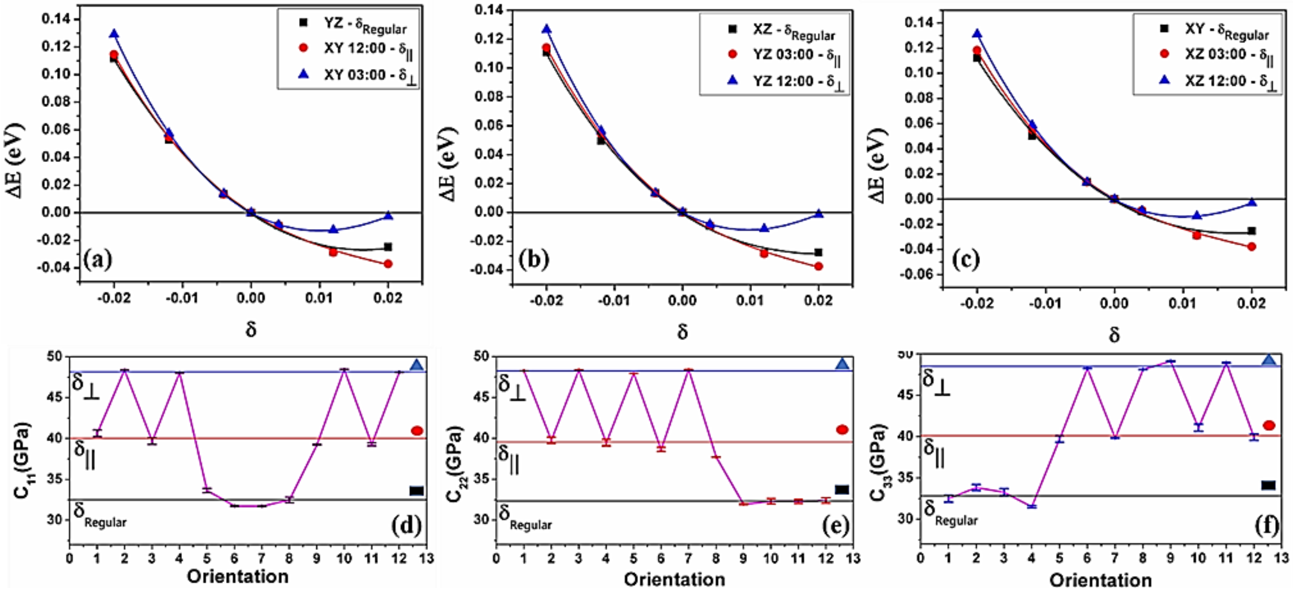

Fig. 6.6. *The figures displayed from (a) to (c) show the ΔEi vs. δi plots along with their respective EC values, from (d) to (f), determined within the strain amplitude δmax<0.02. The associated* c_{11}*,* c_{22}*, and* c_{33} *values show a fluctuating behavior, among three possible elastic responses, as a result of a combination of the FA orientation and the uniaxial deformation case (uniaxial-δregular, uniaxial-δ‖, and uniaxial-δ⊥). The first four points of the orientation-axis displayed from (d) to (f)) correspond to the [XY] FA plane alignment, meanwhile, the remaining two sets of four points hold for both [YZ] and [XZ] FA planes, respectively, all of them following the order: 12:00 to 9:00, in clockwise FA alignments. The calculated uncertainty from*

every c_{ii} value is depicted by error bars centered at each point, and the shape symbol of the possible results correspond to the respective ΔEi vs. δi plots from which it's determined.

For the remaining EC set of values (c_{12}, c_{13}, c_{23}) calculated by means of planar deformations (**Fig. 6.8** (a) to (c)), it is not possible to directly correlate their magnitudes with the orientation of the FA cation, since the second-order coefficient is linearly combined with another two uniaxial EC constants, as shown in the equations 2.33 to 2.35. Therefore, it is expected that the result will be related with the behavior obtained for their respective uniaxial c_{ii} components. For instance, the planar-δregular is now found for orientations over the FA plane that show a combination of either uniaxial-δ⊥ or uniaxial-δ‖ c_{ii} magnitudes, as for the values of c_{12} over the [XY] plane, since neither c_{11} or c_{22} possess a regular behavior, which is an equivalent case observed over both [XZ] and [YZ] planes for c_{13} and c_{23} EC values, respectively.

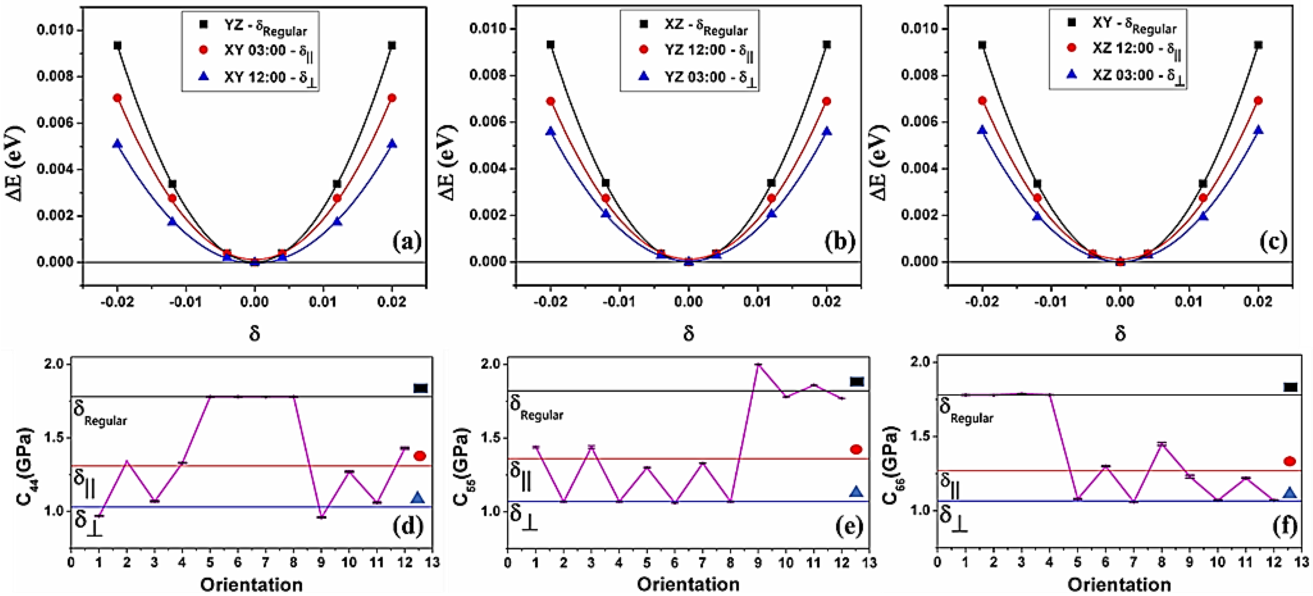

Fig. 6.7. *(a) to (c) show the ΔEi vs. δi plots along with their respective EC values, from (d) to (f), determined within the strain amplitude δmax<0.02. The associated c_{44}, c_{55}, and c_{66} values show a fluctuating behavior, among three possible elastic responses, as a result of a combination of the FA orientation and the planar deformation case (planar-δregular, planar-δ//, planar-δ⊥). The first four points of the orientation-axis (displayed from (d) to (f)) correspond to the [XY] FA plane alignment, meanwhile, the remaining two sets of four points hold for both [YZ] and [XZ] FA planes, respectively, all of them following the order: 12:00 to 9:00, in clockwise FA alignments. The calculated uncertainty from every cii value is depicted by error bars centered at each point, and the shape symbol of the possible results correspond to the respective ΔEi vs. δi plots from which it's determined.*

The latter effect may arise due to a certain compensation among the strain components, that finally generates a non-varying elastic stiffness response in the planar c_{ij} values (8 GPa for both c_{12} and

c_{23} and to 12 GPa for c_{13}), shown in **Fig. 6.8** (d) to (f). For the rest of the cases, it is possible to recognize that only one of the uniaxial components from the linear combination needs to possess a δregular behavior so that the planar c_{ij} magnitude could show variations following the change in the FA cation orientation. The numerical EC values show that both uniaxial-δregular and planar-δregular behaviors are attained at: c_{33}, c_{66}, and c_{12}, each of them with averages around 32.77, 1.78, and 8.09 GPa, for the [XY] FA cation plane, respectively. On the other hand, for non-regular cases, there is an equivalence in the elastic response in between the FA clockwise orientation at 12:00 and 06:00, which is also present at 03:00 and 09:00, for all c_ij values, as it was discussed for the optimized lattice parameters (Table 1, [14]). It is prominent to mention that all deformations below an amplitude equal to 0.02 generate positive elastic constants fulfilling orthorhombic structures' stability criteria (**Table 6.4**).

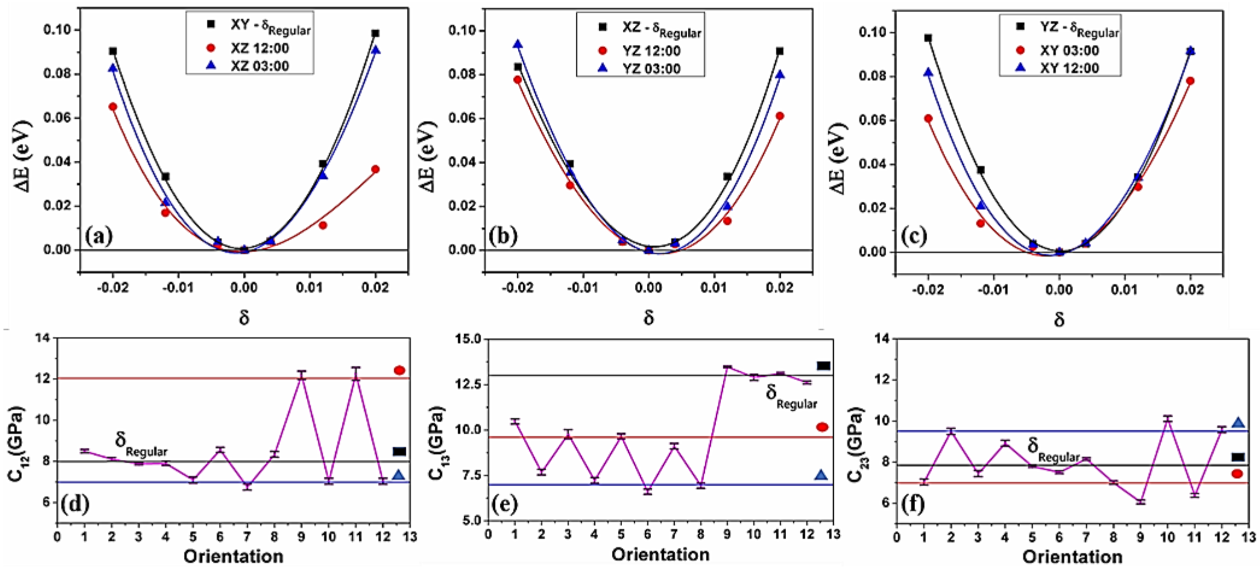

Fig. 6.8. The figures displayed from (a) to (c) show the ΔEi vs. δi plots along with their respective EC values, from (d) to (f), determined within the strain amplitude δmax<0.02. The associated c_{12}, c_{13}, and c_{23} values show a fluctuating behavior, among three possible elastic responses, as a result of a combination of the FA orientation and the planar deformation case (planar-δregular, planar-δ∥, planar-δ⊥). The first four points of the orientation-axis displayed from (d) to (f)) correspond to the [XY] FA plane alignment, meanwhile, the remaining two sets of four points hold for both [YZ] and [XZ] FA planes, respectively, all of them following the order: 12:00 to 9:00, in clockwise FA alignments. The calculated uncertainty from every c_ii value is depicted by error bars centered at each point, and the shape symbol of the possible results correspond to the respective ΔEi vs. δi plots from which it's determined.

Table 6.4. *Orthorhombic EC values calculated for the clockwise configurations of the [XY] FA cation structure, including the propagated uncertainty. The present δmax<0.02 results are in good agreement with pseudo-cubic EC values determined by first-principles calculations, based on DFT+vdW-DF2* [15],

and two sets of cubic EC values experimentally measured by INS [4] *and a theoretically determined by a DFT+vdW-TS scheme* [9].

[XY]	**c_{11}[Gpa]**	**c_{22}[Gpa]**	**c_{33}[Gpa]**	**c_{44}[Gpa]**	**c_{55}[Gpa]**	**c_{66}[Gpa]**	**c_{12}[Gpa]**	**c_{13}[Gpa]**	**c_{23}[Gpa]**
12:00	40.63±0.4	48.26±0.0	32.48±0.4	0.97±0.0	1.44±0.0	1.78±0.0	8.49±0.2	10.48±0.5	07.03±0.1
03:00	48.38±0.0	39.76±0.3	33.83±0.3	1.34±0.0	1.07±0.0	1.78±0.0	8.11±0.2	07.68±0.2	10.05±0.1
06:00	39.68±0.4	48.35±0.0	33.27±0.4	1.07±0.0	1.44±0.0	1.79±0.0	7.89±0.2	09.77±0.3	07.44±0.1
09:00	48.01±0.0	39.46±0.4	31.52±0.1	1.33±0.0	1.07±0.0	1.78±0.0	7.90±0.2	06.47±0.1	08.92±0.1
Ref [15]	30.15	31.0	29.85	2.03	5.33	2.60	2.99	7.22	4.26
Ref [4]	11.20 ±2.0			2.70±0.3			-5.50±2.2		
Ref [9]	20.50			12.30			4.80		

The difference in between the set of conditions that determine the stability of two crystal symmetries, i.e., cubic and orthorhombic, turns the comparison of their own EC values nontrivial. On the one hand, both the uniaxial c_{ii} set and the planar c_{12} are found to be overestimated with respect to the previous results [4]. As shown in equations 2.5 to 2.13, none of the strain tensors used for an orthorhombic structure follow both the isotropic deformation and the tetragonal (or the equivalent orthorhombic) strain tensor used to determine both c_{11} and c_{12} in cubic structures. On the other hand, despite the fact that the set of strain deformations used to obtained c_{44}, c_{55}, and c_{66}, c_{44}, possess a marked resemblance to the symmetric monoclinic tensor, used to determine c_{44} for cubic symmetries [16], the c_{44}, c_{55}, and c_{66} results are underestimated with respect to both the experimentally measured and the calculated cubic EC values, therefore, a direct comparison of the elastic properties among cubic and pseudo-cubic crystalline models is outside the scope of the present paper.

As for the latter case, both bulk (B) and shear (G) moduli, calculated by the Hill-Reuss-Voigt equations [17], possess variations with respect to the cubic-symmetry results (**Table 6.5**). On the one hand, the low B value found experimentally for $FAPbI_3$ (from 0.00 to 2.24 GPa) is a consequence of a negative c_{12} [4], which is not seen in the current result (**Table 6.4**), however, this could be a shred of evidence related to a threshold towards the structural instability, since the cubic second criteria ($c_{11}+2c_{12}>0$) will be equal to 0.1 > 0.0, and as the following discussion shows, the negative EC values are in here found for planar c_{ii} cases. Even though a good agreement could be found among the calculated cubic $FAPbI_3$ bulk modulus [9], [15] and the [XY 12:00] ground state, with a latter value equal to 11.79 GPa, obtained following the current calculation scheme, fitting the equation of state to a set of isotropic deformations [16]. Finally, the shear modulus G considered for δ_max<0.02 show closer values since the Hill- Reuss-Voigt G equations include all planar cii, supporting the accuracy of the present set of models (**Table 6.5**).

Table 6.5. *Calculated Bulk (B) and Shear (G) moduli determined by the Hill-Reuss-Voigt equations, including the propagated uncertainty from the set of c_ij values. For all clockwise orientations of [XY] FA configurations with δmax<0.02. The provided comparison is against experimental* [4] *and ab initio DFT+vdW-TS* [9] *as well as DFT-vdW-DF2* [15] *results.*

	B [Gpa]	**G [Gpa]**
[XY]12:00	10.26±0.172	4.90±0.009
[XY]03:00	10.28±0.124	4.90±0.009
[XY]06:00	10.15±0.147	4.95±0.002
[XY]09:00	09.77±0.101	5.02±0.000
Ref [15]	13.25	5.59
Ref [4]	00.00±2.240	8.35±0.100
Ref [9]	15.3	3.6

6.2.2.2. Strain amplitude equal to 0.04

If the strain amplitude δmax is increased beyond 0.02, it is found that the elastic components: c_{44}, c_{55}, and c_{66} tend to become a negative value (**Table 6.6**), making the structure unstable. In specific, FA configurations that involved planar-δ‖ strains tend to fail the accomplishment of the third, fourth, or fifth orthorhombic stability conditions, respectively (equation 2.24). This result is generated by the ΔEi vs. δi negative curvatures, reaching strained structures that appear below the ground state energy at δ_max=0.04 (**Fig. 6.9** (b)), along with a significant change in the SE up to a ± 0.3 GPa, for all the negative cases. However, it does not represent a strong change in the dispersion of points as compared to the negative cases (SE = ± 2.0 GPa), previously reported [4]. Although the later observation significantly modifies the dispersion generating nonnegligible mismatches during the fitting procedure, this does not change the nonfulfillment of the stability criteria, specifically for c_{44}, c_{55}, and c_{66} (equation 2.24), due to the appearance of negative deformation energy values. For both planar-δ⊥ and planar-δregular cases, no changes in their curvature's signs were seen at δmax=0.04, however, the point dispersion of the strained states also shows an increased difference associated with each planar c_{ii} value up to $\pm 1\times10^{-2}$ Gpa.

As it was discussed, the MC analysis of the strains below 0.02 shows that the chemical bonds among H_4, H_5 and H_2, H_3 and the iodine atom have both similar distances and populations, except for the planar-δregular case (**Table 6.7**), which means that the system shares in a balanced way the charge distribution among the FA cation and the inorganic unit cell. However, at the extended boundary δmax>0.02 under planar-δ⊥ strains, the lowest obtained EC values (c_{44}) show an increased distance in between Hi-I_2 (where i=4,5) atoms, meanwhile, the Hi-I_2 (where i=2,3) length decreases, along with a slight reduction of the bond populations. Under the same strain conditions, the bonding distribution of c_{55} (planar-δ∥) mainly changes from H_2-I_2 & H_3-I_2 to H_2-I_1 & H_3-I_1, i.e., the smallest bond population exchanges the iodine position, this relevant charge transfer happens in an unbalanced manner, since only the H_2-I_1 bond populations seem to reach the Hi-I_2 (where i=4,5) distribution, meanwhile the main charge distribution among halogens and hydrogen distributions increase its bond length with a reduced population (**Table 6.7**). This latter effect follows the strong reduction in the total energy value, which is even more significant than the unstrained energy state, and since the charge transfer is in between two different halogen sites, it implies a tilting of the FA cation outside its initial plane, i.e., around the C-H axis (see **Fig. 6.10** (d)). The obtained MC analysis of the elastic module c_{66}, planar-δregular displays the most prominent bonding population among H_5-I_2 & H_3-I_2, since the only chemical bond occurred this time for the same iodine atom only exchanging the hydrogen termination, therefore, the expected modification in the FA position corresponds this time to a rotation around its plane once the internal coordinates are relaxed.

Table 6.6. *Elastic components values of c_{44}, c_{55}, and c_{66} for all clockwise rotations of the [XY] FA configuration, the values are calculated with six deformations steps under the two tested strain amplitudes: δmax=0.02 and δmax=0.04, with its corresponding standard error.*

	δ	c_{44}[Gpa]	c_{55}[Gpa]	c_{66}[Gpa]
[XY] **12:00**	$\delta_{max} = 0.02$	00.97±0.001	01.44±0.006	01.78±0.001
	$\delta_{max} = 0.04$	01.45±0.034	-20.60±0.402	00.50±0.084
[XY] **03:00**	$\delta_{max} = 0.02$	01.34±0.000	01.07±0.003	01.78±0.000
	$\delta_{max} = 0.04$	-21.45±0.341	01.41±0.034	00.92±0.079
[XY] **06:00**	$\delta_{max} = 0.02$	01.07±0.003	01.44±0.009	01.79±0.002
	$\delta_{max} = 0.04$	01.47±0.0345	-21.30±0.337	01.88±0.067

[XY]	$\delta_{max} = 0.02$	01.33±0.002	01.07±0.003	01.78±0.000
09:00	$\delta_{max} = 0.04$	-22.32±0.352	01.45±0.034	01.43±0.035

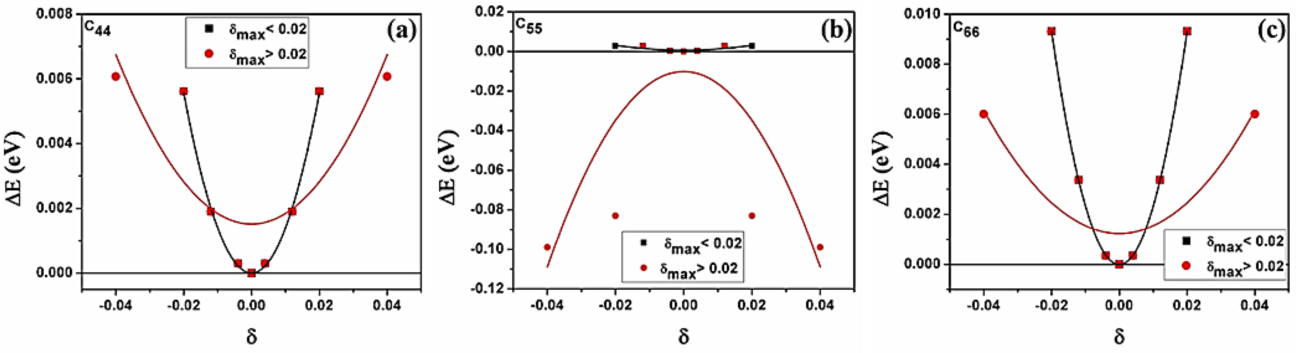

***Fig. 6.9**. Deformation energies obtained for the strain tensors: D_4, D_5, and D_6 (from left to right) applied to the ground state of the [XY] FA 12 o'clock, under the strain amplitude δmax=0.04. The planar-δ∥ strain shows only energy points below the ground state maximum, generating a negative c_{55} value at the strain amplitudes.*

***Table 6.7** The MC analysis at the strained boundaries of the elastic components c_{44}, c_{55}, and c_{66} of the structure [XY] 12'o clock. Both bond population and bond length values at the unstrained are: -0.12 e, 2.82312 Å; -0.12 e, 2.82313 Å;-0.03 e, 2.90293 Å, and -0.03 e, 2.90294 Å, for H_4-I_2, H_5-I_2, H_2-I_2, and H_3-I_2, respectively.*

[XY] 12:00	$\boldsymbol{\delta_{max}} = 0.02$			$\boldsymbol{\delta_{max}} = 0.04$		
	Bond	**Population (e)**	**Length (Å)**	**Bond**	**Population (e)**	**Length (Å)**
$\boldsymbol{C}_{44}$	$H_4 - I_2$	-0.12	2.82329	$H_4 - I_2$	-0.11	2.87344
	$H_5 - I_2$	-0.12	2.82329	$H_5 - I_2$	-0.11	2.89060
	$H_2 - I_2$	-0.03	2.90345	$H_2 - I_2$	-0.02	2.83386
	$H_3 - I_2$	-0.03	2.90250	$H_3 - I_2$	-0.02	2.84344
$\boldsymbol{C}_{55}$	$H_4 - I_2$	-0.12	2.82322	$H_4 - I_2$	-0.09	2.96504
	$H_5 - I_2$	-0.12	2.82322	$H_5 - I_2$	-0.09	2.95160
	$H_2 - I_2$	-0.03	2.90297	$H_2 - I_2$	-	-
	$H_3 - I_2$	-0.03	2.90298	$H_3 - I_2$	-	-
	$H_2 - I_1$	-	-	$H_2 - I_1$	-0.08	2.85976

	$H_3 - I_1$	-	-	$H_3 - I_1$	-0.08	2.85472
$\boldsymbol{C}_{66}$	$H_4 - I_2$	-0.11	2.91139	$H_4 - I_2$	-	-
	$H_5 - I_2$	-0.12	2.73227	$H_5 - I_2$	-0.10	2.74996
	$H_2 - I_2$	-0.03	2.83458	$H_2 - I_2$	-	-
	$H_3 - I_2$	-0.03	2.97583	$H_3 - I_2$	-0.05	2.65178

The EDD plots show the spatial charge distribution as an iso-surface generated from the MC population analysis, where the Blue-White-Red spectrum identifies the areas from electronic lack to enrichment (**Fig. 6.10**). As it was discussed, the unstrained state possesses the most relevant charge distribution located among H_4-I_2 & H_5-I_2. For any deformation below the 0.02 strain amplitude, at the boundary point cases of all c_{44}, c_{55}, and c_{66}, the relaxation shows that the cation molecule does not move at all, therefore the charge distribution remains unchanged with respect to the unstrained state. Nevertheless, over such a strain amplitude (δmax>0.02), c_{44} shows a similar charge distribution, along with a nonnegligible tilting of the organic cation (see **Fig. 6.10** (b)), however, as a result of the strong modification of the charge distribution seen for c_{55}, there is an abrupt FA cation tilt around the C-H_1 FA cation axis, which tends to bring both H_2 and I_1 closer together (**Fig. 6.10** (c)), and finally, due to the present distribution of charge for c_{66}, the observed tilting occurred around the axis of the FA cation plane (**Fig. 6.10** (d)). Despite this prominent effect over perovskite structure, the latter elastic modulus is positive, suggesting the possibility of an energetically favored tilting of the FA along its plane axis. These cation relaxation obtained through modifications generated by planar-δ strains are in agreement with the results of S. Kanno since the authors demonstrated that the rotational energy barrier of the organic cation in $FAPbI_3$ is higher around θ, which is an internal coordinate defined by the rotation along and axis penetrating the FA cation by its carbon atom to its center of mass [12], a similar FA cation tilting that is driven by a strain that could turn the whole structure unstable beyond a certain strain amplitude that may be proved to be also characteristic for the specific halogen atom present in the inorganic cage. The mechanical instability here determined by the numerical value of the elastic constants, followed by both the unbalanced electronic papulation in between hydrogen to halogens and the collective organic cation tilting, could trigger the structural instability that induces the phase transition from black to yellow perovskite [18].

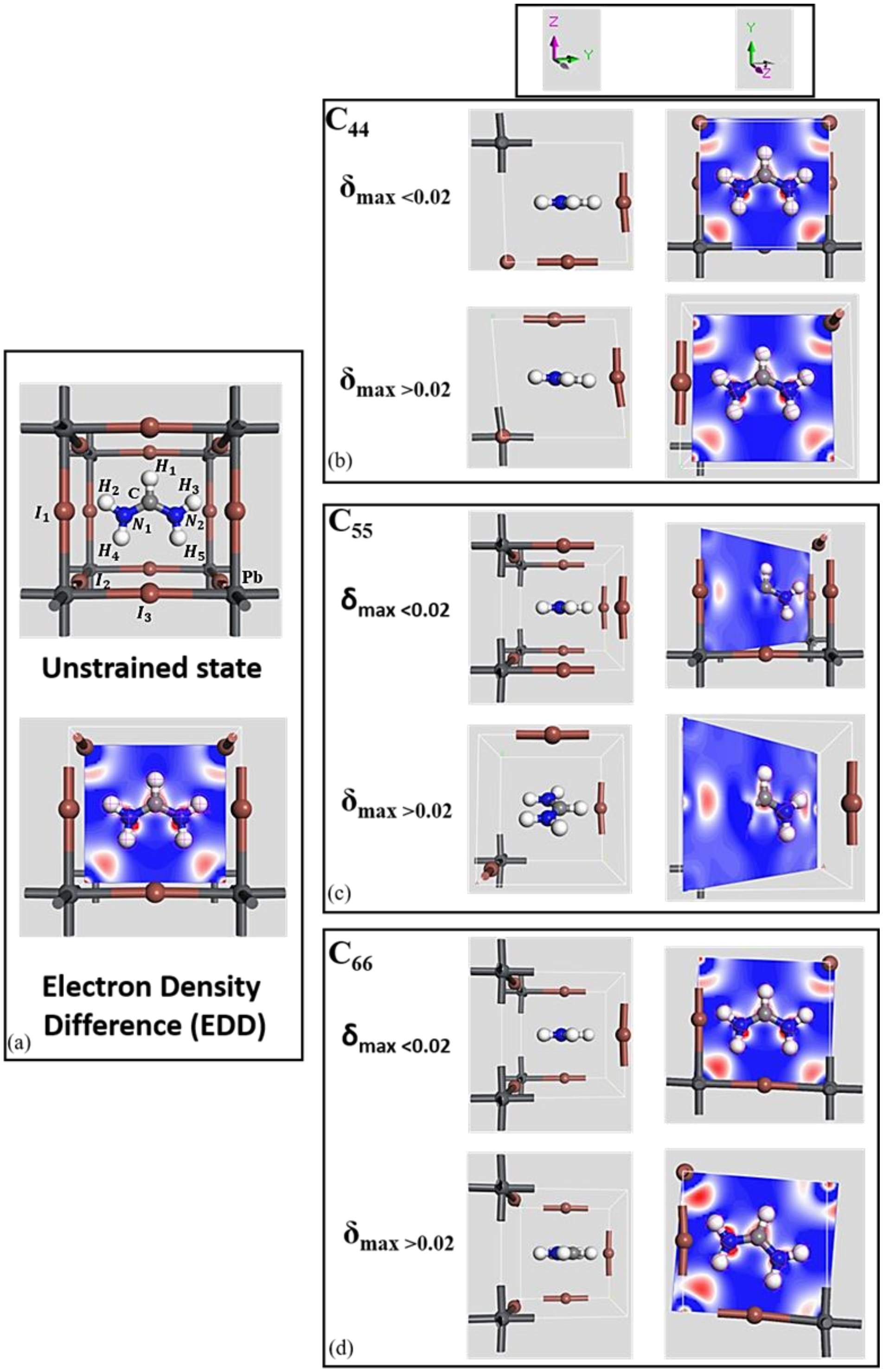

***Fig. 6.10**. The EDD plots at the strain boundaries for the elastic components: c_{44}, c_{55}, and c_{66} of the [XY] FA 12 o'clock configurations, the results are shown for both δmax<0.02 and δmax>0.02 strain amplitudes. Blue-White-Red spectrum displays the electron lack to enrichment, showing a marked charge transfer that describes the FA cation tilting, around the C-H_1 axis for the exchange of the iodine position and around the plane axis while transferring the charge among hydrogen terminations, for c_{66}, at the structure instability state, respectively.*

6.2.3. Mechanical stability study of bulk $FABX_3$ perovskites

In this sub-section, we thoroughly analyze the mechanical stability of six different FA organic cation-based perovskite conventional models such as $FAPbI_3$, $FAPbBr_3$, $FAPbCl_3$, $FASnI_3$, $FASnBr_3$, and $FASnCl_3$ from elastic-constant results using the first-principles DFT calculations with vdW interactions. Our results show that the B and X site substitution over the FA cation perovskite positively affects the structural properties. The obtained Mulliken-charge analysis and elastic-constant results are helping to understand the different behavior of FA cation-based perovskite models.

The unit-cell structure is demonstrated in **Fig. 6.11.** The calculated lattice parameters value, b/a and c/a ratios, volume, and the ground state energy for the six different FA-based perovskite models ($FAPbI_3$, $FAPbBr_3$, $FAPbCl_3$, $FASnI_3$, $FASnBr_3$, and $FASnCl_3$) shown in **Fig. 6.12**. We initiate all the calculations with the same lattice parameter (a= 6.36 Å [19]), and in all the six unit-cell models, we ended with an orthorhombic structure. In general, nine independent strain patterns are needed to determine each adiabatic EC values for an orthorhombic structure [17], [20]. The obtained lattice parameter values of the conventional $FAPbI_3$ model (a= 6.47, b=6.30, c=6.41 Å) is consistent with the previous results [12], [15]. After substituting the different halides, such as Br and Cl, instead of I into the same structure, the lattice parameters were significantly reduced (see **Fig. 6.12**). We also tested with the Sn as a replacement for Pb in the same configured model. Interestingly, the lattice parameter values for the $FASnI_3$ structure (a= 6.40, b=6.19, c=6.30 Å) are significantly diminished than Pb-based models due to the size of the Sn compared to Pb. At the same time, we are placing the various halides instead of I in the Sn-based models, which also follows Pb-based unit cell models' tendency. As a result, the lattice parameter values (a, b, c) for both lead and tin-based perovskites decreasing in the following order, I, Br, and Cl, respectively (see **Fig. 6.12**). Due to the halide size (Br, and Cl smaller than I), it influences the bond angle as well as the bond length (i.e., Pb (Sn) - X (I, Br, Cl) – Pb (Sn)), which is effectively distorted the perovskite structure [15]. The obtained lattice parameter values agree with L. Geo et al. reported results for Sn and lead-based perovskites (a= 6.67, b=6.50, c=6.61 for $FAPbI_3$, a=6.30, b=6.08, c=6.21 for $FAPbBr_3$, a=6.62, b=6.46, c=6.53 for $FASnI_3$ and a=6.26, b=6.03, c=6.14 for $FASnBr_3$), respectively [15]. The values of b/a and c/a ratios confirm that the I-based conventional model ($FAPbI_3$) shows the closest cubic range (pseudo-cubic) value compared to other Pb and Sn-based unit-cell models. The calculated ground state energy and the unit-cell volume values are shown in **Fig. 6.12**. The obtained ground state energy is entirely different for Pb and Sn-based perovskites due to the X (either Pb and Sn) site interaction to halogens. The obtained Mulliken-charge analysis shows that the charge populations and the bond length in between the halogen (I, Br, and Cl) to the FA cation, which influences both the structural and the mechanical stability behavior of all the six conventional models. (see **Table. 6.8**)

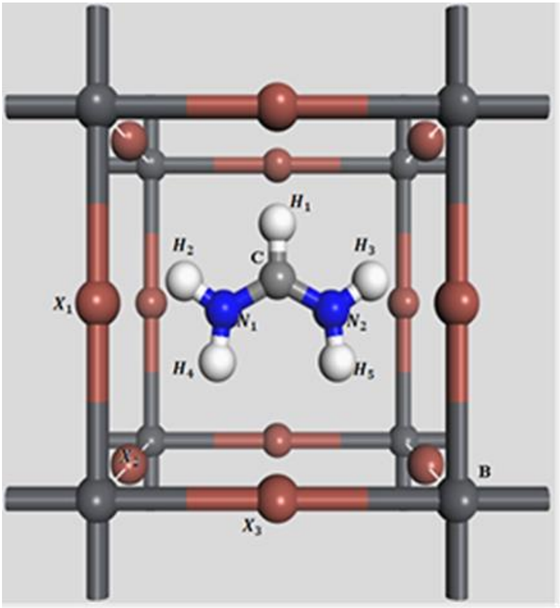

***Fig. 6.11**. FABX$_3$ cubic representation. Where B is lead (Pb) or tin (Sn); X$_1$ is I$_1$, Cl$_1$, Br$_1$; X$_2$ is I$_2$, Cl$_2$, Br$_2$, and X$_3$ is I$_3$, Cl$_3$, Br$_3$.*

Typically, the halogen, which is placed perpendicular to the plane of the molecule, is higher than the other ones. The halogen and X site substitution gives the different charge distribution to the FA organic cation to the inorganic sub-cells. From **Table. 6.8**, it is easily understandable that hydrogen to halogen (I, Br, and Cl) bonding, as well as the charge distribution, is crucial to understand the structural behavior, especially H_4 and H_5 to specific halogen position (i.e., I_2, Br_2, and Cl_2) decides the structural response. I and Br-based models (both Pb and Sn) have the highest bond population value, belonging to H_4 and H_5 to I_2 or Br_2 bonds. At the same time, H_2-Cl_2 and H_3-Cl_2 bonding demonstrate a little higher bond population than H_4-Cl_2 and H_5-Cl_2 bonding for both Cl-based lead and tin models. We noticed no bonding contribution between I to either Pb or Sn in the $FAPbI_3$ and $FASnI_3$ models compared to Br and Cl-based conventional models. (see **Table. 6.8**) Surprisingly, Cl contained models confirm that all three Cl positions (Cl_1, Cl_2, and Cl_3) interact with lead or tin, especially to the Pb1 or Sn1 atom. The contribution occurred between Br1-Pb1, the Br-based Pb-model, and Br_1-Pb_1 & Br_2-Pb_1 bonding for the Sn-based model, which is entirely different from the I and Cl models.

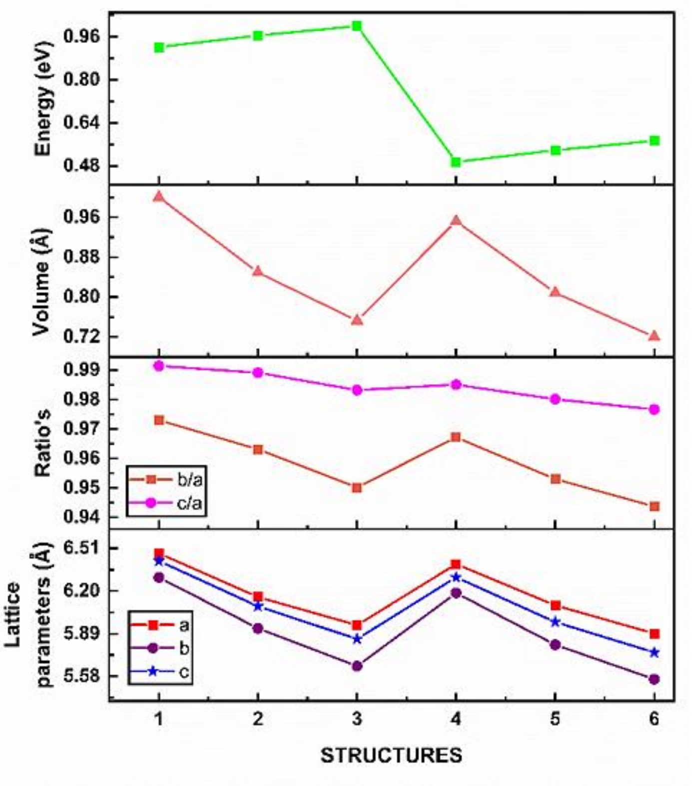

Fig. 6.12. *Results of lattice parameters (a, b, c), volume, and ground-state energy for optimized* $FAMX_3$ *structures. In X-axis 1, 2, 3, 4, 5 and 6 belongs to* $FAPbI_3$, $FAPbBr_3$, $FAPbCl_3$, $FASnI_3$, $FASnBr_3$, $FASnCl_3$, *respectively.*

Table 6.8*. The Mulliken-charge analysis of* $FABX_3$ *conventional models.*

STRUCTURES	Bond	Population (e)	Length (Å)
$FAPbI_3$	H_2-I_2	-0.03	2.90293
	H_3-I_2	-0.03	2.90294
	H_4-I_2	-0.12	2.82312
	H_5-I_2	-0.12	2.82313
$FAPbBr_3$	H_2-Br_2	-0.07	2.56729
	H_3-Br_2	-0.07	2.56729
	H_4-Br_2	-0.15	2.65160
	H_5-Br_2	-0.15	2.65159
	Br_1-Pb_1	-5.05	2.96425

$FAPbCl_3$	H_2-Cl_2	0.04	2.40074
	H_3-Cl_2	0.04	2.40074
	H_4-Cl_2	0.03	2.48088
	H_5-Cl_2	0.03	2.48088
	Cl_1-Pb_1	0.20	2.97605
	Cl_3-Pb_1	0.10	2.81745
	Cl_2-Pb_1	0.07	2.93028
$FASnI_3$	H_2-I_2	-0.05	2.79995
	H_3-I_2	-0.05	2.79961
	H_4-I_2	-0.14	2.78355
	H_5-I_2	-0.14	2.78315
$FASnBr_3$	H_2-Br_2	-0.09	2.52194
	H_3-Br_2	-0.09	2.52152
	H_4-Br_2	-0.19	2.57252
	H_5-Br_2	-0.19	2.57297
	Br_1-Sn_1	-1.20	2.89173
	Br_2-Sn_1	-2.13	2.98997
$FASnCl_3$	H_2-Cl_2	0.04	2.36003
	H_3-Cl_2	0.04	2.36034
	H_4-Cl_2	0.03	2.40618
	H_5-Cl_2	0.03	2.40628
	Cl_2 -Sn_1	0.15	2.87758
	Cl_1-Sn_1	0.24	2.66347
	Cl_3- Sn_1	0.27	2.94575

Later, we launch the EC calculations in order to check the mechanical stability for the optimized structures. In **Table. 6.9**. demonstrate that the obtained EC results for all the lead and tin-based models, and these values are prominent to find the structure's mechanical stability behavior. In order to get a stable structure, all the six orthorhombic (pseudo-cubic) models need to obey the stability condition [21] (equation 2.24). The obtained EC results of all the six FA-based models confirm that the structure is mechanically stable. From **Table. 6.9**, we can recognize that the C_{11}, C_{22}, C_{33}, C_{44}, C_{55}, C_{66}, C_{12}, C_{13}, and C_{23} values are varied based on the halide and the X site substitution. It might be relevant to the bonding between different halogen positions, especially their bond population and bond length values.

Table 6.9*. Calculated EC values of six different FA-based perovskite models.*

	c_{11}	c_{22}	c_{33}	c_{44}	c_{55}	c_{66}	c_{12}	c_{13}	c_{23}	**ref**
FAPbI$_3$	40.6	48.2	32.4	0.9	1.4	1.7	8.4	10.4	7.0	this work
FAPbI$_3$	30.1	31.0	29.8	2.0	5.3	2.6	2.9	7.2	4.2	[15]
FAPbI$_3$	20.5			4.8			12.3			[9]
FAPbBr$_3$	47.4	54.2	40.5	0.8	1.5	3.0	9.7	11.2	6.7	this work
FAPbBr$_3$	37.9	45.2	34.5	3.3	5.3	1.8	7.2	9.9	5.6	[15]
FAPbCl$_3$	54.1	61.8	44.1	1.2	1.8	1.5	11.3	13.9	8.7	this work
FASnI$_3$	26.1	48.7	40.4	4.3	1.6	5.7	9.3	6.8	5.4	this work
FASnI$_3$	29.9	25.2	26.0	2.3	4.9	2.4	6.8	8.2	3.2	[15]
FASnBr$_3$	47.3	52.9	42.6	0.7	1.7	2.3	9.2	12.6	6.8	this work
FASnBr$_3$	35.3	25.6	32.1	3.2	5.6	1.2	5.7	10.8	3.7	[15]
FASnCl$_3$	18.5	52.2	23.9	1.1	1.9	1.8	10.9	13.3	7.2	this work

We observed that the C_{66} value is relatively more significant than C_{44} and C_{55}, indicating a stronger coupling between the direction a and b than a and c or b and c. The obtained results may be varied from the Pb and Sn or different halide (I, Br, and Cl) substitutions in FA perovskite structure. Our calculated EC values are slightly larger than the data calculated by L. Geo et al. [15]. They investigated the elastic moduli behavior for FA cation-based perovskites, and their findings explain that Br-based perovskites have durable anisotropic nature than I-based perovskites. They also demonstrate that replacing Br instead of I either with Pb or Sn perovskite models significantly reduces the bulk modulus, shear modulus, and Young's modulus values. Besides, J. F. Wang et al. demonstrate that the primary interaction that occurred between the organic FA cation and inorganic framework (Pb or Sn and I, Br, and Cl) is through the ionic bonding between NH_2 and I ions, which might decide the stability [9]. Therefore, based on the chosen element and substitution site, determine the structural and mechanical behavior.

In this section, the provided simulation results are only related to the pristine $FAPbI_3$ structure. Based on our observation, the structure is not stable in the higher amplitude range. Therefore, to enhance the structural stability, the appropriate cation/anion doping is essential. In this consideration, several published computational reports demonstrated that doping, especially with smaller inorganic cations (i.e., Cs or Rb), highly improves the $FAPbI_3$ stability [22]–[25]. For example, L. Qiao et al. investigated the electron-hole recombination in pristine $FAPbI_3$ and Cs-doped (25%) $FAPbI_3$ structure employing nonadiabatic molecular dynamics simulation with time-dependent KS-DFT (Grimme-D3) scheme [26]. The results explain that the octahedral tilting (OT) and a lattice contraction occur in the $FAPbI_3$ structure while incorporation smaller Cs ion into the larger FA ion. The bandgap value significantly increased from 1.45 eV (pristine) to 1.57 eV (Cs-doping), which is reliable with the experimental results [27]. The considerable changes were noticed in Pb and I positions and also in the charge densities. The more negligible nonadiabatic electron-phonon coupling is observed for the Cs-doped structure due to reduced inorganic cage distortion as well as the weak polarity of Cs cation than FA cation. Notably, the recombination times are highly reduced from 3.1 to 1.1 while doping the smaller Cs cation, which is beneficial for the PCE enhancement in PSCs due to reducing charge and energy losses.

6.3. Conclusion

In conclusion, the structural behavior and mechanical stability response of $FAPbI_3$ perovskites structures were investigated and presented based on their organic cation position, using DFT- GGA method through the CASTEP module available in Material studio software. Our results explain that the organic cation orientation and the hydrogen (i.e., H_4 and H_5) atoms play a crucial role in the structural and mechanical response behavior. By employing two different strain amplitudes, it was possible to observe a generalized elastic stiffness behavior. First, under a strain amplitude (0.02) limit that generates a set of EC values that fulfill all the stability conditions of pseudo-cubic (orthorhombic) structure, the highest elastic stiffness response is found for uniaxial-$\delta\perp$ strains, meanwhile, those deformations with both displacement components acting over the FA cation plane, show the highest planar c_{ii} magnitude, a value which is independent of the FA orientation. The obtained EC values and both Bulk and Shear moduli results agree with previously reported literature. Secondly, with increasing amplitude (0.04), the planar c_{ii} results start to show negative values, that made the structure unstable, specifically for deformations featuring a planar-$\delta\|$ strain as one of the components. The instability mechanism is described by means of both population and bond length observed among H_i-I_2 (where i=2,3), which is abruptly modified, outside the stability threshold, which is found in between the strain amplitudes δmax=0.02 to 0.04, for pristine $FAPbI_3$, i.e., once δmax>0.02, into an H_2-I_1 distribution with magnitudes as prominent as H_i-I_2 (where i=4,5), followed by a tilting of the FA cation around C-H_1, once the atomic positions are relaxed.

The structural and mechanical stability behavior of six different configurations inside the inorganic cage (i.e., Pb or Sn with I, Br, and Cl) results demonstrate that the lattice parameter values decreasing for Br and Cl based models compared to I-based perovskite models. The MC analysis exhibits that the halogen to FA cation bonding influences EC results, especially H_4 and H_5 to X_2 (where I_2, Br_2, and Cl_2). Meanwhile, we did not observe any bond population between the Pb or Sn to the I halogen in $FAPbI_3$ and $FASnI_3$ models. Our obtained EC result shows that all six conventional pseudo-cubic models are mechanically stable. The present section provides noticeable explanations to understand the instability mechanism of formamidinium based perovskite structures that could be used to describe the black alpha phase to yellow delta phase transition (which is not suitable for photovoltaic applications), implicating the performance of actual devices.

References

[1] C. C. Stoumpos, C. D. Malliakas, and M. G. Kanatzidis, "Semiconducting tin and lead iodide perovskites with organic cations: Phase transitions, high mobilities, and near-infrared photoluminescent properties," *Inorg. Chem.*, 2013, doi: 10.1021/ic401215x.

[2] A. A. Zhumekenov *et al.*, "Formamidinium Lead Halide Perovskite Crystals with Unprecedented Long Carrier Dynamics and Diffusion Length," *ACS Energy Lett.*, 2016, doi: 10.1021/acsenergylett.6b00002.

[3] C. Manspeaker, S. Venkatesan, A. Zakhidov, and K. S. Martirosyan, "Role of interface in stability of perovskite solar cells," *Current Opinion in Chemical Engineering*. 2017, doi: 10.1016/j.coche.2016.08.013.

[4] A. C. Ferreira *et al.*, "Elastic Softness of Hybrid Lead Halide Perovskites," *Phys. Rev. Lett.*, 2018, doi: 10.1103/PhysRevLett.121.085502.

[5] E. D. Indari, T. D. K. Wungu, and R. Hidayat, "Ab-Initio Calculation of Electronic Structure of Lead Halide Perovskites with Formamidinium Cation as an Active Material for Perovskite Solar Cells," in *Journal of Physics: Conference Series*, 2017, doi: 10.1088/1742-6596/877/1/012054.

[6] S. X. Tao, X. Cao, and P. A. Bobbert, "Accurate and efficient band gap predictions of metal halide perovskites using the DFT-1/2 method: GW accuracy with DFT expense," *Sci. Rep.*, 2017, doi: 10.1038/s41598-017-14435-4.

[7] D. Li, J. Meng, Y. Niu, H. Zhao, and C. Liang, "Understanding the low-loss mechanism of general organic-inorganic perovskites from first-principles calculation," *Chem. Phys. Lett.*, 2015, doi: 10.1016/j.cplett.2015.03.028.

[8] A. Tkatchenko and M. Scheffler, "Accurate molecular van der Waals interactions from ground-state electron density and free-atom reference data," *Phys. Rev. Lett.*, 2009, doi: 10.1103/PhysRevLett.102.073005.

[9] J. F. Wang, X. N. Fu, and J. T. Wang, "First-principles analysis of the structural, electronic, and elastic properties of cubic organic-inorganic perovskite HC(NH2)2PbI3," *Chinese Phys. B*, 2017, doi: 10.1088/1674-1056/26/10/106301.

[10] M. A. Carignano, Y. Saeed, S. A. Aravindh, I. S. Roqan, J. Even, and C. Katan, "A close examination of the structure and dynamics of HC(NH2)2PbI3 by MD simulations and group theory," *Phys. Chem. Chem. Phys.*, 2016, doi: 10.1039/c6cp02917e.

[11] K. Lee, É. D. Murray, L. Kong, B. I. Lundqvist, and D. C. Langreth, "Higher-accuracy van der Waals density functional," *Phys. Rev. B - Condens. Matter Mater. Phys.*, 2010, doi: 10.1103/PhysRevB.82.081101.

[12] S. Kanno, Y. Imamura, and M. Hada, "Theoretical Study on Rotational Controllability of Organic Cations in Organic-Inorganic Hybrid Perovskites: Hydrogen Bonds and Halogen Substitution," *J. Phys. Chem. C*, 2017, doi: 10.1021/acs.jpcc.7b07721.

[13] "BIOVIA Materials Studio, Discovery Studio Modeling Environment." San Diego: Dassault systems, r2 (17.2.0.1626) ed. (2017), Accelrys Software Inc., 2017.

[14] S. Karthick, J. J. Rios-Ramirez, and S. Velumani, "12 Possible Orientations of organic Formamidinium cation and its structural analysis by First Principles calculations using Van der Waals-Density functional Theory," in *2018 15th International Conference on Electrical Engineering, Computing Science and Automatic Control, CCE 2018*, 2018, doi: 10.1109/ICEEE.2018.8533994.

[15] L. Guo, G. Tang, and J. Hong, "Mechanical Properties of Formamidinium Halide Perovskites FABX3 (FA=CH(NH2)2; B=Pb, Sn; X=Br, I) by First-Principles Calculations," *Chinese Phys. Lett.*, 2019, doi: 10.1088/0256-307X/36/5/056201.

[16] L. Vitos, *Computational Quantum Mechanics for Materials Engineers: The EMTO Method and Applications*. 2007.

[17] P. Ravindran, L. Fast, P. A. Korzhavyi, B. Johansson, J. Wills, and O. Eriksson, "Density functional theory for calculation of elastic properties of orthorhombic crystals: Application to TiSi2," *J. Appl. Phys.*, 1998, doi: 10.1063/1.368733.

[18] S. Jiang *et al.*, "Phase Transitions of Formamidinium Lead Iodide Perovskite under Pressure," *J. Am. Chem. Soc.*, 2018, doi: 10.1021/jacs.8b09316.

[19] M. T. Weller, O. J. Weber, J. M. Frost, and A. Walsh, "Cubic Perovskite Structure of Black Formamidinium Lead Iodide, α-[HC(NH2)2]PbI3, at 298 K," *J. Phys. Chem. Lett.*, 2015, doi: 10.1021/acs.jpclett.5b01432.

[20] A. H. Reshak and M. Jamal, "DFT calculation for elastic constants of orthorhombic structure within WIEN2K code: A new package (ortho-elastic)," *J. Alloys Compd.*, 2012, doi: 10.1016/j.jallcom.2012.07.107.

[21] F. Mouhat and F. X. Coudert, "Necessary and sufficient elastic stability conditions in various crystal systems," *Phys. Rev. B - Condens. Matter Mater. Phys.*, 2014, doi: 10.1103/PhysRevB.90.224104.

[22] O. A. Syzgantseva, M. Saliba, M. Grätzel, and U. Rothlisberger, “Stabilization of the Perovskite Phase of Formamidinium Lead Triiodide by Methylammonium, Cs, and/or Rb Doping,” *J. Phys. Chem. Lett.*, 2017, doi: 10.1021/acs.jpclett.6b03014.

[23] Z. Zhang and R. Long, "Doping-Induced Rapid Decoherence Suppresses Charge Recombination in Mono/Divalent Cation Mixed Perovskites from Nonadiabatic Molecular Dynamics Simulation," *J. Phys. Chem. Lett.*, 2019, doi: 10.1021/acs.jpclett.9b01330.

[24] J. L. He, Y. H. Zhu, and R. Long, "Charge localization induced by reorientation of FA cations greatly suppresses nonradiative electron-hole recombination in FAPbI3perovskites: A time-domain Ab Initio study," *Chinese J. Chem. Phys.*, 2020, doi: 10.1063/1674-0068/cjcp2006109.

[25] Y. Guo, C. Li, Y. Xue, C. Geng, and D. Tian, "First-principles study of Cs/Rb co-doped FAPbI3 stability and degradation in the presence of water and oxygen," *Mater. Res. Express*, 2018, doi: 10.1088/2053-1591/aaacf2.

[26] L. Qiao, X. Sun, and R. Long, "Mixed Cs and FA Cations Slow Electron-Hole Recombination in FAPbI 3 Perovskites by Time-Domain Ab Initio Study: Lattice Contraction versus Octahedral Tilting," *J. Phys. Chem. Lett.*, 2019, doi: 10.1021/acs.jpclett.8b03729.

[27] R. Prasanna *et al.*, "Band Gap Tuning via Lattice Contraction and Octahedral Tilting in Perovskite Materials for Photovoltaics," *J. Am. Chem. Soc.*, 2017, doi: 10.1021/jacs.7b04981.

7. CHAPTER VII. Experimental and SCAPS simulated Formamidinium perovskite solar cells: A comparison of device performance.

7.1. Introduction

Despite many advantages (see chapter 1), the black colored cubic $\alpha - FAPbI_3$ is found to be metastable at room temperature [1], [2]. The mixed organic/inorganic cation and/or mixed anion strategies have been shown to be of great help to stabilize the $\alpha - FAPbI_3$, simultaneously suppressing the yellow $\delta - FAPbI_3$ phase which is not suitable for photovoltaic applications. In particular, the incorporation of commonly known organic MA^+/inorganic Cs^+ into the A site or substitution of Br^-/Cl^- into the X site are now well established to achieve more stable and efficient photocurrent generation. Number of reports are available in the perovskite research community, to explain Cs^+ and Br^- incorporation evidently suppressing the non-perovskite yellow phase of $FAPbI_3$ to steadying the black colored $\alpha - FAPbI_3$ phase [3]–[9].

A small amount of Cs^+ incorporated into the pristine $FAPbI_3$ structure ($FA_{1-x}Cs_xPbI_3$) provides superior phase durability over 100 hours of light irradiation than unsubstituted $FAPbI_3$. It also exhibits an outstanding resistance against humidity (90% of moisture level for 4 h) compared to the pure phase [10]. This combination of cations quenches the spontaneous phase change from black to yellow or $\delta - phase$, especially due to the preferential formation of CsI which reduces the release of detrimental HI species [11], [12]. Finally, the formamidinium-Cesium ($FA - Cs$) combination demonstrates an excellent photostability, thermal stability, and resistance to moisture than the formamidinium-methylammonium ($FA - MA$) pair [11]–[15]. Regarding the halide site, adding a small amount of Br^- is a well-known strategy towards higher bandgap perovskites (1.5 to 1.7 eV). The bromide incorporation directly modifies the structural, morphological, hence electrical and optical properties of the material. Especially, a larger strain occurs while halide demixing, which is providing the partial support in order to encounter the halide segregation [16]–[19]

In this section, three different types of FA-based perovskite active layers are processed using a one-step solution method and the anti-solvent treatment: (i) pristine $FAPbI_3$, (ii) $FA_{0.85}Cs_{0.15}PbI_3$, and (iii) $FA_{0.85}Cs_{0.15}Pb(I_{0.85}Br_{0.15})_3$. These active layers are integrated into perovskite solar cells using a conventional planar device architecture given by Glass/FTO/ SnO_2/Perovskite/Spiro-OMeTAD/Au. In order to get more insight on the influence of Cs^+ and Br^- cation/halogen addition on device performance, experimental current density-voltage characteristics under solar irradiation, as well as SEM images, and optical spectroscopy spectra are presented. More specifically, simulations of device's electrical responses are made using the SCAPS-1D software, which allows us to discuss the influence of perovskite composition and its effect on parasitic resistances. Although several simulations using SCAPS have been reported in the literature for perovskite solar cells [20]–[23], we especially focus first on ideal devices, which do not account for series or shunt resistance. We then show that the electrical losses are crucial in order to reproduce the trend of experimental devices based on pure FA cation or on mixed systems $(FA - Cs\ and\ I - Br)$. The impact of phase evolution of the FA-based perovskites under ambient conditions can be nicely reproduced by the simulation in these conditions. This contribution provides novel explanations which is intending to tackle the degradation of $\alpha - FAPbI_3$ perovskite phase as well as to enhance the device PCE. As for as our literature review extends, this is the first report elucidating the correlation between experimental and SCAPS-1D simulated formamidinium organic cation based perovskites solar devices, especially on pristine $FAPbI_3$, $FA_{0.85}Cs_{0.15}PbI_3$, and $FA_{0.85}Cs_{0.15}Pb(I_{0.85}Br_{0.15})_3$.

7.2. Results and Discussion

Experimental perovskite solar cells were fabricated according to the procedures reported in the above experimental section. Three active layers, namely pristine $FAPbI_3$, $FA_{0.85}Cs_{0.15}PbI_3$, and $FA_{0.85}Cs_{0.15}Pb(I_{0.85}Br_{0.15})_3$ were considered in this work in order to describe the influence of an additional cation (Cs^+) and/or halide (Br^-) on device performance.

7.2.1. Determination of the absorber layer bandgaps

In order to measure their thickness and optical absorption, the pristine $FAPbI_3$, $FA_{0.85}Cs_{0.15}PbI_3$, and $FA_{0.85}Cs_{0.15}Pb(I_{0.85}Br_{0.15})_3$ perovskite films were prepared on glass substrates, and their optical absorption spectra were recorded using UV-visible spectroscopy (**Fig. 7.1**). The measured spectra evidence the expected absorption profile of the perovskite layer, and especially the slight blue-shift of the optical absorption edge from 835 nm down to 780 nm occurring in the presence of Br^-anion compared to the pristine or Cs-doped perovskite layer.

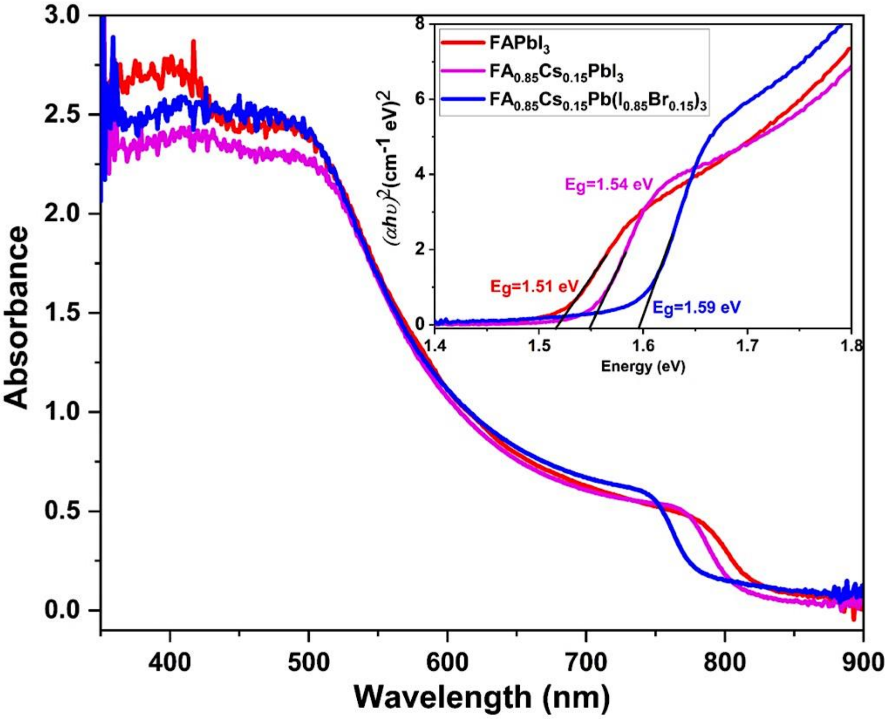

Fig. 7.1. *UV-visible absorbance spectra of pristine* $FAPbI_3$, $FA_{0.85}Cs_{0.15}PbI_3$, *and* $FA_{0.85}Cs_{0.15}Pb(I_{0.85}Br_{0.15})_3$ *perovskite films. The inset shows the corresponding Tauc's plot used for bandgap calculations.*

The optical bandgap (E_g) values of the obtained FA-perovskite films are calculated using Tauc's law in the case of a direct optical transition, [24] :

$$(\alpha h\vartheta)^2 = B(h\vartheta - E_g) \qquad (7.1)$$

Where B is an independent energy constant, h is Planck's constant, α is the absorption coefficient of the perovskite film. The calculated E_g values (1.50 eV for $FAPbI_3$, 1.54 eV for $FA_{0.85}Cs_{0.15}PbI_3$, 1.59 eV for $FA_{0.85}Cs_{0.15}Pb(I_{0.85}Br_{0.15})_3$) are found in good agreement with reported trends for similar perovskite composition [9], [10]. These values were used in the SCAPS simulations of devices D-A (based on pristine $FAPbI_3$), D-B (based on $FA_{0.85}Cs_{0.15}PbI_3$) and D-C (based on $FA_{0.85}Cs_{0.15}Pb(I_{0.85}Br_{0.15})_3$), respectively.

7.2.2. Simulation of ideal devices

In this simulation study, ideal perovskite devices are carefully optimized without considering R_{series} and R_{shunt} resistances. This step, although nonrealistic, but a good tool to evaluate the higher limit of device performance considering an optimal operation. In general, the absorber layer thickness mainly governs the level of photogenerated current, hence the overall device performance, independently of electrical losses, which occurs in non-ideal devices. All the input parameters used in the simulations are given in **Table 5.1**. As already mentioned, we used the experimentally obtained thickness for ETL (70 nm), HTL (165 nm), and perovskite active layers (350 nm), as well as optical band gap values of the three absorber-layers (see Table 5.1). The simulated photovoltaic parameters do not change much as a function of the HTL thickness values (see **Table 7.1**); therefore, in all the simulations, we used 200 nm. Additionally, all other parameters such as electron affinity, dielectric permittivity, effective densities of states at conduction and valence bands, as well as electron e^- and hole h^+ mobility values were taken from previously published results [9], [25]–[29]. Some of these parameters were optimized in order to achieve reproducible and consistent results.

Table 7.1. *Summarized photovoltaic parameters of ideal devices D-A, D-B, and D-C using different HTL thickness values, respectively.*

Device	**HTL (nm)**	J_{sc} $^{mA}/_{cm^{-2}}$	**FF (%)**	V_{oc} **(V)**	**PCE (%)**
D-A	**170**	22.6	77.7	1.2	21.5
	180	22.6	77.6	1.2	21.4
	190	22.6	77.5	1.2	21.4
	200	22.6	77.4	1.2	21.4
D-B	**170**	21.5	78.4	1.2	21.1
	180	21.5	78.3	1.2	21.1
	190	21.5	78.2	1.2	21.1
	200	21.5	78.1	1.2	21.1
D-C	**170**	20.2	72.1	1.29	18.8
	180	20.2	72.1	1.29	18.8
	190	20.2	72.0	1.29	18.8
	200	20.2	72.0	1.30	18.7

Fig. 7.2 displays the optimized current-voltage characteristics (J-V) of the three ideal devices from which the main photovoltaic parameters are extracted: short-circuit density (J_{sc}), fill factor (FF), open-circuit voltage (V_{oc}), and PCE. These values are summarized and presented in **Table 7.2**.

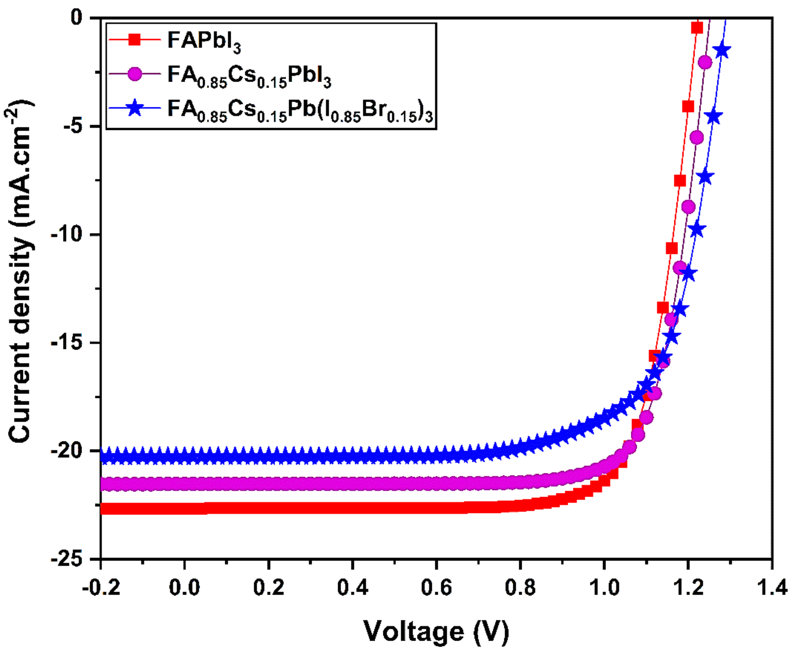

Fig. 7.2. *Simulated J-V characteristics of ideal D-A, D-B, and D-C perovskite devices, respectively.*

Table 7.2. *Summarized photovoltaic parameters of ideal devices D-A, D-B, and D-C, respectively.*

Device	J_{sc} $({}^{mA}/_{cm^2})$	**FF (%)**	V_{oc} **(V)**	**PCE (%)**
D-A	22.6	77	1.2	21.4
D-B	21.5	78	1.2	21.0
D-C	20.2	72	1.3	18.7

Considering similar active layer thicknesses, this first level of simulation shows that pristine $FAPbI_3$ device (D-A) demonstrates the highest PCE compared to the others. This behavior is the result of a trend between the variation of optical bandgaps and charge mobilities (especially for electrons). As a consequence, a noticeable decrease is observed in J_{sc} value from 22.6 ${}^{mA}/_{cm^2}$ down to 20.2 ${}^{mA}/_{cm^2}$ for D-A and D-C devices, respectively. This trend is confirmed by the simulated current density - voltage slope (shown in **Fig. 7.2**). Consequently, all the simulated devices are displaying good efficiencies in the absence of parasitic electrical losses, which is indicating suitable optoelectronic properties of the active layers (suitable charge carrier mobilities), as well as suitable energy band alignment with the SnO_2 (ETL) and Spiro-OMeTAD (HTL) interfacial layers (**Fig. 5.12**).

7.2.3. Experimental devices

From the experimental point of view, we successfully fabricated the D-A, D-B, and D-C devices using a simple one-step solution process with an anti-solvent strategy (see chapters 3 and 4). Note that all devices were processed and characterized in ambient conditions, except the perovskite active layer deposition, which is processed under a nitrogen-filled glovebox. The typical morphology of a device is illustrated in **Fig. 7.3**, which shows the SEM cross-section of device D-C. The image demonstrates a very good homogeneity of the sandwich structure, with a quite compact perovskite layer. Such observation is particularly consistent with the performed SCAPS simulation using a planar structure.

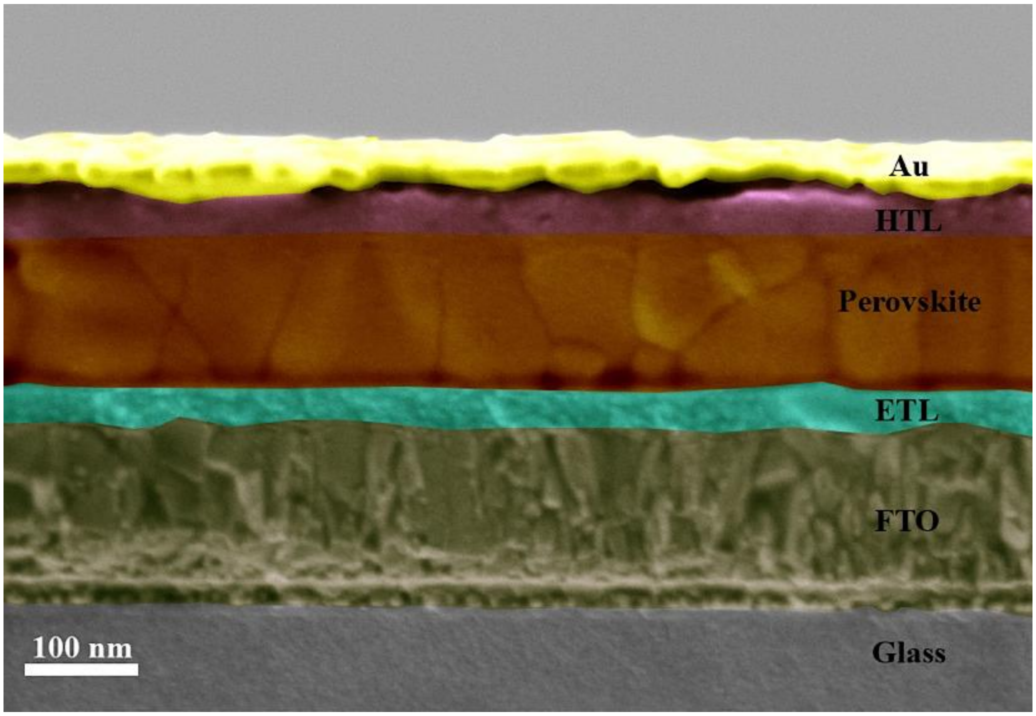

Fig. 7.3. *Cross-sectional SEM image of FTO/ SnO_2/ $FA_{0.85}Cs_{0.15}Pb(I_{0.85}Br_{0.15})_3$/Spiro/Au device.*

The experimental J-V curves were recorded under simulated solar irradiation calibrated to achieve one sun illumination condition (AM1.5G). Both forward and backward scans are displayed in **Fig. 7.4**. The corresponding photovoltaic parameters are presented in **Table 7.3**.

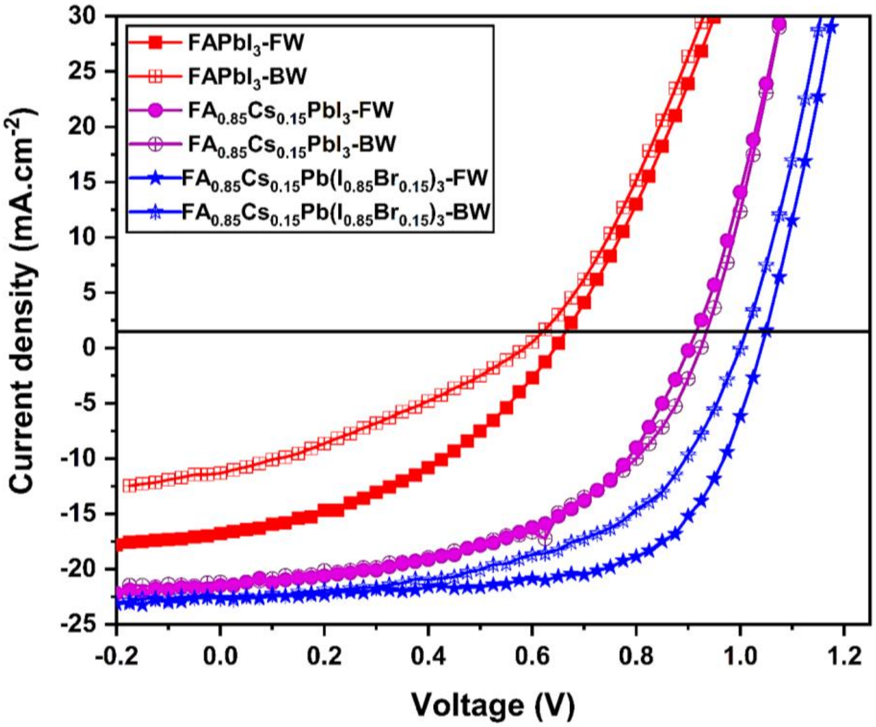

Fig. 7.4. *Experimental J-V characteristics of D-A, D-B, and D-C perovskite devices, respectively.*

Table 7.3. *Summarized photovoltaic parameters (such as short-circuit density* (J_{sc})*, fill factor (FF), open-circuit voltage* (V_{oc})*, power conversion efficiency (PCE), series and shunt resistance* $(R_{shunt}$ *and* $R_{series})$ *values) of experimental D-A, D-B, and D-C devices, respectively. The following table demonstrates three (3) solar cell performances for each case (in similar conditions). The calculated average mean values presented with standard errors.*

Device	**Scan**	J_{SC} $^{mA}/_{cm^2}$	**FF (%)**	V_{oc} **(V)**	**PCE (%)**	R_{series} **(Ω)**	R_{shunt} **(Ω)**
D-A	**FW**	**16.6**	**40.6**	**0.6**	**4.3**	**73**	**744**
	BW	**11.0**	**32.0**	**0.5**	**2.0**	**139**	**582**
	FW	12.2	43.0	0.7	4.1	77	483
	BW	11.7	45.9	0.7	4.0	80	1581
	FW	14.7	36.9	0.7	3.8	74	336
	BW	12.6	40.0	0.6	3.3	87	534
*		13.1±0.86	39.7±1.97	0.6±0.03	3.6±0.34	88.3±10.33	710±182
Ref[30]		13.91±1.60	52.0±2.95	0.75±0.02	5.42±1.0	10.50	1461.65
D-B	**FW**	**21.4**	**51.6**	**0.9**	**9.9**	**45**	**1312**
	BW	**21.1**	**55.5**	**0.9**	**10.7**	**38**	**2219**
	FW	21.3	54.0	0.9	10.4	34	1390
	BW	21.1	50.1	0.9	9.5	42	1319
	FW	21.7	55.0	0.9	10.4	37	827
	BW	20.8	50.0	0.9	9.2	36	1299
*		21.2±0.12	52.7±1.00	0.9±0	10.0±0.24	38.83±1.57	1394±184

Ref[15]		22.78	68.7	1.01	15.87	-	-
D-C	**FW**	**22.6**	**64.4**	**1.0**	**15.1**	**22**	**1854**
	BW	**22.5**	**54.5**	**0.9**	**12.2**	**30**	**1984**
	FW	20.9	65.6	1.0	13.8	40	1718
	BW	20.8	45.2	0.8	8.4	60	1318
	FW	20.5	62.1	1.0	13.5	48	4023
	BW	20.1	46.1	0.9	9.0	66	1988
*		21.2±0.43	56.3±3.72	0.93±0.03	12±1.11	44.3±6.95	2147±388
Ref[31]	**BW**	17.35±0.08	67.55±2.21	1.15±0.01	13.4±0.48	-	-
Ref[4]		19.4	75.1	1.2	17.1	-	-

* **Indicates this work - mean with a standard error of the mean (SEM)**

Unsurprisingly, the experimental performance is found to be much less than the simulated case, especially for device D-A, which corresponds to the pure FA-based lead iodide active layer (PCE of 4.3% only). Independently to the fact that ideal devices were simulated and compared to experimental non-ideal devices, the main origin that explains this observation is associated with the instability of the $FAPbI_3\ \alpha - phase$. In our processing conditions, we indeed observed a fast color change from black to yellow for the active layer of device D-A, as illustrated in **Fig. 7.5**, while devices D-B and D-C remain dark brown in the same conditions.

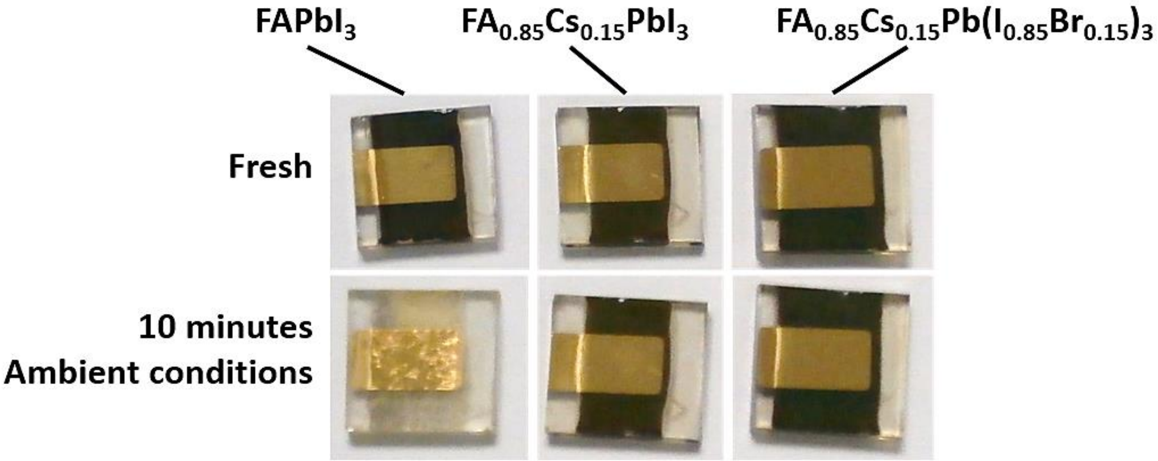

Fig. 7.5. *Photographs of fresh (top) and exposed to air for 10 min (bottom) D-A, D-B, and D-C devices.*

There are several reasons reported (i.e., moisture, humidity, presence of water/solvents in formamidinium) to explain this behavior, especially considering the relatively high level of moisture of our laboratory (>50%). For example, a high humidity level is usually associated with larger voids in the film, which gradually degrade the active layer properties, leading to low PCE [1], [32]. Therefore, we only show preliminary stability assessments, which, however are quite consistent with reported trends, as explained previously. This phenomenon is also usually associated with a large hysteresis effect, which can be seen here for device D-A (**Fig. 7.4**).

Device D-B which incorporates cesium, demonstrates a much-improved PCE of ~10 % in forward scan. Notably, the hysteresis effect is reduced compared to D-A device, which can be due to their excellent resistance against the phase segregation (i.e., black to yellow phase conversion) and the higher thermal healing behavior (i.e., at high temperature, lower weight loss occurred in $FA_{0.85}Cs_{0.15}PbI_3$ than $FAPbI_3$ [11]) (see **Fig. 7.4**). The incorporation of Cs^+ cations into $FAPbI_3$ is known to reduce the decomposition of the perovskite structure, leading to a reduced formation of PbI_2. Consequently, it stabilizes the black phase (as observed in **Fig. 7.5**) which is another prominent reason for the PCE improvement [10]. Due to the reduced photovoltage loss and the improved photocurrent, the extraction of the experimental parasitic resistances gives a higher R_{shunt} and lower R_{series} values, which of course, it comes with this PCE enhancement. We also emphasize, as reported in the literature, that the stability of $FA - Cs$ devices is mainly attributed to the stronger interactions between FA cations and I halogens because of their cubo-octahedral volume reduction than the undoped device [12].

Finally, doping the $FA - Cs$ perovskite film with bromide leads to the wider bandgap layer, but also to the device (D-C) displaying the highest (champion) PCE of 15.1%. We noticed that all the photovoltaic parameters (PCE, J_{sc}, FF, V_{oc}) are largely improved for device D-C compared to devices D-A and D-B. This observation is in line with reported studies, which have shown that the presence of Bromide further enhances the crystallinity and the stability of the 3D formamidinium lead iodide cubic phase, this behavior is associated with the accumulation of strain due to the halide incorporation and their photocarrier recombination phenomenon [17]. The obtained results are thus showing good agreement with previously published reports [33], which emphasize that the SnO_2 ETL clearly shows an excellent band alignment with an appropriate mixed cation/halide perovskite material than pristine one, especially in the planar n-i-p configuration.

The spectral response of different perovskite solar devices is represented by EQE as a function of wavelength of incident light. Both experimental and simulated EQE spectra were shown in **Fig. 7.6**, corresponding to D-A, D-B, and D-C devices, respectively. Note that the simulated EQE curves are generated from the ideal devices, which means an optical reflection of each layer, interfaces, and both resistances (R_{shunt} and R_{series}) are not considered. The following equation representing the traditional SCAPS optical absorption model with $sqrt(h\nu - E_g)$ sub-model, which is used for all the EQE spectra simulation, by means of the bandgap, always depend on the provided E_g value as one of the electronic properties of the layer. [34]

$$\alpha(\lambda) = \left(A + \frac{B}{h\nu}\right)\sqrt{h\nu - E_g} \qquad (7.2)$$

Where α is the optical absorption constant, E_g is the actual band of the layer, A and B are the absorption parameters which is normally set to $1.00E+5$ and $1.00E-12$, respectively.

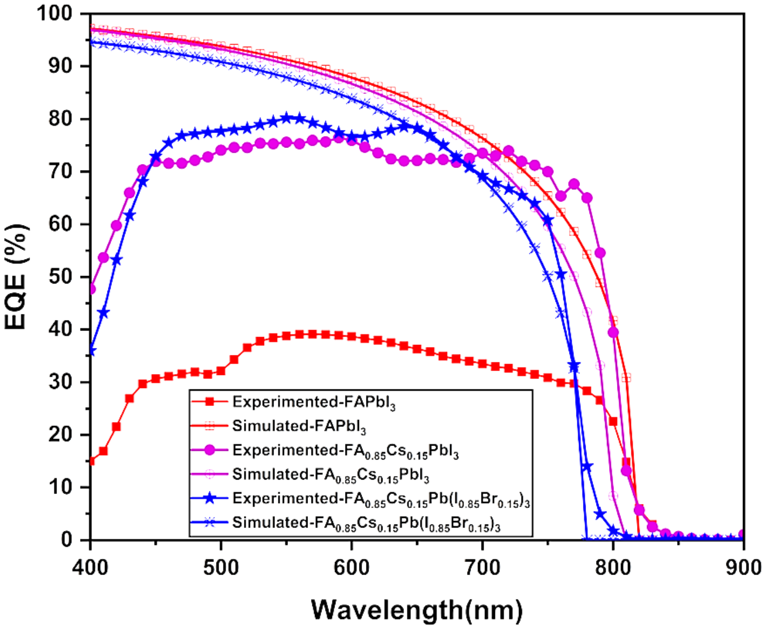

Fig. 7.6. *External quantum efficiency spectra of experimental and simulated (D-A, D-B, and D-C) perovskite solar cells.*

Due to the narrow and wider absorber layer bandgap of device D-A to D-C, optical absorption edge shifts from 830 nm to 780 nm, and the obtained EQE curves cover the complete visible spectrum from 400 nm to 700 nm shown in **Fig. 7.6**. The experimental EQE of device D-A is showing lower efficiency due to the fact that the device shows a strong degradation and phase instability, as mentioned previously; meanwhile, D-B & D-C significantly holds more than 70% quantum efficiency. In practical, experimental devices suffer from different kinds of losses, such as recombination loss and absorption loss. As we mentioned before, the simulated device spectra were calculated using SCAPS, taking into account the experimental bandgaps of the active layer, without considering the optical effects (such as without total reflection) and the recombination losses. Moreover, it looks more similar to the ideal solar device behavior (such as rectangular shape), this is probably due to the absorption law that is used by SCAPS to model the absorption profile of the semiconductors. The resistance losses (R_{shunt} and R_{series}) and ionic migration could be the main reasons for the disagreement between simulated EQE representation to the experimental one [22].

We see a strong correlation between the experimental and simulated EQE spectra, as they exhibit similar trends regarding the active layer spectral sensitivity range as a function of perovskite composition. The Br-doped layer is displaying a reduced sensitivity window (device D-C), in accordance with its larger bandgap value compared to the $FA - Cs$ layer (device D-B). Moreover, it is possible to relate the EQE spectra to the measured short-circuit current densities, as described by the equation [35] :

$$J_{SC} = q \int F(\lambda).EQE\ (\lambda)d(\lambda) \qquad (7.3)$$

where, $F(\lambda)$ is the photon flux and q is the elementary charge.

The obtained experimental EQE J_{sc} values 9.10 ${}^{mA}/{}_{cm^2}$ (D-A), 19.38 ${}^{mA}/{}_{cm^2}$ (D-B) and 21.63 ${}^{mA}/{}_{cm^2}$ (D-C) provides an excellent agreement with measured J_{sc}, shown in **Table 7.3**. In general, most of the reported experimental EQE J_{sc} values are not precisely identical with the measured J_{sc} values due to several reasons, such as different measurement conditions, the light intensity at the specific wavelength, change in interface dynamics based on the measurement time (for example, a longer time for EQE J_{sc} and relatively quick time for measured J_{sc}) and finally, there is a possibility related to the frequency dependence of the EQE [36].

From this first approach, the obtained experimental and simulated ideal devices show different behaviors. First, the simulated D-A device (pure $FAPbI_3$) exhibits a much higher PCE than the experimental one. This can be attributed to the spontaneous and rapid phase transition from the optically active $\alpha - phase$ (black) to the inactive $\delta - phase$ (yellow). This transition is found to be particularly fast in our ambient conditions due to the presence of a high level of moisture and oxygen. The SCAPS simulation does not account for this effect, resulting in a very efficient devices. Then, we observed that the simulated D-B and D-C devices are better describing the experimental trends in terms of photocurrent, due to the consistent influence of the optical bandgap of the layers. However, the experimental devices are obviously largely limited by parasitic resistances. Indeed, several phenomena, such as defect states (especially the surface and interface states) or some local inhomogeneity in the sandwich structure, lead to charge recombination or current leakages, which introduce series (R_{series}) and shunt (R_{shunt}) parasitic resistances. Therefore, we now analyze the effect of these resistances in order to point out the exact influence of cesium and bromide in device operation.

7.2.4. Effect of $R_{series}\ and\ R_{shunt}$

Both R_{shunt} and R_{series} resistances have a crucial impact on device performance, as they govern the shape and slopes of the J-V characteristics. Basically, R_{series} finds its origin in the electrical resistance associated with contacts (FTO and gold), but also with the electrical dissipation occurring in the ETL, HTL, and the active layer. R_{shunt}, which is the manifestation of several alternative charge recombination paths, is also highly influenced by the device design (edge effects). Consequently, a low R_{shunt} results in a photovoltage loss and can also affect the collected photocurrent. In parallel, R_{series} mainly affects the FF and short-circuit current values. It is well known that a low R_{series} and a high R_{shunt} should be achieved in order to demonstrate highly efficient devices. In a first and quite general approach, the following equation is used to understand the consequences of R_{shunt} and R_{series} on the ideal single-diode device performance, [37] :

$$I = I_L - I_0\left[e^{\left(\frac{q(M)}{Ak_BT}\right)} - 1\right] - \left(\frac{M}{R_{Shunt}}\right) \qquad (7.4)$$

where, $M = V + S,\ S = I * R_{series},\ I_L$ is the light-induced current, I_0 is the reverse saturation current of the diode, A is the ideality factor, k_B is Boltzmann constant, T is temperature, and q is the charge of the electron.

To understand the effect of R_{series} and R_{shunt} on ideal device characteristics, we introduced them in the SCAPS model and varied their values between 10 to 100 $\Omega.cm^2$ and 500 to 5000 $\Omega.cm^2$, respectively. The corresponding evolutions of the main photovoltaic parameters are shown in **Fig. 7.7(a) and (b).** Our results clearly illustrate that an increase in R_{series} strongly reduces the FF from 60% to 25% for all types of devices. Moreover, for a R_{series} over 30 $\Omega.cm^2$ J_{SC} is rapidly reduced for all three devices, down to 12 ${}^{mA}/{}_{cm^{-2}}$. Therefore, the overall power conversion efficiency is rapidly decreasing from 18% to only 4% (see **Fig. 7.7(a)**). Normally, V_{OC} is not affected by the R_{series}, the obtained V_{OC} behavior of D-A, D-B, and D-C devices are demonstrated in **Fig. 7.7(a)**. In parallel, increasing R_{shunt} leads to a rapid increase in FF and PCE values (**Fig.**

7.7(b)), While V_{OC} and J_{SC} are only slightly affected by R_{shunt}, the better fill factor mainly explains the improvement in device performance here.

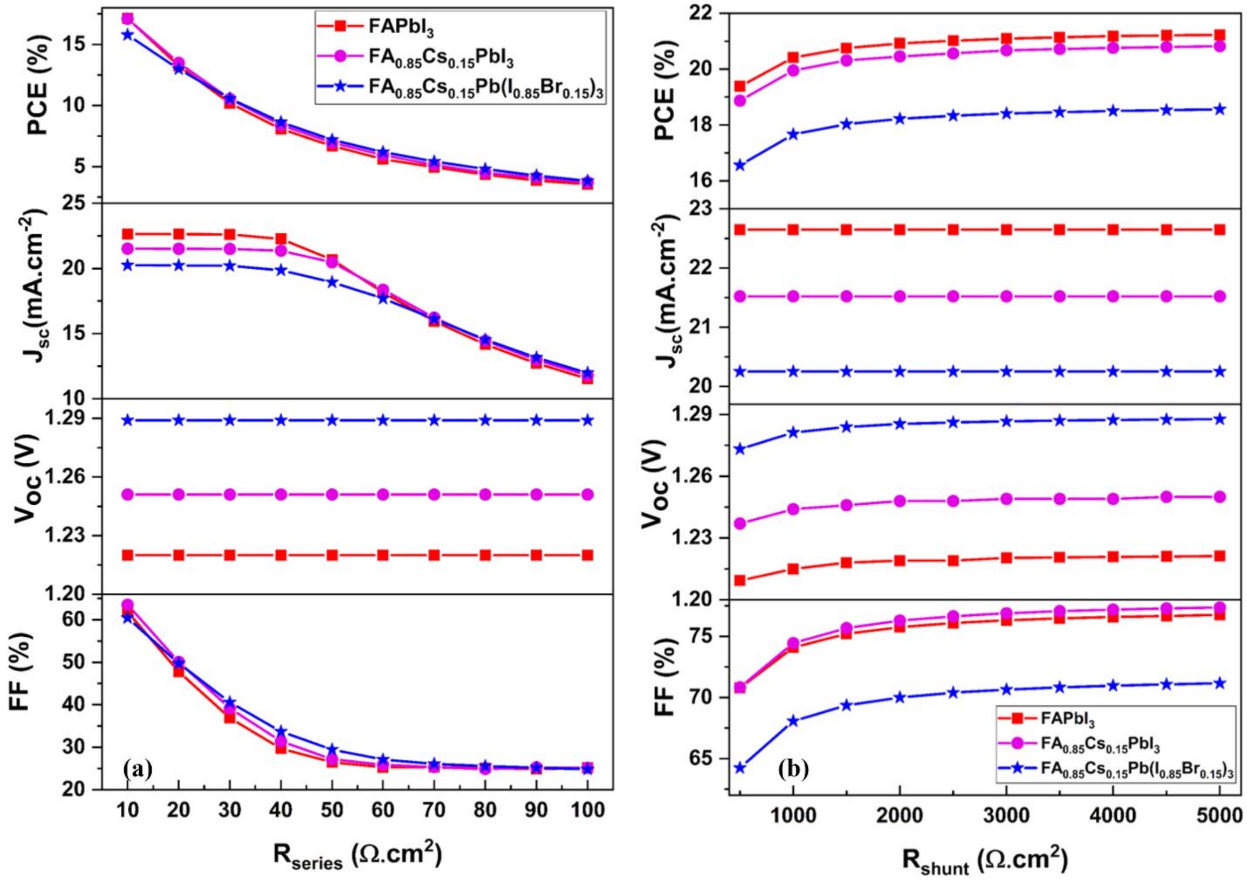

Fig. 7.7. *Effect of R_{series} in the performance of simulated D-A, D-B, and D-C devices. R_{shunt} is assumed as infinite in this case.*

Following these general trends in device behavior, which are obviously consistent with the reported literature on photovoltaic device performance and simulation, we finally tried to feed our SCAPS simulations using the experimental values of parasitic resistances (R_{series} and R_{shunt}) extracted from the measured J-V characteristics shown in **Fig. 7.4**. The simulated J-V characteristics obtained for devices D-A, D-B and D-C in these conditions are plot in **Fig. 7.8** below, while **Table 7.4**. summarizes the photovoltaic parameters obtained on experimental and non-ideal simulated devices. Considerable changes are now occurring for the performance of the simulated devices. All photovoltaic parameters are impacted by the parasitic resistances, which is clearly expected, as discussed previously.

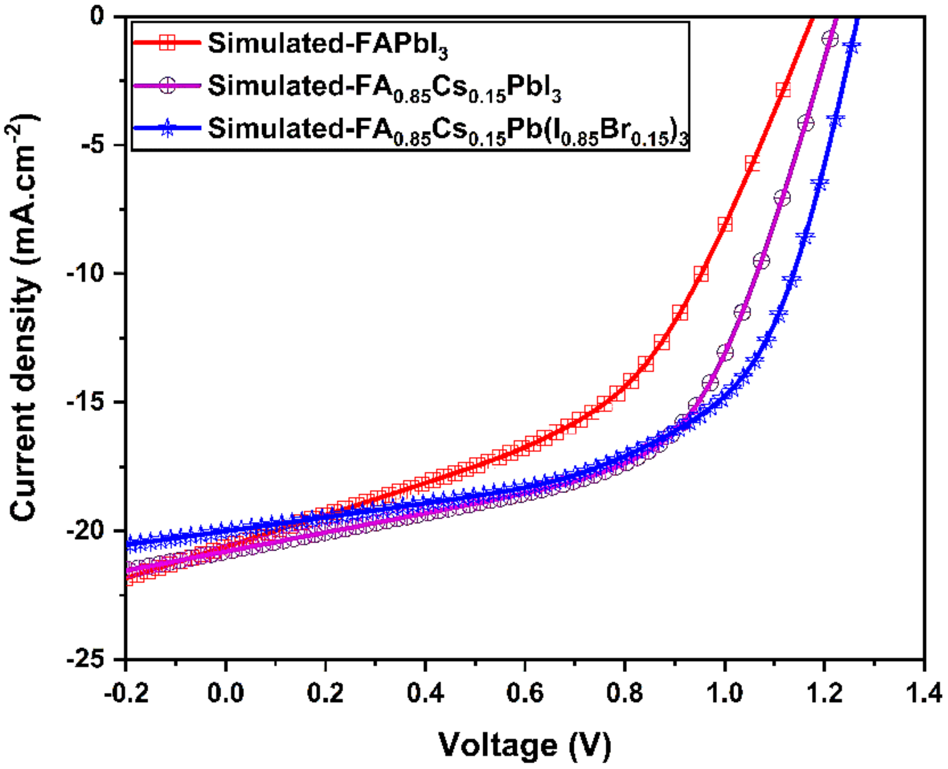

Fig. 7.8. *Simulated J-V characteristic results of D-A, D-B, and D-C.*

Table 7.4. *Comparison of experimental FW scan device performances of D-A, D-B, and D-C with the simulated devices (after feeding R_{series} and R_{shunt}).*

Device	**Data**	**Scan**	J_{SC} mA/cm^2	**FF (%)**	V_{oc} **(V)**	**PCE (%)**	R_{series} **(Ω)**	R_{shunt} **(Ω)**
D-A	Ex	FW	16.6	40.6	0.6	4.3	73	744
	Sim		20.6	47.4	1.1	11.5		
D-B	Ex	FW	21.4	51.6	0.9	9.9	45	1312
	Sim		20.8	56.9	1.2	14.5		
D-C	Ex	FW	22.6	64.4	1.0	15.1	22	1854
	Sim		20.0	58.2	1.2	14.7		

After feeding R_{series} and R_{shunt} values into the simulated D-A, D-B, and D-C devices, we noticed the performances were decreasing compared to ideal devices, as shown in **Table 7.4**. Interestingly, this simple approach shows that the slopes at open-circuit and short-circuit of the simulated J-V characteristics are comparable to experimental data (as pointed out in **Fig. 7.4**). The high V_{oc}, FF, and J_{SC} value of the mixed cation (Cs^+) mixed halide (Br^-) device in terms of improved electronic properties: electron mobility, which is highly improved (so a lower R_{series}). Probably also there are less defect states and interface states, which are responsible for higher R_{shunt}. V_{oc} is also improved due to the larger bandgap (as the conduction band is less deep), so the theoretical V_{oc} should be larger.

Cs^+ and Br^- incorporated D-B and D-C devices showing a highly improved FF value compared to device D-A due to their improved charge transfer capacity. Especially, the absorber layer of device D-C exhibiting the n-type semiconducting behavior by means of an electron being the majority carrier (as mentioned before, high charge carrier mobility) [9]. In addition, both long charge carrier diffusion length and the slow recombination kinetics also strongly modifies the photovoltaic performance [4], [17], those are the main reasons for their enhanced device performance than other two, shown in **Table 5.1** and **Table 7.4**.

7.3. Conclusion

In this section, the experimental and numerically simulated performance of planar FA-based perovskite solar cells is investigated and presented. First, our experimental devices clearly illustrate that the incorporation of both Cs^+ and Br^- ions in the $FAPbI_3$ perovskite structure (device D-C) is leading to the highest photovoltaic response among the tested devices, with a power conversion efficiency above 15%. This performance is a consequence of improved stability in ambient conditions. SCAPS simulations of ideal devices with ideal parasitic resistances confirmed that the pure FA-based perovskite is the most interesting active layer to achieve high photocurrents due to its lower optical bandgap. However, its instability in open-air justifies the use of stabilizing ions such as Cesium or Bromide. Moreover, real devices can be fully understood only by accounting for reasonable series and shunt resistances, which allow the consideration of recombination losses or leakages. Using this strategy, using SCAPS, we were able to estimate the influence of Cesium and Bromide on the FA-based perovskite active layer performance. The combination of both elements is responsible for an improvement of device operation through improved charge transport, reduced recombination, and better stability in ambient conditions. A good correlation between experimental and simulated devices can lead to a better understanding in the charge generation mechanism and active layer performance.

References

[1] S. Wozny *et al.*, "Controlled Humidity Study on the Formation of Higher Efficiency Formamidinium Lead Triiodide-Based Solar Cells," *Chem. Mater.*, 2015, doi: 10.1021/acs.chemmater.5b01691.

[2] Q. Han *et al.*, "Single Crystal Formamidinium Lead Iodide (FAPbI3): Insight into the Structural, Optical, and Electrical Properties," *Adv. Mater.*, 2016, doi: 10.1002/adma.201505002.

[3] Z. Wang *et al.*, "Efficient and Air-Stable Mixed-Cation Lead Mixed-Halide Perovskite Solar Cells with n-Doped Organic Electron Extraction Layers," *Adv. Mater.*, 2017, doi: 10.1002/adma.201604186.

[4] D. P. McMeekin *et al.*, "A mixed-cation lead mixed-halide perovskite absorber for tandem solar cells," *Science (80-.).*, 2016, doi: 10.1126/science.aad5845.

[5] K. A. Bush *et al.*, "23.6%-efficient monolithic perovskite/silicon tandem solar cells with improved stability," *Nat. Energy*, 2017, doi: 10.1038/nenergy.2017.9.

[6] M. Yang *et al.*, "Effect of non-stoichiometric solution chemistry on improving the performance of wide-bandgap perovskite solar cells," *Mater. Today Energy*, 2018, doi: 10.1016/j.mtener.2017.10.001.

[7] Z. Hu, H. Xiang, M. Schoenauer Sebag, L. Billot, L. Aigouy, and Z. Chen, "Compact layer free mixed-cation lead mixed-halide perovskite solar cells," *Chem. Commun.*, 2018, doi: 10.1039/c7cc06183h.

[8] B. G. H. M. Groeneveld *et al.*, "Stable Cesium Formamidinium Lead Halide Perovskites: A Comparison of Photophysics and Phase Purity in Thin Films and Single Crystals," *Energy Technol.*, 2020, doi: 10.1002/ente.201901041.

[9] S. Prathapani, P. Bhargava, and S. Mallick, "Electronic band structure and carrier concentration of formamidinium-cesium mixed cation lead mixed halide hybrid perovskites," *Appl. Phys. Lett.*, 2018, doi: 10.1063/1.5016829.

[10] Z. Li, M. Yang, J. S. Park, S. H. Wei, J. J. Berry, and K. Zhu, "Stabilizing Perovskite Structures by Tuning Tolerance Factor: Formation of Formamidinium and Cesium Lead Iodide Solid-State Alloys," *Chem. Mater.*, 2016, doi: 10.1021/acs.chemmater.5b04107.

[11] J. Huang, P. Xu, J. Liu, and X. Z. You, "Sequential Introduction of Cations Deriving Large-Grain CsxFA1−xPbI3 Thin Film for Planar Hybrid Solar Cells: Insight into Phase-Segregation and Thermal-Healing Behavior," *Small*, 2017, doi: 10.1002/smll.201603225.

[12] J. W. Lee, D. H. Kim, H. S. Kim, S. W. Seo, S. M. Cho, and N. G. Park, "Formamidinium and cesium hybridization for photo- and moisture-stable perovskite solar cell," *Adv. Energy Mater.*, 2015, doi: 10.1002/aenm.201501310.

[13] Y. Yu *et al.*, "Improving the Performance of Formamidinium and Cesium Lead Triiodide Perovskite Solar Cells using Lead Thiocyanate Additives," *ChemSusChem*, 2016, doi: 10.1002/cssc.201601027.

[14] C. Yi *et al.*, "Entropic stabilization of mixed A-cation ABX3 metal halide perovskites for high performance perovskite solar cells," *Energy Environ. Sci.*, 2016, doi: 10.1039/c5ee03255e.

[15] D. Prochowicz *et al.*, "Engineering of Perovskite Materials Based on Formamidinium and Cesium Hybridization for High-Efficiency Solar Cells," *Chem. Mater.*, 2019, doi: 10.1021/acs.chemmater.8b04871.

[16] O. Nazarenko, S. Yakunin, V. Morad, I. Cherniukh, and M. V. Kovalenko, "Single crystals of caesium formamidinium lead halide perovskites: Solution growth and gamma dosimetry," *NPG Asia Mater.*, 2017, doi: 10.1038/am.2017.45.

[17] W. Rehman *et al.*, "Photovoltaic mixed-cation lead mixed-halide perovskites: Links between crystallinity, photo-stability and electronic properties," *Energy Environ. Sci.*, 2017, doi: 10.1039/c6ee03014a.

[18] C. M. Sutter-Fella *et al.*, "Cation-Dependent Light-Induced Halide Demixing in Hybrid Organic-Inorganic Perovskites," *Nano Lett.*, 2018, doi: 10.1021/acs.nanolett.8b00541.

[19] M. Saliba *et al.*, "Cesium-containing triple cation perovskite solar cells: Improved stability, reproducibility and high efficiency," *Energy Environ. Sci.*, 2016, doi: 10.1039/c5ee03874j.

[20] S. Abdelaziz, A. Zekry, A. Shaker, and M. Abouelatta, "Investigating the performance of formamidinium tin-based perovskite solar cell by SCAPS device simulation," *Opt. Mater. (Amst).*, 2020, doi:

10.1016/j.optmat.2020.109738.

[21] F. Azri, A. Meftah, N. Sengouga, and A. Meftah, "Electron and hole transport layers optimization by numerical simulation of a perovskite solar cell," *Sol. Energy*, 2019, doi: 10.1016/j.solener.2019.02.017.

[22] G. Haidari, "Comparative 1D optoelectrical simulation of the perovskite solar cell," *AIP Adv.*, 2019, doi: 10.1063/1.5110495.

[23] Y. Kuang *et al.*, "Low-Temperature Plasma-Assisted Atomic-Layer-Deposited SnO2 as an Electron Transport Layer in Planar Perovskite Solar Cells," *ACS Appl. Mater. Interfaces*, 2018, doi: 10.1021/acsami.8b09515.

[24] J. I. Pankove and D. A. Kiewit, "Optical Processes in Semiconductors," *J. Electrochem. Soc.*, 1972, doi: 10.1149/1.2404256.

[25] S. Tao *et al.*, "Absolute energy level positions in tin- and lead-based halide perovskites," *Nat. Commun.*, 2019, doi: 10.1038/s41467-019-10468-7.

[26] L. C. Chen, Z. L. Tseng, and J. K. Huang, "A study of inverted-type perovskite solar cells with various composition ratios of (FAPBI3)1−x(MAPbBr3)x," *Nanomaterials*, 2016, doi: 10.3390/nano6100183.

[27] F. Ma, J. Li, W. Li, N. Lin, L. Wang, and J. Qiao, "Stable α/δ phase junction of formamidinium lead iodide perovskites for enhanced near-infrared emission," *Chem. Sci.*, 2016, doi: 10.1039/c6sc03542f.

[28] Y. Zhou and G. Long, "Low density of conduction and valence band states contribute to the high open-circuit voltage in perovskite solar cells," *J. Phys. Chem. C*, 2017, doi: 10.1021/acs.jpcc.6b10914.

[29] M. C. Gélvez-Rueda, N. Renaud, and F. C. Grozema, "Temperature Dependent Charge Carrier Dynamics in Formamidinium Lead Iodide Perovskite," *J. Phys. Chem. C*, 2017, doi: 10.1021/acs.jpcc.7b09303.

[30] M. Salado, L. Calio, R. Berger, S. Kazim, and S. Ahmad, "Influence of the mixed organic cation ratio in lead iodide based perovskite on the performance of solar cells," *Phys. Chem. Chem. Phys.*, 2016, doi: 10.1039/c6cp03851d.

[31] Y. Yu *et al.*, "Synergistic Effects of Lead Thiocyanate Additive and Solvent Annealing on the Performance of Wide-Bandgap Perovskite Solar Cells," *ACS Energy Lett.*, 2017, doi: 10.1021/acsenergylett.7b00278.

[32] J. S. Yun *et al.*, "Humidity-Induced Degradation via Grain Boundaries of HC(NH2)2PbI3 Planar Perovskite Solar Cells," *Adv. Funct. Mater.*, 2018, doi: 10.1002/adfm.201705363.

[33] J. P. Correa Baena *et al.*, "Highly efficient planar perovskite solar cells through band alignment engineering," *Energy Environ. Sci.*, 2015, doi: 10.1039/c5ee02608c.

[34] M. Burgelman, P. Nollet, and S. Degrave, "Modelling polycrystalline semiconductor solar cells," *Thin Solid Films*, 2000, doi: 10.1016/S0040-6090(99)00825-1.

[35] U. Rau, "Reciprocity relation between photovoltaic quantum efficiency and electroluminescent emission of solar cells," *Phys. Rev. B - Condens. Matter Mater. Phys.*, 2007, doi: 10.1103/PhysRevB.76.085303.

[36] M. Saliba and L. Etgar, "Current density mismatch in Perovskite solar cells," *ACS Energy Lett.*, 2020, doi: 10.1021/acsenergylett.0c01642.

[37] Y. Li *et al.*, "Ultra-high open-circuit voltage of perovskite solar cells induced by nucleation thermodynamics on rough substrates," *Sci. Rep.*, 2017, doi: 10.1038/srep46141.

8. CHAPTER VIII. Effect of Copper iodide and Bismuth iodide incorporation into the FA-Cs perovskite solar cells.

8.1. Introduction

The chemical composition and stoichiometry of any perovskite structure mainly govern the material's optoelectronic properties and structural stability. For example, the substitution of the MA^{+} cation with FA^{+} allow the reduction of the bandgap of the resulting perovskite. However, while $FAPI$ presents the smallest bandgap among all 3D lead perovskites, it is not thermodynamically stable at room temperature as it turns to the non-perovskite yellow phase (or δ-phase) [1]–[3]. One common solution to address this issue is to mix several cations, such as MA^{+}, FA^{+}, Cs^{+}, or rubidium (Rb^{+}), leading to double, triple, or quadruple-cation perovskite presenting an improved photochemical stability. Such strategies take benefit from simple solution-processing routes for their fabrication and led to highly efficient devices in recent years [4]–[12]. Nevertheless, stability issues still remain to be addressed for these devices in relation with the occurrence of defect-rich interfaces and grain boundaries. Passivation strategies are now widely applied to cure these traps. For example, inserting an interfacial layer (IL) between the electron/hole transporting layer and the perovskite layer can avoid fast degradation due to the perturbed interface, as well as reduce charge carrier recombination [13]–[16]. Other strategies have also been explored in order to stabilize and enhance the intrinsic properties of perovskite active layers, such as doping with hetero elements [17]–[24].

Another major drawback of perovskite devices is the presence of lead (Pb), which is toxic and does not comply with current safety regulations [25], [26]. Lead halide perovskites generally decompose, after a certain time, releasing harmful soluble lead salts [27], [28]. While several approaches are today proposed to avoid Pb release during solar cell operation [29], going towards Pb-free devices appears as a crucial challenge for the commercial reality of perovskite solar cells. To achieve lead-free environmental-friendly devices, several research groups have been focusing on lead substitution by suitable elements. Precisely, full or partial replacement by transition and alkaline earth metals or lanthanide elements gained a lot of attention. While these substitutions significantly alter the electronic properties of the active layer properties, they demonstrate regular improvement in their efficiencies and stability, enabling the demonstration of more unharmful devices [28]. Besides, those substitutions show some issues such as oxidation, which led to poor stability, increasing optical bandgap (E_g) values which constrain the absorbance behavior, or lead to poor conductive properties [17]–[24]. Therefore, with less toxicity and suitable element substitution into the absorber layer is essential to get an environmentally free device with enhanced PV performance. Hence, in this broad context, the following section focused on reduced-lead absorbers-based PSCs, especially the Copper (Cu^+) or Bismuth (Bi^+) are partialy incorporated with Pb in the FA-Cs perovskite composition, and the obtained PV performances were compared with the undoped (or reference) cell.

8.2. Results and Discussion

8.2.1. CuI and BiI$_3$ incorporated mixed cation perovskite solar cells

This sub-section focused on doping a halide perovskite with Copper (Cu^+) or Bismuth (Bi^+) is particularly relevant to reduce the lead content in the active layer while trying to reduce the intrinsic limitations of FAPI devices in terms of stability and defect states. According to the previous reports, Cu- and Bi-doped perovskites can show improved absorption properties (range and threshold), as well as enhanced electrical conductivity [30]–[37]. Some published works on Bi doping [38] and Cu doping [35] show better device performance, but many results show more unsatisfactory performance [31], [39]. Mainly, incorporating Bi generates the recombination center due to their Bi impurities, as well as it creates a shallow and deep level electronic states in the bandgap [39]. So, here we want to give another view of this doping strategy and try to point out the specific aspects that govern the beneficial effect of doping. Therefore, in this section, partial incorporation of Cu and Bi atoms into the reference double cation $FA_{0.85}Cs_{0.15}Pb(I_{0.85}Br_{0.15})_3$ perovskite layer was conducted from the simple addition of Cuprous iodide (CuI) or Triiodobismuthane (BiI_3) into the perovskite precursor solution. We especially focus on the influence of the atomic fraction of the Cu and Bi dopant (x in the range 0 to 0.15) on active layer morphology, structure, and optoelectronic properties, including *n-i-p* planar perovskite solar cell performance. Charge recombination is also assessed, and a preliminary stability study under continuous illumination is also performed to rationalize the main critical parameters governing the doping mechanisms.

Undoped, as well as Cu- and Bi-doped double cation $FA_{0.85}Cs_{0.15}Pb(I_{0.85}Br_{0.15})_3$ perovskite films, with $x = 0.01, 0.05, 0.10$, and 0.15, were prepared from a solution to investigate their structural, morphological, topographical, and optical properties. All the conventional characterizations were performed on the films deposited on glass/SnO_2 substrates. **Fig. 8.1** presents the SEM images of the deposited thin layers as a function of doping ratio x. AFM images, which show very similar features, are shown in **Fig. 8.2**). The images clearly demonstrate that the undoped layer has a quite smooth and compact surface with no pinholes or voids, with an average grain dimension in the order of 48 ± 3.2 nm. The root-mean-square (RMS) surface roughness extracted from AFM analysis is found at 6 nm for the reference layer (see **Table 8.1**).

Through Cu-incorporation, the average grain size regularly increases from 90 ± 5 to 130 ± 5 nm, for the doping ratio of 0.01 and 0.15, respectively. A similar trend was observed in previous reports devoted to Cu doping through various precursors (such as CuI, $CuCl_2$ and $CuBr_2$) [31], [35], [36]. Most importantly, tiny particles are observable at the grain boundaries of films doped with Copper, and it might be associated with Copper-rich inclusions (see **Fig. 8.1c** or **1e**).

The RMS roughness values of the Cu-doped films are found to be smaller than that of the reference, which is in accordance with the larger grains observed. Such reduced surface roughness is generally a requirement towards efficient devices, as it favors a high-quality interface with the HTL improving charge collection [40]. On the other side, doping with Bismuth drastically alters the film morphology (see **Fig. 8.1f-i**). For $x = 0.01$ and 0.05, Bi-doped films have a smaller grain size than the undoped sample (the RMS roughness increases, accordingly). For a larger doping ratio, the morphology is utterly different, with flower-like particles. Bartolomé *et al.* observed such rod-like structures while doping a $MAPI$ perovskite with Bi and they also noticed an increase in the volume of the grains and of the density of the film as a function of Bi content [41].

On the contrary, Bi-containing $FAPI$ perovskite films show a compact and smooth surface, with larger crystal grains than the undoped one [38]. The trend was again different for Bi-doped inorganic cesium based perovskites ($CsPb_{1-x}Bi_xI_3$), which showed a considerable decrease of the grain size while increasing the Bi content [42]. All these observations clearly emphasize the critical influence of Bi on the perovskite layer morphology, where Copper seems to be more easily introduced in the structure (as confirmed by the decreased RMS roughness evidenced, see **Table 8.1**). Considering the quite important fraction of dopants introduced for $x = 0.15$, we also deposited the 100%-containing Bi or Cu materials, by fully substituting the PbI_2 precursor by either CuI or BiI_3.

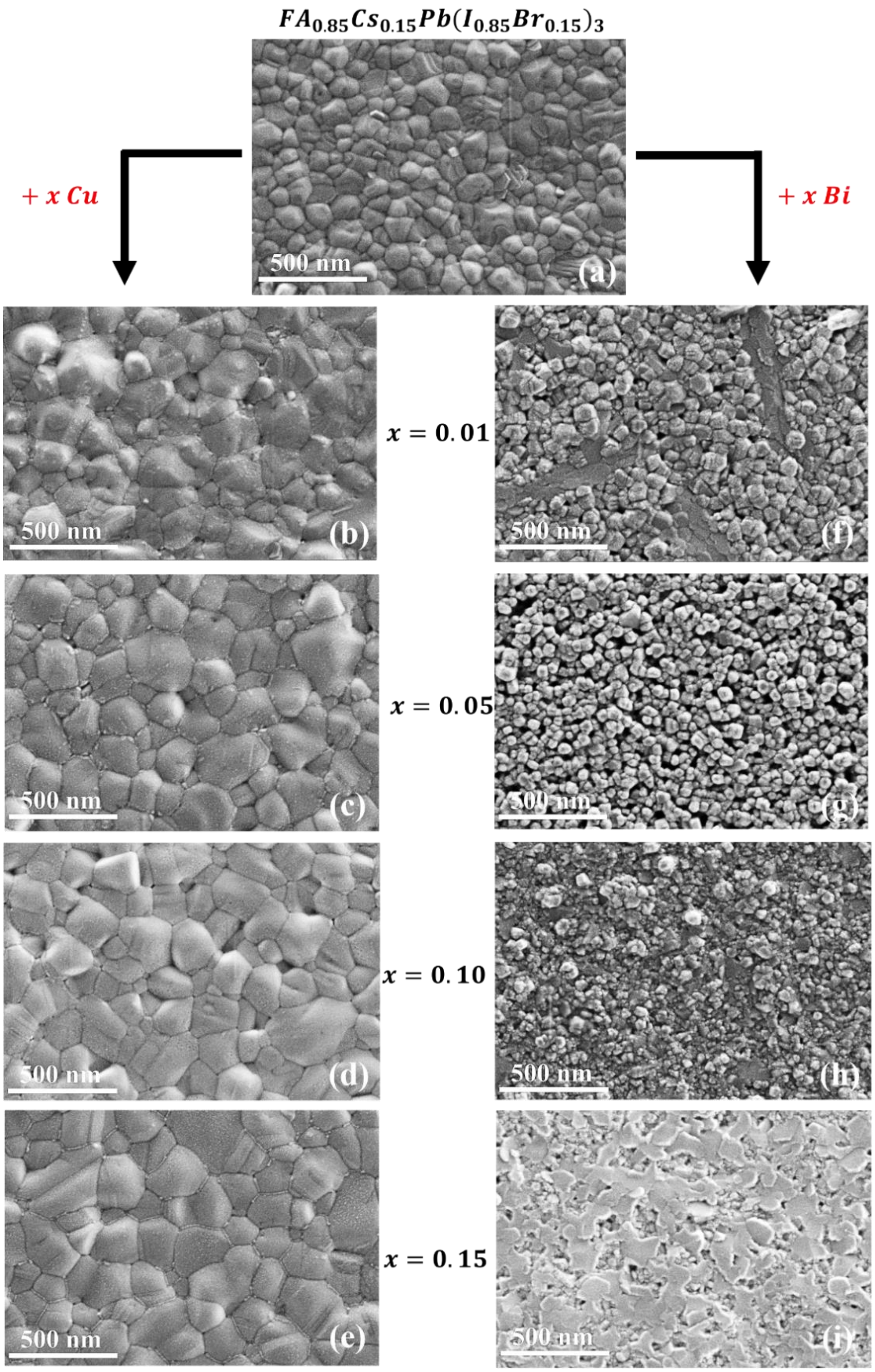

Fig. 8.1. *SEM photographs of undoped* $FA_{0.85}Cs_{0.15}Pb(I_{0.85}Br_{0.15})_3$ *as well as both* Cu *and* Bi *- doped perovskite films. Scale bar: 500 nano-meter.*

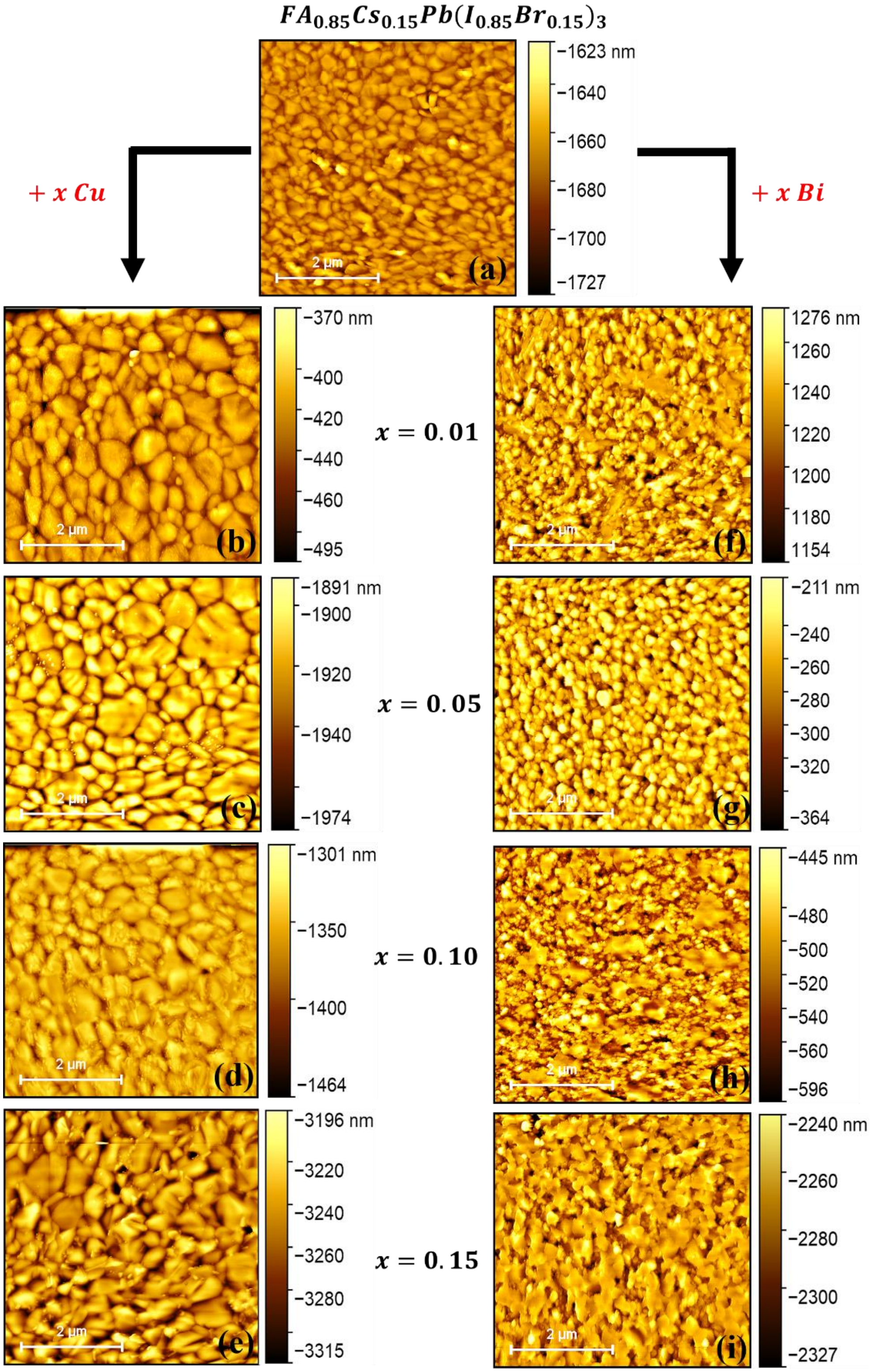

Fig. 8.2. *AFM topographical images of undoped* $FA_{0.85}Cs_{0.15}Pb(I_{0.85}Br_{0.15})_3$*, as well as both* Cu*- and* Bi*-doped perovskite films. Horizontal scale bar: 2 µm.*

Table 8.1. *Estimated grain size and RMS roughness values for the different layers.*

Layers	Grain size (nm)	Root mean square roughness $(\boldsymbol{RMS})$ (nm)
undoped	48 ± 4	6.0
$\mathbf{Cu:\ x = 0.01}$	90 ± 5	4.9
$\mathbf{Cu:\ x = 0.05}$	106 ± 5	3.6
$\mathbf{Cu:\ x = 0.10}$	119 ± 5	4.1
$\mathbf{Cu:\ x = 0.15}$	130 ± 5	3.5
$\mathbf{Bi:\ x = 0.01}$	41 ± 3	7.4
$\mathbf{Bi:\ x = 0.05}$	32 ± 2	11.7
$\mathbf{Bi:\ x = 0.10}$	24 ± 2	6.8
$\mathbf{Bi:\ x = 0.15}$	15 ± 1	5.5

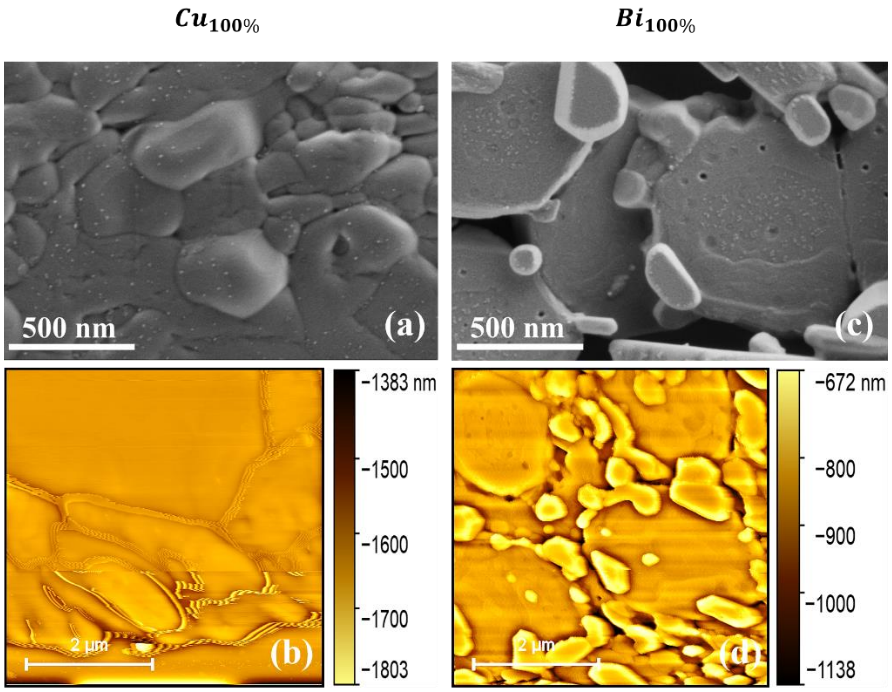

Fig. 8.3. *SEM and AFM images corresponding to fully doped $Cu_{100\%}$ and $Bi_{100\%}$ layers. Scale bar: 500 nm for SEM and Horizontal scale bar: 2 µm for AFM images.*

Table 8.2. *Estimated RMS value for both $Cu_{100\%}$ and $Bi_{100\%}$ doped perovskite films.*

Layers	Root mean square roughness (RMS) (nm)
$\mathbf{Cu_{100\%}}$	4.2
$\mathbf{Bi_{100\%}}$	12.9

The SEM and AFM images corresponding to these so-called $Cu_{100\%}$ and $Bi_{100\%}$ compounds are presented as supplementary materials in **Fig. 8.3**. Their RMS roughness values are also given in

Table 8.2. While their morphology is found to be quite different from that of the perovskite reference, we will show in the next sections that these Pb-free layers also show a different crystalline structure.

Further information are gathered from X-ray diffraction experiments performed on the layers, as reported in **Fig. 8.4a** and **b**. The XRD pattern of the $FA_{0.85}Cs_{0.15}Pb(I_{0.85}Br_{0.15})_3$ reference perovskite film exhibits the main contributions (indicated on the diagram) of the α-phase (black phase), for example, the peak centered around 14.2°, which is assigned to the (100) plane family [10]. The calculated average crystallite size values for $(CuI)_x$ doped films represented as 42.2 nm, 37.2 nm, 36.9 nm, and 42.3 nm for x= 0.01, 0.05, 0.10, 0.15, respectively, simultaneously, 37.2 nm, 33.7 nm, 33.2 nm, and 36.6 nm for $(BiI)_x$ (where, x=0.01, 0.05, 0.10, 0.15) incorporated films showing different tones than undoped films (39.1 nm), it possibly related to their different morphology behavior. While the overall features of the XRD diffractogram, it seems to be maintained through doping with Copper, some more drastic changes are observed in the case of Bismuth, and especially for the large doping content. In both cases, small peak shifts are evidenced: towards higher angle values for Copper and towards smaller angle values for Bismuth (see **Fig. 8.5)**. When such shifts do not come with any significant evolution of the XRD pattern, they can suggest the effective doping of the perovskite lattice by Cu and Bi (at least for low x values in the latter case). Song *et al.* mentioned that the appropriate amount of Cu ions (coming from CuI and $CuCl_2$ in the precursor in this case) into the $FAPI$ perovskite solution can indeed suppress the yellow δ-phase, while promoting a better crystallization of the black α-phase [31].

Our data also agree with Jahandar *et al.* [36] who doped $MAPI$ perovskite using $CuBr_2$ [43]. In this case, the shift in XRD peaks was attributed to a decrease of lattice parameter corresponding to the exchange of larger I^- with smaller Br^- ions, illustrating the influence of the halide. In the case of excess Bi incorporation (for large x values), a fraction of the Pb-free $MA_3Bi_2I_9$ pseudo-perovskite phase can also be formed [41]. In our case, the presence of $FA_3Bi_2I_9$ pseudo-perovskite phase [44] noticed in the 100% Bi-doped XRD peaks (see **Fig. 8.6**). The main plane families belonging to the formamidinium perovskite α-phase are indicated in the evolution of the FWHM of the perovskite (100) plane around $2\theta = 14.2°$ as a function of doping ratio x in both cases, shown in **Fig. 8.5**.

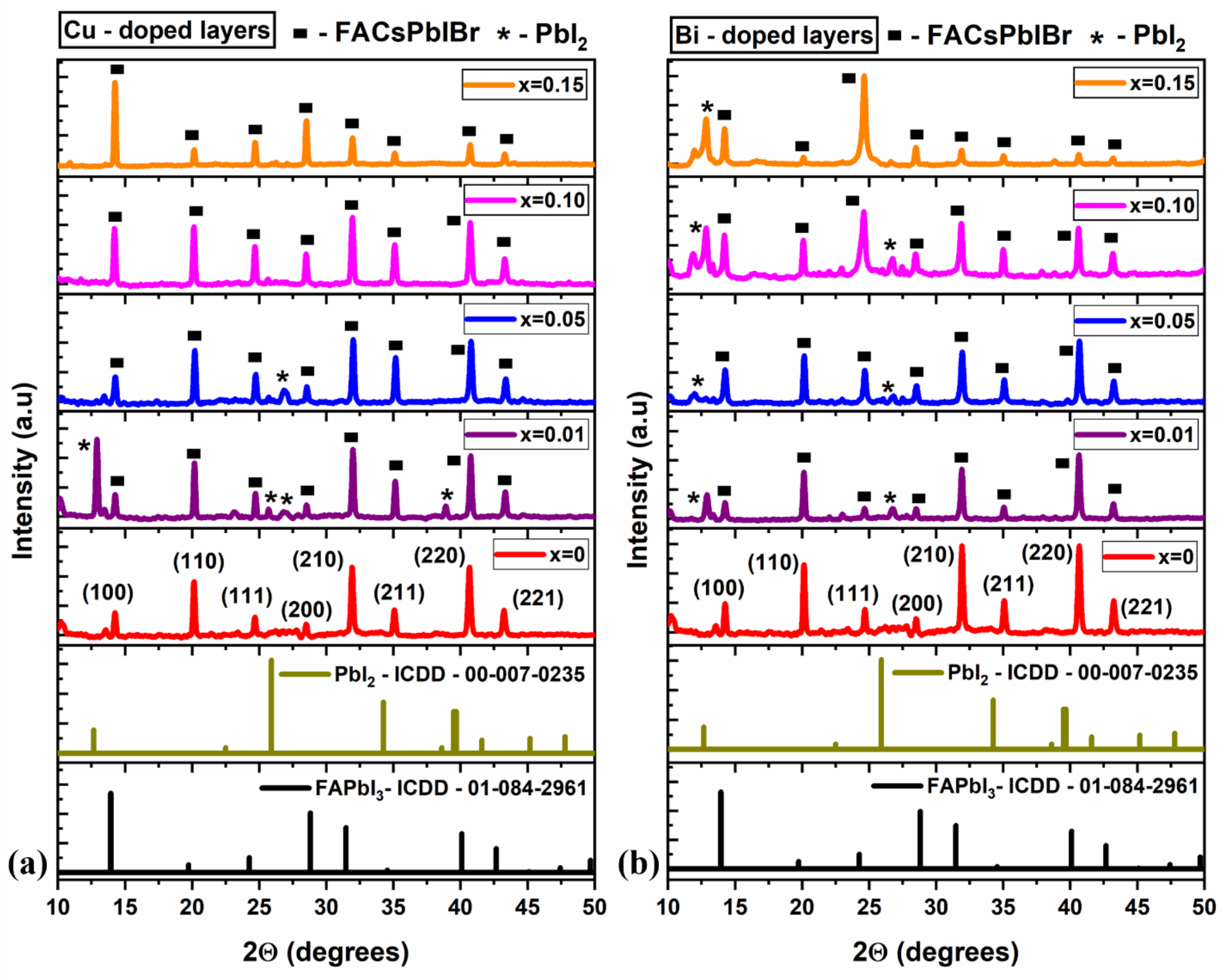

*Fig. 8.4. XRD diffractogram of Cu-doped (a) and Bi-doped (b) perovskite films, including the undoped reference. In the XRD patterns, □ symbols represent the reference $FACsPbIBr$ crystalline α - phase and * represent the presence of PbI_2 phase.*

Noticeably, the intensities of several peaks displayed in the XRD diffractograms (see **Fig. 8.4**) are not unique due to the occurrence of structural defects or imperfections (i.e., such as dislocations, vacancies, and stacking faults, etc.) while incorporating other elements [45], [46]. Also, environmental conditions, especially humidity (oxygen and moisture), affect or modify the peak positions and peak intensities [47], [48]. The recorded XRD diffractogram of 100% Cu- and Bi-doped films ($Cu_{100\%}$ and $Bi_{100\%}$) also demonstrated in **Fig. 8.6**, and it is revealing that the Cu or either Bi 100% substitution instead of PbI_2 into the solution are influences the structural behavior.

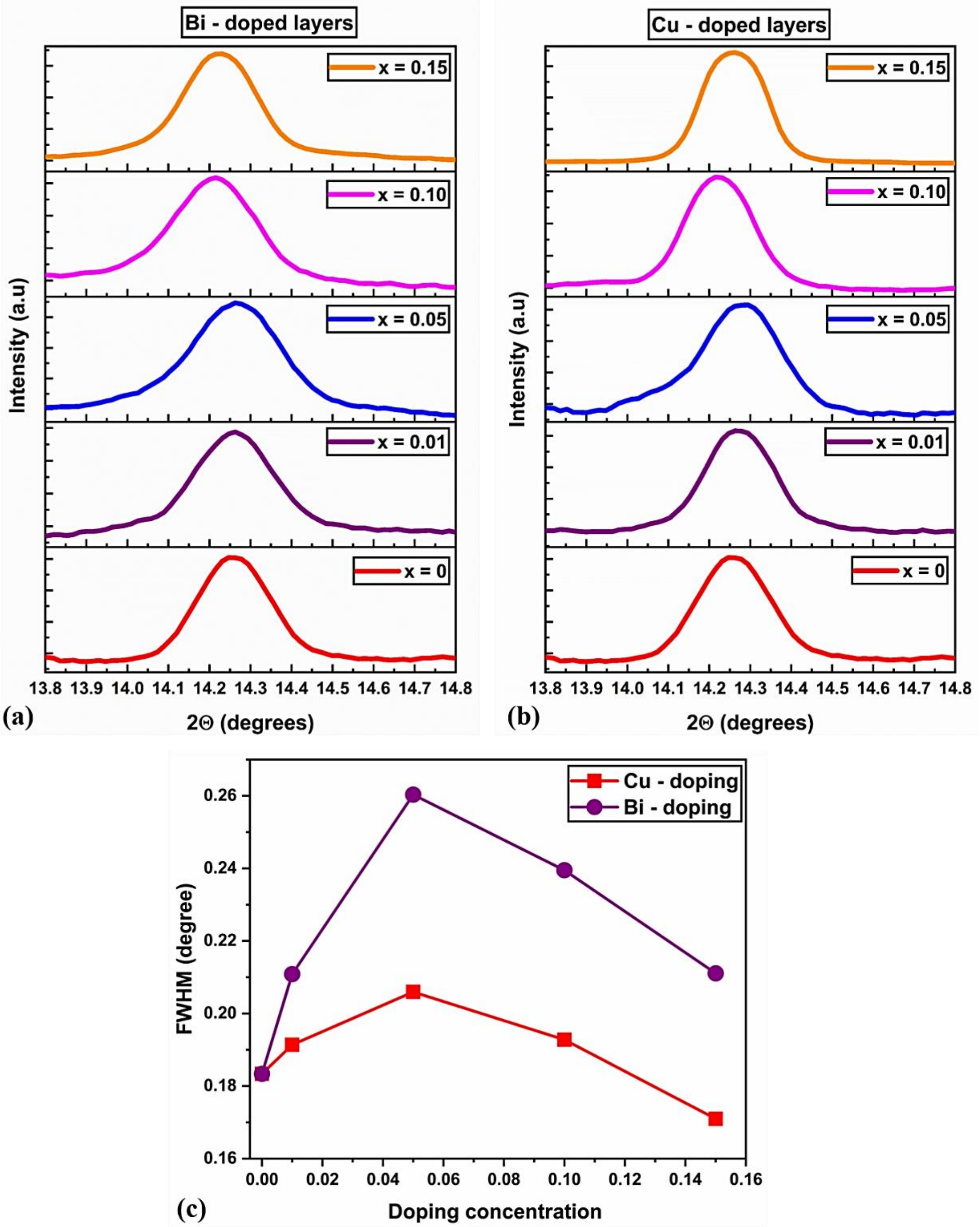

Fig. 8.5. *Magnified XRD diffractogram of 100 planes for* $Cu\,(a)$ *and* $Bi\,(b)$ *doped perovskite films. Evolution of the FWHM (c) of the perovskite (100) plane around* $2\theta = 14.2°$ *as a function of doping ratio* x *in both cases.*

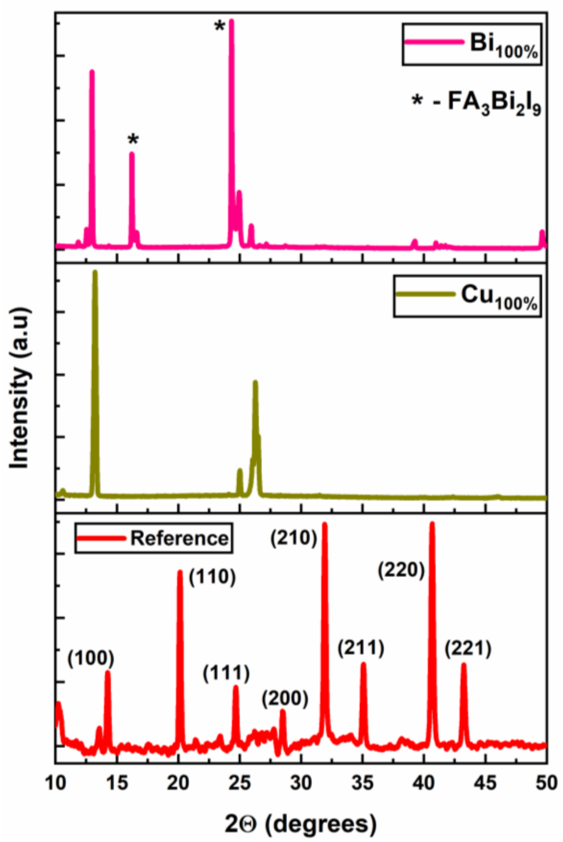

***Fig. 8.6**. Recorded XRD diffractogram of both $Cu_{100\%}$ and $Bi_{100\%}$ doped perovskite films.*

Fig. 8.7 shows the UV-visible absorption spectra of undoped $FA_{0.85}Cs_{0.15}Pb(I_{0.85}Br_{0.15})_3$ layer as well as of doped perovskite layers within the 350 – 900 nm range. The spectra evidence the expected absorption profile of the undoped perovskite layer, with a characteristic absorption band edge at 780 nm [10]. Through doping, we observe a noticeable shift of the optical absorption edge from 780 nm down to ~775 nm in the case of Cu-doped films, while a larger shift (780 nm down to ~750 nm) is observed for Bi-doped films. Also, the recorded Uv-spectra of the $CuI_{100\%}$ and $BiI_{100\%}$ films are presented in **Fig. 8.8**, and importantly, the $CuI_{100\%}$ film demonstrate almost zero absorbance behavior because it's completely transparent compared to the $BiI_{100\%}$ film. There is no evidence for the presence of a significant fraction of the Pb-free $FA_3Bi_2I_9$ phase in these films, as no absorption band can be seen around 550 nm, as in the 100%-containing Bi compounds (see **Fig. 8.8**). Y. Hu *et al.* shows that the inappropriate amount of Bi in $FAPI$ perovskite gradually reduces the absorbance due to the $\delta - phase$ formation [38]. It seems that this effect is occurring in our case, considering the reduction of optical absorption for large x values in the case of Bi doping, in accordance with the evolution of our XRD data presented before (i.e., existence of unavoided PbI_2

peaks). To summarize, the optical absorption of the layers clearly evidences that both doping strategies seem to relatively preserve the optical properties of the undoped perovskite phase, as long as Bi is not introduced in too large amounts.

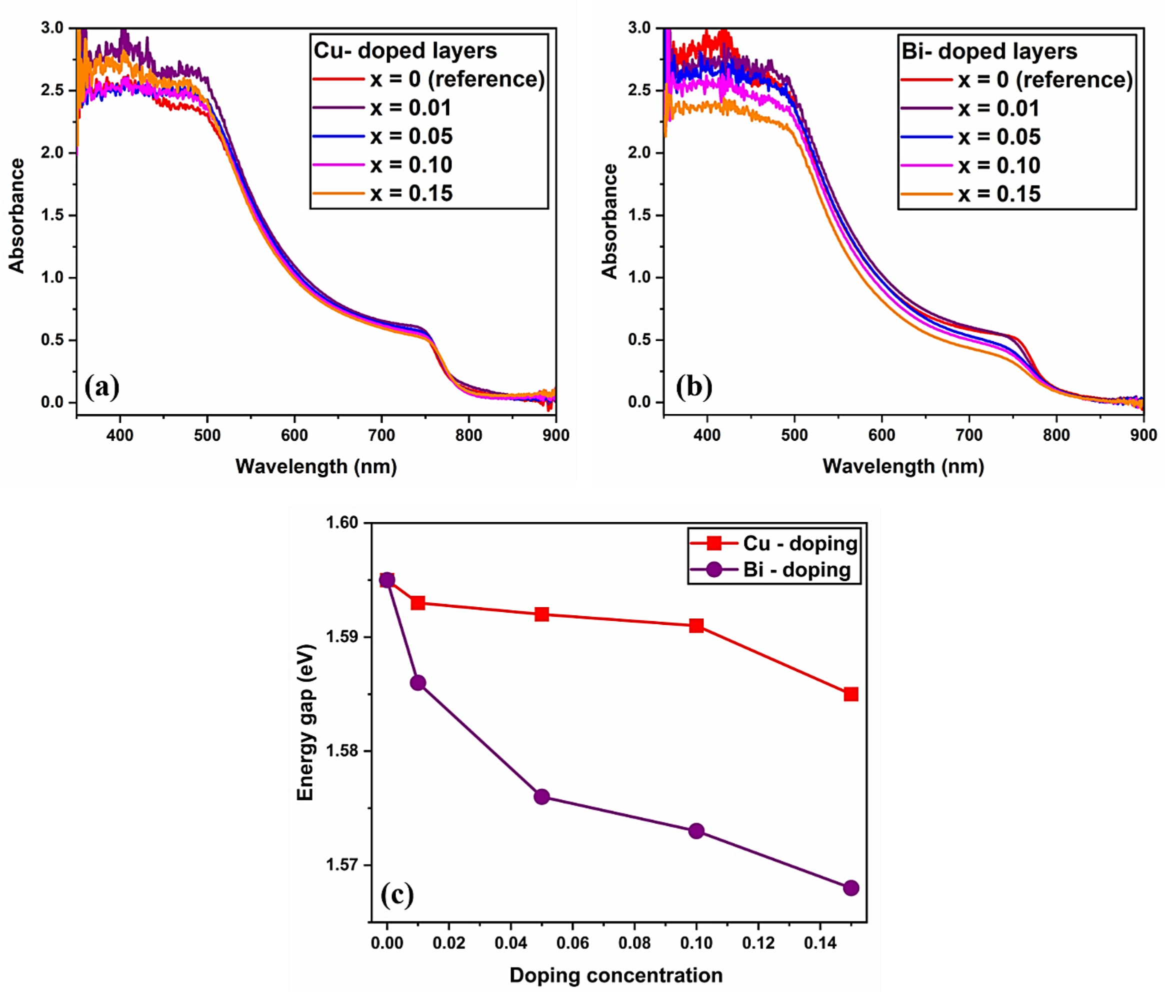

***Fig. 8.7**. Uv-vis absorbance spectra of Cu- (a) and Bi-doped (b) perovskite films. Optical bandgap E_g values (c) estimated from Tauc's law of both Cu- and Bi-doped perovskite films.*

The calculated optical bandgap (E_g) values (see **Fig. 8.7 (c)**, based on Tauc's law for direct optical transitions [10]) are close to that $E_g = 1.59\ eV$ of the undoped reference compounds, as well as Cu- and Bi-doped compounds, which is in good agreement with the reported literatures [10], [31], [41]. A noticeable bandgap reduction is observed as the Bi content increases in the films, this trend being less clear with Copper. A reduction of bandgap is consistent with the cation substitution due to several effects such as the influence of the electronegativity of the dopant on the anti-bonding properties between cations and halides [32], or by the effect of introducing a cation of small ionic radius in B site which can alter the conduction band properties [33]. Both these spotted bandgap narrowing might be associated with the generation of impurity bands within the bandgap [34].

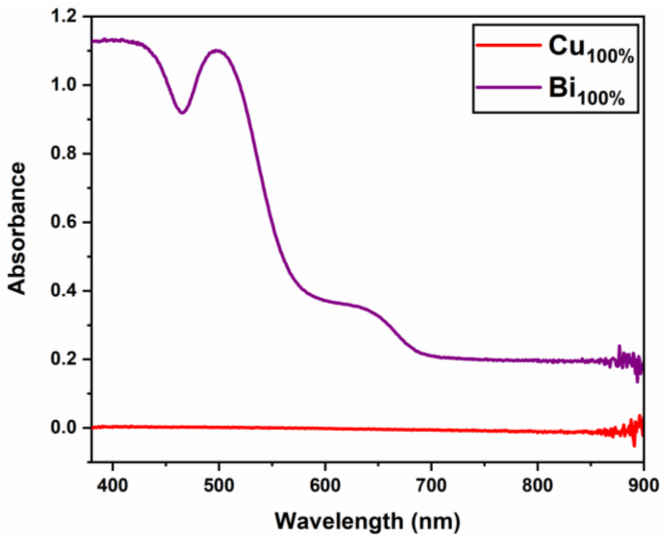

***Fig. 8.8**. Recorded Uv-spectrophotometer photographs of both $Cu_{100\%}$ and $Bi_{100\%}$ doped perovskite films.*

8.2.1.1. Device performance

Cu- and Bi-doped perovskite solar cells were successfully fabricated following the processing steps described in the experimental section.

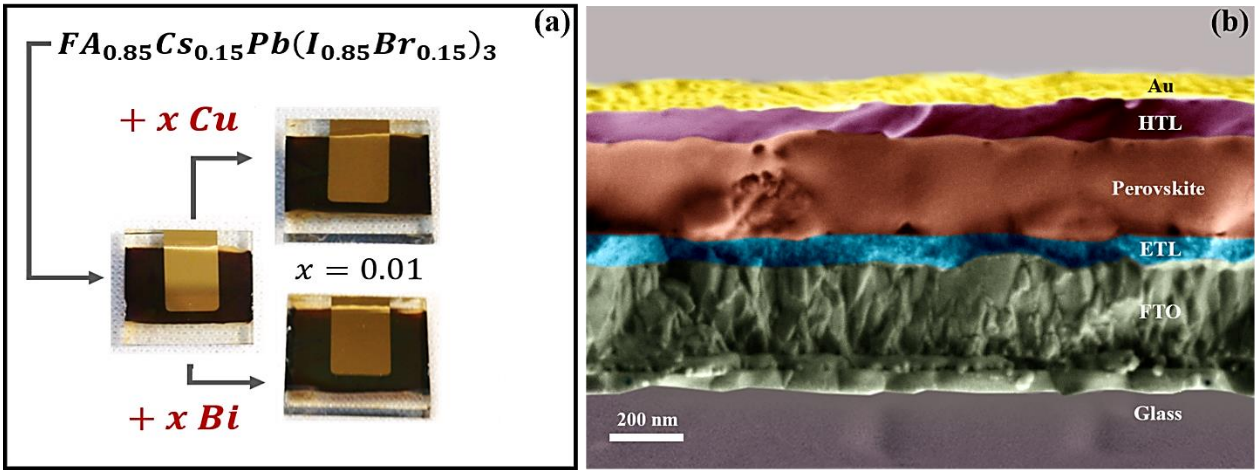

***Fig. 8.9.** (a) Photographs of reference as well as both Cu and Bi-doped perovskite solar cells as a function of dopant content ($x = 0.01$). The substrates are $1{,}2 \times 1{,}2\ mm$. (b) Cross-sectional SEM image of reference device based on the planar FTO/ $SnO_2/perovskites/Sprio/Au$ device configuration.*

The undoped and doped active layers were deposited under an inert atmosphere, while the final unencapsulated devices were characterized in ambient conditions under simulated solar emission

(100 mW.cm^{-2}, AM1.5G). An n-i-p device architecture glass/FTO/SnO_2/Perovskite/Spiro-OmeTAD/Au is employed here, similarly as in our previous work published elsewhere [49]. The photographs and the cross-sectional SEM image of the reference device are presented in **Fig. 8.9.** Also, cross-sectional SEM images of Cu-and Bi-doped devices at $x = 0.15$ are shown in **Fig. 8.10**. In all cases, homogeneous sandwiched structures are observed, with well-defined subsequent planar layers. The cross-section images of the doped devices reflect the morphology evolution of the perovskite active layer, as evidenced by SEM and AFM.

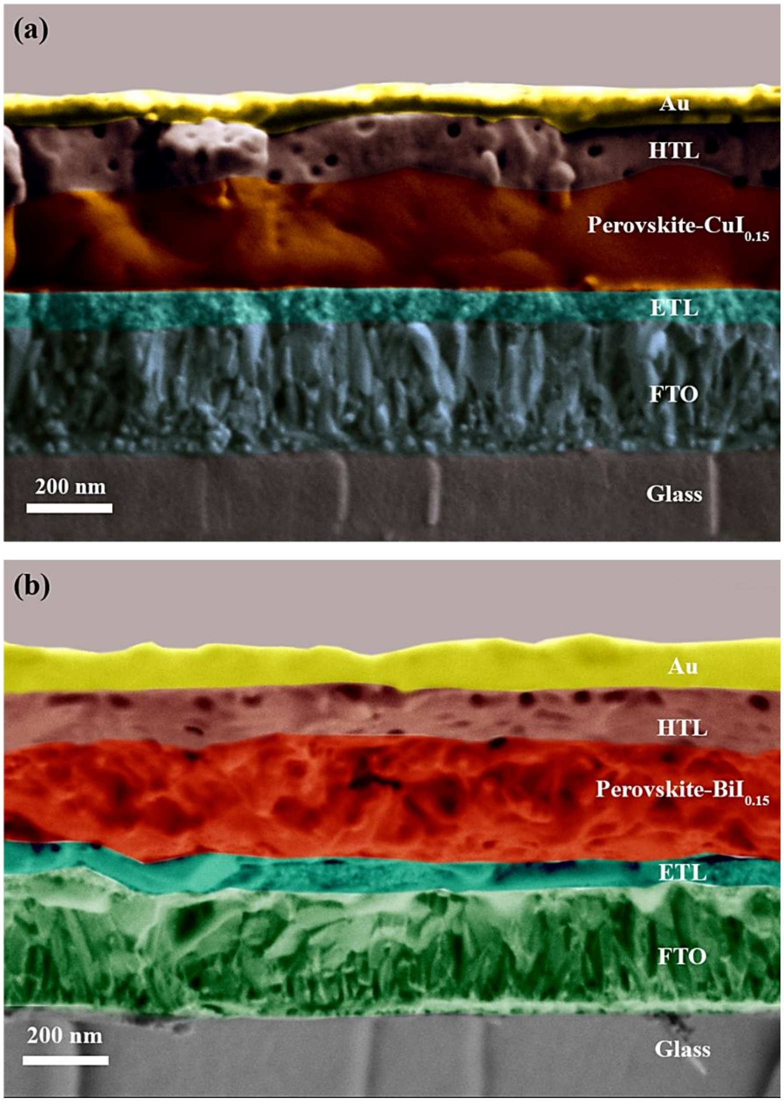

Fig. 8.10. *Cross-sectional SEM images of* Cu $(x = 0.15)$ (a) *and* Bi $(x = 0.15)$ (b) *doped devices based on the planar FTO/* $SnO_2/perovskites/Sprio/Au$ *device configuration.*

Some voids in the HTL layer are observed in the case of the Cu- and Bi-doped devices, compared to the reference. Such voids were largely discussed in the recent literature [50]–[52] and are a consequence of using Li-TFSI and tBP as additives to achieve large charge mobilities and better hole extraction. Although similar HTL preparation and deposition procedure were used in all cases, these voids might also contribute to the reduced photovoltaic performance of doped devices, as presented in the following section. In any case, no pinholes in the active layer are evidenced in all structures.

The current density/voltage characteristics recorded in the backward voltage scan are presented in **Fig. 8.11**, and the corresponding photovoltaic parameters (average values over several cells and champion device) being summarized in **Table 8.3**. The cells displayed a quite large hysteresis effect (see, **Fig. 8.12**), which is related to the fact that no passivation or interfacial engineering strategies were employed in order to reduce the slow transient phenomenon that are responsible for this behavior, such as the migration of halide anions (I^- and Br^-) towards interfaces where space charge can build-up or charge carrier trapping/de-trapping in deep defect states [53], [54].

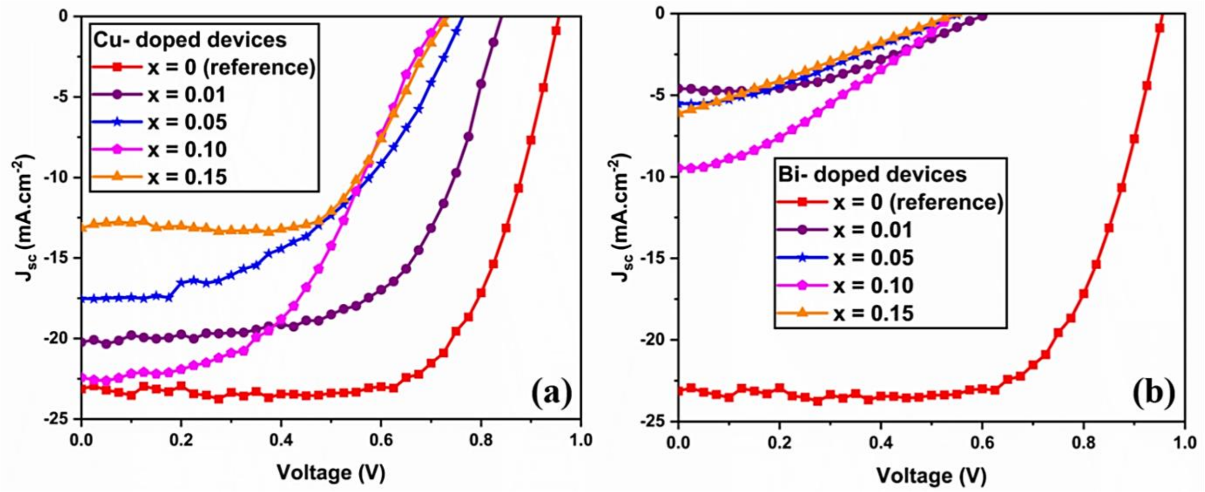

Fig. 8.11. Backward scanned J-V characteristics under standard illumination of undoped, as well as Cu-(a) and Bi-doped (b) perovskite solar devices, as a function of doping ratio x.

In particular, in the case of doped devices, Shi *et al.* theoretically projected that the substitution of Pb by Cu and Bi always generates defects, especially Bi which can produce shallow donor levels near the conduction band edge [55].

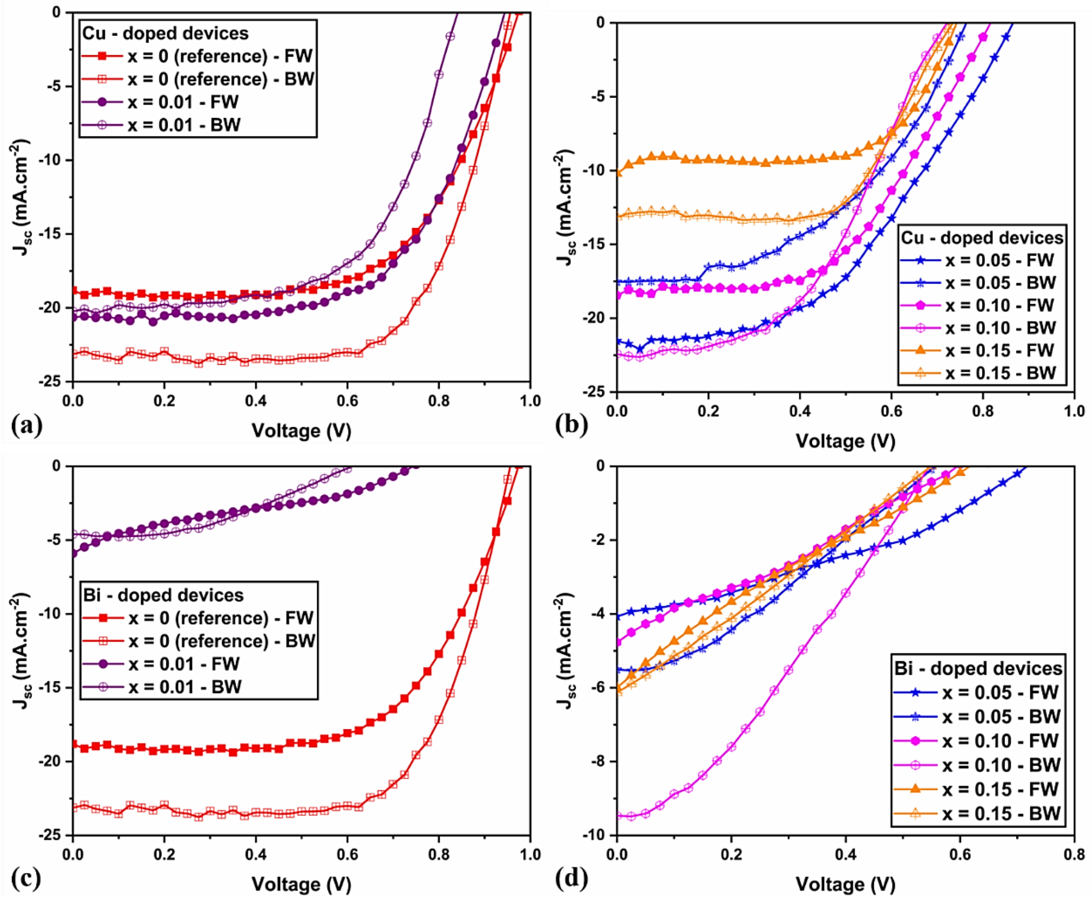

Fig. 8.12. *Recorded J-V characteristics of both* Cu $(a\ and\ b)$ & Bi $(c\ and\ d)$ *incorporated perovskite devices. Both FW and BW corresponding to the forward and backward scans, respectively.*

Table 8.3. *Summarized photovoltaic performance of undoped as well as Cu (a) & Bi (b) doped perovskite devices, respectively. Average values are given in the Table, except for the reference FACs device for which the champion cell is also detailed.*

Device	$J_{sc}\ (^{mA}/_{cm^2})$	FF	V_{oc} (V)	PCE (%)
Reference/Champion cell	23.1	0.68	0.95	15.15
Undoped	22.9 ± 0.9	0.63 ± 0.02	0.93 ± 0.02	13.4 ± 0.8
$\mathbf{Cu:\ x = 0.01}$	20.5 ± 0.9	0.59 ± 0.02	0.91 ± 0.02	10.8 ± 0.9
$\mathbf{Cu:\ x = 0.05}$	19.0 ± 0.9	0.45 ± 0.01	0.81 ± 0.02	7.1 ± 0.4
$\mathbf{Cu:\ x = 0.10}$	17.2 ± 1.2	0.51 ± 0.02	0.76 ± 0.17	6.7 ± 0.4
$\mathbf{Cu:\ x = 0.15}$	12.3 ± 0.8	0.60 ± 0.03	0.65 ± 0.03	4.7 ± 0.3
$\mathbf{Bi:\ x = 0.01}$	4.3 ± 0.6	0.41 ± 0.03	0.58 ± 0.04	1.0 ± 0.1
$\mathbf{Bi:\ x = 0.05}$	4.1 ± 0.5	0.34 ± 0.02	0.52 ± 0.05	0.7 ± 0.1
$\mathbf{Bi:\ x = 0.10}$	5.3 ± 1.0	0.28 ± 0.02	0.49 ± 0.03	0.8 ± 0.2
$\mathbf{Bi:\ x = 0.15}$	4.4 ± 0.7	0.27 ± 0.03	0.57 ± 0.03	0.6 ± 0.1

The best photovoltaic performance is demonstrated for the undoped $FA_{0.85}Cs_{0.15}Pb(I_{0.85}Br_{0.15})_3$ cell, with an average power conversion efficiency (PCE) of 13.4 ± 0.8%. (>15% for the champion cell), This is consistent with our active layer's quality, considering that no specific additive were used to promote a better crystallization nor to cure interfacial defect states. Interestingly, adding a small amount of Cu into the absorber layer significantly reduces device performance down to an average PCE of around 11%, mainly due to a significant diminution in J_{sc}. Meanwhile, increasing x in the case of Copper further reduces the whole performance. While the crystalline quality and overall morphology of the film is maintained for Cu-doped devices, its detrimental effect on device performance might be attributed to the modification of the grain boundaries, especially through the presence of the small particles seen by SEM (**see Fig. 8.1**) and AFM (**see Fig. 8.2**). This effect is accompanied by a significant decrease in V_{OC} (by up to 300 mV), and the R_{Shunt} (from 15500 Ω to ~ 600 Ω) as well as an increment in the R_{Series} (27 Ω to ~ 85 Ω) which tends to indicate that interfacial charge recombination, or localized current leakages due to the presence of highly conductive Copper-rich region [31], are favored in this case. These observations tend to suggest that Cu addition does not positively passivate interfacial trap states, as it was for example seen in CuI incorporated $MAPbI_{3-x}Cl_x$ devices which showed improved efficiency under doping through a decrease of charge carrier recombination [35].

On the other side, a more drastic reduction of photovoltaic performance is observed in the case of Bismuth incorporation, even at low doping level ($x = 0{,}01$), with poor PCE in the order of 1% only. While some improvement in device performance was observed in the literature for $FAPbI_{0.95}Bi_{0.05}I_3$ device [38], our data show that Bismuth incorporation results in a significantly altered layer morphology and crystalline structure, which can therefore explain the drastic reduction of charge carrier photogeneration in our Bi-doped devices. Moreover, the presence of significant fraction of $\delta\text{-}FAPI$ phase with increasing Bi content (especially for $x = 0{,}10$ and $0{,}15$) is consistent with these poor PV performance [38]. The loss of layer homogeneity and smoothness with doping is also a factor strongly affecting the general behavior of the devices in this case, as revealed by our morphology study. The loss in photocurrent can also be related to the perovskite/HTM interface and its energetic configuration. Less favorable or slightly altered band alignment induced by doping is indeed responsible for poor hole injection in the HTM, as reported by several works [56]–[58]. In conclusion, the strong alteration of layer properties in the case of Bi incorporation is limiting the main mechanisms governing the photovoltaic effect. As proposed in related works [30], [39], [59], Bismuth is rapidly introducing a large number of defects, either in bulk or at the interfaces, which drastically limit the efficiency of the devices.

Fig. 8.13 shows the External Quantum Efficiency (EQE) spectra of undoped and doped devices. The trends in absolute EQE values do follow the trends in J_{SC} recorded under solar simulation, with reduced photocurrent for increasing x values. All photocurrents derived from the integration of the EQE spectra over the AM1.5G solar irradiance are found in a ±10% range with those obtained under solar simulator (see **Table 8.4**). The EQE onset is clearly related to the optical bandgap of the layers and is found very similar for all Cu-doped devices, while it shows a similar evolution to that revealed from UV-visible optical measurements (**Fig. 8.7**).

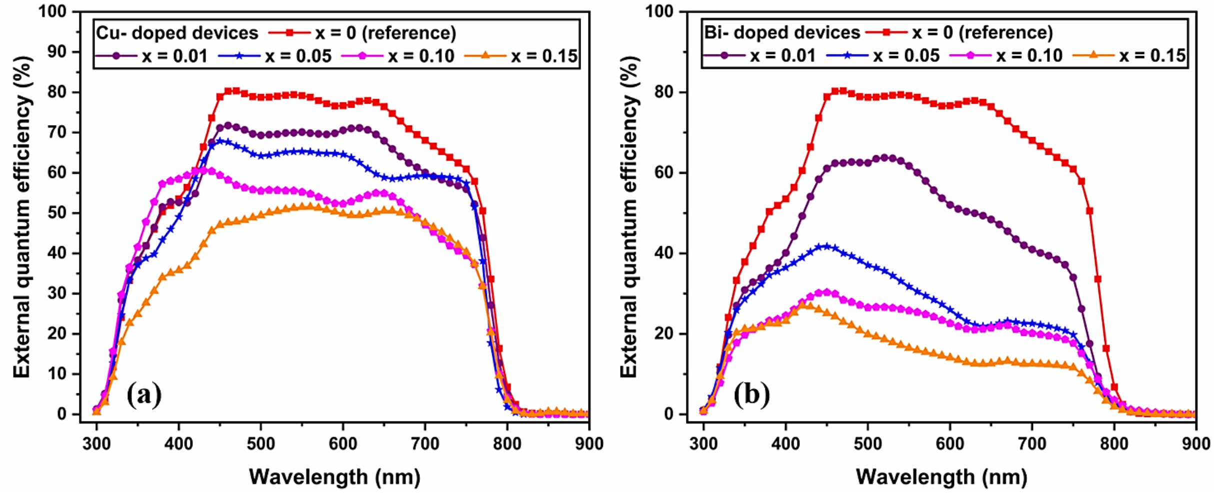

Fig. 8.13*. EQE spectra of undoped, and Cu- (a) and Bi-doped perovskite devices as a function of dopant fraction x.*

Table 8.4. *Recorded* J_{SC} values from EQE measurement for reference, Cu – and Bi-doped devices compared with measured J_{SC} values.

Device	EQE J_{SC} ($^{mA}/_{cm^{-2}}$)	Measured J_{SC} ($^{mA}/_{cm^{2}}$)
Undoped	18.6	22.9
Cu : x = 0.01	16.7	20.5
Cu : x = 0.05	15.6	19.0
Cu : x = 0.10	13.4	17.2
Cu : x = 0.15	12.1	12.3
Bi : x = 0.01	7.8	4.3
Bi : x = 0.05	7.1	4.1
Bi : x = 0.10	6.0	5.3
Bi : x = 0.15	3.2	4.4

Finally, in order to further investigate the influence of Cu- and Bi-doping on device performance, we performed transient photovoltage (TPV) decay measurements [60], which is a simple technique largely used to monitor charge kinetics in photovoltaic devices under realistic working conditions, such as dye-sensitized [61], [62], organic [63], [64], or perovskite solar cells [65], [66]. In the latter case, it was particularly relevant to reveal the contribution of trap states and mobile ions on charge extraction and recombination process, governing the overall device efficiency and hysteresis. However, such electrical transient measurements have been often misinterpreted due to the contribution of the geometric capacitance of the devices, which can overlay the targeted bulk charge carrier recombination mechanisms [30]. Theoretical and experimental studies have revealed the main factors to be considered to overcome this RC limitation, as the necessity to work with thick active layers to minimize the capacitive effect, or under high voltage regime where bulk photo-generated carriers dominates the electrical transient behavior of the device [67], [68]. Some corrections on the measured lifetimes to account for this capacitive decay should also be considered when the aforementioned conditions are not fulfilled [69]. **Fig. 8.14** presents the decay time (referred as τ_{TPV}), which is extracted from TPV measurements made under open-circuit conditions for the undoped and doped devices for $x = 0.15$.

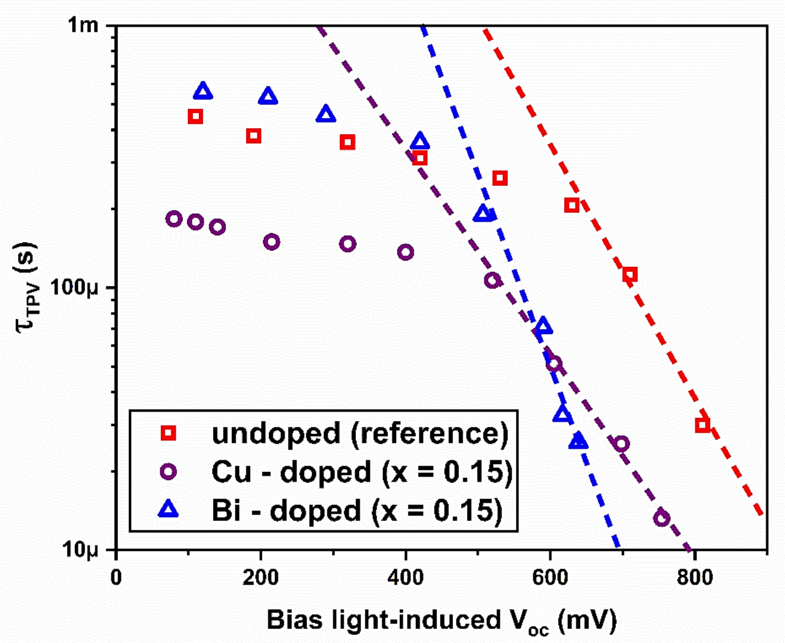

Fig. 8.14. *Decay time extracted from transient photovoltage decay curves under open-circuit conditions as a function of bias-light induced V_{OC} for perovskite devices based on the undoped and doped active layer for $x = 0{,}15$. The recombination regime under high light intensity (hence at high bias-induced V_{OC}) are emphasized by dotted lines in each case.*

Rapid estimation of the electrical resistance and geometric capacitance of our devices, based on impedance spectroscopy measurement (not shown here), gives a RC time constant in the order of the microsecond. This estimation is consistent with recent measurements made on perovskite solar cells as well [70]. Consequently, looking at our TPV data, our measurements do not seem to be limited by this effect, especially in the low illumination regime, as the characteristic decay time is found larger than 100 µs in all cases. The observed transient behavior is likely to be dominated by the recombination dynamics of charge carriers over the whole illumination range probed in this work. This observation is also consistent with the fact that different kinetics are revealed for devices with different doping levels, but of similar design and architecture. While the low illumination regime is generally associated with first-order trap-assisted recombination, we focus on the high V_{OC} regime which is closer from standard illumination conditions in the sun, and which, in any cases, is also more likely to be fully dominated by the intrinsic recombination kinetics of the photo-generated charge carriers [67]. In this regime, the doped devices show faster recombination kinetics than the reference cell, which is consistent with the achievement of reduced open-circuit voltages under standard illumination observed in the corresponding J-V curves (see **Fig. 8.14**). While the Cu-doped and reference devices exhibit similar recombination dynamics, with nearly identical slopes in the $\tau_{TPV} = f(V_{OC})$ representation, the Bi-doped device shows a more drastic acceleration of charge recombination with light-induced photovoltage, hence with photo-generated charge density. Although charge extraction measurements could be done in order to better describe this behavior, such observations are entirely consistent with our previous discussion as well as with reported works [30], [39], which suggested that Bi increases recombination and reduces electron mobility in the bulk region. Our analysis suggests that the incorporation of monovalent Cu atoms, which will favor halide vacancies in the perovskite structure, are finally much less detrimental to device operation than doping with a trivalent element such as Bismuth. Previously reported recombination analysis confirms also that the ion redistribution inside the perovskite absorber layer is responsible for the large hysteresis effect of the layers, as well as for the lower device performance observed [71]**.**

8.2.1.2. Preliminary stability testing conditions

The device stability plays a crucial role in the photovoltaic field. In PSC, the stability depends both on intrinsic and extrinsic factors that govern the degradation mechanism of the materials or their interfaces. They are often triggered by multiple factors such as moisture, oxygen, or light exposure, which impacts the electronic properties of the active layer, but also defect state densities [72], [73]. Some recent reports have in particular helped defining standard protocols which can be applied in the perovskite field, both for outdoor and indoor conditions, such as dark storage shelf-life testing, light or thermal soaking, as well as harsher conditions for cell operation under combined humidity and electrical stress [74]. In this work, we adapt basic level testing conditions (ISOS-D-1), which means that the PSC testing environment is not finely controlled. Such preliminary analysis gives the first feedback on the influence of Cu- and Bi-doping strategies on device degradation. We tested our doped and undoped devices using 30 consecutive cycles under constant one sun illumination in ambient conditions and without any encapsulation, as defined in the ISOS-D-1 conditions. **Fig. 8.15.** shows the evolution of normalized PV parameters for Cu- and Bi-doped solar cells for $x = 0{,}01$, in comparison to the undoped reference (results associated with other x values are presented in **Fig. 8.16** and **Fig. 8.17**). In these conditions, the undoped device is showing excellent stability of its performance up to 30 min, compared to Cu- and Bi-doped devices. For these latters, all PV parameters are decreasing over a short period of time under aging. We also note that 50% of PCE is lost after 20 min for doped devices, while no performance loss can be seen over that period for the control cell. Even if we did not observe any change in active layer color over the aging in all cases, the rapid degradation of performance observed for the doped device could be a direct consequence of interfacial and bulk trap states introduced through doping, and which were responsible for faster charge recombination events (see the previous section). By carefully looking to the Bi-doped devices, it appears that a small amount of dopant ($x = 0{,}05$) can efficiently preserve the PV performance over time (see **Fig. 8.17**). This observation is consistent with the previous report which suggested that an appropriate amount of Bi in the precursor solution can indeed suppress the unwanted $FAPI$ δ-phase [38], [42]. In any case, these preliminary aging tests confirm that the poor PV performance of the doped devices, attributed to the introduction of defect states which promote charge recombination, are also responsible for the short device lifetime evidenced even at low doping ratio.

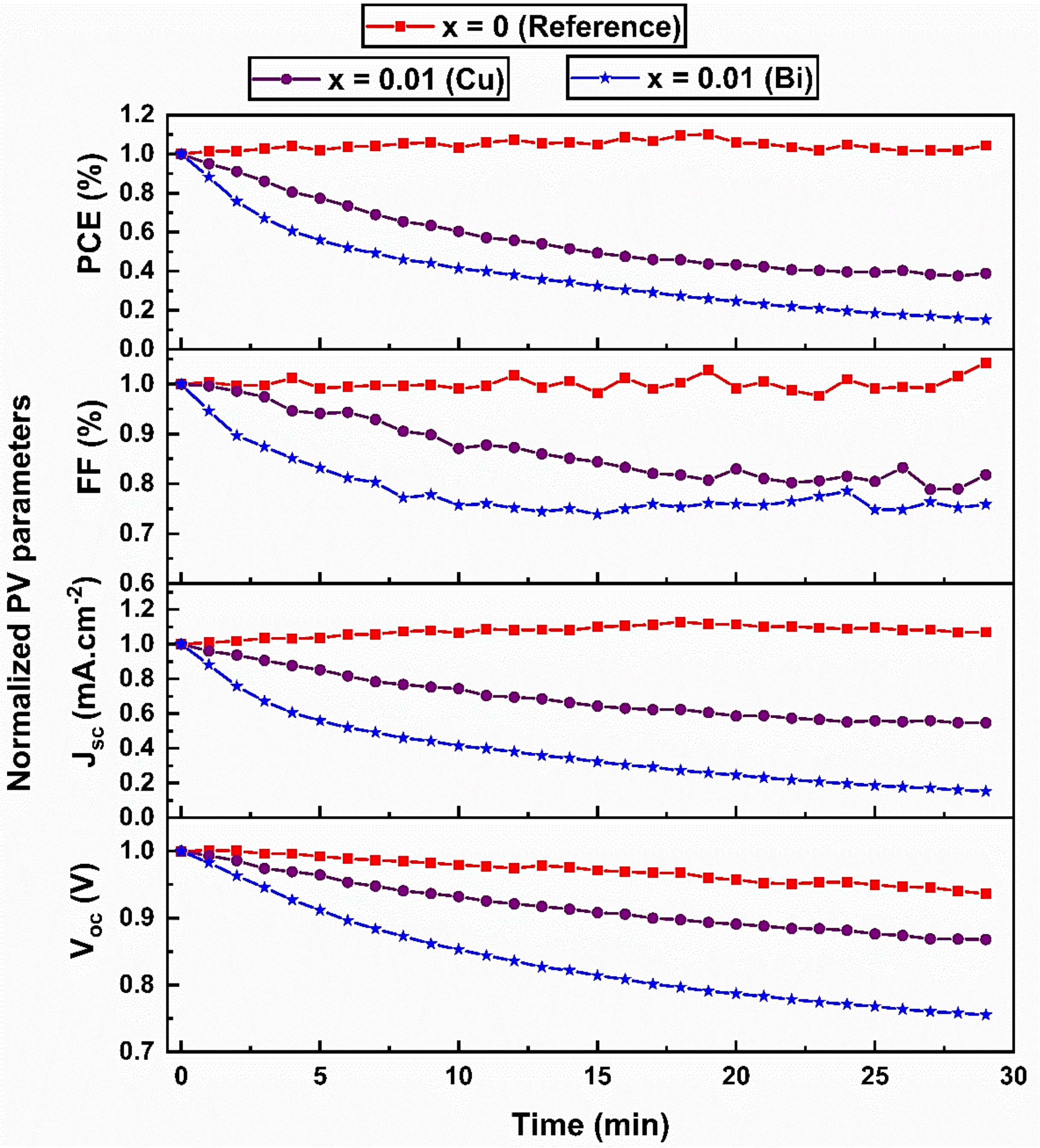

Fig. 8.15. *Evolution of normalized PV parameters under ISOS-D-1 aging conditions (no encapsulation, ambient atmosphere, one sun continuous illumination). The doping level is* $x = 0{,}01$ *for both* Cu*- and* Bi*-doped devices.*

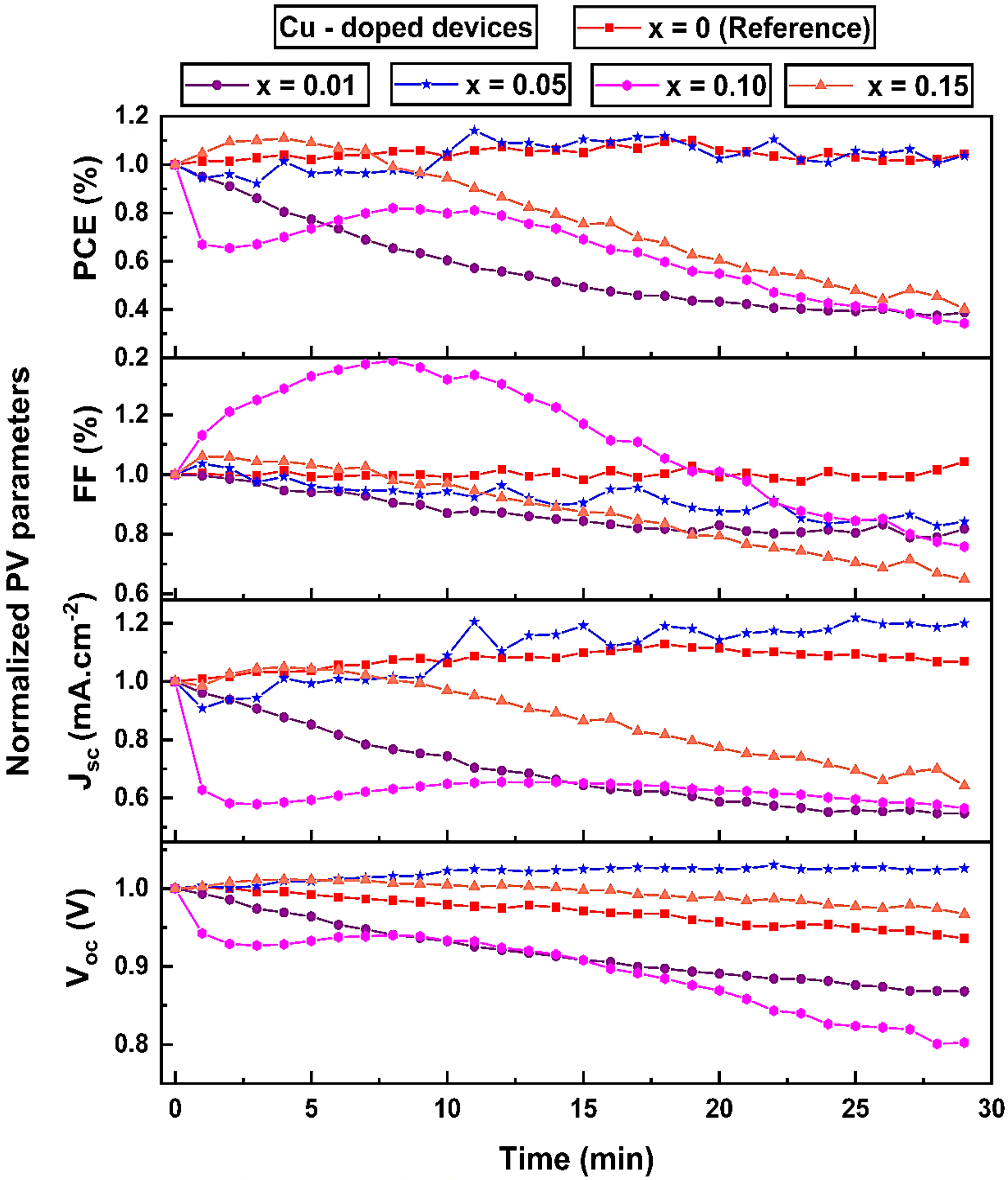

Fig. 8.16. Evolution of normalized PV parameters under ISOS-D-1 aging tests for Cu-doped devices.

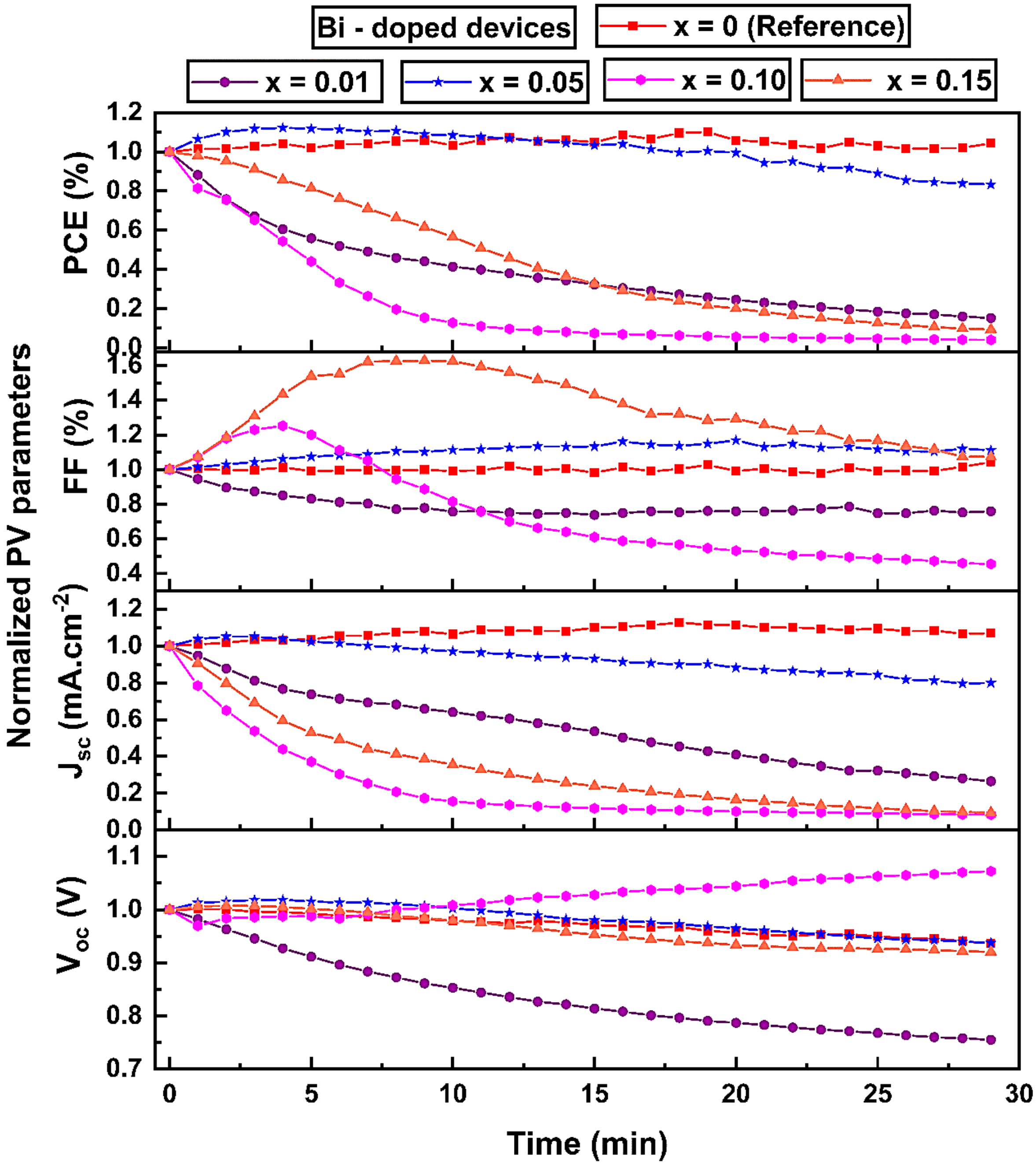

Fig. 8.17. *Evolution of normalized PV parameters under ISOS-D-1 aging tests for Bi-doped devices.*

From the experimental point of view, the following points are crucial for boosting the actual perovskite device performance, such as (1) enhancing the absorber layer phase and its morphology, (2) improving the charge transport behavior, (3) passivating the surface nor interface defects, (4) altering the energy level alignment between the ETL/perovskite and perovskite/HTL interfaces, (5) improving the stability, (6) reducing the hysteresis. In general, removing the traps at the interfaces is beneficial for the charge transfer. In that perspective, an interlayer's addition to the device helps to minimize the traps and suppress the ion immigration. Therefore, interface modifications and the chosen interfacial material directly influence the device stability, performance, and hysteresis behavior. Adding polymers, small molecules, 2D materials, or self-assembled monolayers (SAM) in between the perovskite/HTL interface may improve the charge transfer from the absorber to HTL and electrode [75]. Moreover, for efficient photogeneration of electron (e^-) and hole (h^+) extraction from the perovskite layer and choosing the appropriate e^- and h^+ transport layer (ETL & HTL) is vital to enhance the PCE. It is worth mentioning that the numerical SCAPS device modeling helps the researchers to understand their device architecture before/after making the real experimental device using the same device configuration. Based on our experimental results, it was observed that the BiI_3-doped perovskite film shows almost comparable optical bandgap value (i.e., not altered that much). Moreover, the physical parameter values for the doped films (i.e., exact composition) are not available in the previous reports (see section 5.4). So that, it is difficult to simulate the BiI_3 - doped perovskite device as demonstrated in the previous chapter using SCAPS (see chapter 7). At the same time, based on our knowledge, we constructed the device along with a thin BiI_3 – interlayer (IL) in between the perovskite/HTL interface to understand the impact, and the following explanations are evidently supports with the proposed idea. Also, the IL in between the perovskite absorber layer and the HTL interface is considered as a productive layer to avoid the immediate degradation of the absorber layer from external H_2O & O_2. Additionally, it reduces the recombination at interfaces to improve the whole device's performance [76]**.** In general, 64 % of the total solar model cost is related to the HTL (49 %) and the electrode (15 %), the blocking/interlayer cost approximately 0.6% only [77]. Besides the price, the organic HTL/electrode (Au or Ag) models suffers from the migration (i.e., metal ions from the metal electrode and halide ions from the perovskite absorber). Usually, there are four possible options to place the interfacial layers based on the planar conventional (n-i-p) and inverted (p-i-n) perovskite structures. Such as in the FTO/ETL interface, ETL/perovskite interface, perovskite/HTL interface, and HTL/electrode interface [78]. According to the previous reports, using additional IL in between the perovskite absorber layer and the HTL interface significantly enhances solar cell performance [78]–[84]. For example, N. K. Noel *et al.* introduced the thiophene and pyridine-based IL between perovskite/HTL interface and demonstrated that the IL improved the device efficiency from 13 % (without IL) to 15.3 % (with thiophene IL) and 16.5 % (with pyridine IL). Because of the passivation strategy, which significantly diminishes the nonradiative recombination pathways [79]**.** D. Song *et al.* used the F4TCNQ IL and also achieved an enhanced efficiency from 15 % (without IL) to 18 % (with IL) because of the improved electric field, which mainly decreased the carrier loss at the surface and subsurface of the absorber layer. Also, IL creates an energy barrier for the photogenerated e^- which reduces the recombination adjacent to Perovskite/HTL interface [81]**.** Some research groups used the halide perovskite layer as an IL; for example, J. W. Lee *et al.* deposited the thin $MAPbI_3$ layer over the $FAPbI_3$ absorber layer, they got the efficiency enhancement from 15.5% (without IL) to 16 % (with IL) due to an considerable increment in the conduction band minimum at the interface, leading to higher open-circuit voltage [80]**.** Similarly, K. T. Cho *et al.* achieved an increased PCE from 18.9 % (without IL) to 21.3 % (with IL) using additional $FAPbBr_{3-x}I_x$ layer over the $(FAPbI_3)_{0.85}(MAPbBr_3)_{0.15}$ perovskite absorber, which efficiently suppresses the interfacial charge recombinations [85]**.** In this perspective, using bismuth (Bi) based IL in perovskite device will be beneficial for the device performance. For example, L. Fu *et al.* employed the bismuth telluride (Bi_2Te_3) IL in HTL/Inorganic-Perovskite interface and achieved an improved device performance from 7.4 % (without) to 11.9 % (with IL). These results clearly explain that IL efficiently blocks the iodide ions migrations from the absorber layer [86]**.** Also, bismuth iodide (BiI_3) material gains more attention due to its non-toxic behavior, a narrow bandgap (1.72 eV), a high absorption coefficient, and short carrier lifetimes, considering these properties of BiI_3, it is more suitable for photovoltaic applications [57]–[59], [87]–[89]. Moreover, according to the U. S. national mineral information center report, the Bismuth price is relatively too low compared to the lead [90], therefore based on the material cost, it is considerable than Pb. Recently, Y. Hu *et al.* deposited the pristine BiI_3 IL over the titanium oxide ETL (i.e., ETL/Perovskite interface), and found that it improves the electron transport behavior by passivating the interfacial trap states. As a result, they got an increased PCE from 13.8 % (without) to 17.8 % (with IL) [89]. But still, there is no BiI_3 IL-based simulation/theoretical analysis reported so far in the Perovskite/HTL interface. Therefore, the following section is completely dedicated to BiI_3 IL contained simulated FA-Cs devices. Furthermore, the band alignment between the perovskite/HTL interface is highly beneficial for the balanced charge transfer to enhance the device performance, and also widely used Spiro-OMeTAD-HTL generally increases the interface recombination due to the external doping [91]. In that perspective, the different HTL layers are tested in the same configuration to find the alternate HTL instead of Spiro-OMeTAD. The various electrodes were also tested based on the work function (WF) values to understand the energy level mismatch alignment between HTL/electrode interface. So far, this work does not consist of the CuI IL-based simulated FA-Cs devices, and it will be tested in the near future.

8.2.2. BiI$_3$ interfacial layer with different HTL's in FA-Cs perovskite solar cell – SCAPS - 1D study

In this sub-section, we theoretically introduce a thin BiI_3 IL between $FA_{0.85}Cs_{0.15}Pb(I_{0.85}Br_{0.15})_3$ absorber/Spiro-OMeTAD (HTL) layer using SCAPS-1D to understand the beneficial effect of BiI_3 on the device performance. Firstly, we construct an ideal n-i-p planar device without using the IL layer as a reference, and after placing a thin BiI_3 IL, our simulated device (FTO/ETL/Perovskite/BiI_3/HTL/Electrode) showed enhanced performance compared to the referenced one. Secondly, we carefully investigated the device performance using different HTL candidates, such as 2,2',7,7'-Tetrakis[N, N-di(4-methoxyphenyl)amino]-9,9'-spirobifluorene ($Spiro-OMeTAD$), cuprous oxide (Cu_2O), Strontium Cuprate ($SrCu_2O_2$), Cuprous Aluminate ($CuAlO_2$), copper antimony sulfide ($CuSbS_2$), cupric thiocyanate ($CuSCN$), Cuprous iodide (CuI), Poly(triarylamine) ($PTAA$), poly(3-hexylthiophene-2,5-diyl) ($P3HT$) with and without BiI_3 IL. The final optimized device photovoltaic parameters with IL confirms that the Cu-based Cu_2O, and $SrCu_2O_2$ HTL's are more suitable than other HTL nominees due to their band alignment with BiI_3 IL. Furthermore, we evaluated the effect of several electrodes (Ag, Cr, Cu, Au, Ni, Pt) based on their work function (WF) value with the above-mentioned HTL's. At last, we studied the influence of IL thickness over the perovskite layer thickness and the effect of parasitic resistances (R_{series} and R_{shunt}) with suitable HTL.

8.2.2.1. Ideal device performance

In this simulation, Firstly SnO_2 (ETL) and $Spiro-OMeTAD$ (HTL) based $FAPI$ perovskite ideal device performances are carefully investigated as a reference, which shows a PCE of 19.17 % with a short current density (J_{sc}) value of 22.24 mA/cm^2, a fill factor (FF) of 67.46 %, and an open-circuit voltage (V_{oc}) of 1.27 V that is associated with previously reported results [92], [93]**.** Here, we used the SnO_2 as an ETL instead of TiO_2 and ZnO due to the excellent properties of SnO_2 [94], [95] and also, SnO_2 provides perfect band alignment with the appropriate mixed cation/halide perovskite than TiO_2 [96]**.** The primary and crucial job of the ETL layer is to extract the electron from the absorber layer and simultaneously blocking the holes to avoid recombinations.

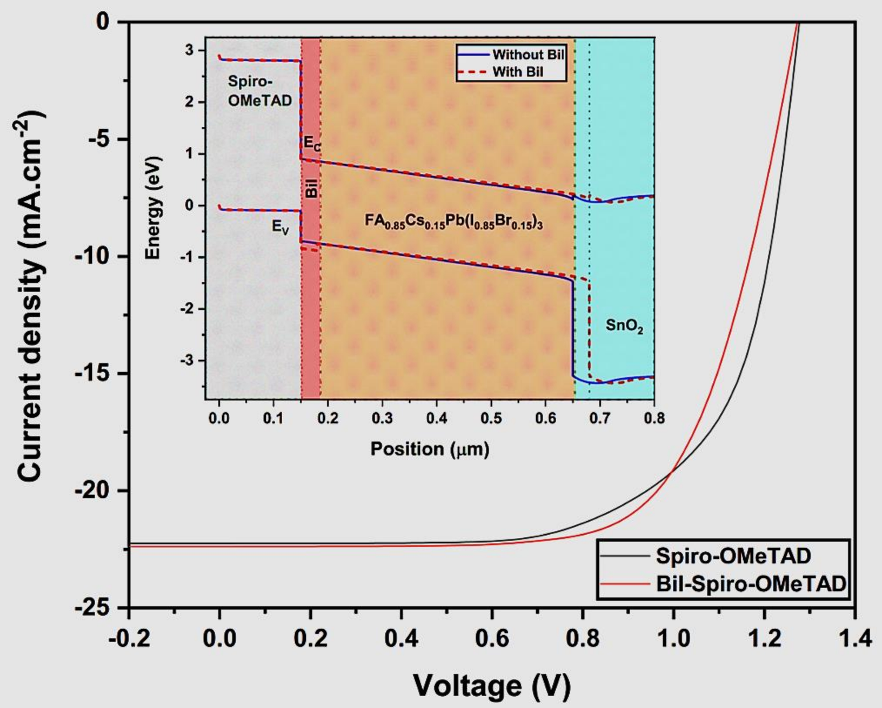

Fig. 8.18. *I-V characteristic curves of both ideal device structures (with and without* BiI_3 *IL). The inset represents the energy band diagram.*

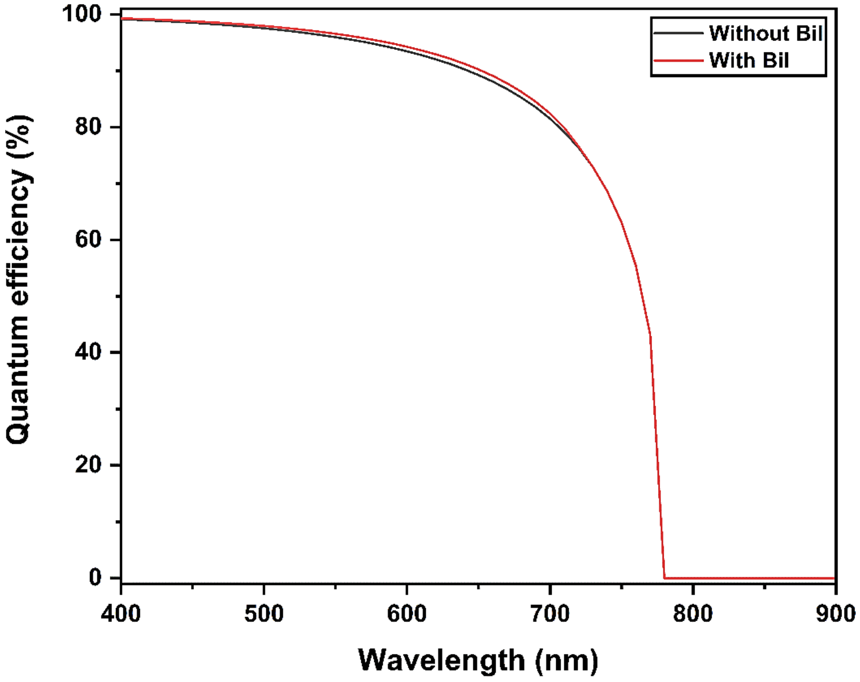

Fig. 8.19. *QE graph of both ideal device structures (with and without* BiI_3 *IL).*

Experimentally, due to the different ETL layer thicknesses, the light transmittance of the film will vary. Therefore, the ETL layer thickness plays a vital role [97]. In general, SnO_2 – ETL layer needs a higher thickness than TiO_2 – ETL to completely cover the TCO substrate due to the larger size of SnO_2 nanoparticles [94]. Fumin Li et al. studies demonstrate that the 66 nm SnO_2 – ETL device showing an improved PV performance than 34 nm and 48 nm ETL devices. The thicker ETL effectively blocks the hole transport, and it reduces the charge carrier recombination at the interfaces, which is beneficial for the device's performance [98]. Also, the 70 nm $Cl - SnO_2$ – ETL device provides an enhanced PCE than 40 nm and 90 nm layer contained devices due to tight interface contact with the TCO substrate and absorber [99].

Furthermore, it is well-known that several factors affect perovskite device performance, including HTL layer thickness. In this simulation, we used an optimized thickness of 150 nm for all different HTL layers. Previous experimental reports justify that the 180 nm HTL layer device offers a higher PV performance than other HTL thicknesses, such as 100, 250, 400, 450, 500, and 700 nm [100]. Apart from the hole extraction and transportation, the absorber layer's safety and suppression of the interface defects are crucial to achieving good device performance. Therefore, the HTL thickness should be thicker than 150 nm to avoid direct contact between the absorber and the electrode. Also, a thick HTL efficiently enhances the charge carrier collection due to an improved reflection from the smooth HTL/electrode interface; thus, the device efficiency is highly improved [101], [102].

Later, we introduced an additional thin BiI_3 IL in between the perovskite/HTL interface (see **Fig. 5.13**). Perovskite/HTL interface engineering is a well-known strategy to efficiently passivate the defects, which generally promotes hole extraction by blocking the secondary electrons [82]**.** Surprisingly, here all the photovoltaic parameters are drastically enhanced, the obtained PCE improved from 19.17 % to 19.28 % ($J_{sc} = 22.38\ mA/cm^2,\ FF = 67.73\ \%, and\ V_{oc} = 1.27$). **Fig. 8.18** illustrates the simulated current density – voltage curves (J-V) of both ideal device structures, and the inset's shows the energy band diagram. The obtained quantum efficiency (QE) graphs were displayed in the supplementary information (see **Fig. 8.19**). Experimentally, introducing IL is not only beneficial for stopping ion migration, and also it modifies the energy level alignment between the layers. In general, the interfacial energy level alignment influences the hole injection rate (i.e., perovskite/HTL interface). The energy barrier (EB) at the interfaces leads to charge carrier recombination losses restricting the charge transfer. The non-appearance of EB at the interfaces helps the smooth and fast charge transfer/injection and efficiently reduces the recombinations [75]. In this case, BiI_3 has a higher bandgap value and larger conduction band than the absorber (see **Table 5.2 and Fig. 5.14**), leading to the favored energy level alignment that efficiently minimizes/reduces the EB at the HTL/perovskite interface.

Henceforth, introducing BiI_3 IL in the Perovskite/HTL interface facilitates the interfacial hole transport and possibly suppresses the interfacial charge recombination. The valence band offset (VBO) is generally defined as the difference between the e^- affinity and bandgap of the perovskite absorber; and e^- affinity and bandgap of the HTL (i.e., $VBO = e^-\text{ affinity}_{HTL} - e^-\text{ affinity}_{perovskite} + bandgap_{HTL} - bandgap_{Perovskite}$) [103]–[105]**.** The negative VBO is obtained in the perovskite/$Spiro - OMeTAD$ interface (-0.58 eV), which signifies that the presence of recombination of minority charge carriers occurs in the interfaces [106]. After adding the BiI_3 IL, the VBO (i.e., $VBO = e^-\text{ affinity}_{BiI_3} - e^-\text{ affinity}_{HTL} + bandgap_{BiI_3} - bandgap_{HTL}$ [107]) turns positive (0.72 eV), by means that the band alignment is modified between the absorber and the HTL interface, which is beneficial for balanced charge carrier transfer; as a result, it boosts the FF value (see **Table 8.5**). Additionally, the current value of BiI_3 IL attached device is higher than that of the reference device, which generally leads to higher charge carrier mobility, helping further PCE improvement.

Table 8.5. *Simulated photovoltaic parameters for $FTO/SnO_2/perovskite/Spiro - OMeTAD/Au$ device.*

HTL		**J_{sc} (mA/cm^2)**	**FF (%)**	**V_{oc} (V)**	**PCE (%)**
Spiro-OMeTAD	W/o BiI_3	22.24	67.46	1.27	19.17
	W BiI_3	22.38	67.73	1.27	19.28

Hence, it is clear that the BiI_3 IL influences the device results, so in the following sections, we are going to check the device performances based on several HTL candidates with and without BiI_3 IL to understand the interfacial layer effect. Finally, we will correlate the influence of the BiI_3 IL thickness with the perovskite absorber layer thickness and also the effect of parasitic resistances, using the most appropriate HTL system.

8.2.2.2. Effect of different HTL's with and without BiI$_3$ IL

Experimentally, $Spiro-OMeTAD$ HTL needs some external doping (such as tri-tert-butyl-pyridine (tBp), lithium bis-tri-fluoro-methane-sulfonimide (Li-TFSI), and other cobalt salts) to improve the internal charge mobility, but at the same time, it is rising the interface recombination, which led to poor device performance [91]. Therefore, finding alternative low-cost and stable HTL is essential to improve device efficiency. Hence, in this section, several HTL ($Cu_2O, CuI, CuAlO_2, CuSbS_2, SrCu_2O_2, CuSCN, PTAA, P3HT$) candidates are studied and presented. Input parameters of the mentioned HTL materials are listed in Table II. By using 70 nm of SnO_2 as an ETL and switching different HTL materials with and without BiI_3 IL, the comparative energy band diagram is illustrated in **Fig. 8.20a** and **b**. Obtained J-V characteristic curves, as well as the appropriate energy band diagrams (inset) for all mentioned HTL devices, are presented in **Fig. 8.21 - Fig. 8.28**, respectively.

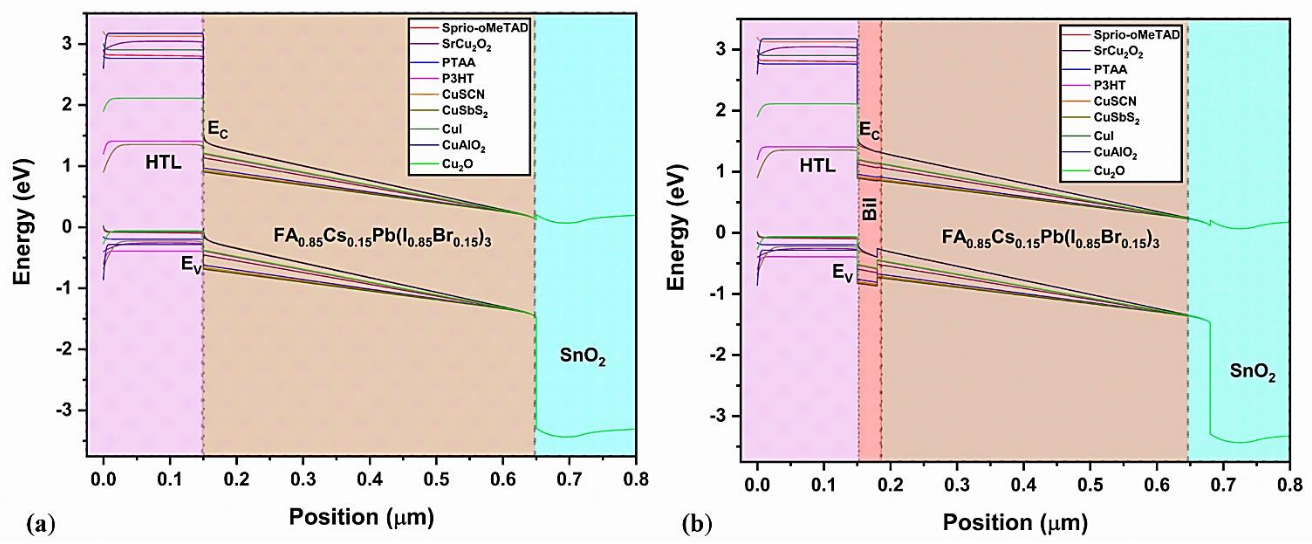

Fig. 8.20. Energy band diagram for the reference device (a), including BiI_3 IL (b) with different HTL candidates.

After testing several HTL candidates over the same configured structure, we noticed that the Cu_2O-HTL based device shows a remarkable PCE of 23.07 % than other competitors due to their excellent hole mobility value (**Table 5.3**) and the energy band alignment with the absorber layer (**see Fig. 8.21**). The obtained FF value (81%) is highly improved compared to the reference $Spiro-OMeTAD$-HTL device (67 %), which can be attributed to the promotion of hole conduction through the HTL. The simulated photovoltaic parameters of all different HTL based device results are illustrated in **Table 8.6**. The VBO is significantly improved (- 0.31) while using Cu_2O-HTL instead of $Spiro-OMeTAD$, that could be a good reason for the enhanced device performance. After adding the BiI_3 IL in between the Perovskite/Cu_2O-HTL interface, as we expected, the overall device performance increased from 23.07 % to 23.29 % compared to the standard device (**see Fig. 8.21** and **Table 8.6**) due to the positive VBO (0.45 eV). The VBO value of BiI_3/Cu_2O interface is lower than the $BiI_3/Spiro-OMeTAD$ interface, yet the device performance is boosted because of the high VBO, which acts as a barrier for the hole diffusion [107] and lead to lower performance (i.e., $Spiro-OMeTAD$-HTL device). Also, hole mobility plays a massive role in efficiently extracting and surpassing the holes from the absorber to HTL and the electrode (**Table 5.3**). For example, in a real device, Elesman *et al.* experimental TRPL results explain the Cu_2O/perovskite films exhibit excellent lifetime than P3HT/perovskite films, which signifies that the Cu_2O/perovskite interface gains more hole extraction than P3HT/perovskite interface [108]. The $SrCu_2O_2$ – HTL device having the second-highest efficiency of 22.75 %, here also the VBO is negative (-0.18 eV) but it is better than the $Spiro-OMeTAD$ and Cu_2O-HTL's, at the same time, the hole mobility is lower than the Cu_2O and higher than $Spiro-OMeTAD$ (**Table 5.3**). The addition of BiI_3 IL furthermore improves the VBO to 0.32 eV, which enhances the device performance from 22.75 % to 23.20 % (**see Fig. 8.22**), it is higher than the previously simulated perovskite device results (**Table 8.6**). The $PTAA$-HTL based device showed PCE of 19.80 %, which is attributed to the VBO (- 0.42 eV) and hole mobility value, it is finer than $Spiro-OMeTAD$-HTL. While adding the BiI_3 IL, the VBO is considerably enhanced (0.56 eV), which directed towards the higher performance from 19.80 % to 20.15 % due to an enhancement in the interface (**see Fig. 8.23**). The previously reported simulated PTAA-HTL device shows higher efficiency (23.5 %) than the current device results because of the higher HTL thickness (1000 nm) and the J_{sc} value (41.03 mA/cm^2) [109]**.** $CuAlO_2$-HTL based device displays 19.98 % of efficiency due to the reduced charge transfer resistance between HTL and the electrode [110], the obtained performance is higher than the reference $Spiro-OMeTAD$-HTL device (**Table 8.6**). In this case, the VBO is positive (0.28 eV) compared to formerly discussed HTL contenders; surprisingly, after including BiI_3 IL, the VBO turns into negative (- 0.14 eV), as a consequence, the V_{oc} value is significantly reduced. Even though, the performance is slightly increased from 19.98 % to 20.04 % due to an enrichment in short-circuit current (**see Fig. 8.24,** and **Table 8.6**). $CuSbS_2$-HTL device demonstrating the PCE of 19.08 %, here also the VBO is positive (0.1 eV), while adding BiI_3 IL, the VBO value is reduced a little bit (0.04 eV), which is reflecting in the FF result; however, the PCE is slightly improved (**see Fig. 8.25,** and **Table 8.6**). Previous SCAPS reports shows that a higher efficiency was obtained using $CuSbS_2$-HTL (24.1 %) because of the larger J_{sc} value (31.7 mA/cm^2) and the HTL thickness (438 nm), [111] is much larger than the current result (22.6 mA/cm^2), shown in Table III. $CuSCN$-HTL device displaying PCE of 19.05 %, the VBO is negative (-0.58 eV), after adding BiI_3 IL, the VBO is significantly improved to 0.72 eV, at the end, the FF is reduced due to the higher VBO, but the device shows the same performance because of the improvement in the J_{sc} value (**see Fig. 8.26,** and **Table 8.6**). Previous report shows that the device performance is not entirely associated with perovskite/$CuSCN$ interface rather than $CuSCN$/electrode [112]**.** Therefore, we will demonstrate the effect of HTL with different electrodes in the following sections. But in reality, experimental $CuSCN$-HTL contained device demonstrates excellent thermal degradation stability than well known $Spiro-OMeTAD$-HTL due to the strong resistance against environmental stress [113]**.** CuI-HTL device exhibiting PCE of 18.81 %, the VBO is negative (-0.6 eV), after inserting BiI_3 IL, the VBO is drastically increased (0.74 eV), the performance is also improved minorly but not more (i.e., 18.81 % to 18.86 %) (**see Fig. 8.27** and **Table 8.6**), the high VBO might restrict the further improvement as we discussed before. Noticeably, $P3HT$-HTL device showing the lowest photovoltaic performance (17.99 %) among all HTL's due to the lower hole mobility value and the lower VBO (0.02 eV). According to the previous report, the significant mismatch between the quasi-Fermi level splitting (QFLS) to V_{oc} affects the results that occur while using the $P3HT$-HTL compared to $PTAA$-HTL, enhancing the interfacial recombination at the interfaces [114] might be another reason for the lower performance. After including the BiI_3 IL, the VBO is changed (0.12 eV), but surprisingly, the FF and V_{oc} values are droped, it further reduces the performance (**see Fig. 8.28, Table 8.6**). Overall, other HTL based device exhibits lower performance than these two (Cu_2O & $SrCu_2O_2$) with and without BiI_3 IL. According to the previous report, the vacancy formation energies are reduced in the order of $Cu_2O < SrCu_2O_2 < CuAlO_2$ and it affects the conduction properties; mainly, it modifies the acceptor defects. The vacancy distribution in Cu_2O impacts the bandgap, and the conduction properties [115]. Our simulated device results are compared with recently published reports, shown in Table III. It emphasizes that the simulated device performance is solely based on the appropriate absorber layer, ETL, HTL arrangement, and energy band alignment [105], [108], [109], [116]–[118].

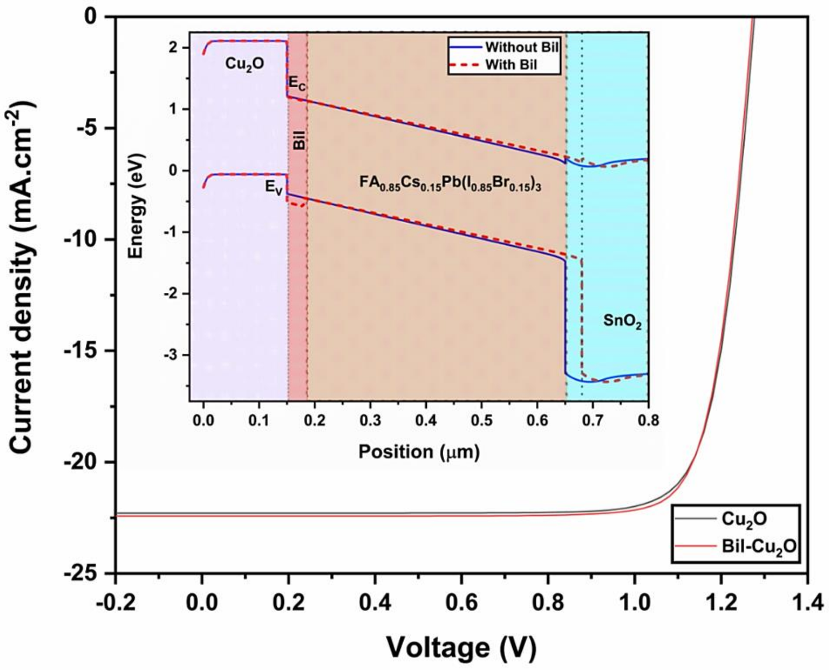

Fig. 8.21. *shows the I-V characteristic curves of both ideal device structures (with and without* BiI_3 *IL) with* Cu_2O*-HTL. The insets represent the energy band diagram.*

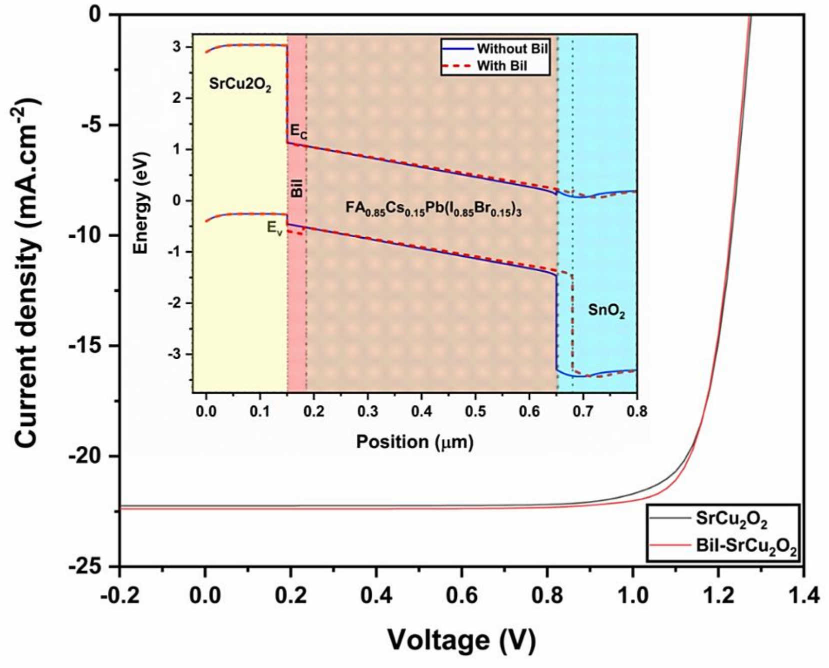

Fig. 8.22. *shows the I-V characteristic curves of both ideal device structures (with and without* BiI_3 *IL) with* $SrCu_2O_2$ *– HTL. The insets represent the energy band diagram.*

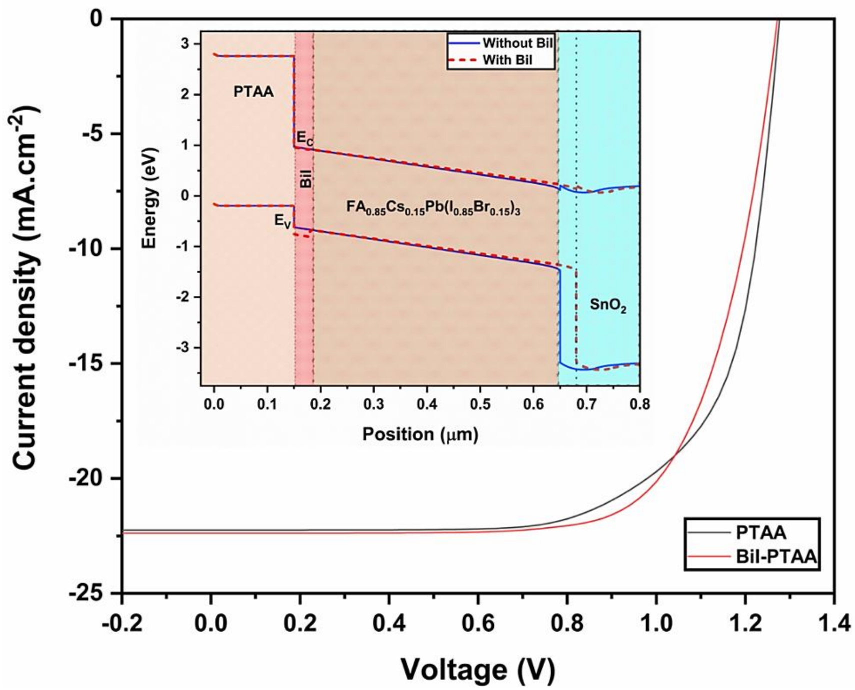

Fig. 8.23. *shows the I-V characteristic curves of both ideal device structures (with and without BiI_3 IL) with $PTAA$-HTL. The insets represent the energy band diagram.*

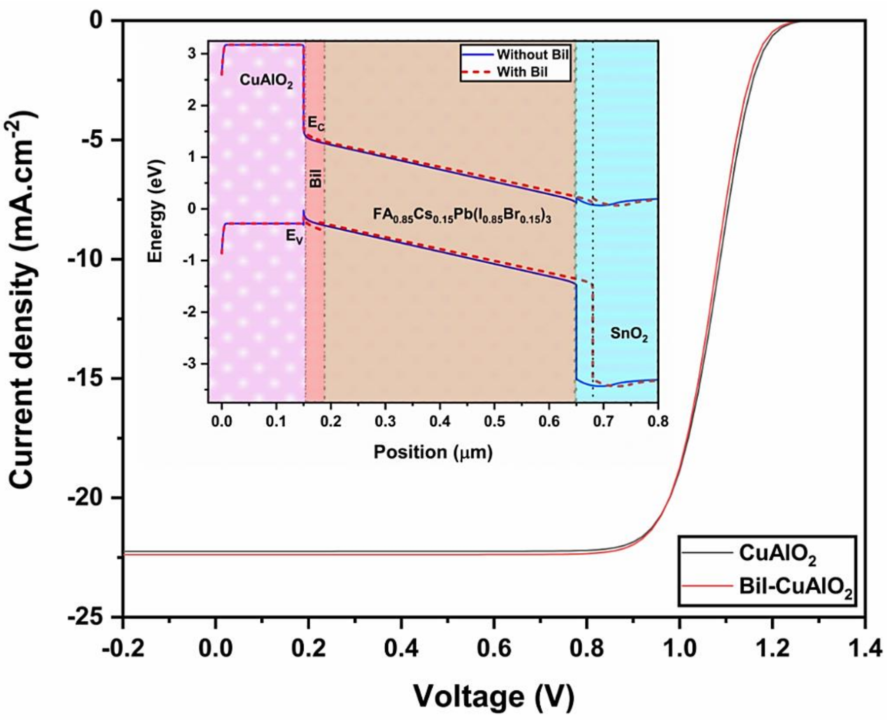

Fig. 8.24. *shows the I-V characteristic curves of both ideal device structures (with and without BiI_3 IL) with $CuAlO_2$-HTL. The insets represent the energy band diagram.*

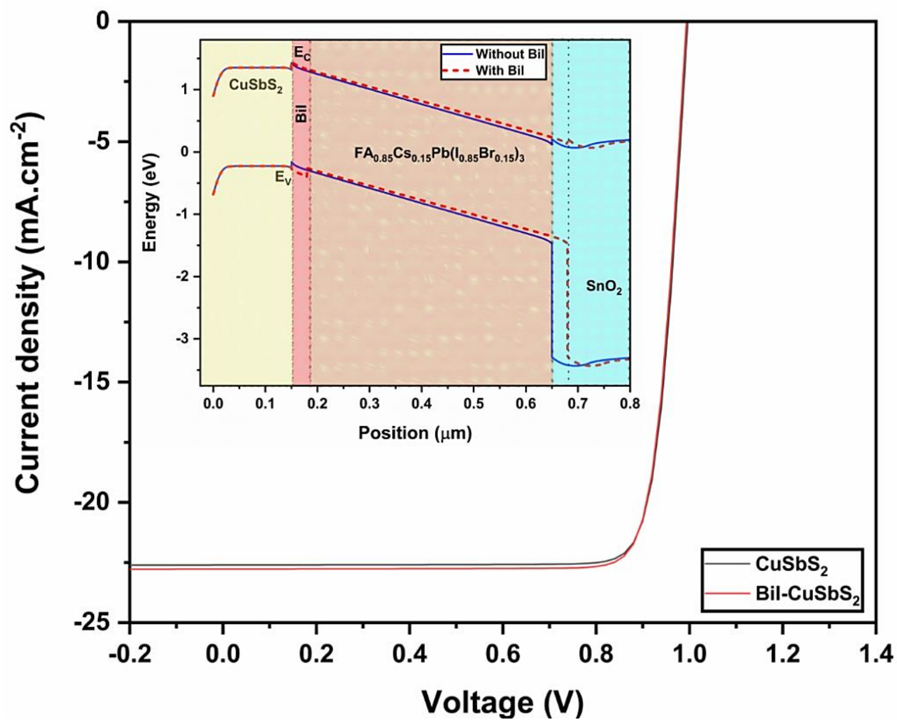

Fig. 8.25. *shows the I-V characteristic curves of both ideal device structures (with and without BiI_3 IL) with $CuSbS_2$-HTL. The insets represent the energy band diagram.*

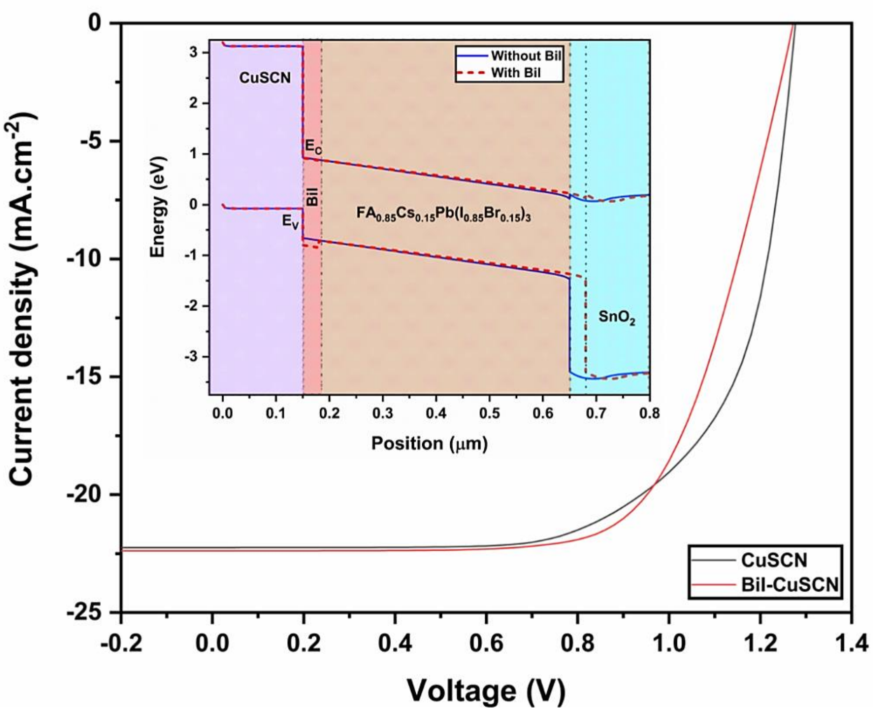

Fig. 8.26. *shows the I-V characteristic curves of both ideal device structures (with and without BiI_3 IL) with $CuSCN$-HTL. The insets represent the energy band diagram.*

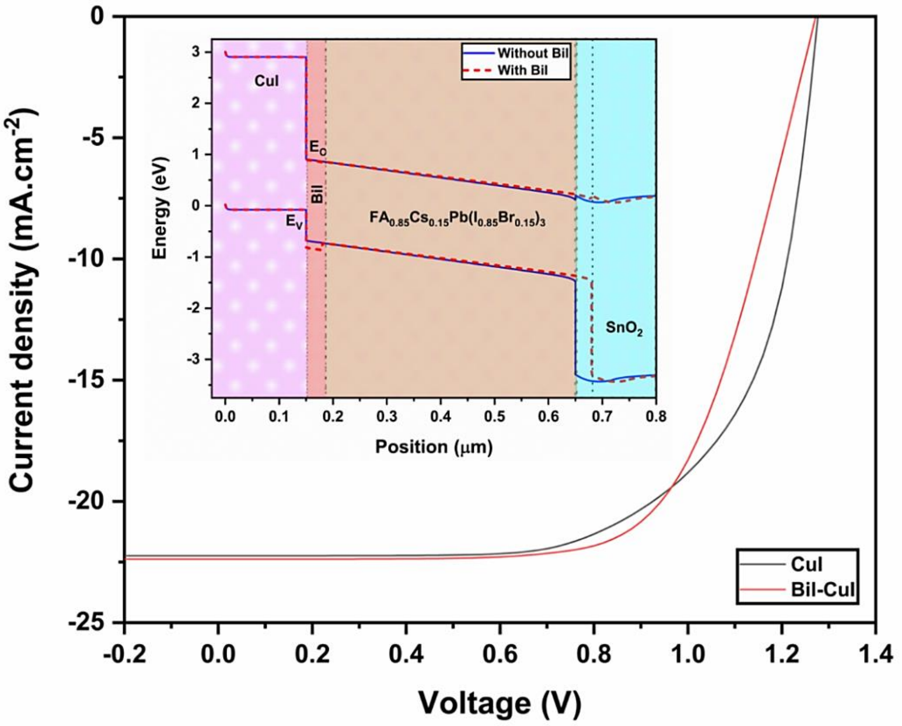

Fig. 8.27. *shows the I-V characteristic curves of both ideal device structures (with and without BiI_3 IL) with CuI-HTL. The insets represent the energy band diagram.*

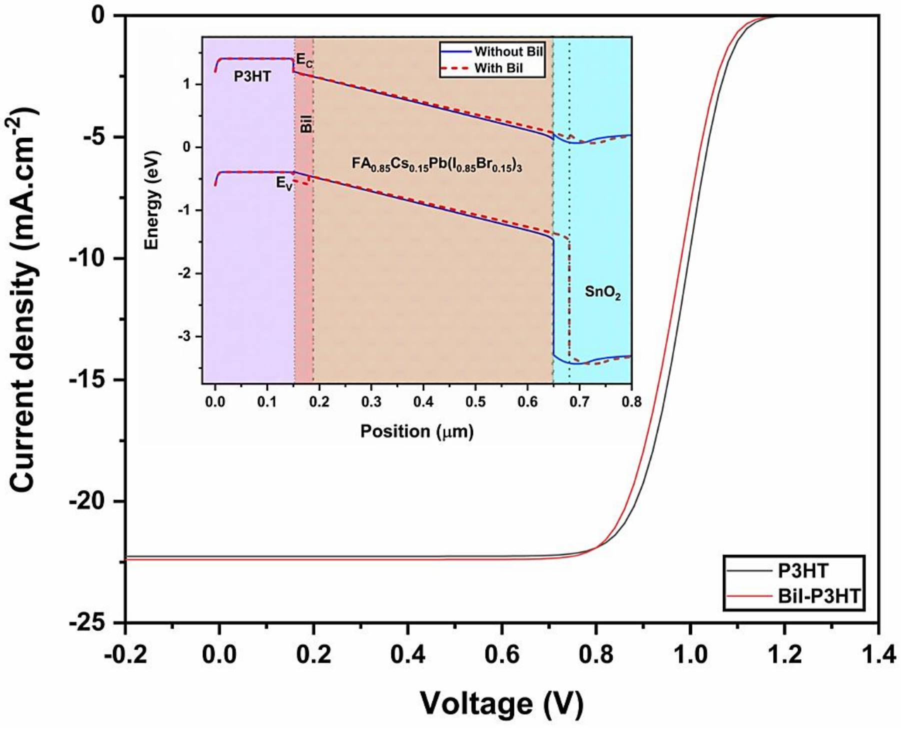

Fig. 8.28. *shows the I-V characteristic curves of both ideal device structures (with and without BiI_3 IL) with $P3HT$-HTL. The insets represent the energy band diagram.*

Therefore, the simulated device with BiI_3 IL enhancing most of the above-mentioned HTL's based device performances compared to the referenced device, especially, the J_{sc} and FF values are improved (**Table 8.6**). The obtained QE behavior of $Spiro - OMeTAD$-HTL referenced device is nearly similar to the BiI_3 IL contained device, shown in **Fig. 8.19**. Hence, it is an evident that the BiI_3 IL with suitable HTL (Cu_2O & $SrCu_2O_2$) directly influences the device performance. In the following sections, we will examine the various electrodes with and without BiI_3 IL (using different HTL's) to understand the effect over the HTL/electrode interface.

Table 8.6 *Recorded photovoltaic parameters for proposed different HTL materials.*

HTL		**J_{sc} (mA/cm^2)**	**FF (%)**	**V_{oc} (V)**	**PCE (%)**
$SrCu_2O_2$	W/o BiI_3	22.25	80.09	1.27	22.75
	W BiI_3	22.38	81.46	1.27	23.20
[105]		23.22	78.50	1.11	20.29
Cu_2O	W/o BiI_3	22.29	81.04	1.27	23.07
	W BiI_3	22.42	81.65	1.27	23.29
[105]		23.26	78.50	1.10	20.14
[108]		22.53	67.36	1.13	17.23
[116]		18.41	81.73	1.06	16.03
$CuAlO_2$	W/o BiI_3	22.24	70.46	1.27	19.98
	W BiI_3	22.38	70.62	1.26	20.04
[105]		23.23	78.40	1.12	20.32
CuSCN	W/o BiI_3	22.25	67.05	1.27	19.05
	W BiI_3	22.38	66.92	1.27	19.05
[116]		18.28	76.34	1.08	15.18
[117]		21.89	83.70	1.27	23.30
$CuSbS_2$	W/o BiI_3	22.60	84.74	0.99	19.08
	W BiI_3	22.77	84.68	0.99	19.15
[111]		31.70	81.0	0.94	24.10
CuI	W/o BiI_3	22.25	66.22	1.27	18.81
	W BiI_3	22.38	66.25	1.27	18.86
[116]		18.29	79.44	1.08	15.79
[117]		21.89	83.21	1.27	23.14
PTAA	W/o BiI_3	22.24	69.68	1.27	19.80
	W BiI_3	22.38	70.75	1.27	20.15
[109]		41.03	74.14	0.77	23.58
P3HT	W/o BiI_3	22.26	67.10	1.20	17.99
	W BiI_3	22.40	66.31	1.19	17.72
[109]		32.25	75.05	0.74	17.98
[117]		21.89	74.05	1.27	20.61

8.2.2.3. Effect of different electrodes with and without BiI$_3$ IL

In this section, the impact of various electrodes such as silver $(Ag - 4.26\ eV)$, chromium $(Cr - 4.5\ eV)$, copper $(Cu - 4.65\ eV)$, gold $(Au - 5.10\ eV)$, nickel $(Ni - 5.15\ eV)$, platinum $(Pt - 5.65\ eV)$ contained device performances were carefully investigated. The electrode work function (WF) values are taken from the previous reports [119], [120]**.** The energy band diagrams of typical and BiI_3 IL included different HTL solar cells with various WF electrodes are depicted in **Fig. 8.29a** and **b**. The band diagram shows that the $Au, Ni,$ and Pt lines are overlapped due to their work function value lies between 5.1 eV to 5.65 eV which is associated with their higher build in voltage behavior (V_{bi}) [116], [121]**.** Other candidates such as $Ag, Cr,$ and $Cu,$ demonstrates the different alignment due to their lower V_{bi} and their work function values (4.2 eV to 4.65 eV) [116]**.**

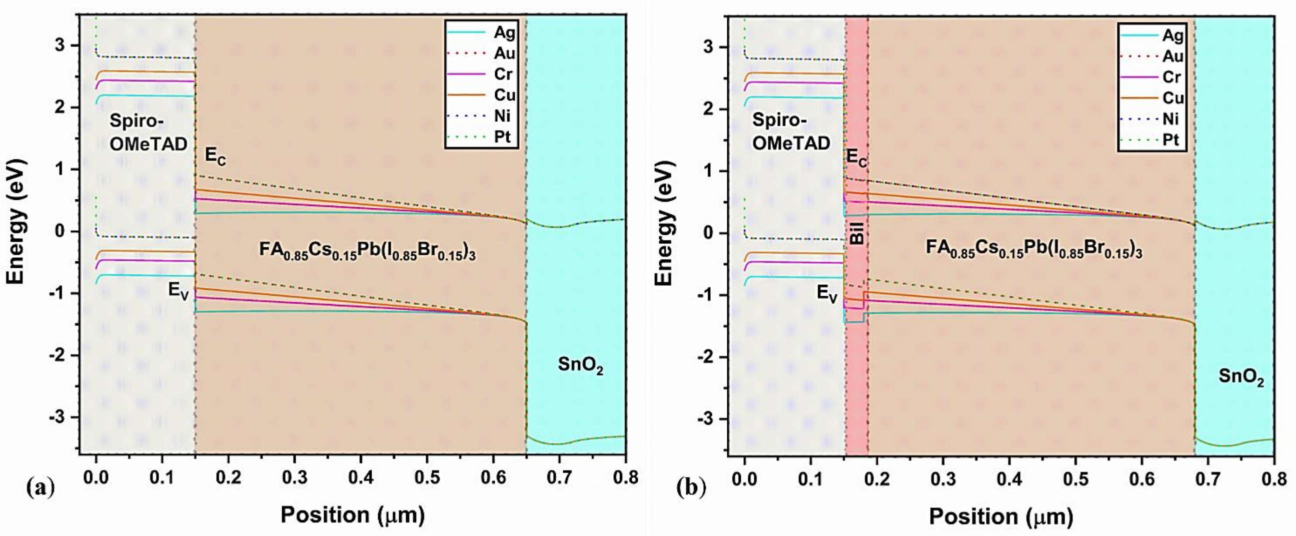

Fig. 8.29. *Energy band diagram for the reference device, including BiI_3 IL with different electrodes.*

Fig. 8.30 demonstrates that the obtained photovoltaic parameters $(J_{sc}, V_{oc}, FF, and\ PCE)$ of the typical devices with different HTL's, especially using various electrodes based on their WF values**.** Apart from the Perovskite/HTL interface, the energy level mismatch alignment between the HTL/electrode interface also decides the device performance [118], [122]**.** The $CuSbS_2$-HTL device possesses the highest $J_{sc},$ and FF values, at the sametime, it has the poor V_{oc} results than other HTL candidates. The enhanced electric field throughout the perovskite layer occurred while increasing the electrode WF value. In general, the reduced device performance corresponding to the high Schottky barriers at the HTL/electrode interface, which restricts the hole extraction [106], [116]**.** Most of the HTL's based devices showing similar PCE values for $Ni, and\ Pt$ electrodes, except for $CuAlO_2, CuSbS_2, PTAA,$ and $P3HT$ (**Fig. 8.30 (d)** and **Table 8.7**). The above mentioned HTL devices exhibits entirely enhanced photovoltaic parameters demonstrated in **Fig. 8.7**. It is evident that either higher or lower electrode WF directly influences the results, and also, it is related to HTL properties (i.e, hole mobility and VBO). The obtained quantum efficiency curves for typical devices are illustrated in **Fig. 8.32(a)**. Simulated Ag-electrode device presenting the lower QE compared to other electrode devices, and it increases significantly based on the electrode WF values.

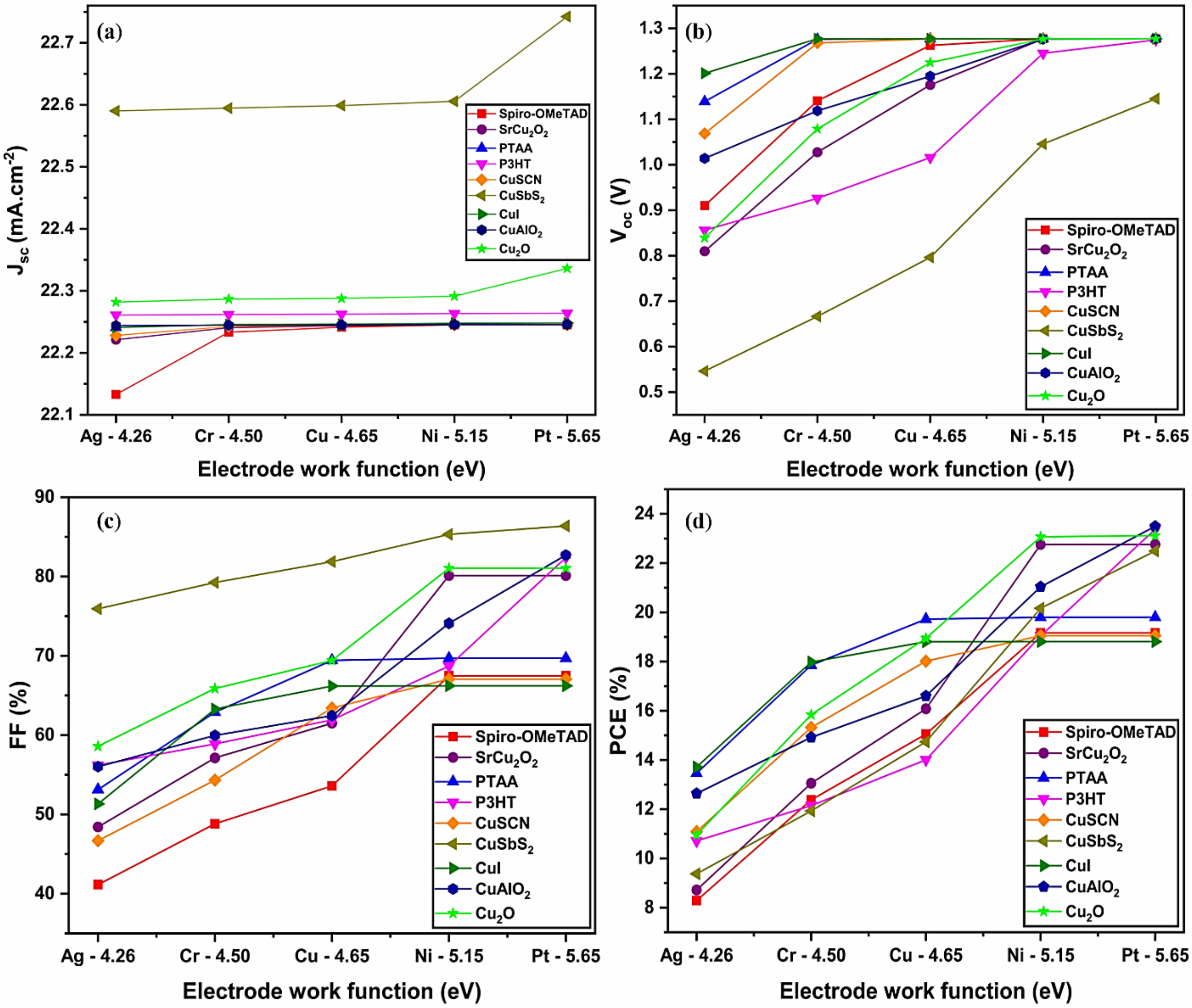

Fig. 8.30. *The photovoltaic parameters for the reference device with different HTL's and electrodes.*

From the QE graphs, it is easier to understand that the $Au, Ni,$ and Pt electrodes displaying the same behavior, the lines are overlapped, which agrees with the band diagram result (**see Fig. 8.29**). Previous reports exhibit that the oxidation from silver (Ag) to silver iodide (AgI) or silver bromide

$(AgBr)$ due to the ion migration from the perovskite layer through the HTL influence the device result. Also, the low formation energy (FE) and the low diffusion barrier (DB) value (0.27 eV) of Ag compared to other electrodes which manipulates the device performance [119], [120], [123], [124]. The Cu has much better corrsion resistance and improved DB value (0.42 eV) than Ag, even though it is not diifused into the perovskite layer. Therefore, Cu device performance was much better than Ag devices [120], [125].

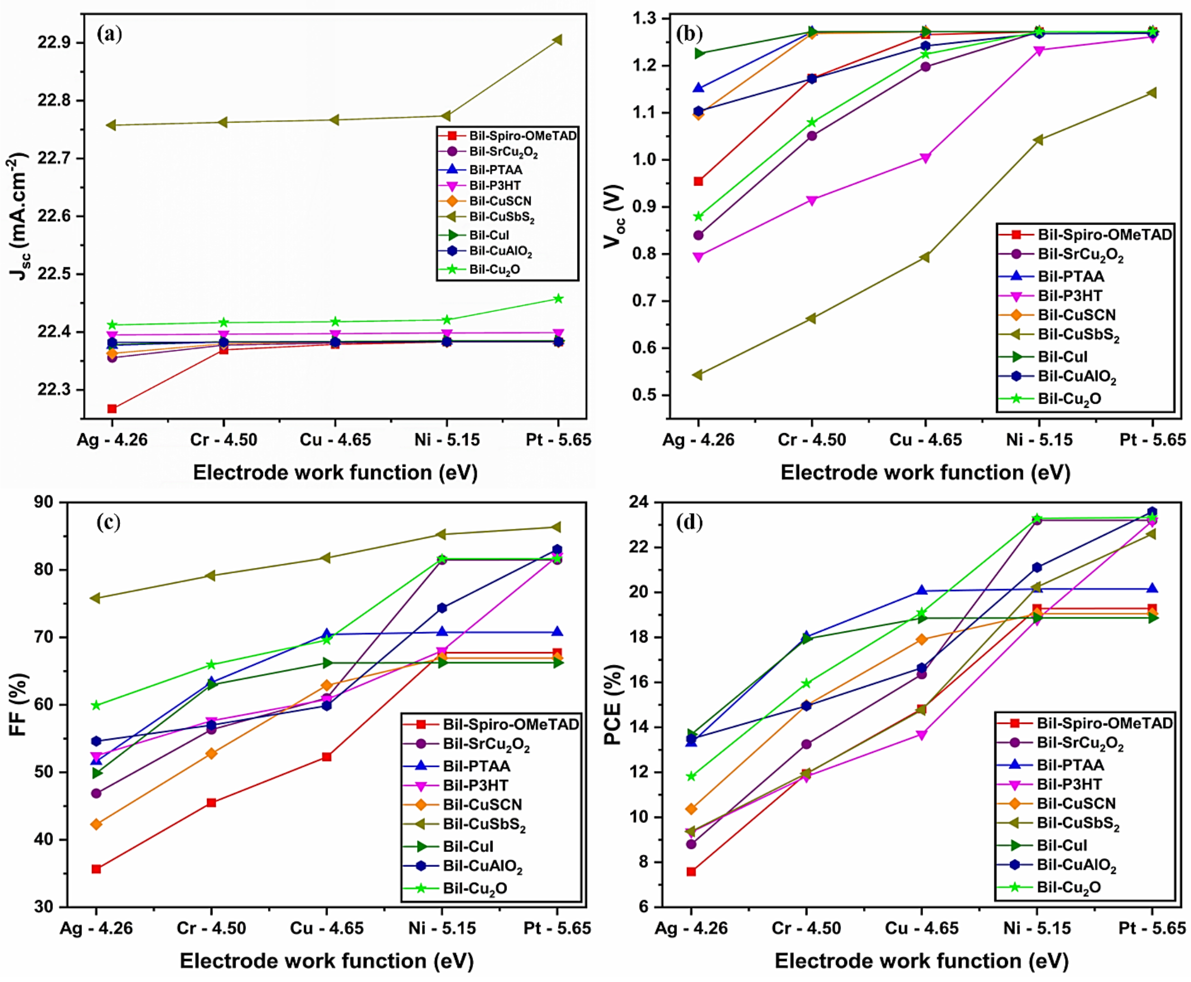

Fig. 8.31. *The photovoltaic parameters for the BiI_3 IL contained devices with different HTL and electrodes.*

The higher DB value (0.83 eV) and the lower FE of Cr helps to enhance the PCE than Ag, meanwhile, the R_{Series} might be rising because of their high resistivity value [120]**.** Due to the improved WF value from Ag, Cr to Cu electrodes (**see Fig. 8.29**), it is clear that the holes efficiently transferred from HTL to electrode, and it influence the device performances (**see Fig. 8.30**) Possibly, the higher recombination problem occurs at the perovskite/HTL or HTL/electrode interfaces in $Ag, Cr,$ and Cu based devices than Au, Ni, and Pt devices. The higher WF electrode devices exhibit excellent photovoltaic parameters than others (see **Fig. 8.30**) [119]**.** Therefore, it is recommended that the higher WF electrodes, such as Au, Ni, and Pt, are more suitable candidates for mixed cation/halide perovskite solar cells.

The obtained photovoltaic parameters ($J_{sc}, V_{oc}, FF, and\ PCE$) for the BiI_3 IL devices with different HTL and electrodes, as shown in **Fig. 8.31**. The obtained QE curves for the reference device, including IL, are demonstrated in **Fig. 8.32**. After adding the BiI_3 IL, we noticed that the device performance significantly improved while using higher WF electrodes (Au, Ni, and Pt). Simultaneously, the $Spiro - OMeTAD$-HTL devices show a decrement in photovoltaic parameters for Ag, Cr to Cu electrodes due to their lower WF value as well as it possibly creates the high Schottky barrier at the HTL/electrode interface which reduce the hole transport from HTL to an electrode (**Table 8.7**).

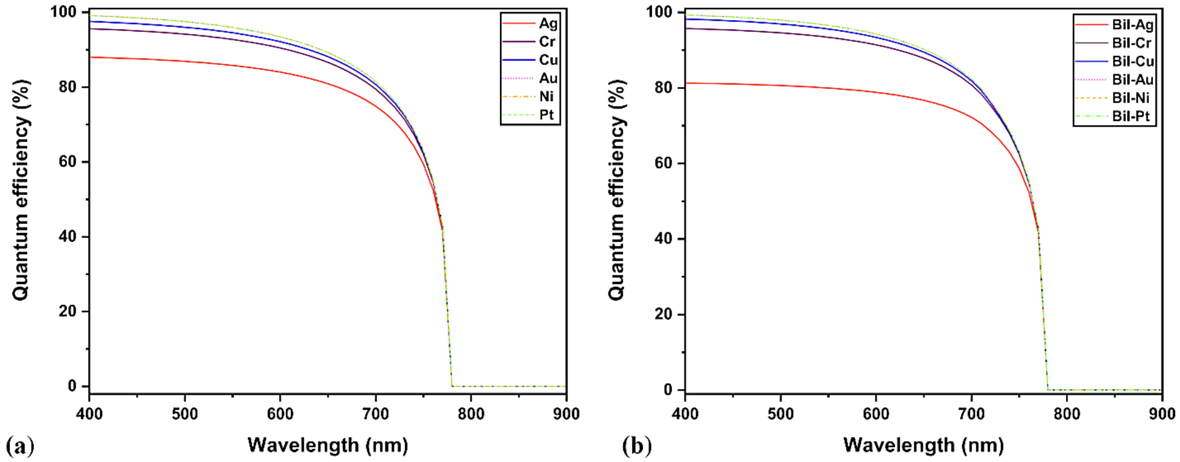

Fig. 8.32. *Quantum efficiency graph for the reference device (a) and BiI_3 IL contained device (b) with different electrodes.*

The case of $P3HT$-HTL devices (for all anodes) demonstrates a slightly lowered performance than the normal one. Most HTL candidates prove that a thin BiI_3 IL efficiently enhances the device results with all the electrodes mentioned above. The device performance is strongly affected due to the formation of the resistance layer at the HTL/electrode interface, so it is crucial to use the appropriate valence and conduction band energy levels having HTL [119]**.** Moreover, the reported experimental result shows that placing a thin Cr interfacial layer inbetween HTL and Au interface significantly reduced the electrode diffusion at the higher temperature, which is beneficial for higher performance devices [126]**.** Therefore, adding an IL between the interfaces could be an excellent strategy to improve solar cell performance. In the following section, we will demonstrate the influence of BiI_3 IL thickness over the absorber layer thickness.

Table 8.7. *Recorded photovoltaic parameters for $FTO/SnO_2/perovskite/HTL/Au$ devices. Where $HTL = Spiro - OMeTAD, Cu_2O, CuI, CuAlO_2, CuSbS_2, SrCu_2O_2, CuSCN, PTAA, P3HT$.*

			J_{sc} (mA/cm^2)	**FF (%)**	**V_{oc} (V)**	**PCE (%)**
Spiro-OMeTAD	W/o BiI_3	Ag	22.13	41.15	0.91	08.29
		Cr	22.23	48.82	1.14	12.37
		Cu	22.24	53.59	1.26	15.05
		Ni	22.25	67.46	1.27	19.16
		Pt	22.25	67.47	1.27	19.16
	W BiI_3	Ag	22.27	35.66	0.95	07.58
		Cr	22.37	45.48	1.17	11.94
		Cu	22.38	52.28	1.26	14.81
		Ni	22.38	67.72	1.27	19.28
		Pt	22.38	67.73	1.27	19.28
$SrCu_2O_2$	W/o BiI_3	Ag	22.22	48.42	0.81	8.71
		Cr	22.24	57.12	1.02	13.05
		Cu	22.24	61.50	1.17	16.50
		Ni	22.24	80.11	1.27	22.76
		Pt	22.24	80.11	1.27	22.76
	W BiI_3	Ag	22.35	46.88	0.84	08.80
		Cr	22.38	56.33	1.05	13.25
		Cu	22.38	60.99	1.19	16.35
		Ni	22.38	81.48	1.27	23.20
		Pt	22.38	81.49	1.27	23.20
PTAA	W/o BiI_3	Ag	22.24	53.13	1.14	13.46
		Cr	22.24	62.89	1.27	17.85
		Cu	22.24	69.42	1.27	19.72
		Ni	22.25	69.68	1.27	19.79
		Pt	22.25	69.69	1.27	19.80
	W BiI_3	Ag	22.37	51.62	1.15	13.29
		Cr	22.38	63.33	1.27	18.02
		Cu	22.38	70.44	1.27	20.06
		Ni	22.38	70.74	1.27	20.15
		Pt	22.38	70.74	1.27	20.15
P3HT	W/o BiI_3	Ag	22.26	56.20	0.85	10.71
		Cr	22.26	58.89	0.92	12.14
		Cu	22.26	61.92	1.01	14.00
		Ni	22.26	68.70	1.24	19.05
		Pt	22.26	82.39	1.27	23.38

	W BiI_3	Ag	22.39	52.46	0.79	09.34
		Cr	22.39	57.64	0.91	11.82
		Cu	22.39	60.80	1.00	13.69
		Ni	22.39	68.00	1.23	18.79
		Pt	22.39	82.02	1.26	23.17
CuSCN	W/o BiI_3	Ag	22.22	46.68	1.06	11.09
		Cr	22.24	54.33	1.26	15.32
		Cu	22.24	63.42	1.27	18.01
		Ni	22.25	67.05	1.27	19.04
		Pt	22.25	67.05	1.27	19.04
	W BiI_3	Ag	22.36	42.29	1.09	10.37
		Cr	22.38	52.78	1.26	14.98
		Cu	22.38	62.88	1.27	17.90
		Ni	22.38	66.92	1.27	19.05
		Pt	22.38	66.92	1.27	19.05
CuSbS$_2$	W/o BiI_3	Ag	22.59	75.93	0.54	9.37
		Cr	22.59	79.24	0.66	11.93
		Cu	22.59	81.87	0.79	14.73
		Ni	22.60	85.31	1.04	20.16
		Pt	22.74	86.38	1.14	22.49
	W BiI_3	Ag	22.76	75.81	0.54	09.37
		Cr	22.76	79.14	0.66	11.95
		Cu	22.76	81.78	0.7933	14.77
		Ni	22.77	85.26	1.04	20.24
		Pt	22.90	86.34	1.14	22.59
CuI	W/o BiI_3	Ag	22.24	51.33	1.20	13.71
		Cr	22.24	63.29	1.27	17.98
		Cu	22.24	66.19	1.27	18.80
		Ni	22.25	66.22	1.27	18.81
		Pt	22.25	66.22	1.27	18.81
	W BiI_3	Ag	22.37	49.88	1.22	13.68
		Cr	22.38	62.98	1.27	17.93
		Cu	22.38	66.21	1.27	18.85
		Ni	22.38	66.24	1.27	18.86
		Pt	22.38	66.24	1.27	18.86
CuAlO$_2$	W/o BiI_3	Ag	22.24	56.02	1.01	12.64
		Cr	22.24	59.96	1.11	14.92
		Cu	22.24	62.46	1.19	16.60
		Ni	22.24	74.10	1.27	21.04
		Pt	22.24	82.70	1.27	23.49
	W BiI_3	Ag	22.38	54.61	1.10	13.49
		Cr	22.38	56.99	1.17	14.95
		Cu	22.38	59.86	1.24	16.64
		Ni	22.38	74.36	1.26	21.11
		Pt	22.38	83.03	1.27	23.58

Cu_2O	W/o BiI_3	Ag	22.28	58.59	0.84	10.96
		Cr	22.28	65.88	1.08	15.84
		Cu	22.29	69.41	1.22	18.95
		Ni	22.29	81.04	1.27	23.07
		Pt	22.33	81.05	1.27	23.12
	W BiI_3	Ag	22.41	59.92	0.88	11.81
		Cr	22.41	65.93	1.08	15.95
		Cu	22.42	69.60	1.22	19.11
		Ni	22.42	81.65	1.27	23.29
		Pt	22.46	81.65	1.27	23.33

8.2.2.4. Effect of BiI_3 IL and absorber layer thickness

Generally, the properties of the perovskite absorber layer determine the device's performance. Mainly, the layer thickness is one of the leading parameter to enhance photon absorption, significantly improving the device results. After careful investigation, the Cu_2O-HTL was selected to perform the mentioned thickness analysis. Therefore, in this section, the influence of the perovskite layer and the BiI_3 IL thickness over the Cu_2O-HTL based device performance was carefully investigated. The absorber layer thickness differs from 500 to 1000 nm, as well as the interfacial layer thickness varied from 10 to 100 nm, and the other listed parameters in **Table 5.2** remain the same.

Fig. 8.33 demonstrates that the device PCE considerably enhances (23 % to 24 %) while increasing the absorber layer thickness from 500 to 1000 nm. It continuously improves up to 900 nm, then slightly decreases. Several experimental reports reveal that a thick perovskite layer will absorb more photons, especially in the red to the near-infrared region [127], [128], which is appropriate for solar devices. For example, Jiehuan Chen et al. studied the solar cell performance based on the different perovskite layer thickness, especially beyond 700 nm (i.e., 700, 850, 1000, 1150, 1400, and 1650 nm) using a simple hot casting method [129]. The 850 nm thicker absorber perovskite device provides the highest PCE (19.54%) among all other absorbers. Noticeably, the device maintains the stable PCE value of 19% from 700 to 1150 nm thickness range, and the device holds 80% of its initial PCE after 30 days. Therefore, using an optimum thicker perovskite absorber and the IL is beneficial for device improvement [76], [130]. Shaohang Wu et al. studied the inverted perovskite solar cell PV performance and stability while inserting a bismuth (Bi) interlayer (thickness - 5, 10, 20,40, and 80 nm) [76]. The results show that the thicker Bi film offers a uniform and good coverage film than a thin layer. Due to increased contact resistance, a thicker Bi layered

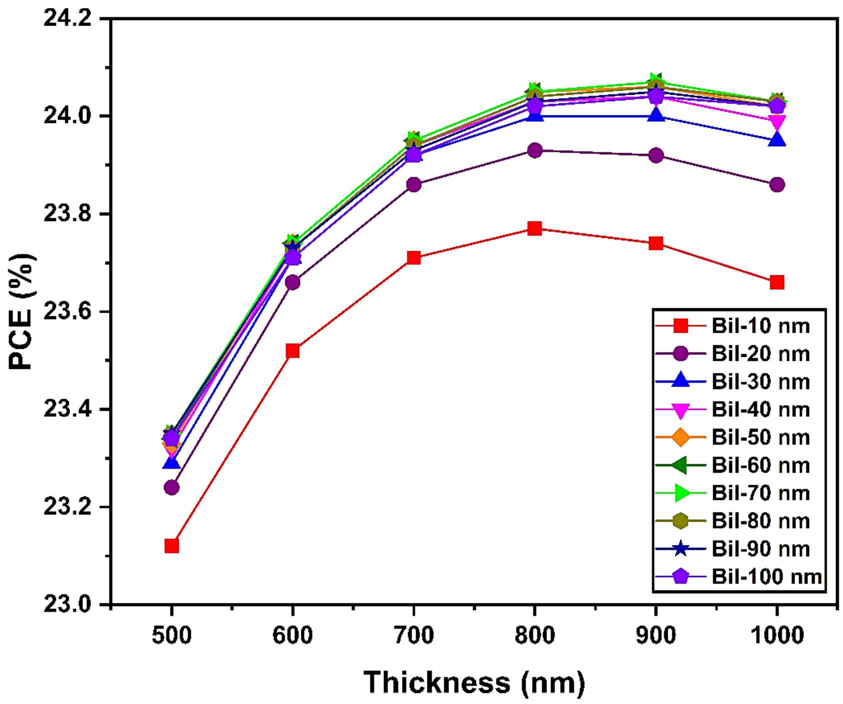

Fig. 8.33. *The variation of PCE (a) with different perovskite layer (500 nm to 1000 nm) and BiI_3 IL (10 nm to 100 nm) thickness.*

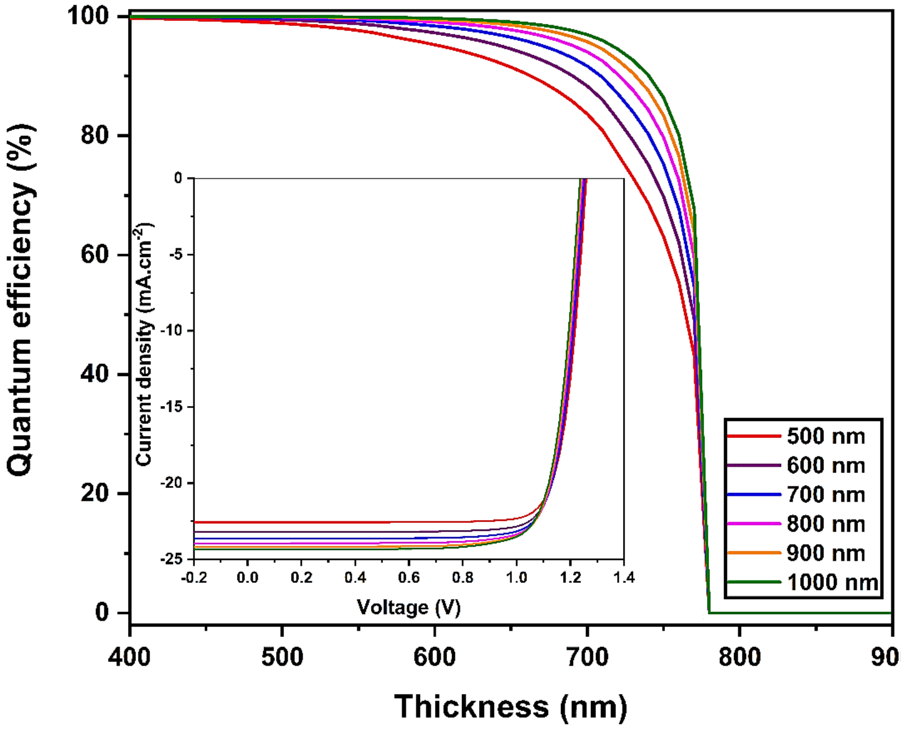

Fig. 8.34. *QE and J-V characteristics (inset) of a different perovskite absorber layer thickness (500 nm to 1000 nm), including 70 nm of BiI_3 IL.*

(i.e., 40 nm) solar cell reduces the device efficiency; most importantly, thicker IL lessens the degradation induced from ambient moisture leading to the stability enhancement (6000 h). In that perspective, we simultaneously investigated the BiI_3 IL thickness with different perovskite layer thickness and makes it evident that the increment substantially improves the PCE (see **Fig. 8.33**). So, the optimum BiI_3 IL thickness was found at 70 nm, which corresponds to the superior PCE (i.e., PCE = 24.07%, J_{sc} = 24.18 mA/cm^2, FF = 80.25%, $and\ V_{oc}$ = 1.24 V). Moreover, the thick perovskite (more than 900 nm) layered device possibly suffered from higher recombination issues at the interface due to the absorber thickness that is larger than the diffusion length of charge carriers, which led to poor device performance. **Fig. 8.34** exhibits that the obtained QE graph's tendency is consistent with the PCE results (see **Fig. 8.33**). The current density – voltage characteristics (inset) also proves the previously mentioned behavior.

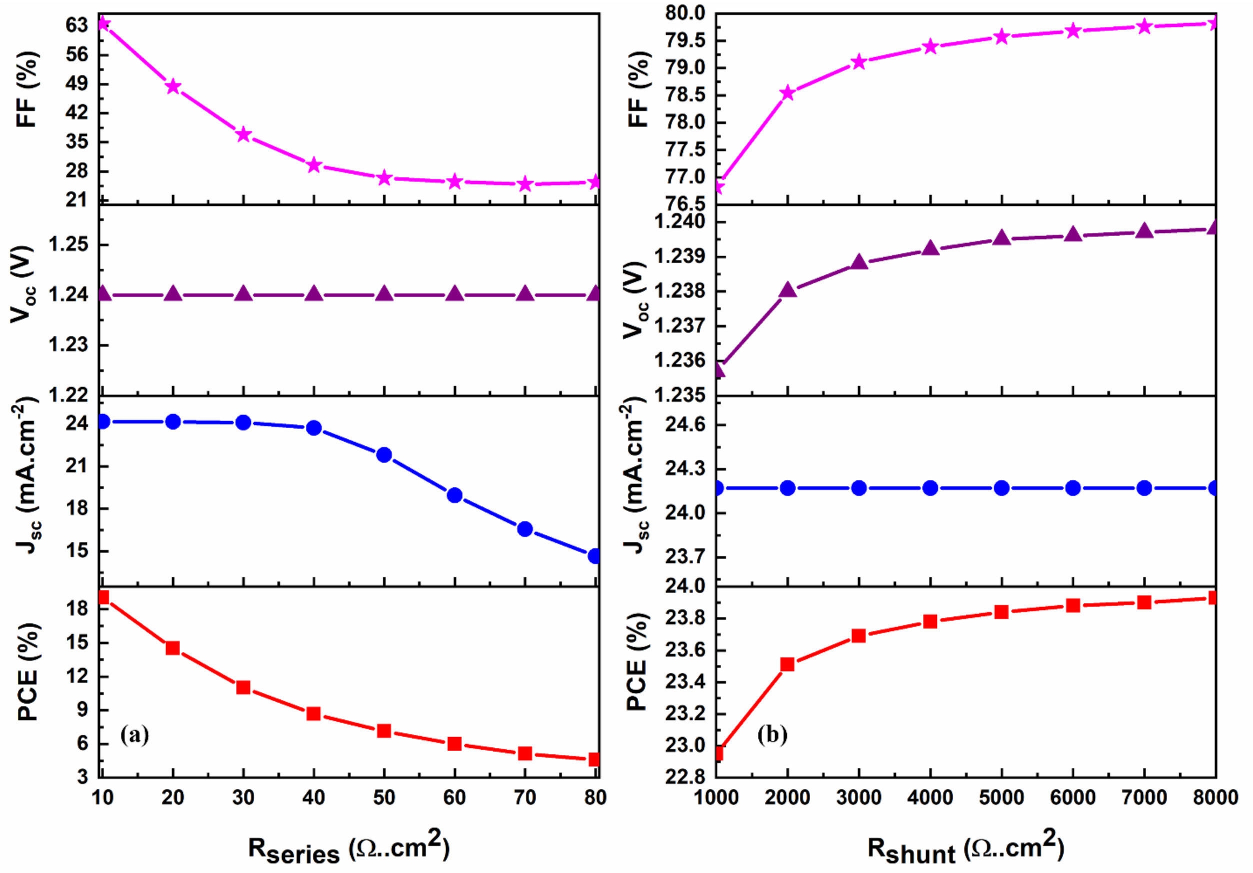

Fig. 8.35. *Effect of R_{series} (a) and R_{shunt} (b) in the performance of simulated Cu_2O-HTL device with BiI_3 IL.*

The simulation findings suggest that the 900 nm perovskite layer with 70 nm BiI_3 IL is appropriate for an excellent $FAPI$ based perovskite device. However, the parasitic resistances (R_{series} and

R_{shunt}) are largely influence the experimental device performance. For example, a higher efficiency device must be having a low R_{series} and a high R_{shunt}. Our previous work clearly demonstrates that the effect of these resistances over three different perovskite absorber layer-based devices [49]. Therefore, here we investigated the impact of these resistances over the Cu_2O-HTL device to understand the device behavior.

We varied the R_{series} and R_{shunt} values between 10 – 80 $\Omega.cm^2$ and 1000 – 5000 $\Omega.cm^2$, respectively, and the corresponding evolution of the photovoltaic parameters are demonstrated in **Fig. 8.35 (a) and (b).** Our obtained results show that an increase in R_{series} from 10 to 80 $\Omega.cm^2$ strongly decreases the FF from 63% to 25%. Moreover, for a R_{series} over 40 $\Omega.cm^2$, J_{sc} is rapidly reduced from 24 to 14 mA/cm^2. Also, the overall PCE is rapidly decreased from 24% to only 4.5% (see **Fig. 8.35 (a)**). Usually, R_{series} does not influence the V_{oc}, and the obtained V_{oc} behavior is shown in **Fig. 8.35 (a)**. In comparison, increasing R_{shunt} enhances the FF and PCE values (see **Fig. 8.35 (b)**), at the same time, it slightly affects the V_{oc} and J_{sc} values. So, the high R_{shunt} is an indication of less defect and interface states present in the device. While varying the R_{series} and R_{shunt} values into the optimized device, considerable changes occur in the photovoltaic parameters. Therefore, it is clear that these parasitic resistances efficiently affect device performance. Finally, we also employed the optimized thicknesses (absorber and IL layer) in $SrCu_2O_2$-HTL solar cell and it shows a PCE of 23.91 % with a short current density (J_{sc}) value of 24.17 mA/cm^2, a fill factor (FF) of 79.73 %, and an open-circuit voltage (V_{oc}) of 1.24 V. As a result, based on our report, a further insightful experimental study is necessary to understand the mechanism behind the BiI_3 IL over the device performance.

8.3. Conclusion

In this chapter, we systematically introduce Cu^+ and Bi^{3+} in $FA_{0.85}Cs_{0.15}Pb(I_{0.85}Br_{0.15})_3$ double cation planar perovskite solar cells, from the simple addition of CuI and BiI_3 in the precursor solutions and as a function of doping ratio (x) ranging from 0.01 to 0.15. The morphological studies revealed a drastic alteration of active layer morphology upon Bismuth incorporation, even at low doping level, while layer-based on Cu show a significant increase of grain dimensions, with Copper-rich grain boundaries. The structural characterizations also show a beneficial effect of Copper addition on the crystalline quality of the perovskite phase, while Bismuth induces drastic changes even for low doping levels. While the fabricated undoped reference device displays quite high photovoltaic performance (PCE >15%), the Cu and Bi-doped devices demonstrate much poorer efficiencies. The TPV measurement evidence that the faster recombination kinetics for the doped devices compared to the reference cell, even at low doping levels. This observation confirms that any strategy aiming at substituting lead by a metallic cation alternative should carefully be controlled to avoid the creation of detrimental defects, either at the interface or in the bulk. These defects reduce the device efficiency but also impact device lifetime, as observed under preliminary aging tests performed in ambient conditions. Finally, our study emphasizes that the substitution of lead by a monovalent cation might be less detrimental to the perovskite structure than a trivalent alternative such as Bi, even if a low doping ratio can indeed lead to efficient or stable devices.

Also, the $FA_{0.85}Cs_{0.15}Pb(I_{0.85}Br_{0.15})_3$ perovskite absorber layer-based n-i-p planar device with and without BiI_3 interfacial layer tested with different HTL's and various electrodes were carefully analyzed and presented using SCAPS. The simulated results exhibit that the Cu based HTL's, especially Cu_2O & $SrCu_2O_2$ shows excellent photovoltaic performance than other HTL competitors. The optimized 900 nm perovskite layer with a thin (70 nm) interfacial BiI_3 layer has a more substantial influence on the solar cell results, which significantly boosted the photovoltaic parameters by reducing the perovskite/HTL interface defects. Therefore, both $Cu_2O\ and\ SrCu_2O_2$ HTL's are considered as suitable HTL's (with and without BiI_3 IL) for $FA_{0.85}Cs_{0.15}Pb(I_{0.85}Br_{0.15})_3$ based planar device. Also, the impact of different electrodes was examined using various HTL candidates, and our results emphasize that the higher work function electrodes such as Au, Ni, and Pt are more considerable than Ag, Cr to Cu. From the result, the simulated device displaying an efficiency of around 24 % with a suitable Cu_2O-HTL. Here, the absence of parasitic electrical losses (without considering the optical reflectance of each layer at the interface nor surface) could be the prominent reason for the obtained higher efficiency than the reported experimental reports. The optimized absorber, IL thickness, and parasitic resistances are also crucial for efficient devices. These experimental and simulation findings are useful for further understanding of the BiI_3 doping or IL in between perovskite/HTL interface and enhancing the mixed cation/halide perovskite solar cells.

References

[1] Q. Han *et al.*, "Single Crystal Formamidinium Lead Iodide (FAPbI3): Insight into the Structural, Optical, and Electrical Properties," *Adv. Mater.*, 2016, doi: 10.1002/adma.201505002.

[2] G. E. Eperon, S. D. Stranks, C. Menelaou, M. B. Johnston, L. M. Herz, and H. J. Snaith, “Formamidinium lead trihalide: A broadly tunable perovskite for efficient planar heterojunction solar cells,” *Energy Environ. Sci.*, 2014, doi: 10.1039/c3ee43822h.

[3] S. Wozny *et al.*, “Controlled Humidity Study on the Formation of Higher Efficiency Formamidinium Lead Triiodide-Based Solar Cells,” *Chem. Mater.*, 2015, doi: 10.1021/acs.chemmater.5b01691.

[4] D. Prochowicz *et al.*, “Engineering of Perovskite Materials Based on Formamidinium and Cesium Hybridization for High-Efficiency Solar Cells,” *Chem. Mater.*, 2019, doi: 10.1021/acs.chemmater.8b04871.

[5] O. Nazarenko, S. Yakunin, V. Morad, I. Cherniukh, and M. V. Kovalenko, “Single crystals of caesium formamidinium lead halide perovskites: Solution growth and gamma dosimetry,” *NPG Asia Mater.*, 2017, doi: 10.1038/am.2017.45.

[6] W. Rehman *et al.*, “Photovoltaic mixed-cation lead mixed-halide perovskites: Links between crystallinity, photo-stability and electronic properties,” *Energy Environ. Sci.*, 2017, doi: 10.1039/c6ee03014a.

[7] C. M. Sutter-Fella *et al.*, “Cation-Dependent Light-Induced Halide Demixing in Hybrid Organic-Inorganic Perovskites,” *Nano Lett.*, 2018, doi: 10.1021/acs.nanolett.8b00541.

[8] M. Saliba *et al.*, “Cesium-containing triple cation perovskite solar cells: Improved stability, reproducibility and high efficiency,” *Energy Environ. Sci.*, 2016, doi: 10.1039/c5ee03874j.

[9] B. G. H. M. Groeneveld *et al.*, “Stable Cesium Formamidinium Lead Halide Perovskites: A Comparison of Photophysics and Phase Purity in Thin Films and Single Crystals,” *Energy Technol.*, 2020, doi: 10.1002/ente.201901041.

[10] S. Prathapani, P. Bhargava, and S. Mallick, “Electronic band structure and carrier concentration of formamidinium-cesium mixed cation lead mixed halide hybrid perovskites,” *Appl. Phys. Lett.*, 2018, doi: 10.1063/1.5016829.

[11] J. W. Lee, D. H. Kim, H. S. Kim, S. W. Seo, S. M. Cho, and N. G. Park, “Formamidinium and cesium hybridization for photo- and moisture-stable perovskite solar cell,” *Adv. Energy Mater.*, 2015, doi: 10.1002/aenm.201501310.

[12] P. Selvarajan, K. Kundu, C. I. Sathish, S. Umapathy, and A. Vinu, “Enriched Photophysical Properties and Thermal Stability of Tin(II) Substituted Lead-Based Perovskite Nanocrystals with Mixed Organic–Inorganic Cations,” *J. Phys. Chem. C*, 2020, doi: 10.1021/acs.jpcc.0c02223.

[13] S. Akin, N. Arora, S. M. Zakeeruddin, M. Grätzel, R. H. Friend, and M. I. Dar, “New Strategies for Defect Passivation in High-Efficiency Perovskite Solar Cells,” *Advanced Energy Materials*. 2020, doi: 10.1002/aenm.201903090.

[14] G. Yang, P. Qin, G. Fang, and G. Li, “A Lewis Base-Assisted Passivation Strategy Towards Highly Efficient and Stable Perovskite Solar Cells,” *Sol. RRL*, 2018, doi: 10.1002/solr.201800055.

[15] Y. Chen, J. Yang, S. Wang, Y. Wu, N. Yuan, and W. H. Zhang, “Interfacial Contact Passivation for Efficient and Stable Cesium-Formamidinium Double-Cation Lead Halide Perovskite Solar Cells,” *iScience*, 2020, doi: 10.1016/j.isci.2019.100762.

[16] J. Kim, A. Ho-Baillie, and S. Huang, “Review of Novel Passivation Techniques for Efficient and Stable Perovskite Solar Cells,” *Solar RRL*. 2019, doi: 10.1002/solr.201800302.

[17] Y. Ogomi *et al.*, “CH3NH3SnxPb(1-x)I3 perovskite solar cells covering up to 1060 nm,” *J. Phys. Chem. Lett.*, 2014, doi: 10.1021/jz5002117.

[18] X. Liu *et al.*, “Improved efficiency and stability of Pb-Sn binary perovskite solar cells by Cs substitution,” *J. Mater. Chem. A*, 2016, doi: 10.1039/c6ta07712a.

[19] J. Navas *et al.*, “New insights into organic-inorganic hybrid perovskite CH3NH3PbI3 nanoparticles. An experimental and theoretical study of doping in Pb2+ sites with Sn2+, Sr2+, Cd2+ and Ca2+,” *Nanoscale*,

2015, doi: 10.1039/c5nr00041f.

[20] M. R. Filip and F. Giustino, “Computational Screening of Homovalent Lead Substitution in Organic-Inorganic Halide Perovskites,” *J. Phys. Chem. C*, 2016, doi: 10.1021/acs.jpcc.5b11845.

[21] M. T. Klug *et al.*, “Tailoring metal halide perovskites through metal substitution,” *Energy Environ. Sci.*, 2017, doi: 10.1039/c6ee03201j T4 - Influence on photovoltaic and material properties M4 - Citavi.

[22] L. A. Frolova, D. V. Anokhin, K. L. Gerasimov, N. N. Dremova, and P. A. Troshin, “Exploring the Effects of the Pb2+ Substitution in MAPbI3 on the Photovoltaic Performance of the Hybrid Perovskite Solar Cells,” *J. Phys. Chem. Lett.*, 2016, doi: 10.1021/acs.jpclett.6b02122.

[23] J. Zhang *et al.*, “N-Type Doping and Energy States Tuning in CH3NH3Pb1-xSb2x/3I3 Perovskite Solar Cells,” *ACS Energy Lett.*, 2016, doi: 10.1021/acsenergylett.6b00241.

[24] S. Shahbazi *et al.*, “Ag Doping of Organometal Lead Halide Perovskites: Morphology Modification and p-Type Character,” *J. Phys. Chem. C*, 2017, doi: 10.1021/acs.jpcc.6b09722.

[25] W. Ke and M. G. Kanatzidis, “Prospects for low-toxicity lead-free perovskite solar cells,” *Nature Communications*. 2019, doi: 10.1038/s41467-019-08918-3.

[26] R. Nie, R. R. SUMUKAM, S. H. Reddy, M. Banavoth, and S. Il Seok, “Lead-Free Perovskite Solar Cells Enabled by Hetero-Valent Substitutes,” *Energy Environ. Sci.*, 2020, doi: 10.1039/d0ee01153c.

[27] F. Giustino and H. J. Snaith, “Toward Lead-Free Perovskite Solar Cells,” *ACS Energy Letters*. 2016, doi: 10.1021/acsenergylett.6b00499.

[28] S. Chatterjee and A. J. Pal, “Influence of metal substitution on hybrid halide perovskites: Towards lead-free perovskite solar cells,” *J. Mater. Chem. A*, 2018, doi: 10.1039/c7ta09943f.

[29] X. Li, F. Zhang, H. He, J. J. Berry, K. Zhu, and T. Xu, “On-device lead sequestration for perovskite solar cells,” *Nature*, 2020, doi: 10.1038/s41586-020-2001-x.

[30] Z. S. Wang, F. Ebadi, B. Carlsen, W. C. H. Choy, and W. Tress, “Transient Photovoltage Measurements on Perovskite Solar Cells with Varied Defect Concentrations and Inhomogeneous Recombination Rates,” *Small Methods*, 2020, doi: 10.1002/smtd.202000290.

[31] Z. Song *et al.*, “Copper Incorporation in Organic-Inorganic Hybrid Halide Perovskite Solar Cells,” *ChemistrySelect*, 2018, doi: 10.1002/slct.201802792.

[32] C. Soykan and H. Gocmez, “The physical properties of bismuth replacement in lead halogen perovskite solar cells: CH3NH3Pb1−xBixI3 compounds by ab-initio calculations,” *Results Phys.*, 2019, doi: 10.1016/j.rinp.2019.102278.

[33] A. Walsh, “Principles of chemical bonding and band gap engineering in hybrid organic-inorganic halide perovskites,” *J. Phys. Chem. C*, 2015, doi: 10.1021/jp512420b.

[34] R. Wang *et al.*, “Bi3+-doped CH3NH3PbI3: Red-shifting absorption edge and longer charge carrier lifetime,” *J. Alloys Compd.*, 2017, doi: 10.1016/j.jallcom.2016.11.125.

[35] S. Ye *et al.*, “A Breakthrough Efficiency of 19.9% Obtained in Inverted Perovskite Solar Cells by Using an Efficient Trap State Passivator Cu(thiourea)I,” *J. Am. Chem. Soc.*, 2017, doi: 10.1021/jacs.7b01439.

[36] M. Jahandar *et al.*, “Highly efficient metal halide substituted CH3NH3I(PbI2)1−X(CuBr2)X planar perovskite solar cells,” *Nano Energy*, 2016, doi: 10.1016/j.nanoen.2016.07.022.

[37] M. Abdi-Jalebi, M. Ibrahim Dar, A. Sadhanala, S. P. Senanayak, M. Grätzel, and R. H. Friend, “Monovalent cation doping of CH3NH3PBI3 for efficient perovskite solar cells,” *J. Vis. Exp.*, 2017, doi: 10.3791/55307.

[38] Y. Hu, T. Qiu, F. Bai, X. Miao, and S. Zhang, “Enhancing moisture-tolerance and photovoltaic performances of FAPbI3 by bismuth incorporation,” *J. Mater. Chem. A*, 2017, doi: 10.1039/c7ta08824h.

[39] M. Yavari *et al.*, “How far does the defect tolerance of lead-halide perovskites range? The example of Bi impurities introducing efficient recombination centers,” *J. Mater. Chem. A*, 2019, doi: 10.1039/c9ta01744e.

[40] J. Carrillo *et al.*, “Ionic Reactivity at Contacts and Aging of Methylammonium Lead Triiodide Perovskite Solar Cells,” *Adv. Energy Mater.*, 2016, doi: 10.1002/aenm.201502246.

[41] J. Bartolomé *et al.*, “Huge Photostability Enhancement in Bismuth-Doped Methylammonium Lead Iodide Hybrid Perovskites by Light-Induced Transformation,” *Chem. Mater.*, 2019, doi: 10.1021/acs.chemmater.9b00270.

[42] Y. Hu *et al.*, “Bismuth Incorporation Stabilized α-CsPbI3 for Fully Inorganic Perovskite Solar Cells,” *ACS Energy Lett.*, 2017, doi: 10.1021/acsenergylett.7b00508.

[43] Y. Zhao, A. M. Nardes, and K. Zhu, “Mesoporous perovskite solar cells: Material composition, charge-carrier dynamics, and device characteristics,” *Faraday Discuss.*, 2014, doi: 10.1039/c4fd00128a.

[44] R. Nishikubo and A. Saeki, “Comparative study of charge carrier dynamics in bismuth-based dimer and double perovskites,” *J. Photopolym. Sci. Technol.*, 2019, doi: 10.2494/photopolymer.32.735.

[45] P. K. Nayak *et al.*, “Impact of Bi3+ Heterovalent Doping in Organic-Inorganic Metal Halide Perovskite Crystals,” *J. Am. Chem. Soc.*, 2018, doi: 10.1021/jacs.7b11125.

[46] Y. Lin *et al.*, “Metallic surface doping of metal halide perovskites,” *Nat. Commun.*, 2021, doi: 10.1038/s41467-020-20110-6.

[47] D. Di Girolamo *et al.*, “Dual effect of humidity on cesium lead bromide: Enhancement and degradation of perovskite films,” *J. Mater. Chem. A*, 2019, doi: 10.1039/c9ta00715f.

[48] P. Chhillar, B. P. Dhamaniya, V. Dutta, and S. K. Pathak, “Recycling of Perovskite Films: Route toward Cost-Efficient and Environment-Friendly Perovskite Technology,” *ACS Omega*, 2019, doi: 10.1021/acsomega.9b01053.

[49] S. Karthick, S. Velumani, and J. Bouclé, “Experimental and SCAPS simulated formamidinium perovskite solar cells: A comparison of device performance,” *Sol. Energy*, 2020, doi: 10.1016/j.solener.2020.05.041.

[50] E. J. Juarez-Perez, M. R. Leyden, S. Wang, L. K. Ono, Z. Hawash, and Y. Qi, “Role of the Dopants on the Morphological and Transport Properties of Spiro-MeOTAD Hole Transport Layer,” *Chem. Mater.*, 2016, doi: 10.1021/acs.chemmater.6b01777.

[51] S. Wang *et al.*, “Role of 4-tert-Butylpyridine as a Hole Transport Layer Morphological Controller in Perovskite Solar Cells,” *Nano Lett.*, 2016, doi: 10.1021/acs.nanolett.6b02158.

[52] Y. Liu *et al.*, “Inhibited aggregation of lithium salt in spiro-OMeTAD toward highly efficient perovskite solar cells,” *Nano Energy*, 2020, doi: 10.1016/j.nanoen.2020.104483.

[53] C. Eames, J. M. Frost, P. R. F. Barnes, B. C. O’Regan, A. Walsh, and M. S. Islam, “Ionic transport in hybrid lead iodide perovskite solar cells,” *Nat. Commun.*, 2015, doi: 10.1038/ncomms8497.

[54] H. J. Snaith *et al.*, “Anomalous Hysteresis in Perovskite Solar Cells-Supporting Information,” *J. Phys. Chem. Lett.*, 2014.

[55] T. Shi, W. J. Yin, and Y. Yan, “Predictions for p-type CH3NH3PbI3 perovskites,” *J. Phys. Chem. C*, 2014, doi: 10.1021/jp508328u.

[56] E. Greul, M. L. Petrus, A. Binek, P. Docampo, and T. Bein, “Highly stable, phase pure Cs2AgBiBr6 double perovskite thin films for optoelectronic applications,” *J. Mater. Chem. A*, 2017, doi: 10.1039/c7ta06816f.

[57] L. C. Lee, T. N. Huq, J. L. Macmanus-Driscoll, and R. L. Z. Hoye, “Research Update: Bismuth-based perovskite-inspired photovoltaic materials,” *APL Materials*. 2018, doi: 10.1063/1.5029484.

[58] U. H. Hamdeh, R. D. Nelson, B. J. Ryan, U. Bhattacharjee, J. W. Petrich, and M. G. Panthani, “Solution-processed BiI3 thin films for photovoltaic applications: Improved carrier collection via solvent annealing,”

Chem. Mater., 2016, doi: 10.1021/acs.chemmater.6b02347.

[59] R. E. Brandt *et al.*, “Investigation of Bismuth Triiodide (BiI3) for Photovoltaic Applications,” *J. Phys. Chem. Lett.*, 2015, doi: 10.1021/acs.jpclett.5b02022.

[60] P. R. F. Barnes *et al.*, “Interpretation of optoelectronic transient and charge extraction measurements in dye-sensitized solar cells,” *Advanced Materials*. 2013, doi: 10.1002/adma.201201372.

[61] N. Kopidakis, K. D. Benkstein, J. Van De Lagemaat, and A. J. Frank, “Transport-limited recombination of photocarriers in dye-sensitized nanocrystalline TiO2 solar cells,” *J. Phys. Chem. B*, 2003, doi: 10.1021/jp0304475.

[62] B. Xu *et al.*, “Integrated design of organic hole transport materials for efficient solid-state dye-sensitized solar cells,” *Adv. Energy Mater.*, 2015, doi: 10.1002/aenm.201401185.

[63] A. Maurano *et al.*, “Recombination dynamics as a key determinant of open circuit voltage in organic bulk heterojunction solar cells: A comparison of four different donor polymers,” *Adv. Mater.*, 2010, doi: 10.1002/adma.201002360.

[64] T. M. Clarke, C. Lungenschmied, J. Peet, N. Drolet, and A. J. Mozer, “A comparison of five experimental techniques to measure charge carrier lifetime in polymer/fullerene solar cells,” *Adv. Energy Mater.*, 2015, doi: 10.1002/aenm.201401345.

[65] R. S. Sanchez *et al.*, “Slow dynamic processes in lead halide perovskite solar cells. Characteristic times and hysteresis,” *J. Phys. Chem. Lett.*, 2014, doi: 10.1021/jz5011187.

[66] B. C. O’Regan, P. R. F. Barnes, X. Li, C. Law, E. Palomares, and J. M. Marin-Beloqui, “Optoelectronic studies of methylammonium lead iodide perovskite solar cells with mesoporous TiO2: Separation of electronic and chemical charge storage, understanding two recombination lifetimes, and the evolution of band offsets during J - V hysteresis,” *J. Am. Chem. Soc.*, 2015, doi: 10.1021/jacs.5b00761.

[67] D. Kiermasch, L. Gil-Escrig, A. Baumann, H. J. Bolink, V. Dyakonov, and K. Tvingstedt, “Unravelling steady-state bulk recombination dynamics in thick efficient vacuum-deposited perovskite solar cells by transient methods,” *J. Mater. Chem. A*, 2019, doi: 10.1039/c9ta04367e.

[68] M. Azzouzi *et al.*, “Overcoming the Limitations of Transient Photovoltage Measurements for Studying Recombination in Organic Solar Cells,” *Sol. RRL*, 2020, doi: 10.1002/solr.201900581.

[69] D. Kiermasch, A. Baumann, M. Fischer, V. Dyakonov, and K. Tvingstedt, “Revisiting lifetimes from transient electrical characterization of thin film solar cells; A capacitive concern evaluated for silicon, organic and perovskite devices,” *Energy Environ. Sci.*, 2018, doi: 10.1039/c7ee03155f.

[70] N. Mica *et al.*, “Triple cation perovskite solar cells for visible light communications,” *Photonics Res.*, 2020, doi: 10.1364/prj.393647.

[71] A. Pockett and M. J. Carnie, “Ionic Influences on Recombination in Perovskite Solar Cells,” *ACS Energy Lett.*, 2017, doi: 10.1021/acsenergylett.7b00490.

[72] Q. Fu *et al.*, “Recent Progress on the Long-Term Stability of Perovskite Solar Cells,” *Advanced Science*. 2018, doi: 10.1002/advs.201700387.

[73] R. Wang, M. Mujahid, Y. Duan, Z. K. Wang, J. Xue, and Y. Yang, “A Review of Perovskites Solar Cell Stability,” *Advanced Functional Materials*. 2019, doi: 10.1002/adfm.201808843.

[74] M. V. Khenkin *et al.*, “Consensus statement for stability assessment and reporting for perovskite photovoltaics based on ISOS procedures,” *Nat. Energy*, 2020, doi: 10.1038/s41560-019-0529-5.

[75] S. Shao and M. A. Loi, “The Role of the Interfaces in Perovskite Solar Cells,” *Advanced Materials Interfaces*. 2020, doi: 10.1002/admi.201901469.

[76] S. Wu *et al.*, “A chemically inert bismuth interlayer enhances long-term stability of inverted perovskite solar cells,” *Nat. Commun.*, 2019, doi: 10.1038/s41467-019-09167-0.

[77] L. Qiu, S. He, L. K. Ono, S. Liu, and Y. Qi, “Scalable Fabrication of Metal Halide Perovskite Solar Cells and Modules,” *ACS Energy Letters*. 2019, doi: 10.1021/acsenergylett.9b01396.

[78] A. N. Cho and N. G. Park, “Impact of Interfacial Layers in Perovskite Solar Cells,” *ChemSusChem*. 2017, doi: 10.1002/cssc.201701095.

[79] N. K. Noel *et al.*, “Enhanced photoluminescence and solar cell performance via Lewis base passivation of organic-inorganic lead halide perovskites,” *ACS Nano*, 2014, doi: 10.1021/nn5036476.

[80] J. W. Lee, D. J. Seol, A. N. Cho, and N. G. Park, “High-efficiency perovskite solar cells based on the black polymorph of HC(NH2)2PbI3,” *Adv. Mater.*, 2014, doi: 10.1002/adma.201401137.

[81] D. Song *et al.*, “Dual function interfacial layer for highly efficient and stable lead halide perovskite solar cells,” *J. Mater. Chem. A*, 2016, doi: 10.1039/c6ta00577b.

[82] L. Gil-Escrig *et al.*, “Efficient photovoltaic and electroluminescent perovskite devices,” *Chem. Commun.*, 2015, doi: 10.1039/c4cc07518h.

[83] Y. Liu *et al.*, “Ultrahydrophobic 3D/2D fluoroarene bilayer-based water-resistant perovskite solar cells with efficiencies exceeding 22%,” *Sci. Adv.*, 2019, doi: 10.1126/sciadv.aaw2543.

[84] S. Gharibzadeh *et al.*, “Record Open-Circuit Voltage Wide-Bandgap Perovskite Solar Cells Utilizing 2D/3D Perovskite Heterostructure,” *Adv. Energy Mater.*, 2019, doi: 10.1002/aenm.201803699.

[85] K. T. Cho *et al.*, “Highly efficient perovskite solar cells with a compositionally engineered perovskite/hole transporting material interface,” *Energy Environ. Sci.*, 2017, doi: 10.1039/c6ee03182j.

[86] L. Fu, Y. Nie, B. Li, N. Li, B. Cao, and L. Yin, “Bismuth Telluride Interlayer for All-Inorganic Perovskite Solar Cells with Enhanced Efficiency and Stability,” *Sol. RRL*, 2019, doi: 10.1002/solr.201900233.

[87] N. F. Coutinho *et al.*, “The Thermomechanical Properties of Thermally Evaporated Bismuth Triiodide Thin Films,” *Sci. Rep.*, 2019, doi: 10.1038/s41598-019-48194-1.

[88] B. Yoo *et al.*, “Improved Charge Separation and Photovoltaic Performance of BiI3 Absorber Layers by Use of an in Situ Formed BiSI Interlayer,” *ACS Appl. Energy Mater.*, 2019, doi: 10.1021/acsaem.9b00838.

[89] Y. Hu, S. Zhang, W. Ruan, D. Wang, Y. Wu, and F. Xu, “Interfacing pristine BiI3 onto TiO2 for efficient and stable planar perovskite solar cells,” *Appl. Surf. Sci.*, 2020, doi: 10.1016/j.apsusc.2019.144769.

[90] U. National Minerals Information Center, “mcs2020.pdf - Mineral Commodity Summaries 2020.”

[91] A. Gheno, S. Vedraine, B. Ratier, and J. Bouclé, “π-Conjugated materials as the hole-transporting layer in perovskite solar cells,” *Metals*. 2016, doi: 10.3390/met6010021.

[92] Y. Yu *et al.*, “Improving the Performance of Formamidinium and Cesium Lead Triiodide Perovskite Solar Cells using Lead Thiocyanate Additives,” *ChemSusChem*, 2016, doi: 10.1002/cssc.201601027.

[93] D. P. McMeekin *et al.*, “Crystallization Kinetics and Morphology Control of Formamidinium–Cesium Mixed-Cation Lead Mixed-Halide Perovskite via Tunability of the Colloidal Precursor Solution,” *Adv. Mater.*, 2017, doi: 10.1002/adma.201607039.

[94] D. Liu *et al.*, “ SnO 2 -Based Perovskite Solar Cells: Configuration Design and Performance Improvement ,” *Sol. RRL*, 2019, doi: 10.1002/solr.201800292.

[95] Q. Jiang, X. Zhang, and J. You, “SnO2: A Wonderful Electron Transport Layer for Perovskite Solar Cells,” *Small*. 2018, doi: 10.1002/smll.201801154.

[96] J. P. Correa Baena *et al.*, “Highly efficient planar perovskite solar cells through band alignment engineering,” *Energy Environ. Sci.*, 2015, doi: 10.1039/c5ee02608c.

[97] L. Xiong *et al.*, “Review on the Application of SnO2 in Perovskite Solar Cells,” *Advanced Functional Materials*. 2018, doi: 10.1002/adfm.201802757.

[98] F. Li *et al.*, “UV Treatment of Low-Temperature Processed SnO2 Electron Transport Layers for Planar Perovskite Solar Cells,” *Nanoscale Res. Lett.*, 2018, doi: 10.1186/s11671-018-2633-z.

[99] J. Duan, Q. Xiong, B. Feng, Y. Xu, J. Zhang, and H. Wang, “Low-temperature processed SnO 2 compact layer for efficient mesostructure perovskite solar cells,” *Appl. Surf. Sci.*, 2017, doi: 10.1016/j.apsusc.2016.06.187.

[100] G. W. Kim, D. V. Shinde, and T. Park, “Thickness of the hole transport layer in perovskite solar cells: Performance versus reproducibility,” *RSC Adv.*, 2015, doi: 10.1039/c5ra18648j.

[101] L. Lei *et al.*, “Influence of hole transport material/metal contact interface on perovskite solar cells,” *Nanotechnology*, 2018, doi: 10.1088/1361-6528/aab795.

[102] N. Marinova *et al.*, “Light harvesting and charge recombination in CH3NH3PbI3 perovskite solar cells studied by hole transport layer thickness variation,” *ACS Nano*, 2015, doi: 10.1021/acsnano.5b00447.

[103] A. Sahu and A. Dixit, “Inverted structure perovskite solar cells: A theoretical study,” *Curr. Appl. Phys.*, 2018, doi: 10.1016/j.cap.2018.10.008.

[104] S. Abdelaziz, A. Zekry, A. Shaker, and M. Abouelatta, “Investigating the performance of formamidinium tin-based perovskite solar cell by SCAPS device simulation,” *Opt. Mater. (Amst).*, 2020, doi: 10.1016/j.optmat.2020.109738.

[105] M. Shasti and A. Mortezaali, “Numerical Study of Cu2O, SrCu2O2, and CuAlO2 as Hole-Transport Materials for Application in Perovskite Solar Cells,” *Phys. Status Solidi Appl. Mater. Sci.*, 2019, doi: 10.1002/pssa.201900337.

[106] L. Lin, L. Jiang, P. Li, B. Fan, and Y. Qiu, “A modeled perovskite solar cell structure with a Cu2O hole-transporting layer enabling over 20% efficiency by low-cost low-temperature processing,” *J. Phys. Chem. Solids*, 2019, doi: 10.1016/j.jpcs.2018.09.024.

[107] T. Minemoto and M. Murata, “Theoretical analysis on effect of band offsets in perovskite solar cells,” *Sol. Energy Mater. Sol. Cells*, 2015, doi: 10.1016/j.solmat.2014.10.036.

[108] A. M. Elseman *et al.*, “Efficient and Stable Planar n-i-p Perovskite Solar Cells with Negligible Hysteresis through Solution-Processed Cu2O Nanocubes as a Low-Cost Hole-Transport Material,” *ChemSusChem*, 2019, doi: 10.1002/cssc.201901430.

[109] A. B. Coulibaly, S. O. Oyedele, N. R. Kre, and B. Aka, “Comparative Study of Lead-Free Perovskite Solar Cells Using Different Hole Transporter Materials,” *Model. Numer. Simul. Mater. Sci.*, 2019, doi: 10.4236/mnsms.2019.94006.

[110] F. Igbari, M. Li, Y. Hu, Z. K. Wang, and L. S. Liao, “A room-temperature CuAlO2 hole interfacial layer for efficient and stable planar perovskite solar cells,” *J. Mater. Chem. A*, 2015, doi: 10.1039/c5ta07957h.

[111] C. Devi and R. Mehra, “Device simulation of lead-free MASnI3 solar cell with CuSbS2 (copper antimony sulfide),” *J. Mater. Sci.*, 2019, doi: 10.1007/s10853-018-03265-y.

[112] N. Arora *et al.*, “Perovskite solar cells with CuSCN hole extraction layers yield stabilized efficiencies greater than 20%,” *Science (80-.).*, 2017, doi: 10.1126/science.aam5655.

[113] M. Jung *et al.*, “Thermal Stability of CuSCN Hole Conductor-Based Perovskite Solar Cells,” *ChemSusChem*, 2016, doi: 10.1002/cssc.201600957.

[114] P. Caprioglio *et al.*, “On the Relation between the Open-Circuit Voltage and Quasi-Fermi Level Splitting in Efficient Perovskite Solar Cells,” *Adv. Energy Mater.*, 2019, doi: 10.1002/aenm.201901631.

[115] M. Nolan, “Defects in Cu2O, CuAlO2 and SrCu2O2 transparent conducting oxides,” *Thin Solid Films*, 2008, doi: 10.1016/j.tsf.2008.04.020.

[116] L. Lin *et al.*, “Simulated development and optimized performance of CsPbI3 based all-inorganic perovskite solar cells,” *Sol. Energy*, 2020, doi: 10.1016/j.solener.2020.01.081.

[117] F. Azri, A. Meftah, N. Sengouga, and A. Meftah, “Electron and hole transport layers optimization by numerical simulation of a perovskite solar cell,” *Sol. Energy*, 2019, doi: 10.1016/j.solener.2019.02.017.

[118] X. Zheng *et al.*, “Boron Doping of Multiwalled Carbon Nanotubes Significantly Enhances Hole Extraction in Carbon-Based Perovskite Solar Cells,” *Nano Lett.*, 2017, doi: 10.1021/acs.nanolett.7b00200.

[119] F. Behrouznejad, S. Shahbazi, N. Taghavinia, H. P. Wu, and E. Wei-Guang Diau, “A study on utilizing different metals as the back contact of CH3NH3PbI3 perovskite solar cells,” *J. Mater. Chem. A*, 2016, doi: 10.1039/c6ta05938d.

[120] W. Ming, D. Yang, T. Li, L. Zhang, and M. H. Du, “Formation and Diffusion of Metal Impurities in Perovskite Solar Cell Material CH3NH3PbI3: Implications on Solar Cell Degradation and Choice of Electrode,” *Adv. Sci.*, 2018, doi: 10.1002/advs.201700662.

[121] T. Minemoto and M. Murata, “Impact of work function of back contact of perovskite solar cells without hole transport material analyzed by device simulation,” *Curr. Appl. Phys.*, 2014, doi: 10.1016/j.cap.2014.08.002.

[122] Z. Wu *et al.*, “Highly Efficient and Stable Perovskite Solar Cells via Modification of Energy Levels at the Perovskite/Carbon Electrode Interface,” *Adv. Mater.*, 2019, doi: 10.1002/adma.201804284.

[123] S. Svanström, T. J. Jacobsson, G. Boschloo, E. M. J. Johansson, H. Rensmo, and U. B. Cappel, “Degradation Mechanism of Silver Metal Deposited on Lead Halide Perovskites,” *ACS Appl. Mater. Interfaces*, 2020, doi: 10.1021/acsami.9b20315.

[124] Y. Kato, L. K. Ono, M. V. Lee, S. Wang, S. R. Raga, and Y. Qi, “Silver Iodide Formation in Methyl Ammonium Lead Iodide Perovskite Solar Cells with Silver Top Electrodes,” *Adv. Mater. Interfaces*, 2015, doi: 10.1002/admi.201500195.

[125] J. Zhao *et al.*, “Is Cu a stable electrode material in hybrid perovskite solar cells for a 30-year lifetime?,” *Energy Environ. Sci.*, 2016, doi: 10.1039/c6ee02980a.

[126] K. Domanski *et al.*, “Not All That Glitters Is Gold: Metal-Migration-Induced Degradation in Perovskite Solar Cells,” *ACS Nano*, 2016, doi: 10.1021/acsnano.6b02613.

[127] Z. Chen *et al.*, “Thin single crystal perovskite solar cells to harvest below-bandgap light absorption,” *Nat. Commun.*, 2017, doi: 10.1038/s41467-017-02039-5.

[128] Z. Yuan *et al.*, “Approximately 800-nm-Thick Pinhole-Free Perovskite Films via Facile Solvent Retarding Process for Efficient Planar Solar Cells,” *ACS Appl. Mater. Interfaces*, 2016, doi: 10.1021/acsami.6b12637.

[129] J. Chen *et al.*, “High-Performance Thickness Insensitive Perovskite Solar Cells with Enhanced Moisture Stability,” *Adv. Energy Mater.*, 2018, doi: 10.1002/aenm.201800438.

[130] E. M. Sanehira *et al.*, “Influence of Electrode Interfaces on the Stability of Perovskite Solar Cells: Reduced Degradation Using MoOx/Al for Hole Collection,” *ACS Energy Lett.*, 2016, doi: 10.1021/acsenergylett.6b00013.

General conclusion

Organic-inorganic perovskite absorber materials are promising competitors in the PV field due to their unique properties and a sky-rocketed efficiency of over 25 % than other absorbers. The work presented in this thesis intends to enhance the phase stability and the PCE of the pristine $FAPbI_3$ perovskite device.

- ✓ Theoretical results show that the FA cation orientation influence the structural properties; specifically, a stronger electronic density distribution is found among the H_4 and H_5 hydrogens and the particular iodine atom (i.e., I_2). A weaker distribution of charge is noticed in between the Pb atoms and the FA cation.
- ✓ Employing two different strain amplitudes (i.e., 0.02 & 0.04) over the $FAPbI_3$ structure, it is possible to observe a generalized elastic stiffness behavior. The structure generates a set of EC values under a 0.02 limit that fulfills all the stability conditions of the orthorhombic structure (i.e., a stable structure), and with increasing the limit (i.e., 0.04), some of the EC results start to show negative values; thus, the structure is unstable. The instability mechanism is described based on both population and bond length observed among Hi - I_2 (where i = 2-5), which is abruptly modified outside the stability threshold (i.e., 0.04) associated with a tilting of the FA cation around C - H_1. These changes might be related to describe the α- phase to the δ-phase transition, implicating the performance of actual devices. However, using Sn instead of Pb and the Br and Cl instead of I in the same structure diminishes the lattice parameter values. Hence, based on our theoretical observation and according to the previous computational reports, to stabilize the pristine $FAPbI_3$ structure, it is essential to incorporate a small amount of appropriate cation/anion into the perovskite composition.
- ✓ Experimental results clearly illustrate and support the previous justifications, which means incorporating both Cs & Br in the pristine $FAPbI_3$ perovskite leads to the highest stabilized PV response among the other tested devices (i.e., PCE>15%). The improved phase stability in ambient conditions, charge transport, reduced recombination, and the enhanced FA cation interaction with halogens are responsible for the PV performance enhancement.
- ✓ In general, a good correlation between experimental & simulated devices can lead to a better understanding of the charge generation mechanism and active layer performance.

Therefore, we estimated Cs & Br influence on the FA-based perovskite absorber performance using SCAPS simulations. The results confirmed that the pristine $FAPbI_3$ perovskite is the most attractive absorber to get high photocurrents due to its lower optical bandgap. However, its instability in open-air justifies the use of stabilizing ions such as Cs & Br. Moreover, the effect of parasitic resistances was carefully tested, and feeding the experimental $R_{series,}$ and R_{shunt} values to SCAPS allows us to interpret the main limitations of the device's I-V characteristics.

- ✓ The results also give an insightful view of CuI or BiI doping strategy with a halide perovskite and point out the physical insight into the knowledge of doping with perovskite in relation to device performance.
- ✓ The morphological & structural characterizations revealed a drastic alteration of active layer morphology and crystalline quality of the perovskite phase upon BiI incorporation, even at low doping level, while layer-based on CuI show a significant increase of grain dimensions, with CuI-rich grain boundaries.
- ✓ The undoped device displays quite high PV performance (PCE >15%), the CuI & BiI-doped devices demonstrate poor efficiencies.
- ✓ The TPV measurements show faster recombination kinetics for the doped devices than the reference cell, even at low doping levels. Our study emphasizes that the substitution of Pb by a monovalent cation might be less detrimental to the perovskite structure than a trivalent alternative such as Bi.
- ✓ The effect of BiI_3 IL was carefully tested with different HTL's & various electrodes using SCAPS. The results exhibit that the Cu_2O & $SrCu_2O_2$ HTL's show excellent PV performance than other HTL competitors and the higher work function electrodes such as Au, Ni, and Pt are more considerable than Ag, Cr to Cu.
- ✓ The results show that the device efficiency is improved with a BiI_3 IL between Perovskite/HTL interface. The results presented in this thesis work can help to shape future research; further investigations are needed to develop commercial perovskite device architecture.

Future directions

This thesis work is entirely dedicated to the planar n-i-p perovskite architecture without employing any passivation or encapsulation strategies. Hence, there are some possible aspects as being essential to enhance the device efficiency and stability further. So, the aim of future direction is related to the following ideas,

- ✓ It would be attractive to utilize the passivation approaches to efficiently avoid bulk defects and recombination issues.
- ✓ Further study on the effect of both Copper and Bismuth iodide incorporation into the perovskite composition is necessary to understand the device mechanism.
- ✓ Some pinholes or voids are noticed in the HTL layer, especially in the Cu and Bi-doped devices compared to the standard device. It is desirable to find the alternative HTL based on the hole mobility, thermal stability, high hole extraction, and electron blocking behavior with a proper band alignment to the perovskite absorber.
- ✓ Finding the alternate chemically and physically stable electrode is essential to avoid diffusion through the HTL layer.
- ✓ Using a 2-D or 3-D based *software* program is vital to understanding the device physics than 1-D.

List of Publications

Publications in Peer-Reviewed Journals

- **S. Karthick**, H. Hawashin, N. Parou, S. Vedraine, S. Velumani, J. Bouclé, "Copper and Bismuth incorporated mixed cation perovskite solar cells by one-step solution process." Solar Energy 218 (2021) 226–236. https://doi.org/10.1016/j.solener.2021.02.053
- **S. Karthick**, J. Bouclé, S. Velumani, "Effect of Bismuth iodide (BiI_3) interfacial layer with different HTL's in FAPI based perovskite solar cell – SCAPS - 1D study." Solar Energy 218 (2021) 157–168. https://doi.org/10.1016/j.solener.2021.02.041
- **S. Karthick**, J. J. Rios-Ramirez, S. Velumani, K. S. Martirosyan, and H. Castaneda, "Stability threshold of formamidinium lead iodide determined by strain amplitudes," J. Phys. D: Appl. Phys. 53 (2020) 504003. https://doi.org/10.1088/1361-6463/abb50b.
- **S. Karthick**, S. Velumani, J. Bouclé, "Experimental and SCAPS simulated formamidinium perovskite solar cells: A comparison of device performance," Solar Energy 205 (2020) 349–357. https://doi.org/10.1016/j.solener.2020.05.041.
- **S. Karthick**, J.J. Ríos-Ramírez, S. Chakaravarthy, S. Velumani, "Electrical, Optical, and Topographical Properties of RF Magnetron Sputtered Aluminum-doped Zinc Oxide (AZO) Thin Films Complemented by First-Principles Calculations," Journal of Materials Science: Materials in Electronics, 29, 15383–15395, (2018). https://doi.org/10.1007/s10854-018-8920-8.

Publications in conference proceedings

- S. Karthick, J. J. Ríos-Ramírez and S. Velumani, "Mechanical Stability Study of BULK $FAXM_3$ Perovskites," 2020 17th International Conference on Electrical Engineering, Computing Science and Automatic Control (CCE), Mexico City, 2020, pp. 1-4. https://doi.org/10.1109/CCE50788.2020.9299135.
- S. Karthick, J. J. Ríos-Ramírez and S. Velumani, "12 Possible Orientations of organic Formamidinium cation and its structural analysis by First-Principles calculations using Van der Waals-Density functional Theory," 2018 15th International Conference on Electrical Engineering, Computing Science and Automatic Control (CCE), Mexico City, 2018, pp. 1-5. https://doi.org/10.1109/ICEEE.2018.8533994.

Annex I

Electrical, optical, and topographical properties of RF magnetron sputtered aluminum-doped zinc oxide (AZO) thin films complemented by first-principles calculations

Aluminum doped zinc oxide (AZO) is an established ETL candidate due to its excellent conductivity and transparency, especially in the visible-near-infrared (Vis–NIR) spectral range. The systematic study was carried out to understand AZO properties by both experimental and computational approaches, as far as these methodologies permit. Experimentally, AZO thin films deposited using radio frequency sputtering technique under two different sets of conditions, batch-I (150, 175, and 200 W; 0.2 mTorr; 20 min) and batch-II (70 W; 2 mTorr; 75 min). The structural, morphological, topographical, and optical properties of the deposited films were carefully investigated. The results are complemented by first-principles calculations based on the DFT performed over a 2 × 2 × 2 and 3 × 2 × 2 supercells of wurtzite ZnO to assess the effect of one aluminum atom substitution on the structural, electronic, and optical properties of the solid. Thus, we could discuss obtained computational results by comparing with the experimental measurements through a reliable construction of aluminum doping percentage models (3.12 and 2.08 at.%).

Reference

- **S. Karthick**, J.J. Ríos-Ramírez, S. Chakaravarthy, S. Velumani, "Electrical, Optical, and Topographical Properties of RF Magnetron Sputtered Aluminum-doped Zinc Oxide (AZO) Thin Films Complemented by First-Principles Calculations," Journal of Materials Science: Materials in Electronics, 29, 15383–15395, (2018). https://doi.org/10.1007/s10854-018-8920-8.